

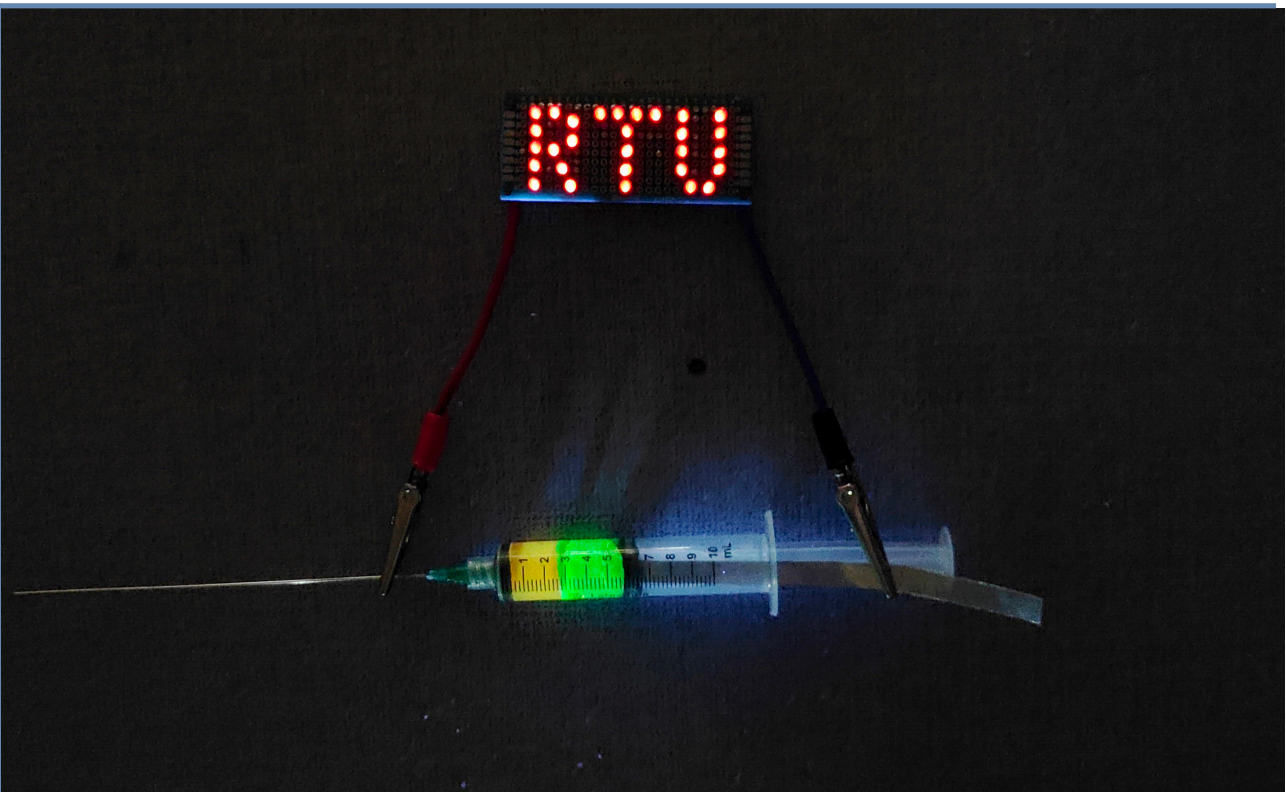
Ramona Zukule

**ELEKTRODU UN ELEKTROLĪTU IZPĒTE AMFOTĒRISKAS
ATSAISTĪTAS $Zn-MnO_2$ UZLĀDĒJAMAS BATERIJAS
IEGŪŠANAI**

Promocijas darbs

**INVESTIGATION OF ELECTRODES AND ELECTROLYTES
FOR OBTAINING AMPHOTERIC DECOUPLED $Zn-MnO_2$
RECHARGEABLE BATTERIES**

Doctoral Thesis



RĪGAS TEHNISKĀ UNIVERSITĀTE

Dabaszinātņu un tehnoloģiju fakultāte

Fizikas un materiālzinātnes institūts

RIGA TECHNICAL UNIVERSITY

Faculty of Natural Sciences and Technology

Institute of Physics and Materials Science

Ramona Zukule

Doktora studiju programmas “Ķīmija, materiālzinātne un tehnoloģijas” doktorante

Doctoral Student of the Study Programme “Chemistry, Materials Science and Engineering”

ELEKTRODU UN ELEKTROLĪTU IZPĒTE AMFOTĒRISKAS ATSAISTĪTAS Zn-MnO₂ UZLĀDĒJAMAS BATERIJAS IEGŪŠANAI

INVESTIGATION OF ELECTRODES AND ELECTROLYTES FOR OBTAINING AMPHOTERIC DECOUPLED Zn-MnO₂ RECHARGEABLE BATTERIES

Promocijas darbs

Doctoral Thesis

Zinātniskie vadītāji / Scientific supervisor

vadošais pētnieks *Dr. chem.* / Senior Researcher *Dr. chem.*

REINIS DRUNKA

vadošais pētnieks *Dr. chem.* / Senior Researcher *Dr. chem.*

GUNĀRS BAJĀRS

RTU Izdevniecība

RTU Press

Rīga 2025

Zukule R. Elektrodu un elektrolītu izpēte amfotēriskas atsaistītas Zn-MnO₂ uzlādējamas baterijas iegūšanai. Promocijas darbs. – Rīga: RTU Izdevniecība, 2025. – 145 lpp.

Zukule, R. Investigation of Electrodes and Electrolytes for Obtaining Amphoteric Decoupled Zn-MnO₂ Rechargeable Batteries. Doctoral Thesis. – Rīga: RTU Press, 2025. – 145 p.

Publicēts saskaņā ar promocijas padomes “RTU P-02” 2025. gada 4. septembra lēmumu, protokols Nr. 04030-9.2/5.

Published in accordance with the decision of the Promotion Council “RTU P-02” of September 4, 2025, Minutes No. 04030-9.2/5.

Promocijas darbs izstrādāts FLPP projektā “Elektrodu un elektrolītu izpēte amfotēras atsaistītas uzlādējamas baterijas iegūšanai” Nr. Izp-2021/1–0142.

Promocijas darbs izstrādāts ar Eiropas Sociālā fonda atbalstu darbības programmas “Izaugsmes un nodarbinātība” 8.2.2. specifiskā atbalsta mērķa “Stiprināt augstākās izglītības institūciju akadēmisko personālu stratēģiskās specializācijas jomās” projektā Nr. 8.2.2.0/20/I/008 “Rīgas Tehniskās universitātes un Banku augstskolas doktorantu un akadēmiskā personāla stiprināšana stratēģiskās specializācijas jomās”.

Pētījums tapis ar Rīgas Tehniskās universitātes Doktorantūras grantu programmas atbalstu.



The Doctoral Thesis was developed within the framework of the FLPP project “Investigation of electrodes and electrolytes for obtaining amphoteric decoupled rechargeable batteries” No. Izp-2021/1–0142.

This research was supported

- 1) by the European Social Fund within the Project No. 8.2.2.0/20/I/008 “Strengthening of PhD students and academic personnel of Riga Technical University and BA School of Business and Finance in the strategic fields of specialization” of the Specific Objective 8.2.2 “To Strengthen Academic Staff of Higher Education Institutions in Strategic Specialization Areas” of the Operational Programme “Growth and Employment”;
- 2) by Riga Technical University's Doctoral Grant programme.



PATEICĪBA

Izsaku visdziļāko pateicību visiem, kuri ir mani atbalstījuši un vadījuši visa doktorantūras ceļa laikā!

Vispirms sirsnīgi pateicos maniem galvenajiem darba vadītājiem – *Dr. chem.* Gunāram Bajāram un *Dr. chem.* Reiniem Drunkam – par viņu izcilo, profesionālo vadību un nenovērtējamo atgriezenisko saiti! Viņu padziļinātie ieteikumi un konstruktīvā kritika būtiski veicināja šīs promocijas darba izveidi.

Vēlos izteikt patiesu pateicību arī *Dr. phys.* Pāvelam Onufrijevam, kurš ir licis pamatus gan manai akadēmiskajai, gan profesionālajai attīstībai. Viņa kompetence, iedrošinājums un saprotošā attieksme kalpoja par nepārtrauktu iedvesmas avotu.

Novērtēju arī lielisko sadarbību ar pētniecības grupas kolēģiem – *Ph. D.* Anzelmu Zukulu un Ņikitu Griščenko – par viņu atbalstu, sadarbību un bagātinošajām diskusijām projekta izstrādes procesā. Kopā ar kolēģiem Mairi Iesalnieku, Lindu Laimu Alsiņu un Mārtiņu Vanagu esam bijuši daļa no daudzām rosinošām sarunām, kas ne tikai paplašināja redzesloku, bet arī palīdzēja sasniegt jaunas pētniecības virsotnes.

Esmu pateicīga arī Fizikas un materiālu zinātnes institūta kolēģiem, kā arī *Dr. chem.* Nelli Batenko un *Ph. D.* Anastasijai Gailei par viņu neatlaidīgo palīdzību un iedrošinājumu, kas manu pētniecības pieredzi padarīja gan produktīvu, gan patiesi aizraujošu.

Visbeidzot, vēlos izteikt sirsnīgu pateicību savam dzīvesbiedram un ģimenei – viņu nelokāmā mīlestība un bezgalīgais atbalsts bija patiess balsts visa šī ceļa laikā. Viņu ticība man un emocionālais atbalsts bija izšķiroši, lai es spētu saglabāt fokusu un motivāciju pat vissarežģītākajos brīžos.

PROMOCIJAS DARBS IZVIRZĪTS ZINĀTNES DOKTORA GRĀDA IEGŪŠANAI RĪGAS TEHNISKAJĀ UNIVERSITĀTĒ

Promocijas darbs zinātnes doktora (*Ph. D.*) grāda iegūšanai tiek publiski aizstāvēts 2025. gada 10. decembrī Rīgas Tehniskās universitātes Materiālzinātnes nozares promocijas padomes “RTU P-02” atklātā sēdē tiešsaistē *Zoom* platformā: <https://rtucloud1.zoom.us/j/96283313764>; ID: 962 8331 3764

OFICIĀLIE RECENZENTI

Profesors *Dr. chem.* Donāts Erts
Latvijas universitāte, Latvija

Profesors *Ph. D.* Agris Bērziņš
Latvijas universitāte, Latvija

Asociētais profesors *Ph. D.* Alar Jānes
Tartu Universitāte, Igaunija

APSTIPRINĀJUMS

Apstiprinu, ka esmu izstrādājusi šo promocijas darbu, kas iesniegts izskatīšanai Rīgas Tehniskajā universitātē zinātnes doktora (*Ph. D.*) grāda iegūšanai. Promocijas darbs zinātniskā grāda iegūšanai nav iesniegts nevienā citā universitātē.

Ramona Zukule (paraksts)

Datums:

Promocijas darbs sagatavots kā tematiski vienotu zinātnisko publikāciju kopa ar kopsavilkumu latviešu un angļu valodā. Promocijas darbs apkopo četras oriģinālpublikācijas un vienu apskatrakstu *Scopus* indeksētos žurnālos. Publikācijas zinātniskajos žurnālos uzrakstītas angļu valodā, to kopējais apjoms, neieskaitot pielikumus, ir 57 lappuses.

SATURS

PROMOCIJAS DARBA VISPĀRĒJS RAKSTUROJUMS.....	7
Tēmas aktualitāte.....	7
Pētījuma mērķis un uzdevumi.....	8
Aizstājamās tēzes	9
Zinātniskā novitāte.....	9
Darba praktiskā nozīme.....	9
Darba struktūra un apjoms	10
Darba aprobācija un publikācijas	10
Zinātniskās publikācijas	10
Nozīmīgākā dalība konferencēs	10
LITERATŪRAS APSKATS UN REZULTĀTI.....	12
1. Literatūras apskats par ūdens elektrolīta Zn-MnO ₂ bateriju darbību atkarībā no elektrolīta vides pH.....	12
1.1. Sārma elektrolīta Zn-MnO ₂ baterijas.....	12
1.2. Neitrāla un skāba elektrolīta Zn-MnO ₂ baterijas.....	14
1.3. Duāla/amfotēra elektrolīta Zn-MnO ₂ baterijas.....	15
2. Galvenie rezultāti par MnO ₂ katoda veiktspējas uzlabošanu skābā elektrolītā.....	17
2.1. Metodoloģija.....	17
2.2. Rezultāti.....	18
3. Galvenie rezultāti par Zn anoda veiktspējas uzlabošanu sārmainā elektrolītā.....	24
3.1. Metodoloģija.....	24
3.2. Rezultāti.....	25
4. Galvenie rezultāti par amfotēras baterijas izveidi ar dažādas vides pH hidrogelu elektrolītiem.....	31
4.1. Metodoloģija.....	31
4.2. Rezultāti.....	32
SECINĀJUMI	36
LITERATŪRAS SARAKSTS	71

LIETOTIE SAĪSINĀJUMI

<i>OCV</i>	atvērta ķēdes spriegums (<i>open circuit voltage</i>)
<i>CB</i>	sīkdispersa ogle (<i>carbon black</i>)
<i>CV</i>	cikliskā voltampēometrija
<i>EIS</i>	elektroķīmiskā impedances spektroskopija
<i>GCD</i>	galvanostatiskā uzlāde-izlāde (<i>galvanostatic charge-discharge</i>)
<i>HER</i>	ūdeņraža izdalīšanās reakcija (<i>hydrogen evolution reaction</i>)
<i>NMP</i>	N-metil-2-pirolidons
<i>OER</i>	skābekļa izdalīšanās reakcija (<i>oxygen evolution reaction</i>)
<i>SEM</i>	skenējošais elektronu mikroskops
<i>XPS</i>	rentgenstaru fotoelektronu spektroskopija (<i>X-ray photoelectron spectroscopy</i>)
<i>XRD</i>	rentgenstaru difrakcija (<i>X-ray diffraction</i>)

PROMOCIJAS DARBA VISPĀRĒJS RAKSTUROJUMS

Tēmas aktualitāte

Līdz ar pieaugošo atjaunojamo enerģijas avotu izmantošanu un dažādu nozaru elektrifikāciju globālais pieprasījums pēc efektīviem un ilgtspējīgiem enerģijas uzglabāšanas risinājumiem tikai pieaug [1]–[5]. Atjaunojamajiem enerģijas avotiem ir raksturīga enerģijas ražošanas neregularitāte, piemēram, Saules enerģiju ir iespējams iegūt tikai diennakts gaišajā laikā [6]–[8]. Tādēļ uzlādējamām baterijām ir būtiska nozīme atjaunojamo energoresursu neregularitātes mazināšanā, nodrošinot uzticamu enerģijas uzglabāšanu un stabilu elektroenerģijas apgādi pēc pieprasījuma [9]–[12]. Patlaban viena no izplatītākajām un veiksmīgākajām elektroenerģijas uzkrāšanas iespējām ir litija jonu uzlādējamās baterijas [13]–[17]. Tām ir augsts enerģijas (līdz 500 Wh/g) un jaudas (līdz 300 W/kg) blīvums, Li anodam ir liela teorētiskā kapacitāte jeb lādiņietilpība (3860 mA h/g), augsts darbības spriegums ($> 3,7$ V), kā arī augsta uzlādes-izlādes stabilitāte (vairāk nekā 10 000 ciklu) ar zemu pašizlādi [18]–[24]. Tomēr litija jonu uzlādējamo bateriju galvenie trūkumi ir to drošība, kas saistīta ar pārkaršanu un iespējamo pašai aizdegšanos [25]–[29], kā arī ierobežotās litija ieguves iespējas [30]–[33]. Šie aspekti ir mudinājuši meklēt alternatīvas, attīstot jaunas vai uzlabojot esošās bateriju tehnoloģijas.

No jau esošajām bateriju tehnoloģijām ievērojamu uzmanību ir piesaistījušas ūdens elektrolīta Zn-MnO₂ baterijas, kas jau šobrīd dominē neuzlādējamo bateriju tirgū [34], [35]. Tām ir zemākas izmaksas, augstāka drošība, tās ir videi draudzīgākas, salīdzinot ar litija jonu uzlādējamajām baterijām [36]–[38]. Tomēr nākotnes mērķiem nepieciešams attīstīt šo bateriju potenciālo lietojumu uzlādējamo bateriju jomā, un tas saistīts ar vairākiem izaicinājumiem, piemēram, elektrolīta stabilitāte, elektrodu degradācija un veikspējas ierobežojumi [19],[39]–[43].

Viena no problēmām, kas raksturīga Zn-MnO₂ uzlādējamām baterijām, ir zemais darba spriegums un sliktā ciklējāmība, kas izriet no MnO₂ katoda nestabilitātes un nevēlamajām blakusreakcijām, tādām kā MnO₂ disproporcionēšanās un šķīšana, fāžu pārejas uz ķīmiski neaktīvām fāzēm, skābekļa izdalīšanās reakcija (*OER*) un ķīmiski neaktīvu savienojumu veidošanās ar Zn²⁺ joniem [44], [45]. Lai optimizētu šo uzlādējamo bateriju veikspēju, ir pētīti dažādi elektrolītu sastāvi, tostarp sārmaini [19], [38], [46], [47], neitrāli [48]–[51] un skābi [52], [53], tomēr katra pieeja nevēlami ietekmē cikla ilgumu, efektivitāti un reakcijas kinētiku. Piemēram, sārmaina elektrolīta apstākļos izlādes procesā Mn²⁺ joni reaģē ar OH⁻ un veido nešķīstošas Mn(OH)₂ nogulsnes, skābā elektrolītā Zn anods korodē, neitrālā elektrolītā veidojas ķīmiski neaktīvas fāzes kā ZnMn₂O₄. Savukārt tālāka elektrolītu pielāgošana un izpēte, veidojot pH gradienta elektrolītus un divu elektrolītu sistēmas, veicina ievērojamus uzlabojumus Zn-MnO₂ sistēmu elektroķīmiskajā stabilitātē un darba sprieguma palielināšanā. Rūpīgi pielāgojot elektrolīta vidi ap anodu un katodu, iespējams paplašināt elektroķīmisko ūdens sadalīšanās diapazonu, vienlaikus mazinot nevēlamās blakusreakcijas [54]–[59].

Papildus elektrolītu optimizācijai nepieciešams pievērst uzmanību arī MnO₂ katoda strukturālajai stabilitātei. MnO₂ ir vairāki polimorfī, un tiem ir dažādas elektroķīmiskās īpašības atkarībā no to kristāla struktūras. Attiecīgajai fāžu rindai $\alpha > \delta > \beta$, teorētiskā kapacitāte

samazinās, tādējādi dažādas fāzes uzrāda atšķirīgu elektroķīmisko ciklējamību un jonu difūziju [60]–[62]. Ja sāmainos elektrolītos MnO_2 katods veido elektroķīmiski neaktīvas fāzes kā $\text{Mn}(\text{OH})_2$, Mn_2O_3 un Mn_3O_4 [19], tad skābos elektrolītos blakusreakciju rezultātā tas var izšķīst vai pāriet citā polimorfā [40], [63], kas izraisa kapacitātes samazināšanos. Heteroatomu ievadīšana elektrodu struktūrā ir potenciāls šo problēmu risinājums, lai uzlabotu elektroķīmiskās īpašības [64]. Līdz šim ir veikti pētījumi, apskatot heteroatomu ietekmi uz MnO_2 , sārmainos un neitrālos elektrolītos. Piemēram, dopēšana ar Co [65]–[67], kā arī Mo [68], [69] veicina defektu rašanos MnO_2 kristālrežģī, kas stabilizē kādu konkrētu polimorfo struktūru. Savukārt dopēšana ar Bi [34],[70]–[73] sašaurina MnO_2 aizliegtās zonas platumu, kas palielina MnO_2 elektrisko vadītspēju, lai ļautu efektīvāk pārvietoties elektroķīmiskajai reakcijai nepieciešamajiem elektroniem, tādējādi veicinot elektroķīmiskās šķīšanas un nogulsnešanās procesu.

Vēl viens būtisks ierobežojums ūdens elektrolīta Zn jonu baterijām ir metāliskā Zn anoda nestabilitāte, kā rezultātā veidojas dendrīti, norisinās ūdeņraža izdalīšanās reakcija (*HER*) un notiek virsmas pasīvācija [41]–[43]. Lai novērstu šīs nevēlamās blakusreakcijas, ir pētītas dažādas virsmas modifikācijas metodes ar mērķi uzlabot Zn anoda elektroķīmiskās īpašības. Galvenie virzieni ir saistīti ar elektroda virsmas pārklāšanu vai elektrolīta modificēšanu, kas kontrolē anoda elektroķīmiskās šķīšanas un nogulsnešanās reakcijas. Daži no pārklājumu veidiem iekļauj CaCO_3 [74], ZnO [75]–[77], ZrO_2 [78]–[80] un TiO_2 [81]–[83], kā arī dažādu polimēru pārklājumu veidošanu [84]–[87].

Šo pētījumu tālāka attīstīšana, kas ietver elektrolītu izstrādi, katoda stabilizāciju, Zn virsmas modificēšanu un integrāciju baterijās, ir nozīmīgs solis ceļā uz uzlādējamu ūdens elektrolīta Zn-MnO₂ bateriju komercializāciju. Tādēļ šajā promocijas darbā pievērsta uzmanība galvenajiem ierobežojumiem elektrolīta, katoda un anoda līmenī ar mērķi veicināt tādas uzlādējamās baterijas attīstību, kurai ir lielāks enerģijas blīvums, uzlabota drošība un kas ir elektroķīmiski ciklējama.

Pētījuma mērķis un uzdevumi

Promocijas darba mērķis ir izstrādāt konceptu ūdens elektrolīta Zn-MnO₂ bateriju sprieguma palielināšanai virs 2 V, kā arī izpētīt nepieciešamās elektrolīta, katoda un anoda modifikācijas šī koncepta realizēšanai.

Darba mērķa sasniegšanai tika definēti vairāki uzdevumi.

1. Izstrādāt stratēģiju ūdens bāzes elektrolīta lādējamu bateriju darba sprieguma palielināšanai virs 2 V, apejot ūdens sadalīšanās sprieguma ierobežojumus.
2. Sintezēt MnO_2 pulverus, kas dopēti ar Bi un Mo joniem. Novērtēt iegūto materiālu īpašības, izmantojot dažādas analīžu metodes, un sagatavot plānos pārklājumus uz oglekļa papīra. Veikt elektroķīmiskos mērījumus sagatavotajiem pārklājumiem skābā elektrolītā.
3. Modificēt Zn plāksnes ar impulsu lāzeru pie dažādām enerģijas plūsmām. Veikt sagatavoto paraugu raksturošanu, izmantojot dažādas analīžu metodes, un veikt elektroķīmiskos mērījumus bāziskā elektrolītā.
4. Izveidot pH gradienta elektrolītu, izmantojot hidrogelus. Izveidot Zn-MnO₂ bateriju, izmantojot sagatavoto pH gradienta elektrolītu, veikt elektroķīmiskos mērījumus un

noteikt, vai ir iespējams paplašināt ūdens elektrolīta darbības sprieguma diapazonu virs 2 V.

Aizstāvamās tēzes

1. pH gradienta elektrolīta sistēma, kurā pie anoda ir sārmaina vide, pie katoda – skāba vide, palielina ūdens elektroķīmisko sadalīšanās sprieguma diapazonu.
2. MnO₂ katoda dopēšana ar Bi³⁺ un Mo⁶⁺ joniem uzlabo elektroķīmisko darbību skābā elektrolītā.
3. Zn anoda stabilitāti sārmainā elektrolītā uzlabo anoda virsmas strukturēšana ar impulsu lāzeru.
4. Izmantojot *Pluronic F-127* micellu tipa hidrogelu, ir izveidojama lādējama amfotēra ūdens elektrolīta Zn-MnO₂ baterija.
5. Ūdens elektrolīta Zn-MnO₂ bateriju ar spriegumu virs 2 V ir iegūstama, izmantojot divu atšķirīgu pH elektrolītu jeb amfotēru sistēmu.

Zinātniskā novitāte

Šajā promocijas darbā izstrādāta un realizēta inovatīva pieeja ūdens Zn-MnO₂ uzlādējamas baterijas dizainam, tādējādi novēršot fundamentālus ierobežojumus elektrodu un elektrolītu līmenī. Darbā apvienotas stratēģijas elektrodu materiālu modificēšanā, elektrolītu inženierijā un bateriju dizaina pilnveidē, lai paplašinātu baterijas darba sprieguma diapazonu un uzlabotu elektroķīmisko veiktspēju. Veikti pētījumi, lai uzlabotu materiālu stabilitāti un elektroķīmiski veiktspēju dažādās pH elektrolīta vidēs un izstrādāta jauna bateriju koncepcija, kuras pamatā ir atdalītas katoda un anoda elektrolīta telpas. Darba rezultāti atspoguļo ūdens bāzes elektrolīta bateriju komponentu struktūras un īpašību attiecības, ko iespējams lietot alternatīvu enerģijas uzkrāšanas sistēmu pilnveidē.

Darba praktiskā nozīme

1. Ūdens elektrolīta Zn-MnO₂ uzlādējamu bateriju izstrāde ar palielinātu darba spriegumu, lai veicinātu drošāku un efektīvāku alternatīvu enerģijas uzkrāšanas sistēmu izstrādi.
2. Divu elektrolītu sistēmas koncepta izveide, kas samazina parazītiskās reakcijas uz elektrodiem, tādējādi uzlabojot elektroķīmisko stabilitāti, kā alternatīva tradicionālajām bateriju konstrukcijām.
3. Mērogojamu metožu (pusvadītāju dopēšanas ar heteroatomiem hidrotēmālās metodes ceļā un metālu virsmas strukturēšanas ar impulsu lāzeru) izstrāde elektrodu modificēšanai, kas palielina specifisko kapacitāti.
4. Uzlādējamu bateriju izveide, kā elektrodu materiālus izmantojot Zemes garozā bieži sastopamus elementus, veidojot alternatīvu bateriju tehnoloģiju, kas nav atkarīga no kritiskām izejvielām.

Darba struktūra un apjoms

Promocijas darbs sagatavots kā tematiski vienota zinātnisko publikāciju kopa, kas veltīta pētījumiem par amfotēras ūdens elektrolīta Zn-MnO₂ uzlādējamās baterijas izveidi un tās elektrolītu un elektrodu atsevišķu pilnveidi. Promocijas darbs ietver četras oriģinālpublikācijas un vienu apskatrakstu *Scopus* indeksētos žurnālos.

Darba aprobācija un publikācijas

Promocijas darba galvenie rezultāti publicēti četrās zinātniskajās oriģinālpublikācijās un vienā apskatrakstā. Promocijas darba izstrādes laikā sagatavots viens apskatraksts. Pētījumu rezultāti prezentēti 17 zinātniskajās konferencēs.

Zinātniskās publikācijas

1. **R. Durena**, N. Griscenko, L. Orlova, M. Bertins, A. Viksna, M. Iesalnieks, A. Zukuls. Synthesis, structure, and electrochemical performance of Bi-induced stabilization of MnO₂ cathodes for use in highly acidic aqueous electrolytes (pH <2). *Journal of Alloys and Compounds*, 1010, **2025**, 177904. <https://doi.org/10.1016/j.jallcom.2024.177904> (IF 5,8, CiteScore 11,1).
2. **R. Dūrena**, L. Fedorenko, Ņ. Griščenko, M. Vanags, L. Orlova, P. Onufrijevs, S. Stanionyte, T. Malinauskas A. Zukuls. Irradiating the Path to High-Efficiency Zn-Ion Batteries: An Electrochemical Analysis of Laser-Modified Anodes. *Global Challenges*, 8 (10), **2024**, 2400105. <https://doi.org/10.1002/gch2.202400105> (IF 4,4, CiteScore 8,7).
3. Ņ. Griščenko, **R. Dūrena**, M. Iesalnieks, M. Bērtiņš, A. Viksna, A. Zukuls. Improvement of manganese dioxide cathode by molybdenum doping in highly acidic electrolyte. *Journal of Energy Storage*, 76, **2024**, 109847. <https://doi.org/10.1016/j.est.2023.109847> (IF 8,9, CiteScore 11,8).
4. **R. Durena**, A. Zukuls. A Short Review: Comparison of Zinc–Manganese Dioxide Batteries with Different pH Aqueous Electrolytes. *Batteries*, **2023**, 9 (6), 311. <https://doi.org/10.3390/batteries9060311> (IF 5,3).
5. **R. Durena**, A. Zukuls, M. Vanags, A. Šutka. How to increase the potential of aqueous Zn-MnO₂ batteries: The effect of pH gradient electrolyte. *Electrochimica Acta*, **2022**, 434, 141275. <https://doi.org/10.1016/j.electacta.2022.141275> (IF 5,5, CiteScore 11,3).

Nozīmīgākā dalība konferencēs

1. **R. Dūrena**, Ņ. Griščenko, A. Zukuls. High-Potential 2 V Rechargeable Zinc-Manganese Dioxide Batteries Enabled by Polymer Hydrogels. *2024 MRS Fall Meeting*. Bostona, ASV. 01.12.–06.12., **2024**. EN08.08.25.
2. **R. Dūrena**, Ņ. Griščenko, A. Zukuls. Extending the Electrochemical Window of Aqueous Zn-MnO₂ Batteries through pH Gradient Dual-Electrolyte. *Battery 2030+’s 4th Annual Conference & Young Scientists gathering*. Grenoble, Francija. 27.05.–29.05., **2024**. P37.

3. **R. Dūrena**, N. Griščenko, A. Zukuls. Enhanced capacity retention of MnO₂ cathode enabled by Bi doping. *8th Baltic Electrochemistry Conference: Finding New Inspiration 2*. Tartu, Igaunija. 14.04.–17.04., **2024**. P24.
4. **R. Dūrena**, A. Zukuls, M. Vanags. Amphoteric Zinc-Manganese Dioxide Aqueous Battery Exceeding 2V Potential. *16th International Conference on materials chemistry*. Dublin, Īrija. 03.06.–06.06., **2023**. P256.
5. **R. Dūrena**, A. Zukuls, M. Vanags. 2.4 V Open-Circuit Potential Aqueous Zn-MnO₂ Rechargeable Battery with pH gradient hydrogel electrolyte. *European Materials Research Society Spring Meeting*. Strasbūra, Francija, 29.05.–02.06., **2023**. D_P01-33.

LITERATŪRAS APSKATS UN REZULTĀTI

Promocijas darba literatūras apskats un rezultāti izklāstīti četrās nodaļās, kas apvieno vienu apskatrakstu un četras oriģinālpublikācijas.

1. Literatūras apskats par ūdens elektrolīta Zn-MnO₂ bateriju darbību atkarībā no elektrolīta vides pH, kā arī duālās baterijas koncepta izvērtējums un skaidrojums, kas apkopots apskatrakstā (1. pielikums).
2. Pētījuma par MnO₂ katoda darbības un veiktspējas uzlabošanu ļoti skābā elektrolītā, iesaistot Bi un Mo jonus MnO₂ struktūrā, rezultāti, kas apkopoti 1. oriģinālpublikācijā (2. pielikums) un 2. oriģinālpublikācijā (3. pielikums).
3. Pētījuma par Zn anoda darbības un veiktspējas uzlabošanu sārmainā elektrolītā, izmantojot virsmas strukturēšanu ar augstas jaudas impulsu lāzeru, rezultāti, kas apkopoti 3. oriģinālpublikācijā (4. pielikums).
4. Pētījuma par duālas ūdens elektrolīta Zn-MnO₂ uzlādējamās baterijas izveidi un elektroķīmiskajiem parametriem, rezultāti, kas apkopoti 4. oriģinālpublikācijā (5. pielikums).

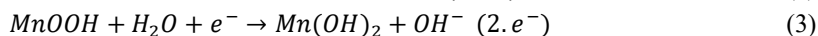
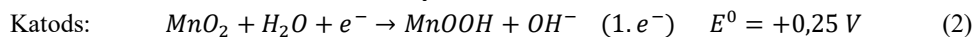
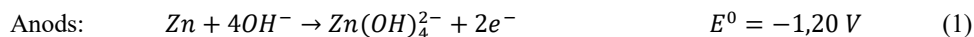
1. Literatūras apskats par ūdens elektrolīta Zn-MnO₂ bateriju darbību atkarībā no elektrolīta vides pH

Ūdens elektrolīta Zn-MnO₂ neuzlādējamo bateriju pirmsākumi meklējami 1866. gadā, kad franču zinātnieks Žoržs Leklanšē izgatavoja un patentēja pirmo Zn-MnO₂ neuzlādējamo bateriju, sauktu par Leklanšē šūnu [7]. Šo neuzlādējamo bateriju tālāko pilnveidi 20. gadsimta 50. gados veica kanādiešu inženieris Luiss Urrijs, kurš 1960. gadā patentēja sārma Zn-MnO₂ neuzlādējamo bateriju [88]–[91]. Zinātnieki un inženieri vēl aizvien turpina pilnveidot šīs neuzlādējamās baterijas, cenšoties pagarināt to efektīvo lietošanas ilgumu un aizvietot bīstamos elementus, piemēram, dzīvsudrabu, kas tiek pievienots, lai mazinātu tādas nevēlamas blakusreakcijas kā ūdeņraža gāzes izdalīšanos. Tādējādi ūdens sārma Zn-MnO₂ neuzlādējamās baterijas ir visilgāk un visplašāk izmantotā neuzlādējamo bateriju tehnoloģija, kas joprojām dominē pasaules tirgu [92]. Tas varētu būt saistīts ar to, ka ūdens elektrolīta Zn-MnO₂ neuzlādējamās baterijas nerada lielus drošības riskus, Zn metālam ir zems toksiskums (LD50 = 630 mg/kg – žurkām) [93], Zn²⁺/Zn divu elektronu reakcijai ir salīdzinoši augsta teorētiskā kapacitāte – 820 mAh/g [36], [37], MnO₂/Mn²⁺ divu elektronu reakcijas teorētiskā kapacitāte ir 617 mAh/g [38], [94], [95], turklāt gan cinks, gan mangāns Zemes garozā ir plaši izplatīti elementi [36], [37].

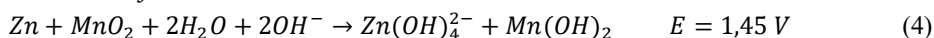
1.1. Sārma elektrolīta Zn-MnO₂ baterijas

Ūdens sārma Zn-MnO₂ baterija sastāv no Zn metāla anoda, MnO₂ katoda, kā arī koncentrēta KOH ūdens šķīduma (> 30 %) elektrolīta. Katodam parasti tiek pievienota sīkdispersas ogles *carbon black* (CB) daļiņas, lai nodrošinātu katoda vadītspēju, jo pats MnO₂ ir nevadošs. Šīs neuzlādējamās baterijas shēma redzama 1.1. attēlā – Zn anods iesaistās elektroķīmiskajā

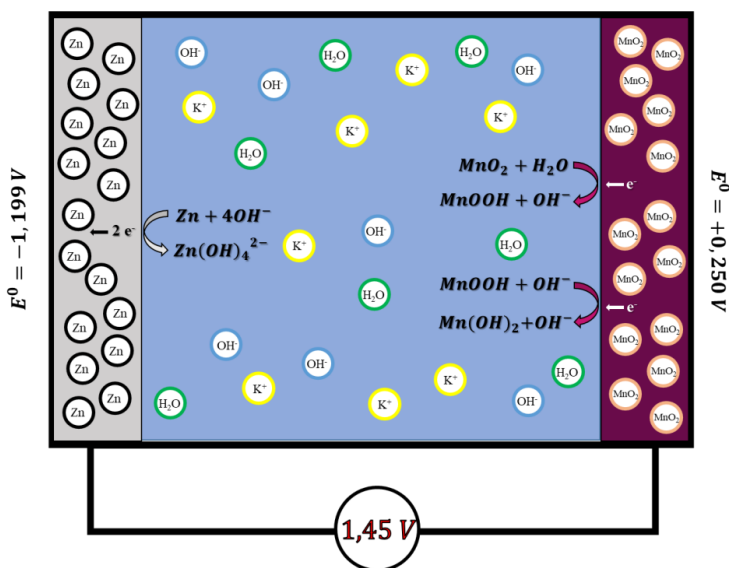
reakcijā (1) ar standartpotenciālu $-1,199\text{ V}$, savukārt katoda aktīvā komponente MnO_2 reakcijās (2) un (3) ar standartpotenciālu $+0,250\text{ V}$. Tādējādi sārma baterijā kopumā notiek reakcija (4), kā rezultātā baterijas OCV ir $1,45\text{ V}$ [6], [94], [96], [97].



Summārā reakcija:



Sārma Zn-MnO₂ baterijas ir jau ilgstoši zināma tehnoloģija, un tās vēl aizvien tiek pētītas. Lai gan šīs baterijas ir plaši izplatītas kā neuzlādējamā tipa baterijas, tās vēl aizvien nav izplatītas kā uzlādējamās baterijas. Tas galvenokārt saistīts ar elektroķīmiski neaktīvu mangāna oksīdu Mn₃O₄ un ZnMn₂O₄ veidošanos. Šie savienojumi veidojas dziļās izlādes procesā [88], [98]. Tādējādi dažu pirmo uzlādes-izlādes ciklu laikā elektroķīmiski neaktīvie savienojumi pārklāj katoda aktīvā MnO₂ savienojuma daļiņas, apturot tālāku reakcijas gaitu, kas strauji samazina baterijas kapacitāti. Zinātniskajā literatūrā ir aprakstīti dažādi veidi, kā sārma elektrolītā šo nevēlamo efektu samazināt vai novērst, piemēram, MnO₂ katodu dopējot ar Bi vai Cu joniem [94], [99], kā arī modificējot elektrolītu, pievienojot papildu jonus [100]–[102], piemēram, Li⁺ [98].

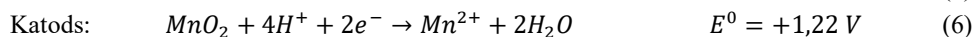


1.1. att. Sārma ūdens elektrolīta Zn-MnO₂ bateriju shematisks darbības mehānisms.

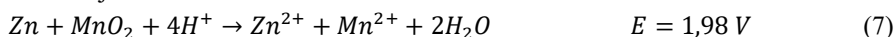
1.2. Neitrāla un skāba elektrolīta Zn-MnO₂ baterijas

Elektrolīta modifikācija Zn-MnO₂ baterijās ir virzīta arī tālāk, samazinot elektrolīta pH no bāziska līdz neitrālam un pat skābam, tādējādi izmainot baterijā notiekošās reakcijas, kā redzams skāba ūdens elektrolīta Zn-MnO₂ baterijas shematiskajā attēlā (1.2. att.). Tajās KOH, NaOH un LiOH [97], [98], [103]–[105] bāziskais elektrolīts ir aizstāts ar ZnSO₄, MnSO₄, K₂SO₄, Na₂SO₄ [106]–[111] sāļu šķīdumiem un/vai atšķaidītas skābes elektrolītu [52], [53]. Kā redzams mangāna savienojumu Purbē (*Pourbaix*) diagrammā (1.3. a. att.), kas attēlo elementa standartpotenciāla izmaiņas ūdens elektrolītā atkarībā no vides pH, pie augstākām pH vērtībām MnO₂ elektroķīmiskā reakcija norisinās pie standartpotenciāla 0,250 V, kā arī pastāv iespējami veidoties elektroķīmiski neaktīvajai Mn₂O₃ fāzei. Savukārt, pazeminot elektrolīta pH līdz skābam, MnO₂ katoda sastāvā esošais skābekļa atoms var savienoties ar H⁺ joniem no elektrolīta, veidojot ūdens molekulu. Tādējādi Mn⁴⁺ joni var tikt reducēti uz Mn²⁺ joniem, kas tālāk nonāk elektrolīta šķīdumā bez elektroķīmiski neaktīvās Mn₂O₃ fāzes veidošanās. Turklāt attiecīgā MnO₂ reakcija skābā vidē norisinās pie standartpotenciāla virs 1,2 V. Tomēr šis elektrolīta vides pH samazinājums palielina Zn anoda elektroķīmiskās reakcijas potenciālu. Kā redzams cinka savienojumu Purbē diagrammā (1.3. b. att.), reakcijas standartpotenciāla pieaugums ir no –1,199 V sārmainā vidē līdz –0,762 V skābā vidē.

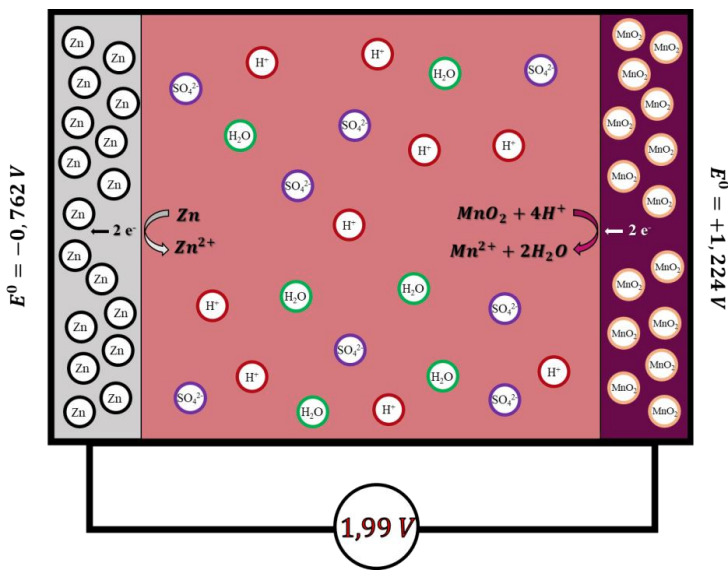
Neskatoties uz Zn anoda standartpotenciāla palielinājumu, kopumā šādas baterijas konstrukcija rezultējas ar augstāku baterijas darbības spriegumu līdz pat 2 V saskaņā ar 5.–7. reakciju [112].



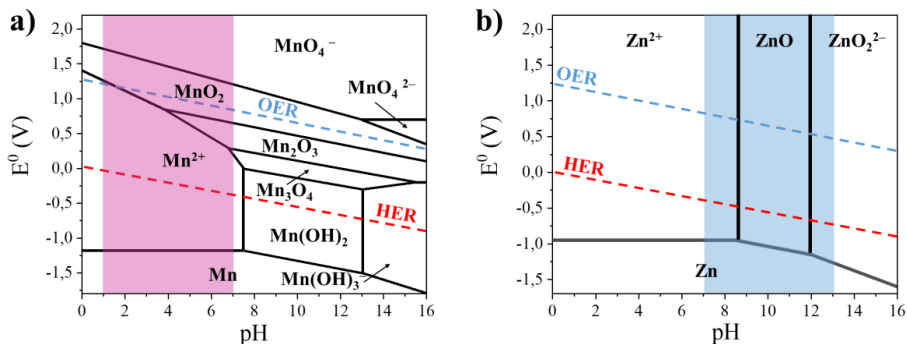
Summārā reakcija:



Tomēr skābā vidē norisinās parazītiska reakcija – Zn anoda korozija. Šajā procesā Zn anods disociē elektrolītā kā Zn²⁺ joni un izdalās H₂ gāze. Šī parazītiskā reakcija ne tikai samazina baterijas kapacitāti, bet arī var izraisīt baterijas šūnas sagrūšanu [113]. Anoda parazītiskās reakcijas norise var tikt mazināta, pārklājot Zn anodu ar dūmkvarcu un polietilēnglikolu (ar molmasu 300 g/mol) [114]. Lai novērstu iespējamu MnO₂ šķīšanu, elektrolītam tiek pievienots 0,1 M MnSO₄ [107]–[110]. Tomēr arī šāda tipa baterijās ir novērota ZnMn₂O₄ fāzes veidošanās, kas ir ķīmiski neaktīva un izraisa kapacitātes sarukumu, vairojot reakcijas neatgriezeniskumu [115]. Tas liecina, ka gan sārma, gan neitrāla-skāba ūdens elektrolīta Zn-MnO₂ baterijām ir līdzīgas problēmas.



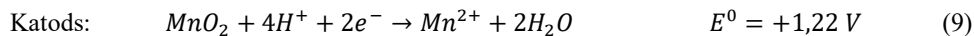
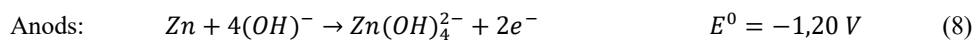
1.2. att. Skāba ūdens elektrolīta Zn-MnO₂ bateriju shematisks darbības mehānisms.



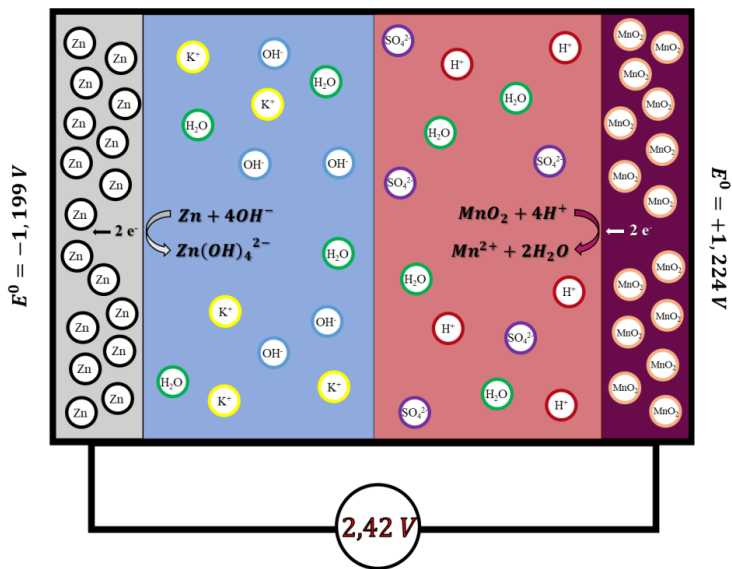
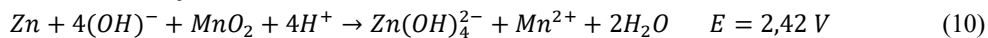
1.3. att. Purbē diagrammas ar atzīmētiem ūdens sadalīšanās potenciāliem: a) mangāna savienojumiem; b) cinka savienojumiem [116].

1.3. Duāla/amfotēra elektrolīta Zn-MnO₂ baterijas

Lai apvienotu pozitīvās īpašības no ūdens elektrolīta bāziskās un skābās vides, tika izveidota jauna tipa šūna, ar kuras palīdzību ir iespējams palielināt ūdens sadalīšanās spriegumu virs 2 V. Šī šūna sastāv no diviem atšķirīgas vides elektrolītiem tā, lai Zn anods darbotos bāziskā elektrolītā, savukārt MnO₂ katods – skābā elektrolītā. Šis unikālais baterijas dizains, kura darbības princips redzams 1.4. attēlā, nodrošina šūnas OCV palielināšanos līdz 2,45 V saskaņā ar 8.–10. reakciju [54], [113], [114].



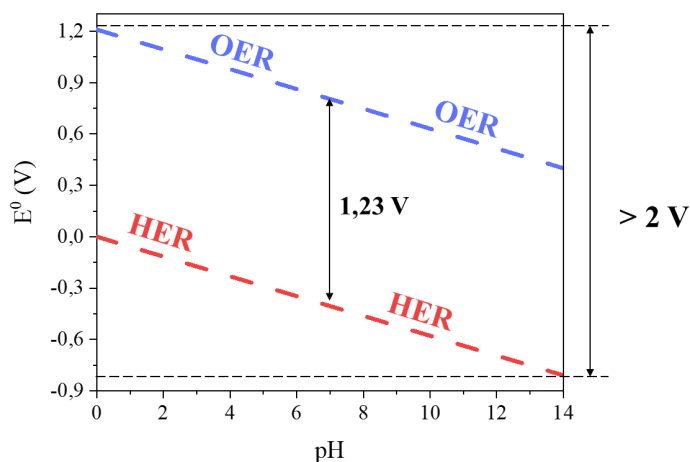
Summārā reakcija:



1.4. att. Duāla/amfotēra ūdens elektrolīta Zn-MnO₂ bateriju shematisks darbības mehānisms.

Paplašinātais ūdens sadalīšanas sprieguma diapazons var tikt izskaidrots arī ar Purbē diagrammu. Kā redzams 1.5. attēlā, ja baterijas šūna sastāv no viena elektrolīta ar konstantu pH, ūdens sadalīšanās spriegums ir 1,23 V. Tādējādi, izmantojot ūdens elektrolīta bateriju plašākā sprieguma diapazonā, var norisināties nevēlamā *OER* un *HER*. Savukārt, ja tiek izmantota duālā/amfotērā elektrolītu sistēma, ir iespējams iegūt stabilu ūdens elektrolīta elektroķīmisko sprieguma diapazonu virs 2 V. Turklāt, ņemot vērā to, ka saskaņā ar Tāfela vienādojumu ūdeņraža izdalīšanai uz Zn ir liels virspotenciāls [117], [118] un skābekļa izdalīšanai ir liels virspotenciāls [56] un lēna reakcijas kinētika [119], ir iespējams ūdens elektrolīta izmantošanas spriegumu palielināt līdz pat 3 V.

Kopumā duāla elektrolīta tipa koncepts un palielināta ūdens stabilitātes sprieguma logs ir aprakstīts jau kopš 2005. gada [55]–[57]. Vēlāk šis duālā elektrolīta koncepts ir aprakstīts arī dažādām bateriju sistēmām, tādām kā Al-gaiss [120]–[123], Zn-gaiss [121], [124], [125], Mg-gaiss [121], [126], Zn-PbO₂ [127]–[129], Zn-Br₂ [130] un Zn-MnO₂ [54], [58], [131]. Tomēr visu šo bateriju darbības laiku un efektivitāti limitē neitralizācijas reakcija un jonu difūzija elektrolītā.



1.5. att. Ūdens Purbē diagramma [116].

2. Galvenie rezultāti par MnO_2 katoda veiktspējas uzlabošanu skābā elektrolītā

Šajā nodaļā aprakstīta MnO_2 katoda veiktspējas uzlabošana ļoti skābā ($\text{pH} < 2$) ūdens elektrolītā, lietojot MnO_2 dopēšanu ar Bi un Mo joniem. Dopanta jonu ietekme izvērtēta, izpētot Bi un Mo jonu koncentrācijas ietekmi uz MnO_2 strukturālajām un elektroķīmiskajām īpašībām atkarībā no koncentrācijas robežās no 0 mol% līdz 10 mol%, kā arī apskatot Bi un Mo mehānisko lomu MnO_2 stabilizēšanā uzlādes-izlādes ciklu laikā.

2.1. Metodoloģija

Ar Bi un Mo dopēti MnO_2 pulveri tika iegūti hidrotermālās sintēzes ceļā, izmantojot KMnO_4 kā mangāna prekursoru. BiCl_3 izmantots kā bismuta prekursors un ievadīts koncentrācijās no 0 mol% līdz 10 mol%, savukārt ar Mo dopētu paraugu sagatavošanā izmantots Na_2MoO_4 koncentrācijā no 0 mol% līdz 5 mol%. Katrai sintēzei nepieciešamie sāļi tika izšķīdināti destilētā ūdenī. Sintēzēs papildus ievadīts arī fiksēts *CB* daudzums. Tālāk iegūtais šķīdums tika ievietots autoklāvā un atstāts uz 12 h vai 24 h krāsnī $120\text{ }^\circ\text{C}$ temperatūrā. Pēc hidrotermālās sintēzes visi iegūtie pulverveida paraugi tika vairākkārtēji mazgāti ar destilētu ūdeni un 24 h žāvēti krāsnī $60\text{ }^\circ\text{C}$ temperatūrā.

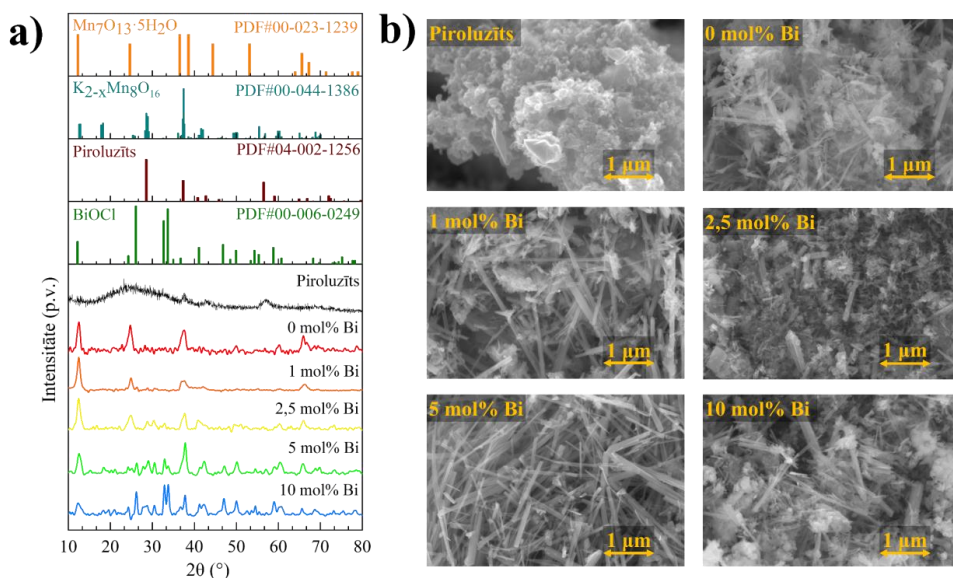
Papildus tika pētīts komerciāli iegūta MnO_2 (piroluzīta fāzē jeb $\beta\text{-MnO}_2$) paraugs kā reference sintezētajiem paraugiem. Lai izveidotu katodus, piroluzīta iegūtie pulverveida paraugi tika sajaukti ar papildu *CB* attiecībā 13 : 5, lai uzlabotu katoda elektrovadītspēju. Tālāk no iegūta pulveru maisījuma tika sagatavota katoda suspensija, pievienojot tāda paša svara polivinilidēna fluorīda šķīdumu N-metil-2-pirolidonā (NMP) (1 : 9). Izveidotā suspensija tika

uzklāta ar spraugas aplikatoru uz ogles papīra, tika iztvaicēts NMP un izcirsti nepieciešamā izmēra katodi.

2.2. Rezultāti

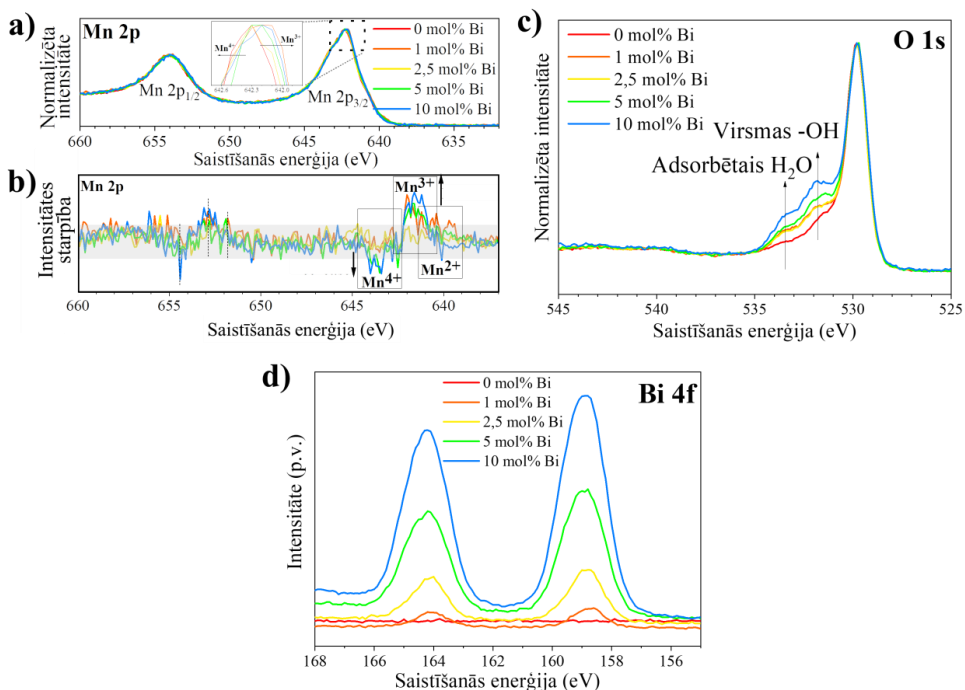
2.2.1. Ar Bi dopēts MnO₂ katods

Pēc XRD rezultātiem, kas redzami 2.1. a. attēlā, sintezētajos paraugos tika identificēti divu fāžu maisījums – δ -MnO₂ (Mn₇O₁₃·5 H₂O) jeb birnesīts un α -MnO₂ (K_{2-x}Mn₈O₁₆) jeb holandīts. Papildus pie lielākām dopanta koncentrācijām novērojama BiOCl fāzes veidošanās. Palielinot Bi jonu koncentrāciju paraugos, novērojama δ -MnO₂ fāzes maksimuma intensitātes samazināšanās pie 24,6° un α -MnO₂ fāzes maksimumu intensitātes palielināšanās pie 29° un 42°. Tas liecina, ka Bi jonu ievadīšana paraugā veicina α -MnO₂ fāzes veidošanos, kurai piemīt 2 × 2 tuneļveidīga kristālrežģa struktūra. Šajā gadījumā Bi joni ieņem brīvās vietas MnO₂ 2 × 2 tuneļveida struktūrā kā aizpildījums, kas neļauj MnO₂ ieņemt slāņveidīgo δ -MnO₂ struktūru [70], [72], [132]–[134]. Tuneļveidīgās α -fāzes veidošanās ir šajā gadījumā vēlamāka, jo tās tuneļa struktūra atvieglo jonu kustību cauri kristālrežģim, tādējādi uzlabojot elektroķīmisko kinētiku. Turpretī MnO₂ bez dopantu joniem dominēja δ -fāze, kas bija jutīgāka pret šķīšanu skābas vides apstākļos. Paraugu skenējošās elektronu mikroskopijas (SEM) attēlos (2.1. b. att.) redzams, ka sintezētie pulveri sastāv no mazāku un lielāku adatveida struktūru kopām, kas raksturīgi dažādām MnO₂ polimorfajām struktūrām [135]–[137]. Savukārt piroluzīta paraugs sastāv no noapaļotas formas daļiņu kopas.



2.1. att. Ar Bi dopēto MnO₂ paraugu un piroluzīta XRD difraktogrammas (a) un SEM mikrofotogrāfijas (b).

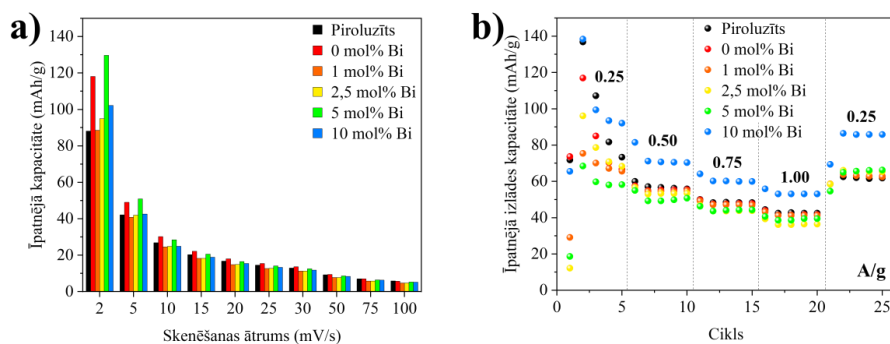
Lai precīzāk raksturotu sintezētos paraugus, veikta arī rentgenstaru fotoelektronu spektroskopijas (*XPS*) analīze. Normalizētos Mn 2p *XPS* spektros (2.2. a. att.) redzama maksimuma nobīde Mn³⁺ jonu saistīšanās enerģijas virzienā, kas, palielinoties Bi³⁺ koncentrācijai paraugā, kļūst izteiktāka. Papildus normalizēto *XPS* spektru starpības (2.2. b. att.) uzrāda Mn⁴⁺ signāla samazināšanos un Mn³⁺ signāla palielināšanos, palielinoties Bi³⁺ jonu koncentrācijai paraugā. Līdzīgi novērojumi par Mn³⁺ un Mn⁴⁺ valences stāvokļa veidošanos līdzīgos sintēzes procesa apstākļos dažādām metālu oksīdu sistēmām apskatīti arī literatūrā [138], [139], kas skaidro MnO₂ kristāla struktūrā ievadīto heteroatomu lomu metastabilo Mn³⁺ jonu stabilizēšanā, kas parasti disproporcionējas oksīdu kristālu struktūrās [140]. Normalizētajos O 1s spektros, kas redzami 2.2. c. attēlā, palielinoties Bi³⁺ jonu koncentrācijai paraugā, palielinās arī hidroksilgrupu un adsorbētā ūdens daudzums uz virsmas. Saskaņā ar literatūras datiem, saistīšanās enerģija, kas atrodas pie 531–535 eV, ir cieši saistīta ar virsmas hidroksilgrupām, ūdeni vai organiskiem, skābekļa atomus saturošiem blakusproduktiem [141]. Apskatot Bi 4f *XPS* spektros (2.2. d. att.) redzams, ka 0 mol% Bi paraugam nav novērojams šis signāls un, palielinot Bi³⁺ jonu koncentrāciju paraugā, signāls palielinās, kā arī visos Bi jonus saturošajos paraugos Bi atomi atrodas 3+ oksidācijas stāvoklī [142], [143].



2.2. att. Ar Bi dopēto MnO₂ paraugu un piroluzīta normalizēti Mn 2p *XPS* spektri (a) un to starpība (b); Bi 4f spektri (c) un normalizēti O 1s spektri (d).

Tālāk sagatavotajiem katodiem veikti cikliskās voltampēriemijas (CV) mērījumi, pēc kuru datiem aprēķināta katra katoda īpatnējā kapacitāte (2.3. a. att.). No šiem rezultātiem pie lēnākiem skenēšanas ātrumiem katods ar 5 mol% Bi jonu saturu uzrāda visaugstāko īpatnējo kapacitāti 130 mAh/g, savukārt katods bez Bi joniem – tikai 120 mAh/g un piroluzīta katods – 90 mAh/g.

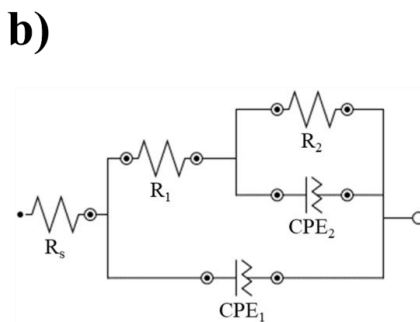
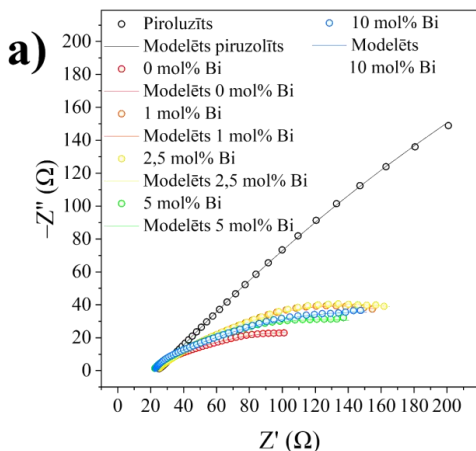
Lai novērtētu kapacitātes saglabāšanas spējas, veikti arī galvanostatiskās uzlādes-izlādes (GCD) mērījumi pie mainīgiem strāvas blīvumiem (2.3. b. att.). Pirmajos piecos ciklos notiek materiāla aktivizēšana un katoda stabilizācija. Piroluzīta katodam un katodam bez Bi joniem ir nepieciešami visi pieci cikli, lai pilnībā stabilizētos. Turpretim Bi jonus saturošie paraugi stabilizējas 2–3 ciklos. Sekojošajos 15 ciklos, palielinot strāvas blīvumu no 0,25 A/g līdz 1,0 A/g, piroluzīta katods uzrāda līdzīgu kapacitāti kā 0–5 mol% Bi jonus saturošie katodi. Savukārt, samazinot strāvas blīvumu līdz sākotnējiem 0,25 A/g, katoda materiāli ar lielāku Bi jonu saturu uzrāda labāku kapacitātes saglabāšanās spēju.



2.3. att. Ar Bi dopēto MnO_2 paraugu un piroluzīta īpatnējā kapacitāte, kas iegūta no CV mērījumiem dažādos skenēšanas ātrumos (a), īpatnējā izlāde kapacitāte no GCD mērījumiem pie dažādiem strāvas blīvumiem (b).

Visu paraugu elektroķīmiskas impedances spektroskopijas (EIS) rezultāti pēc CV mērījumiem ir redzami 2.4. a. attēla EIS diagrammās. Papildus redzamas arī modelētas līknes saskaņā ar ekvivalento shēmu, kas redzama 2.4. b. attēlā. Shēma sastāv no pretestībām – R_s , R_1 un R_2 – un konstantas fāzes elementiem – CPE_1 un CPE_2 – paralēli attiecīgajām pretestībām. Visas šo komponentu vērtības apkopotas 2.1. tabulā. Elektrolīta omiskā pretestība atbilst komponentam R_s un visiem paraugiem ir aptuveni 22–23 Ω . Pretestība R_1 un konstantas fāzes elements CPE_1 atbilst lādiņa pārnesei pretestībai starp elektrodu un elektrolītu un dubultslāņa kapacitātei. Modelētās vērtības liecina, ka hidrotermāli sintezētajiem katoda materiāliem ir samazināta dubultslāņa kapacitāte ar visnozīmīgāko samazinājumu 10 mol% Bi MnO_2 paraugam. Šis novērojums saistāms ar 2.2. c. attēlā redzamo virsmas hidroksilgrupu pieaugumu. Virsmas hidroksilgrupu daudzuma izmaiņas nosaka elektrodu slapēšanas īpašības un ietekmē mijiedarbību starp elektroda virsmu un elektrolītu, tādējādi ietekmējot lādiņa pārnesei pretestību. Otrās paralēlās komponentes – pretestība R_2 un konstantas fāzes elements

CPE₂ – atbilst atsevišķo katoda materiāla daļiņu kopējai pretestībai un kopējai kapacitātei starp tām, jo katods sastāv no individuālu pusvadītāja MnO₂ un CB daļiņu maisījuma. Saskaņā ar modelētajām vērtībām sintezētajiem paraugiem ir ievērojami zemāka pretestība starp atsevišķām daļiņām. Salīdzinot piroluzīta un 0 mol% Bi paraugu, sintēzes laikā pievienotais CB samazina atsevišķu daļiņu pretestību vairāk nekā deviņas reizes.



2.4. att. Ar Bi dopēto MnO₂ paraugu un piroluzīta EIS diagrammas ar izmēritajiem datiem un ar modelētajiem datiem (a) saskaņā ar ekvivalento shēmu (b).

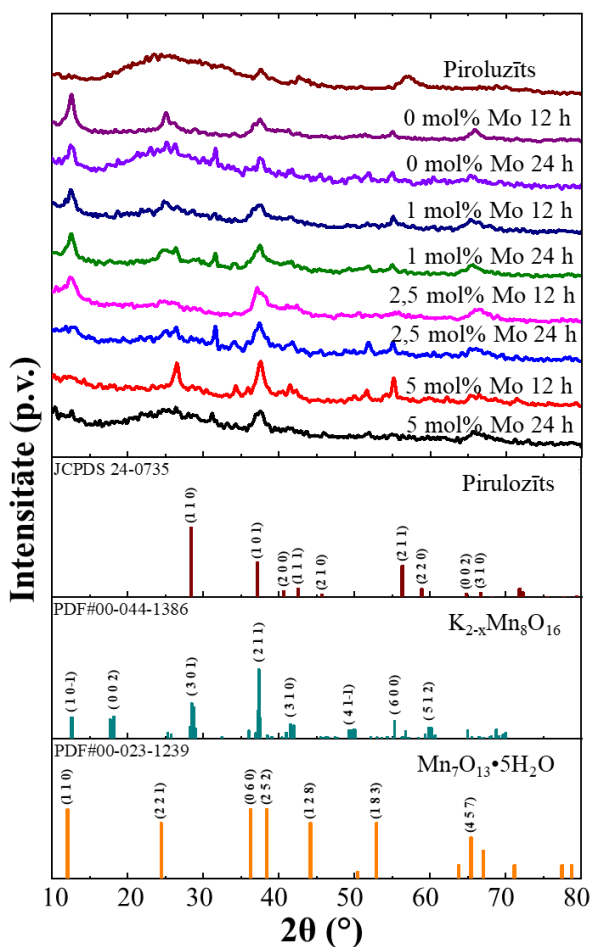
2.1. tabula

EIS modelēto datu ekvivalentās shēmas parametri

Paraugs	R _s Ω	R ₁ Ω	CPE ₁		R ₂ Ω	CPE ₂		χ ²
			Y ⁰	N		Y ⁰	N	
			mS · s ^N			mS · s ^N		
Piroluzīta	23,82	5,05	1,13	0,54	1474,8	1,93	0,52	0,00039
0 mol% Bi	21,66	9,49	0,29	0,68	161,94	6,30	0,34	0,00045
1 mol% Bi	23,75	49,03	1,52	0,52	162,74	3,32	0,45	0,00106
2,5 mol% Bi	23,74	39,57	1,38	0,53	195,00	3,54	0,40	0,00148
5 mol% Bi	21,71	6,23	0,16	0,74	204,60	4,68	0,36	0,00208
10 mol% Bi	22,37	8,04	0,13	0,77	242,74	4,80	0,35	0,00210

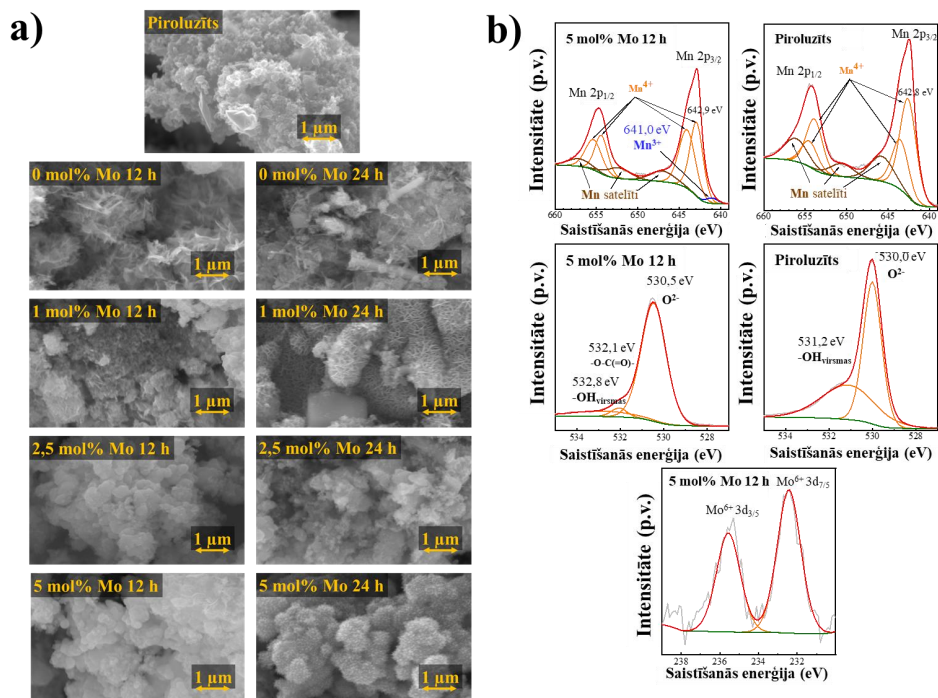
2.3.2. Ar Mo dopēts MnO₂ katods

Paraugos, kas dopēti ar Mo, pēc *XRD* difraktogrammām, kas redzamas 2.5. attēlā, arī ir iespējams identificēt divas fāzes: δ -MnO₂ (Mn₇O₁₃·5H₂O) jeb birnesīts un α -MnO₂ (K_{2-x}Mn₈O₁₆) jeb holandīts. Līdzīgi kā paraugiem, kas tika dopēti ar Bi, ar Mo dopētiem paraugiem, palielinot Mo koncentrāciju paraugā, arī novērojama δ -MnO₂ fāzes samazināšanās un α -MnO₂ fāzes palielināšanās. Tas liecina, ka Mo dopanta pievienošana veicina α -MnO₂ fāzes veidošanos. Papildus novērojams, ka sintēzes ilgumam ir ietekme uz parauga kristāliskumu, jo paraugiem ar 24 h sintēzes ilgumu un Mo koncentrāciju līdz 2,5 mol% ir novērojami izteiktāki difrakcijas maksimumi. Tas var liecināt par lielāku kristālītu veidošanos paraugos [144], kas sasaucas arī ar paraugu SEM attēliem, kas redzami 2.6. a. attēlā, kur ilgāk sintezētajiem paraugiem novērojamas izteiktākas struktūras, savukārt 12 h paraugi sastāv no nejaušu formu aglomerātiem.



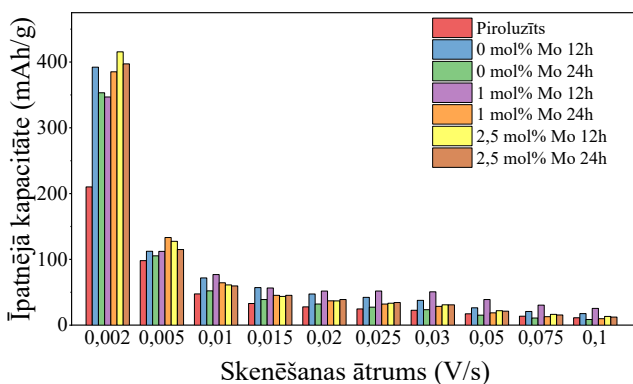
2.5. att. Ar Mo dopēto MnO₂ paraugu un piroluzīta rentgenogrammas.

Paraugiem veikta arī *XPS* analīze, kuras spektri redzami 2.6. b. attēlā, lai noteiktu sastāvā esošo elementu oksidācijas pakāpes. Visi paraugi satur Mn^{4+} jonus, kā arī sintezētie paraugi satur oglekļa-skābekļa saites, jo sintēzes procesā tika pievienots *CB*. Turklāt ar Mo dopētie MnO_2 paraugi satur Mo^{6+} jonus un metastabilos Mn^{3+} jonus, kas liecina, ka arī Mo jonu piedeva stabilizē Mn^{3+} jonus [145].



2.6. att. Ar Mo dopēto MnO_2 paraugu un piroluzīta SEM attēli (a) un Mn 2p, O 1s un Mo 3d spektri (b).

Tālāk no ar Mo dopētajiem MnO_2 paraugiem tika sagatavoti katodi un veikti CV mērījumi, pēc kuru datiem aprēķināta katra katoda īpatnējā kapacitāte (2.7. a. att.). Visi sintezētie paraugi uzrāda lielāku īpatnējo kapacitāti nekā piroluzīta paraugs, turklāt sintezēto paraugu īpatnējā kapacitāte palielinās, pievienojot Mo atomus. Iemesls vispārējam īpatnējās kapacitātes pieaugumam starp piroluzīta un sintezētajiem paraugiem var būt saistīts ar fāžu atšķirībām, jo, kā liecina *XRD* rezultāti (2.5. att.), sintezētie paraugi satur δ - MnO_2 un α - MnO_2 . Vislielākā īpatnējā kapacitāte – 415 mAh/g pie 0,002 V/s – iegūta no ar 2,5 mol% Mo dopēta MnO_2 parauga ar sintēzes laiku 12 h. Tomēr turpmākās pārbaudes atklāj, ka ar 1 mol% Mo dopētais paraugs, kas sintezēts 12 h, labāk saglabā savu īpatnējo kapacitāti, palielinot skenēšanas ātrumu. Kopumā no CV mērījumiem var secināt, ka ar Mo dopēti paraugi uzrāda īpatnējās kapacitātes pieaugumu līdz 2,5 mol% Mo koncentrācijas sasniegšanai.



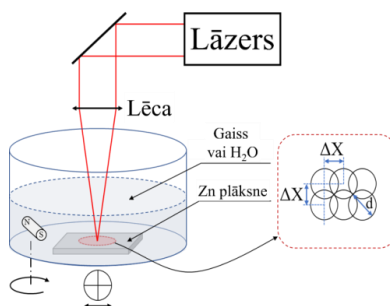
2.7. att. Ar Mo dopēto MnO₂ paraugu un piroluzīta īpatnējā kapacitāte.

3. Galvenie rezultāti par Zn anoda veiktspējas uzlabošanu sārmainā elektrolītā

Šajā nodaļā aprakstīta cinka anoda elektroķīmisko īpašību uzlabošana, kas veikta, apstarojot Zn virsmu ar impulsu lāzeru. Novērtēta lāzera apstarošanas ietekme uz Zn anoda strukturālajām un morfoloģiskajām īpašībām. Iegūtajiem anodu materiāliem apskatītas tādas elektroķīmiskās īpašības kā virsmas īpatnējā kapacitāte un lādiņa pārnese pretestība. Aprakstīti iespējamie mehānismi lāzera modifikācijas ietekmei uz Zn anoda darbību.

3.1. Metodoloģija

Cinka plāksnes ar 99,95 % tīrību tika modificētas, izmantojot nanosekunžu impulsa *Nd:YAG* lāzeru divos viļņu garumos (266 nm un 1064 nm) gaisa un dejonizēta ūdens vidē. Apstarošanas procesa shematiskais attēlojums redzams 3.1. attēlā. Galvenie lāzera parametri – enerģijas plūsma (no 0,32 J/cm² līdz 2,66 J/cm²), kas variē atkarībā no apstarošanas procesa, un impulsa ilgums (6 ns) – sistemātiski mainīti un apkopoti 3.1. tabulā. Tālāk iegūtie Zn anodu paraugi pēc virsmas izpētes testēti elektroķīmiskajā pusšūnā ar 1 M KOH elektrolītu, Pt pretektrodu un Ag/AgCl (3M KCl) references elektrodu.



3.1. att. Lāzera apstarošanas procesa shematiskais attēlojums.

Lāzera apstarošanas parametri

Parauga šifrs*	Lāzera viļņa garums, nm	Vide, kurā veikta apstarošana	Enerģijas plūsma, J/cm ²
Zn	neapstarots	–	–
Zn-A-2,66*	266	Gaiss	2,66
Zn-A-0,38	1064	Gaiss	0,38
Zn-A-0,59	1064	Gaiss	0,59
Zn-A-0,64	1064	Gaiss	0,64
Zn-A-0,71	1064	Gaiss	0,71
Zn-W-0,32*	266	Dejonizēts ūdens	0,32
Zn-W-0,53*	266	Dejonizēts ūdens	0,53
Zn-W-0,69	1064	Dejonizēts ūdens	0,69
Zn-W-1,29	1064	Dejonizēts ūdens	1,29
Zn-W-1,42	1064	Dejonizēts ūdens	1,42
Zn-W-1,60	1064	Dejonizēts ūdens	1,60

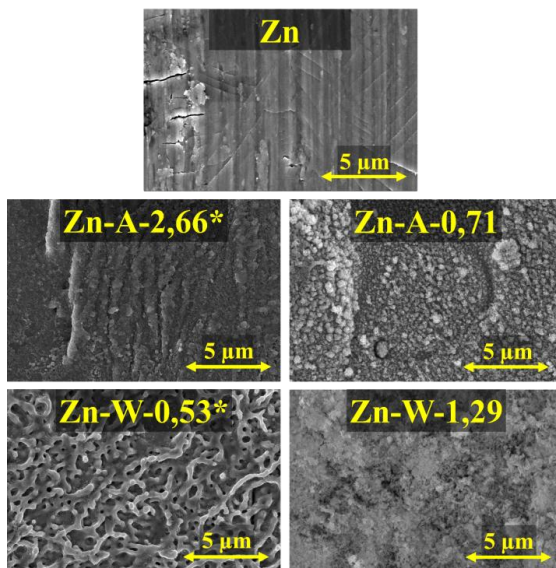
*“A” – gaisa vide, “W” – ūdens vide.

3.2. Rezultāti

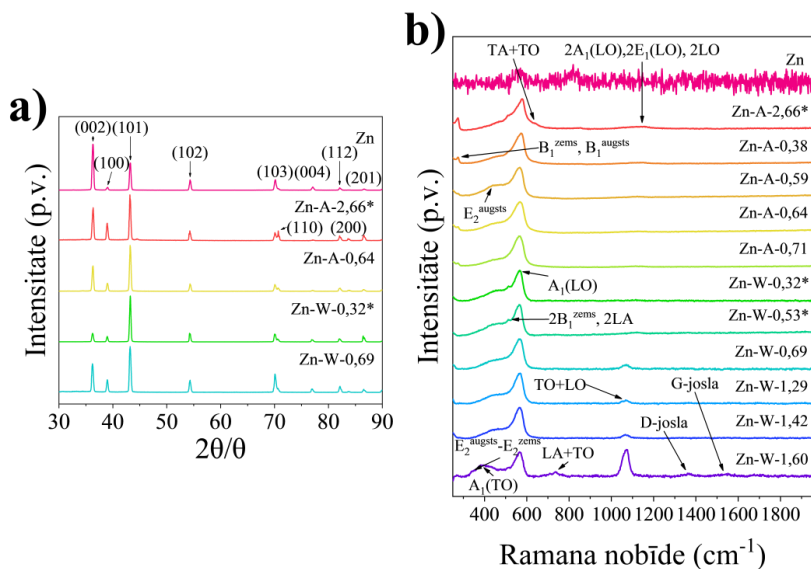
Paraugu apstarošana ar impulsu lāzeru izraisīja nozīmīgas morfoloģiskas izmaiņas virsmā, kā redzams SEM mikrofotogrāfijās (3.2. att.). Neapstarotam cinka paraugam novērojama gluda virsma ar ražošanas procesiem raksturīgām velmēšanas pazīmēm, savukārt ar lāzeru apstrādātiem paraugiem uz virsmām novērojamas dažādas morfoloģijas atkarībā no apstarošanas vides. Paraugi, kas apstaroti gaisa vidē ar 1064 nm lāzeru, uzrāda intensīvu kušanu apstarošanas laikā. Tā rezultātā paraugiem uz virsmas izveidojušās pilienvēda sasalušas struktūras. Savukārt paraugiem, kas ar tādu pašu viļņa garumu apstaroti ūdens vidē, uz virsmas novērojamas krokotas struktūras ar homogēni izkliedētiem pilieniem zem tām. Paraugi, kas apstaroti ar 266 nm lāzeru gaisa vidē, uzrāda mēreni izkusušu virsmu ar vienmērīgāku tekstūru, savukārt apstarošana ūdens vidē izraisīja ZnO augšanu un izveidoja kroatu kausējuma struktūru.

Neapstarotas Zn plāksnes XRD (*Theta/2theta*) difraktogrammas (3.3. a. att.) uzrāda polikristālisku Zn ar dominējošu (002) pamata plakni, kas ir paralēla loksnes virsmai. Tas saistās ar ražošanas laikā izraisītajām deformācijām velmēšanas dēļ [146]. Savukārt paraugu apstrādāšana ar lāzeru samazina dominējošās (002) pamatplaknes intensitāti difraktogrammās. Tas saistīts ar virsmas izkausēšanu lāzera apstrādes dēļ, kā rezultātā tiek atsegta pamatnē esošā polikristāliskā struktūra, kurā dominē (101) plakne. Šīs izmaiņas veicina vienmērīgāku cinka nogulsnešanas elektroķīmisko procesu laikā. Tomēr Ramana spektri, kas redzami 3.3. b. attēlā, apstiprināja heksagonālā ZnO veidošanos uz apstaroto paraugu virsmām. Papildus tam Ramana

spektros nosakāmi dažādi ZnO defekti: skābekļa vakances ($A_1(LO)$ maksimums pie 574 cm^{-1}), starprežģa Zn atomi (plašs maksimums pie $250\text{--}300\text{ cm}^{-1}$), ar slāpekli saistītie defekti (maksimums pie 275 cm^{-1}) [147], [148].



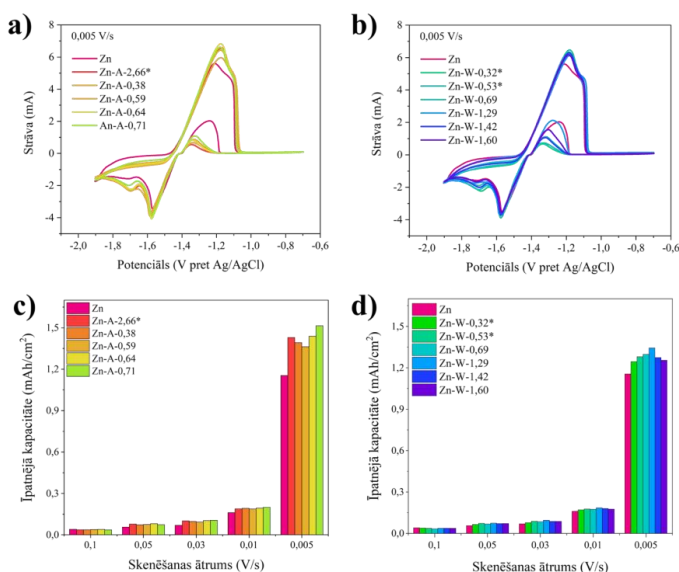
3.2. att. Neapstarota un ar impulsu lāzeru pie dažādām enerģijas plūsmām apstarotu (“A” – gaisa vidē un “W” – ūdens vidē) Zn paraugu SEM mikrofotogrāfijas.



3.3. att. Neapstarota un apstarota Zn paraugu XRD difraktogrammas (a) un Ramana spektri (b).

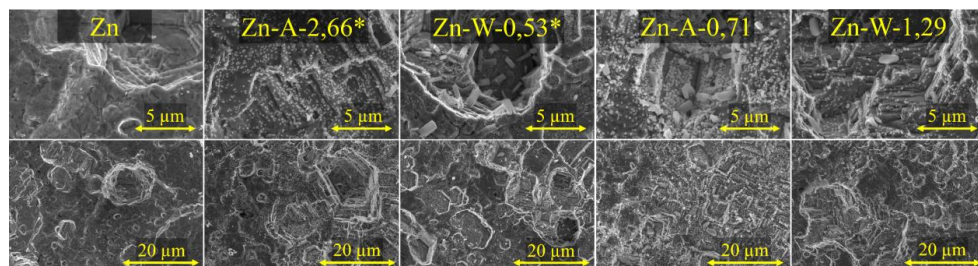
CV mērijumos, kas redzami 3.4. a. un b. attēlā, novērojami būtiski elektroķīmisko īpašību uzlabojumi ar lāzeru apstarotajiem paraugiem. Anodiskās oksidācijas reakcijas virzienā notiek Zn parauga elektroķīmiskā izšķīšana (saskaņā ar 1. reakciju) līdz brīdim, kad elektrolīts vairs nevar sasniegt aktīvo Zn virsmu turpmākai reakcijai. Šīs reakcijas laikā veidojas $Zn(OH)_4^{2-}$, kas uzreiz pārvēršas ZnO un nosedz anoda virsmu. Savukārt katodiskās reducēšanās reakcijas laikā novērojama strauja strāvas palielināšanās pie $-1,3$ V [149], [150]. Šajā potenciāla reģionā, kad ZnO reducējas atpakaļ par Zn, vēl iepriekš neizreagējusi Zn virsma tiek atklāta elektrolītam. To var novērot kā strauju strāvas pieaugumu, kura pamatā ir Zn oksidācijas procesa atsākšanās. Jāatzīmē, ka ar lāzeru apstarotajiem paraugiem ir novērojams mazāks strāvas pieaugums šajā reģionā. Tas liecina, ka ar lāzeru apstrādātajiem paraugiem oksidēšanās reakcija ir kontrolētāka un ZnO aug vienmērīgāk, neskatoties uz to, ka oksidācija ir ar lielāku maksimālo strāvu. Tas norāda, ka virsmas apstrāde ar lāzeru uzlabo Zn elektroda vispārējo ciklisko veiktspēju, turklāt apstrādātajām virsmām ir augstākas oksidēšanās un reducēšanās strāvas, kas liecina par uzlabotu reakcijas kinētiku.

Papildus no CV mērijumiem tika noteiktas arī īpatnējās virsmas kapacitātes (3.4. c. un d. att.), kur pie $0,005$ V/s skenēšanas ātruma gaisā vidē apstarotiem paraugiem ir nedaudz lielāka ($1,35$ – $1,50$ mAh/cm²) virsmas īpatnējā kapacitāte, salīdzinot ar paraugiem, kas apstaroti ūdens vidē ($1,25$ – $1,35$ mAh/cm²), un ievērojami lielāka par neapstarotu Zn ($1,15$ mAh/cm²). Kopumā ar lāzeru apstarotie paraugi uzrāda kapacitātes pieaugumu par 8 – 30 % atkarībā no apstrādes parametriem. Šo kapacitātes pieaugumu var saistīt ar palielinātu virsmas raupjumu un vairāk aktīvajām reakcijas vietām, ko veicinājusi lāzera izraisīta kušana un atkārtota sacietēšana.



3.4. att. Neapstarota un gaisā apstarotu Zn paraugu CV mērijumi (a) un īpatnējā virsmas kapacitāte (c). Neapstarota un ūdenī apstarotu Zn paraugu: b) CV mērijumi (b) un īpatnējā virsmas kapacitāte (d).

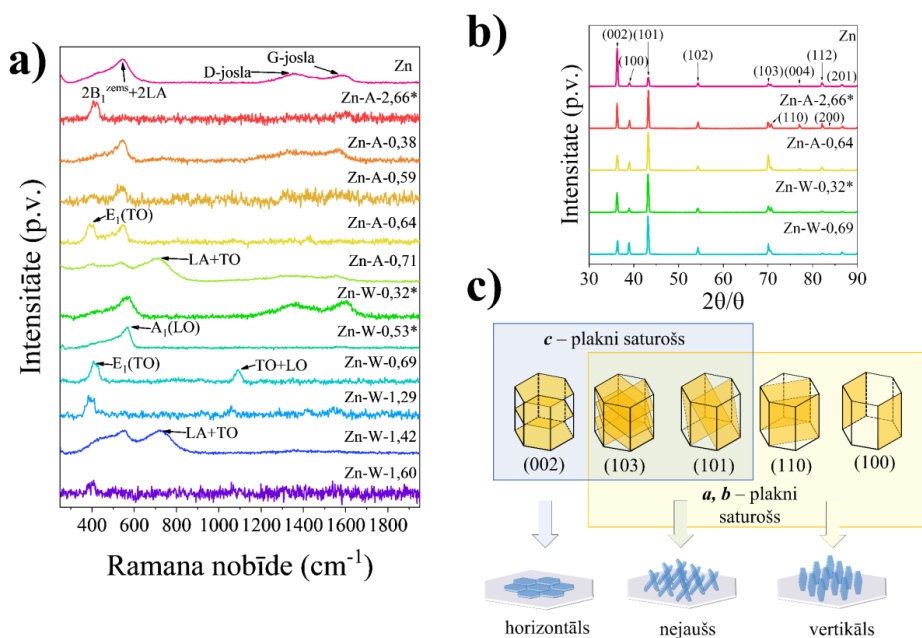
Pēc elektroķīmiskiem mērījumiem paraugi tika vēlreiz aplūkoti ar SEM (3.5. att.), lai noteiktu virsmas izmaiņas. Apstarotajiem paraugiem šajos attēlos ir redzamas graudu struktūras ar izteiktām heksagonālā Zn kristālrežģa virsmām. Turpretim neapstarotā Zn parauga virsma nav ar izteiktām kristālu graudu virsmām, un uz tā virsmas ir redzamas nejaušas augšanas pazīmes.



3.5. att. Neapstarota un apstarotu Zn paraugu SEM mikrofotogrāfijas pēc CV mērījumiem.

Apstaroto paraugu Ramana spektri, kas redzami 3.6. a. attēlā, pēc elektroķīmiskiem mērījumiem ir ar palielinātu fonu, un ZnO raksturīgie maksimumi ir grūti identificējami. Turpretim neapstarotajam Zn paraugam uz virsmas ir redzami ZnO raksturīgie maksimumi pie 382 cm^{-1} , 441 cm^{-1} un 585 cm^{-1} . Tas liecina, ka Zn virsmas apstrāde ar lāzeru uzlabo Zn anoda elektroķīmiskās reakcijas, veicinot vienmērīgāku ZnO augšanu uz elektroda virsmas un pilnīgāku pārveidošanos atpakaļ uz metālisku Zn. Savukārt neapstarotajam Zn paraugam notiek tikai daļēja uzlāde (ZnO reducēšanās uz Zn), kā rezultātā palielinās ZnO saturs uz virsmas un attiecīgi uzlabojas ZnO Ramana signāls. Šis novērojums saskan ar neapstarotā Zn parauga CV mērījumiem (3.4. a. un b. att.), kur redzams izteiktāks fenomens pie $-1,3\text{ V}$, kas saistīts ar palielinātu ZnO veidošanos uz virsmas.

Paraugu virsmām pēc CV mērījumiem arī atkārtoti uzņemtas XRD ($Theta/2theta$) difraktogrammas, kas redzamas 3.6. b. attēlā. Neapstarotajam Zn paraugam novērots izteikts (002) plaknes intensitātes pieaugums un (101) plaknes intensitātes samazinājums, kas liecina par augšanu galvenokārt (002) plaknes virzienā. Papildus novērojams neliels (100) plaknes pieaugums, kas liecina par dendrītiem līdzīgu un irdenu struktūru veidošanos [151]. Turpretim apstarotie paraugi pēc CV mērījumiem saglabā polikristāliskās (101) struktūras. Redzams pieaugums arī (002) c plaknes virzienā, kas nodrošina vairāk horizontālu struktūru veidošanos. Papildu neliela intensitātes samazināšanās (100) un (200) plaknēs liecina, ka virsmas ir izturīgākas pret dendrītveida struktūru augšanu. Kā redzams 3.6. c. attēlā, Zn raksturīgo plakņu augšanas virzieni ietekmē potenciālās virsmas struktūras. Raksturīgās plaknes (002) pieaugums var liecināt par gludu, horizontālu struktūru veidošanos, savukārt (110) un (100) plakņu pieaugums var liecināt par dendrītu un irdenu struktūru veidošanos.

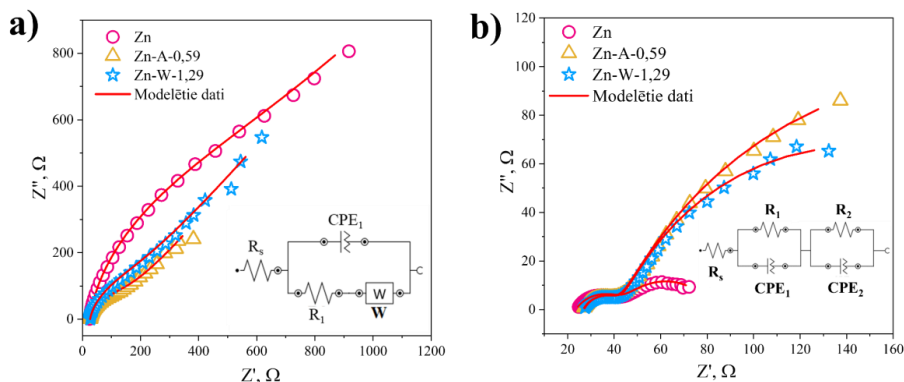


3.6. att. Neapstarota un apstarotu Zn paraugu rezultāti pēc CV mērījumiem. a) Ramana spektri; b) *XRD* difraktogrammas; c) heksagonālā Zn raksturīgās kristāla plaknes un attiecīgie augšanas modeļi.

Tālāk elektroda-elektrolīta robežvirsmas raksturošanai veikta EIS analīze. EIS spektri pie negatīvas līdzstrāvas komponentes -150 mV no *OCV* redzami 3.7. a. attēlā, spektri pie pozitīvas līdzstrāvas komponentes $+150$ mV no *OCV* redzami 3.7. b. attēlā. Papildus tika veikta arī EIS spektru modelēšana saskaņā ar grafikos iekļautajām ekvivalentajām shēmām, un iegūtās komponentu vērtības apkopotas 3.2. tabulā. Negatīva sprieguma gadījumā R_1 visiem paraugiem ir ap 27Ω un atbilst elektrolīta omiskajai pretestībai. Pretestība R_2 raksturo faradejiskā procesa lādiņa pārnese pretestību, un tā ir samazināta ar lāzeru apstarotajiem paraugiem. Savukārt CPE vērtība, kas raksturo elektriskā dubultā slāņa kapacitāti, ir palielināta apstarotajiem paraugiem. Šis nelielais pieaugums liecina par makroskopisku virsmas laukuma palielināšanos ar lāzeru apstarotajiem paraugiem. Visi spektri pie zemām frekvencēm pāriet slīpā taisnē, kas atbilst Varburga pretestībai un raksturo ar difūziju saistītos ierobežojošos procesus.

Iegūtajām EIS diagrammām pie pozitīvas sprieguma novirzes, kur notiek Zn oksidēšanas un ZnO veidošanās, tika lietots paplašināts ekvivalentās ķēdes modelis. Tāpat kā iepriekšējā gadījumā, R_s raksturo elektrolīta pretestību un ir ap 27Ω . Pirmais R_1 un CPE_1 paralēlais savienojums raksturo elektriskā dubultā slāņa stāvokli – jonu polarizācijas pretestību R_1 un elektriskā dubultā slāņa kapacitāti CPE_1 . Dubultslāņa kapacitātes vērtības paraugiem ir līdzīgas, liecinot, ka ar lāzeru apstrādātā makrovirsmas elektroķīmiskās reakcijas laikā nemainās. Otrā paralēlā CPE_2 un R_2 ķēde apraksta faradejisko procesu, kurā R_2 norāda lādiņa pārnese pretestību. Neapstarotam Zn paraugam šī vērtība ir 38Ω , savukārt ar lāzeru apstarotajiem

paraugiem – ap 200 Ω . Šis ievērojams pieaugums ir saistīts ar dažādiem lāzera apstrādes laikā izveidotajiem defektiem, kas novērojami arī Ramana spektros pēc elektroķīmiskiem mērījumiem (3.6. a. att.). Tas palielina lādiņa pārnesei pretstāvējošo apstarotajiem paraugiem un samazina reakcijas ātrumu Zn oksidācijai. CPE₂ raksturo Zn oksidācijas procesa kapacitāti un ir par vairākām kārtām lielāka nekā dubultslāņa kapacitāte. Šis kapacitātes samazinājums ir saistīts ar reakcijas palēnināšanos, ko savukārt izraisa palielinātā apstaroto paraugu pretstība.



3.7. att. Neapstarota un apstarotu Zn paraugu EIS spektri pie negatīvas līdzstrāvas komponentes -150 mV no *OCV* (a) un EIS spektri pie pozitīvas līdzstrāvas komponentes $+150$ mV no *OCV* (b).

3.2. tabula

EIS modelēto datu ekvivalentās shēmas parametri

Paraugs	R_s	R_1	CPE ₁		R_2	CPE ₂	
			Y^0	N		Y^0	N
			Ω	Ω		$\mu S \cdot s^N$	Ω
Pie negatīva sprieguma pret <i>OCV</i>							
Zn	24,7	668	70	0,90	–	–	–
Zn-A-0,59	26,5	185	103	0,87	–	–	–
Zn-W-1,29	26,5	132	124	0,84	–	–	–
Pie pozitīva sprieguma pret <i>OCV</i>							
Zn	23,6	20,5	369	0,63	38	6,35	0,67
Zn-A-0,59	26,7	15,5	292	0,70	304	3,95	0,72
Zn-W-1,29	27,0	16,0	290	0,70	200	3,79	0,72

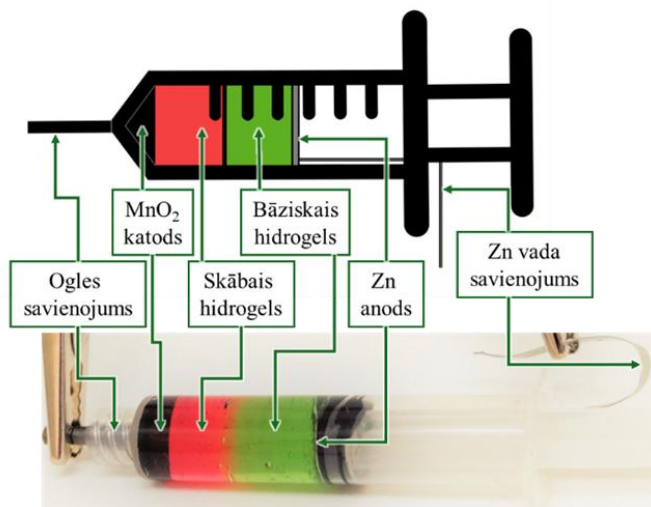
4. Galvenie rezultāti par amfotēras baterijas izveidi ar dažādas vides pH hidrogelu elektrolītiem

Šajā nodaļā aprakstīta inovatīva dizaina ūdens elektrolīta Zn-MnO₂ baterijas izveide un tās elektroķīmisko īpašību izvērtējums. Šī inovatīvā dizaina pamatā ir paaugstināts *OCV* virs komerciāli pieejamās sārma Zn-MnO₂ 1,5 V baterijas. Tas paveikts bez membrānu izmantošanas, lietojot atšķirīgas pH vides hidrogelu elektrolītus, kur Zn anods atrodas sārmainā (KOH) hidrogela elektrolītā un MnO₂ katods skābā (H₂SO₄) elektrolītā. Papildus izvērtēta arī abu elektrolītu robežslāņa (K₂SO₄) hidrogela lietošana. Šādas duālās vides izmantošana samazina nevēlamas blakusreakcijas, piemēram, Zn anoda koroziju skābā elektrolītā, kā arī ķīmiski neaktīvu Mn savienojumu rašanos bāziskā elektrolītā.

4.1. Metodoloģija

Bateriju izveidei kā elektrolīti tika izmantoti 30 wt% *Pluronic F-127* micellu šķīdumi, kas izšķīdināti attiecīgi skābes (0,5 M H₂SO₄), bāzes (1M KOH) un neitrālas sāls (0,5 M K₂SO₄) šķīdumos. Elektrolītu šķīdumiem papildus tika pievienoti pH indikatori, lai būtu iespējams vizuāli identificēt elektrolītu pH izmaiņas. Zn plāksne ar noteiktu diametru izmantota kā anods. Kā katods izmantots ogles files, kas piesūcināts ar MnO₂ (piroluzīta fāzē) un *CB* maisījumu attiecībā 13 : 5, kas papildus sajaukts ar skābā elektrolīta hidrogelu līdz viendabīgas masas iegūšanai.

Lai novērtētu katra elektroda un tā atbilstošā hidrogela darbību, tika veikti pusšūnu mērījumi, kur katods vai anods ir darba elektrods, viens platīna elektrods ir pretelektrods un otrs platīna elektrods ir references elektrods. Pēc tam konstruēta baterija šļirces korpusā (4.1. att.), kas ļāva darbības laikā novērot elektrolītu izmaiņas. Vispirms šļirces galā ievietots MnO₂ katoda files, pēc tam 0,5 M H₂SO₄ skābais hidrogels, 0,4–0,6 M K₂SO₄ neitrālais hidrogels (tikai trīsslāņu baterijām), 1 M KOH bāziskais hidrogels un noslēdzoši Zn anods, kas piestiprināts pie šļirces virzuļa gala. Visu bateriju konstrukciju gadījumā kopējais elektrolīta daudzums tika fiksēts un bija vienāds ar 3 mL.



4.1. att. Izveidotās baterijas shēma un fotogrāfija ar attiecīgajām komponentēm.

4.2. Rezultāti

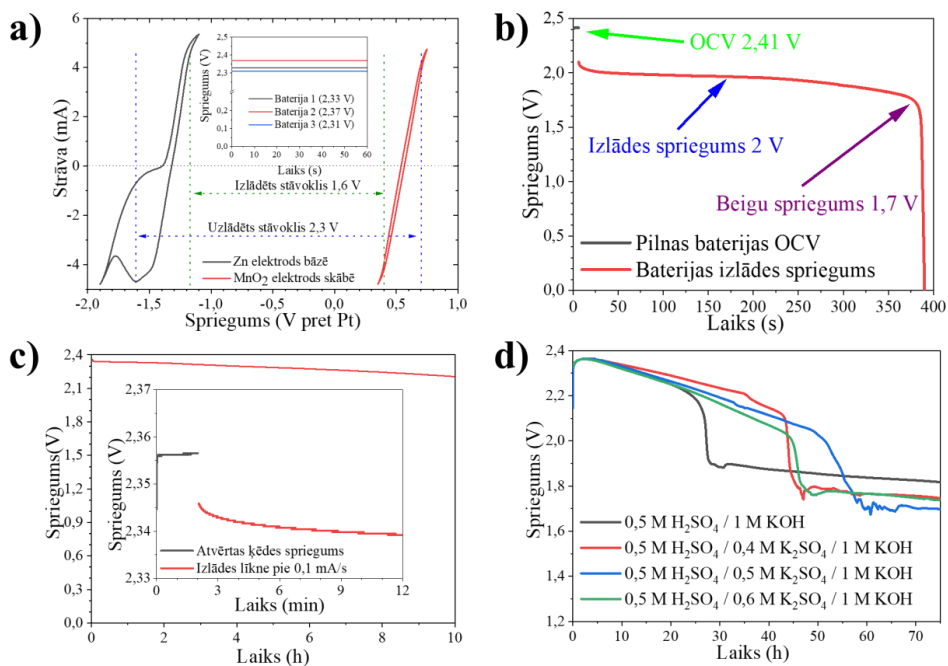
Lai noteiktu teorētisko katoda un anoda uzvedību baterijas darbības laikā, tika veikti pusšūnu CV mērījumi. MnO_2 katoda pusšūna ar skābu ($0,5 \text{ M H}_2\text{SO}_4$) hidrogelu un Zn anoda pusšūna ar bāzisku (1 M KOH) hidrogelu testēta pret Pt pretelektrodu un Pt references elektrodu. Saskaņā ar uzrādītajiem kombinētajiem datiem (4.2. a. att.) amfotēras baterijas *OCV* ir aptuveni $2,3 \text{ V}$, un vairāku sagatavoto amfotēro Zn- MnO_2 bateriju *OCV* mērījumi (4.2. a. att.) apstiprina, ka šādas baterijas spriegums svārstās no $2,3 \text{ V}$ līdz $2,4 \text{ V}$.

Savukārt paredzamajam minimālajam baterijas izlādes spriegumam saskaņā ar kombinētajiem datiem jābūt ap $1,6 \text{ V}$. Lai novērtētu šo teorētisko vērtību, tika veikta amfotēras Zn- MnO_2 baterijas pilnīga izlāde (4.2. b. att.) ar izlādes strāvu 10 mA/s . Pirms izlādes sākuma *OCV* bija $2,4 \text{ V}$, izlādes sākuma līdzsvars ap $2,0 \text{ V}$, bet izlādes beigu spriegums – $1,7 \text{ V}$, kas saskan ar novērojumiem no pusšūnu CV mērījumiem. Papildus, novērtējot baterijas darbību ar izlādes strāvu $0,1 \text{ mA/s}$ (4.2. c. att.), izlādes sākuma spriegums bija $2,34 \text{ V}$, kas 10 h izlādes periodā samazinājās līdz $2,2 \text{ V}$.

Visu mērījumu laikā tika novērota redzama pH neitrālā slāņa veidošanās starp abiem diviem hidrogeliem. To var skaidrot ar H^+ un OH^- jonu difūziju no skābā un bāziskā elektrolīta, kur tie robežslānī viens otru neutralizē, veidojot ūdeni, kas vēl vairāk atšķaida skābo un bāzisko hidrogelu un rada papildu elektrolīta pretestību. Lai novērtētu neitrālā slāņa ietekmi uz amfotēras baterijas konstrukciju, tika veikti arī *OCV* mērījumi ar papildu neitrālo slāni starp skābo un bāzisko hidrogelu. Neitrālā elektrolīta koncentrācija tika variēta attiecība pret skābes/bāzes koncentrācijām ar attiecīgi zemāku ($0,4 \text{ M}$), vienādu ($0,5 \text{ M}$) vai augstāku ($0,6 \text{ M}$) K_2SO_4 normalitāti. Saskaņā ar mērījumiem, kas redzami 4.2. d. attēlā, baterijas ar trīs slāņu hidrogelu elektrolītiem saglabā stabilu spriegumu vairāk nekā 45 h . Tas ir ilgāk nekā divslāņu hidrogelu elektrolīta baterijai, kas spriegumu saglabāja aptuveni 27 h līdz nokritās līdz $1,7 \text{ V}$

neitralizācijas reakcijas dēļ. Salīdzinot neitrālā hidrogela koncentrācijas ietekmi, redzams, ka visilgāko sprieguma stabilitāti (~ 52 h) uzrādīja līdzsvara koncentrācijas hidrogels, savukārt baterijas ar samazinātas vai paaugstinātas koncentrācijas neitrālo hidrogelu attiecībā pret skābes/bāzes hidrogeliem uzrādīja *OCV* stabilitāti tikai līdz 45 h. Kopumā trīsslāņu hidrogelu elektrolītu bateriju pH gradienta stabilitāte ir izteiktāka nekā divslāņu hidrogelu elektrolītu baterijai.

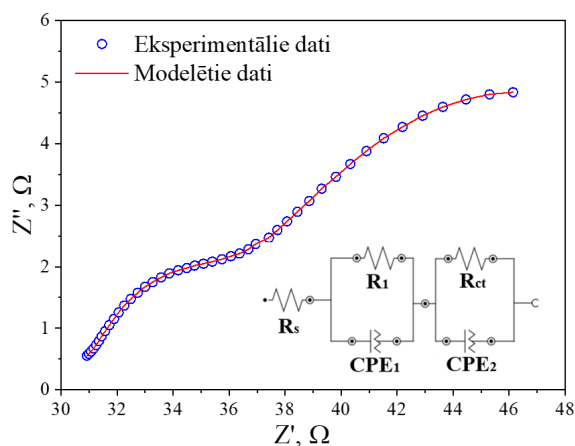
Lai novērtētu iekšējās baterijas pretestības, tika veikts EIS mērījums pilnai amfotērai Zn-MnO₂ baterijai un papildus arī modelēti iegūtie dati saskaņā ar 4.3. attēlā redzamo ekvivalento shēmu. Iegūtās komponentu vērtības apkopotas 4.1. tabulā. Sērijas pretestība R_s ar vērtību 30,5 Ω atbilst elektrolītu pretestībai un ir samērā liela ierobežotās jonu kustības dēļ, kuras kinētiku traucē hidrogela micellas. Pirmais pusloks augstās frekvencēs raksturo robežslāni starp elektrolītu un elektrodu, kas ekvivalentajā shēmā atzīmēts kā R_1 un CPE_1 paralēlais slēgums. Modelī iegūtā R_1 vērtība ir 17 Ω , un CPE_1 ekvivalentā kapacitāte ir 102 mF. Abi šie parametri ir jutīgi pret elektrolīta sastāvu [152] un elektroda virsmas porainību [153], [154]. Otrais pusloks zemo frekvenču diapazonā atspoguļo reakciju procesus, kur R_{ct} raksturo lādiņa pārnese pretestību, un modelī iegūtā vērtība ir 6,7 Ω . Savukārt CPE_2 raksturo dubultslāņa kapacitāti, un tā vērtība ir 39 mF.



4.2. att. Amfotēras baterijas īpašības. a) Baterijas elektrodu pusšūnu CV mērījumi atbilstošajos elektrolītos (skenēšanas ātrums 0,01 V/s) un sagatavoto bateriju *OCV* mērījumi; b) *OCV* un izlādes spriegums pie izlādes strāva 10 mA/s; c) *OCV* un izlādes spriegums pie izlādes strāva 0,1 mA/s; d) *OCV* mērījumi divslāņu un trīsslāņu (ar variējošu koncentrāciju) elektrolītu baterijām.

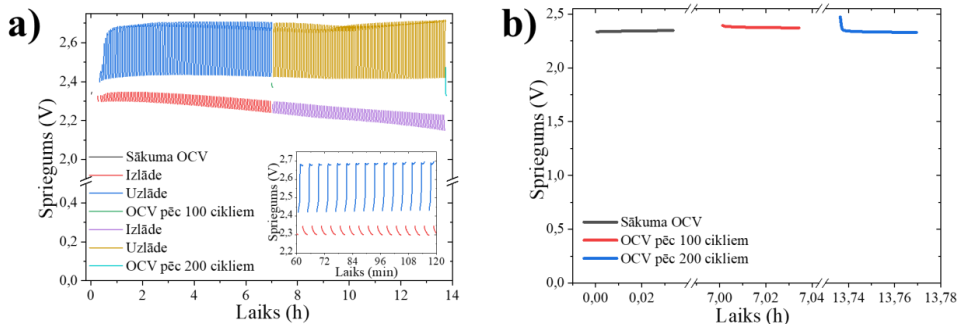
Modelētās parametru vērtības saskaņā ar ekvivalento shēmu, kas iegūtas no EIS mērījumiem

Parametrs	Vērtība	Kļūda, %
R_s	30,5 Ω	0,2
R_1	17,2 Ω	6
CPE_1	106 mF	3
R_{ct}	6,7 Ω	7
CPE_2	39 mF	4



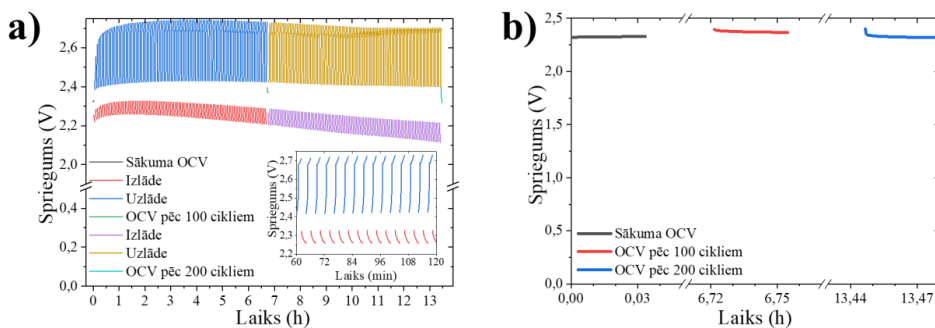
4.3. att. EIS spektrs ar modelēto spektru un ekvivalentā shēma.

Hronopotenciometrijas rezultāti amfotērai Zn-MnO₂ uzlādējamai baterijai ar divslāņu hidrogeļu elektroliem (1 M KOH un 0,5 M H₂SO₄) redzami 4.4. a. attēlā, *OCV* mērījumi pirms izlādes uzsākšanas, pēc 100 cikliem un pēc 200 cikliem – 4.4. b. attēlā. Baterijas augšējais uzlādes spriegums bija ap 2,7 V, zemākais izlādes spriegums 2,2–2,3 V. Papildus *OCV* mērījumi liecina, ka 2,34 V spriegums saglabājas stabils visā 14 h uzlādes-izlādes mērījumu laikā. Mērīšanas laikā tika novērota jonu difūzija ar redzamu pH neitrāla slāņa veidošanos starp abiem hidrogeļiem. To var attiecināt uz H⁺ un OH⁻ jonu difūziju un neitralizāciju, veidojot ūdeni. Tas vēl vairāk atšķaida skābo un bāzisko elektroliem, radot papildu iekšējo pretestību. Turklāt K⁺ un SO₄²⁻ joni (kas ir bāzes un skābes pretjoni, kā arī nodrošina jonu vadītspēju elektroliem) migrē arī uz baterijas vidusdaļu un veido kristālisku kālija sulfātu. Tas skaidrojams ar ierobežoto K₂SO₄ šķīdību ūdenī (120 g/L pie 25 °C), kas savukārt palielina baterijas iekšējo pretestību.



4.4. att. Divu (skāba un bāziska) hidrogelu slāņu amfotēras Zn-MnO₂ baterijas hronopotenciometrijas mērījumi. (a) Uzlādes-izlādes līknes; (b) *OCV* pirms izlādes, pēc 100 un pēc 200 uzlādes-izlādes cikliem. Uzlādes-izlādes strāva +/- 1 mA/s.

Lai novērtētu neitrālā slāņa ietekmi baterijas konstrukcijā, tika veikti arī hronopotenciometrijas un *OCV* mērījumi baterijām ar trīsslāņu elektrolītu – 1 M KOH, 0,5 M K₂SO₄ un 0,5 M H₂SO₄ (4.5. a. un b. att.). Trīsslāņu hidrogela baterijas uzlādes spriegums bija par 0,5 V lielāks, un izlādes spriegums bija par 0,5 V zemāks nekā divslāņu hidrogela baterijas spriegums (4.4. a. att.). Šī uzlādes un izlādes sprieguma neatbilstība ir saistīta ar lielāku hidrogela elektrolīta pretestību trīsslāņu hidrogela elektrolītā. Skābā (0,5 M H₂SO₄) hidrogela vadītspēja ir 83,6 mS/cm (pie 23 °C), bāziskā (1 M KOH) hidrogela vadītspēja ir 78,6 mS/cm (pie 23 °C), savukārt neitrālā (0,5 M K₂SO₄) hidrogela vadītspēja ir vairāk nekā sešas reizes zemāka – 12,6 mS/cm (pie 23 °C). Tas nozīmē, ka trīsslāņu elektrolīta kopējā pretestība ir ievērojami lielāka nekā divu slāņu elektrolīta pretestība un rada izlādes un uzlādes sprieguma neatbilstību abām baterijām. Turpretim *OCV* 2,32 V trīsslāņu hidrogela baterijai, kā redzams 4.5. b) attēlā, saglabājās stabils, līdzīgi kā divslāņu baterijai (4.4. b. att.).



4.5. attēls. Trīs (skāba, neitrāla un bāziska) hidrogelu slāņu amfotēras Zn-MnO₂ baterijas hronopotenciometrijas mērījumi. (a) Uzlādes-izlādes līknes; (b) *OCV* pirms izlādes, pēc 100 un pēc 200 uzlādes-izlādes cikliem. Uzlādes-izlādes strāva +/- 1 mA/s.

SECINĀJUMI

1. Izmantojot pH gradienta elektrolītu sistēmu, kur Zn anoda darbība ir sāmāinā vidē un MnO₂ katoda darbība ir skābā vidē, tiek novirzīta ūdeņraža izdalīšanās reakcija uz zemāku potenciālu (līdz -0,81 V) un skābekļa izdalīšanās reakcija uz lielāku potenciālu (līdz +1,2 V), palielinot ūdens elektroķīmisko sadalīšanās sprieguma diapazonu.
2. Dopējot MnO₂ katodu ar Bi³⁺ un Mo⁶⁺ joniem, materiālā notiek Mn³⁺ jonu stabilizācija, kas veicina elektroķīmiski aktīvākās α-MnO₂ fāzes struktūras izveidi. Noteiktas optimālās koncentrācijas: 5–10 mol% Bi un 2,5 mol% Mo.
3. Apstarojot Zn anodu ar impulsu lāzeru, par 30 % palielinās īpatnējās virsmas kapacitāte un samazinās lādiņa pārnese pretestība, kas uzlabo elektroķīmiskās reakcijas kinētiku 1 M KOH elektrolīta šķīdumā.
4. Izmantojot *Pluronic F-127* micellu hidrogelus, iegūstama lādējama amfotēra ūdens elektrolīta Zn-MnO₂ baterija, kur Zn anods atrodas 1 M KOH elektrolīta šķīdumā, bet MnO₂ katods 0,5 M H₂SO₄ elektrolīta šķīdumā.
5. Amfotērs ūdens elektrolīta Zn-MnO₂ baterijas atvērta ķēdes spriegums ir 2,4 V, pH gradienta stabilitāte saglabājas vairāk nekā 25 stundas, izlādes spriegums pie 0,1 mA/s ir 2,34 V un stabili 200 uzlādes-izlādes cikli pie 1 mA/s.

ACKNOWLEDGEMENTS

I express my deepest gratitude to all those who have supported and guided me throughout the entire doctoral journey.

First, I would like to extend my heartfelt thanks to my main supervisors, Dr. chem. Gunārs Bajārs and Dr. chem. Reinis Drunka, for their outstanding professional guidance and invaluable feedback. Their in-depth suggestions and constructive criticism significantly contributed to the creation of this Thesis.

I would also like to express sincere gratitude to Dr. phys. Pāvels Onufrijevs, who laid the foundation for both my academic and professional development. His competence, encouragement, and understanding attitude have served as a continuous source of inspiration.

I also appreciate the excellent collaboration with my research group colleagues – PhD Anzelms Zukuls and Ņikita Griščenko – for their support, cooperation, and the enriching discussions during the project development process. Together with my colleagues Mairis Iesalnieks, Linda Laima Alsīņa, and Mārtiņš Vanags, we have participated in many stimulating conversations that not only broadened our horizons but also helped us reach new peaks in our research.

I am equally grateful to the colleagues from the Institute of Physics and Materials Science, as well as to Dr. chem. Nelli Batenko and PhD Anastasija Gaile for their assistance and encouragement, which made my research experience both productive and truly exciting.

Finally, I would like to express my heartfelt gratitude to my life partner and family – whose unwavering love and boundless support were a true pillar throughout this journey. Their faith in me and emotional support were crucial in helping me maintain focus and motivation, even during the most challenging moments.

DOCTORAL THESIS PROPOSED TO RIGA TECHNICAL UNIVERSITY FOR PROMOTION TO THE SCIENTIFIC DEGREE OF DOCTOR OF SCIENCE

To be granted the scientific degree of Doctor of Science (PhD), the present Doctoral Thesis has been submitted for defence at the open meeting of RTU Promotion Council “RTU P-02” on December 10, 2025, in an open meeting online on the Zoom platform: <https://rtucloud1.zoom.us/j/96283313764>; ID: 962 8331 3764

OFFICIAL REVIEWERS

Professor Dr. chem. Donāts Erts
University of Latvia, Latvia

Professor PhD Agris Bērziņš
University of Latvia, Latvia

Associate Professor PhD Alar Jānes
University of Tartu, Estonia

DECLARATION OF ACADEMIC INTEGRITY

I hereby declare that the Doctoral Thesis submitted for review to Riga Technical University for promotion to the scientific degree of Doctor of Science (PhD) is my own. I confirm that this Doctoral Thesis has not been submitted to any other university for promotion to a scientific degree.

Ramona Zukule (signature)

Date:

The Doctoral Thesis has been prepared as a collection of thematically related scientific publications complemented by summaries in both Latvian and English. The Thesis unites four original research articles and one review article published in Scopus-indexed journals. The scientific publications have been written in English, with a total volume of 57 pages, not including supplementary data.

CONTENTS

GENERAL OVERVIEW OF THE THESIS	41
Introduction.....	41
Aims and objectives.....	42
Thesis statements to be defended.....	43
Scientific novelty.....	43
Practical significance.....	43
Structure and volume of the Thesis.....	44
Publications and approbation of the Thesis.....	44
Scientific publications.....	44
Most significant conference participation.....	44
LITERATURE REVIEW AND RESULTS.....	46
1. Literature review on the performance of an aqueous electrolyte Zn-MnO ₂ battery depending on the pH of the electrolyte medium.....	46
1.1. Alkaline electrolyte Zn-MnO ₂ batteries.....	46
1.2. Neutral and acidic electrolyte Zn-MnO ₂ batteries.....	48
1.3. Dual/amphoteric electrolyte Zn-MnO ₂ batteries.....	49
2. Main results about the improvement of MnO ₂ cathode performance in acidic electrolyte.....	51
2.1. Methodology.....	51
2.2. Results.....	52
3. Main results about improving the performance of the Zn anode in alkaline electrolyte.....	58
3.1. Methodology.....	58
3.2. Results.....	59
4. Main results about the development of amphoteric batteries using hydrogels with different pH environments.....	65
4.1. Methodology.....	65
4.2. Results.....	66
CONCLUSIONS.....	70
REFERENCES.....	71

ABBREVIATIONS

OCV	open circuit voltage
CB	carbon black
CV	cyclic voltammetry
EIS	electrochemical impedance spectroscopy
GCD	galvanostatic charge-discharge
HER	hydrogen evolution reaction
NMP	N-methyl-2-pyrrolidone
OER	oxygen evolution reaction
SEM	scanning electron microscope
XPS	X-ray photoelectron spectroscopy
XRD	X-ray diffraction

GENERAL OVERVIEW OF THE THESIS

Introduction

Global demand for efficient and sustainable energy storage solutions continues to rise alongside the increasing use of renewable energy sources and the electrification of various sectors [1]–[5]. Renewable energy sources are characterized by irregular energy production – for example, solar energy can only be harnessed during daylight hours [6]–[8]. Therefore, batteries play a crucial role in mitigating the intermittency of renewables by ensuring reliable energy storage and a stable electricity supply on demand [9]–[12]. Currently, one of the most widespread and successful energy storage technologies is rechargeable lithium-ion batteries [13]–[17]. They offer high energy (up to 500 Wh/g) and power (up to 300 W/kg) densities, a large theoretical capacity (890 mA h/g), high operating voltage (> 3.7 V), and excellent charge-discharge stability (over 10,000 cycles) with low self-discharge [18]–[24]. However, key drawbacks of rechargeable lithium-ion batteries include safety concerns due to overheating and potential self-ignition [25]–[29], as well as limited lithium resources [30]–[33]. These issues have prompted the search for alternatives by developing new or improving existing battery technologies.

Among existing battery technologies, aqueous electrolyte Zn-MnO₂ batteries have attracted considerable attention, as they already dominate the non-rechargeable battery market [34], [35]. They offer lower costs, higher safety, and are more environmentally friendly compared to chargeable lithium-ion batteries [36]–[38]. However, to meet future needs, it is necessary to develop their potential application as rechargeable batteries, which presents several challenges, such as electrolyte stability, electrode degradation, and performance limitations [19], [39]–[43].

One of the problems typical for rechargeable Zn-MnO₂ batteries is their low operating voltage and poor cyclability, stemming from the instability of the MnO₂ cathode and unwanted side reactions, such as MnO₂ disproportionation and dissolution, phase transitions to electrochemically inactive forms, oxygen evolution reaction (OER), and the formation of electrochemically inactive compounds with Zn²⁺ ions [44], [45]. To optimize performance, various electrolyte compositions have been studied, including alkaline [19], [38], [46], [47], neutral [48]–[51], and acidic [52], [53] electrolytes. However, each approach undesirably affects cycle life, efficiency, and reaction kinetics. Further adaptation and exploration of electrolytes. i.e., creating pH gradient electrolytes and dual-electrolyte systems, offer significant improvements in electrochemical stability and operating voltage for Zn-MnO₂ systems. By carefully tailoring the electrolyte environment around the anode and cathode, it is possible to extend the electrochemical water decomposition window while mitigating side reactions [54]–[59].

In addition to electrolyte optimization, attention must be paid to the structural stability of the MnO₂ cathode. MnO₂ exists in several polymorphs, each with distinct electrochemical properties depending on its crystal structure. For the sequence $\alpha > \delta > \beta$, the theoretical capacity decreases, meaning the different phases exhibit varying cyclability and ion diffusion properties [60]–[62]. In alkaline electrolytes, the MnO₂ cathode may form electrochemically inactive phases such as Mn(OH)₂, Mn₂O₃, and Mn₃O₄ [19], while in acidic environments, it may

dissolve or transition into another polymorph due to side reactions [40], [63], leading to capacity loss. Introducing heteroatoms into the electrode structure is a potential solution to improve electrochemical properties [64]. Studies have explored the effects of heteroatoms on MnO₂ in alkaline and neutral electrolytes. For example, doping with Co [65]–[67] and Mo [68], [69] promotes defect formation in the MnO₂ crystal lattice, stabilizing certain polymorphs. Meanwhile, Bi doping [34], [70]–[73] narrows the MnO₂ bandgap and facilitates electrochemical dissolution–deposition processes

Another key limitation of aqueous Zn-ion batteries is the instability of the metallic Zn anode, which leads to dendrite formation, hydrogen evolution reaction (HER), and surface passivation [41]–[43]. To prevent these side reactions, various surface modification methods have been explored to improve the electrochemical properties of Zn anodes. The main approaches include surface coating and electrolyte modification to control the Zn deposition–dissolution reactions. Coating types include CaCO₃ [74], ZnO [75]–[77], ZrO₂ [78]–[80], TiO₂ [81]–[83], and various polymer coatings [84]–[87].

Further development of this research, which includes electrolyte development, cathode stabilization, Zn surface modification, and integration into batteries, is an important step towards the commercialization of rechargeable aqueous electrolyte Zn-MnO₂ batteries. Therefore, this Doctoral Thesis focuses on the main limitations at the electrolyte, cathode, and anode levels with the aim of advancing rechargeable batteries with higher energy density, better cyclability, and improved safety.

Aims and objectives

This Doctoral Thesis aims to develop a concept of increasing the voltage of aqueous Zn-MnO₂ batteries above 2 V and to investigate the required modifications to the electrolyte, cathode, and anode to realize this concept.

To achieve this aim, the following objectives were set:

1. Develop a strategy for increasing the operating voltage of water-based electrolyte rechargeable batteries above 2 V, bypassing the water decomposition voltage limitations.
2. To synthesize MnO₂ powders doped with Bi and Mo ions. To evaluate the properties of the obtained materials using non-destructive analytical methods and prepare thin coatings on carbon paper. To conduct electrochemical measurements of the prepared coatings in an acidic electrolyte solution.
3. To modify Zn plates using pulsed laser irradiation at different energy fluencies. To characterize the prepared samples using non-destructive analysis and perform electrochemical measurements in an alkaline electrolyte solution.
4. To create a pH gradient electrolyte using Pluronic F-127 hydrogel. To assemble a Zn-MnO₂ battery using the pH-gradient electrolyte, conduct electrochemical measurements, and determine whether the operating voltage window of the aqueous electrolyte can be extended beyond 2 V.

Thesis statements to be defended

1. A pH gradient electrolyte system, where there is an alkaline environment at the anode and an acidic environment at the cathode, increases the electrochemical window of water.
2. Doping the MnO_2 cathode with Bi^{3+} and Mo^{6+} ions improves electrochemical performance in acidic electrolyte.
3. The stability of the Zn anode in an alkaline electrolyte is improved by structuring the anode surface with a pulsed laser.
4. A rechargeable amphoteric aqueous electrolyte Zn- MnO_2 battery can be created using Pluronic F-127 micelle-type hydrogel.
5. An aqueous electrolyte Zn- MnO_2 battery with a voltage above 2 V can be obtained by using two different pH electrolytes, or amphoteric systems.

Scientific novelty

In the Doctoral Thesis, an innovative approach to the design of an aqueous Zn- MnO_2 rechargeable battery has been developed and implemented, thus overcoming fundamental limitations at the electrode and electrolyte levels. The study combines strategies in electrode material modification, electrolyte engineering, and battery design improvement to expand the operating voltage range of the battery and improve electrochemical performance. Research has been conducted to improve the stability and electrochemical performance of materials in different pH electrolyte environments, and a new battery concept has been developed based on separated cathode and anode electrolyte spaces. The results of the study reflect the relationships between the structure and properties of water-based electrolyte battery components, which can be used in the development of alternative energy storage systems.

Practical significance

1. Development of aqueous electrolyte Zn- MnO_2 rechargeable batteries with increased operating voltage to promote the development of safer and more efficient alternative energy storage systems.
2. Development of a dual electrolyte system concept that reduces parasitic reactions on the electrodes, thereby improving electrochemical stability, as an alternative to traditional battery designs.
3. Development of scalable methods (doping of semiconductors with heteroatoms via the hydrothermal method and structuring of metal surfaces with a pulsed laser) for modifying electrodes that increase specific capacity.
4. Construction of rechargeable batteries using elements commonly found in the Earth's crust as electrode materials, creating an alternative battery technology that does not depend on critical raw materials.

Structure and volume of the Thesis

The Doctoral Thesis is presented as a thematically unified collection of scientific publications focused on the development of an amphoteric aqueous Zn-MnO₂ battery and the individual improvement of its electrolyte and electrodes. The Thesis includes four original research articles and one review article published in Scopus-indexed journals.

Publications and approbation of the Thesis

The main results of the Thesis are published in four scientific research articles. One review article was also prepared during the development of the Thesis. The research results have been presented at 17 scientific conferences.

Scientific publications

1. **R. Durena**, N. Griscenko, L. Orlova, M. Bertins, A. Viksna, M. Iesalnieks, A. Zukuls. Synthesis, structure, and electrochemical performance of Bi-induced stabilization of MnO₂ cathodes for use in highly acidic aqueous electrolytes (pH < 2). *Journal of Alloys and Compounds*, 1010, **2025**, 177904. <https://doi.org/10.1016/j.jallcom.2024.177904> (IF 5.8, CiteScore 11.1)
2. **R. Dūrena**, L. Fedorenko, Ņ. Griščenko, M. Vanags, L. Orlova, P. Onufrijevs, S. Stanionyte, T. Malinauskas, A. Zukuls. Irradiating the Path to High-Efficiency Zn-Ion Batteries: An Electrochemical Analysis of Laser-Modified Anodes. *Global Challenges*, 8 (10), **2024**, 2400105. <https://doi.org/10.1002/gch2.202400105> (IF 4.4, CiteScore 8.7)
3. Ņ. Griščenko, **R. Dūrena**, M. Iesalnieks, M. Bērtiņš, A. Viksna, A. Zukuls. Improvement of manganese dioxide cathode by molybdenum doping in highly acidic electrolyte. *Journal of Energy Storage*, 76, **2024**, 109847. <https://doi.org/10.1016/j.est.2023.109847> (IF 8.9, CiteScore 11.8)
4. **R. Durena**, A. Zukuls. A Short Review: Comparison of Zinc–Manganese Dioxide Batteries with Different pH Aqueous Electrolytes. *Batteries*, **2023**, 9(6), 311. <https://doi.org/10.3390/batteries9060311> (IF 5.3)
5. **R. Durena**, A. Zukuls, M. Vanags, A. Šutka. How to increase the potential of aqueous Zn-MnO₂ batteries: The effect of pH gradient electrolyte. *Electrochimica Acta*, **2022**, 434, 141275. <https://doi.org/10.1016/j.electacta.2022.141275> (IF 5.5, CiteScore 11.3)

Most significant conference participation

1. **R. Dūrena**, Ņ. Griščenko, A. Zukuls. High-Potential 2 V Rechargeable Zinc-Manganese Dioxide Batteries Enabled by Polymer Hydrogels. *2024 MRS Fall Meeting*. Boston, USA. 1–6 December **2024**. EN08.08.25
2. **R. Dūrena**, Ņ. Griščenko, A. Zukuls. Extending the Electrochemical Window of Aqueous Zn-MnO₂ Batteries through pH Gradient Dual-Electrolyte. *Battery 2030+ 's 4th Annual Conference & Young Scientists gathering*. Grenoble, France. 27–29 May **2024**. P37

3. **R. Dūrena**, N. Griščenko, A. Zukuls. Enhanced capacity retention of MnO₂ cathode enabled by Bi doping. *8th Baltic Electrochemistry Conference: Finding New Inspiration 2*. Tartu, Estonia. 14–17 April **2024**. P24
4. **R. Dūrena**, A. Zukuls, M. Vanags. Amphoteric Zinc-Manganese Dioxide Aqueous Battery Exceeding 2V Potential. *16th International Conference on Materials Chemistry*. Dublin, Ireland. 3–6 June **2023**. P256
5. **R. Dūrena**, A. Zukuls, M. Vanags. 2.4 V Open-Circuit Potential Aqueous Zn-MnO₂ Rechargeable Battery with pH gradient hydrogel electrolyte. *European Materials Research Society Spring Meeting*. Strasbourg, France, 29.05–02.06, **2023**. D_P01-33.

LITERATURE REVIEW AND RESULTS

Literature review and results of the Doctoral Thesis are presented in four main chapters, which combine one review article and four original publications:

1. Literature review on the performance of an aqueous electrolyte Zn-MnO₂ battery depending on the pH of the electrolyte medium, as well as an evaluation and explanation of the dual battery concept, summarizing the review article (Appendix 1).
2. Results of the research on improving the operation and performance of MnO₂ cathode in a highly acidic electrolyte by incorporating Bi and Mo ions into the MnO₂ structure, summarized in original Publication 1 (Appendix 2) and original Publication 2 (Appendix 3).
3. Results of the research on improving the operation and performance of Zn anode in alkaline electrolyte using surface structuring with a high-power pulsed laser, summarized in original Publication 3 (Appendix 4).
4. Results of the research on the development and electrochemical parameters of a dual aqueous electrolyte Zn-MnO₂ rechargeable battery, summarized in original Publication 4 (Appendix 5).

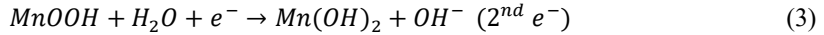
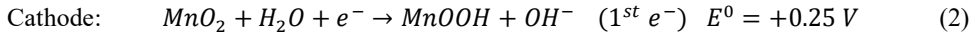
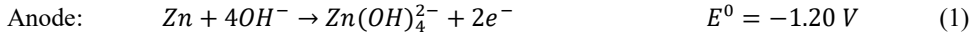
1. Literature review on the performance of an aqueous electrolyte Zn-MnO₂ battery depending on the pH of the electrolyte medium

The origins of aqueous electrolyte Zn-MnO₂ batteries date back to 1866, when French scientist Georges Leclanché manufactured and patented the first Zn-MnO₂ non-rechargeable battery, called the Leclanché cell [7]. These batteries were further developed in the 1950s by Canadian engineer Lewis Urry, who patented the alkaline Zn-MnO₂ battery in 1960 [88]–[91]. These batteries are still being improved, trying to extend their effective lifespan and replace hazardous elements such as mercury. Thus, aqueous alkaline Zn-MnO₂ batteries are the longest-standing and most widely used non-rechargeable battery technology, still dominating the global market [92]. This could be due to the fact that aqueous electrolyte Zn-MnO₂ batteries do not pose major safety risks, Zn metal has low toxicity (LD50 = 630 mg/kg – in rats) [93], Zn²⁺/Zn two-electron reaction has a relatively high theoretical capacity of 820 mAh/g [36], [37], as well as the theoretical capacity of MnO₂/Mn²⁺ two-electron reaction is 617 mAh/g [38], [94], [95]. Moreover, both zinc and manganese are common elements in the Earth's crust [36], [37].

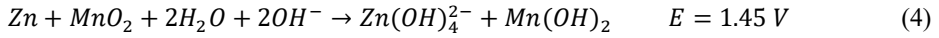
1.1. Alkaline electrolyte Zn-MnO₂ batteries

An aqueous alkaline Zn-MnO₂ battery consists of a Zn metal anode, a MnO₂ cathode, and a concentrated KOH aqueous solution (> 30 %) electrolyte. Carbon black (CB) particles are usually added to the cathode to ensure its conductivity, as MnO₂ itself is non-conductive. The schematic of this non-rechargeable battery is shown in Fig. 1.1, where the Zn anode undergoes electrochemical Reaction (1) with a standard potential of –1.199 V, while the cathode active component MnO₂ undergoes Reactions (2) and (3) with a standard potential of +0.250 V. Thus,

overall Reaction (4) occurs in the alkaline battery, resulting in an OCV of 1.45 V for the battery [6], [94], [96], [97].



Overall reaction:



Alkaline Zn-MnO₂ batteries are a long-established technology and are still being researched. Although these batteries are widespread as non-rechargeable batteries, they are still not widespread as rechargeable batteries. This is mainly due to the formation of electrochemically inactive manganese oxides Mn₃O₄ and ZnMn₂O₄. These compounds are formed during the deep discharge process [88], [98]. Thus, during the first few discharge-charge cycles, electrochemically inactive compounds cover the particles of the active MnO₂ compound of the cathode, stopping further reaction, which rapidly reduces the battery capacity. The scientific literature describes various ways to reduce or eliminate this undesirable effect in alkaline electrolytes, for example, doping the MnO₂ cathode with Bi or Cu ions [94], [99], as well as modifying the electrolyte by adding extra ions [100]–[102], such as Li⁺ [98].

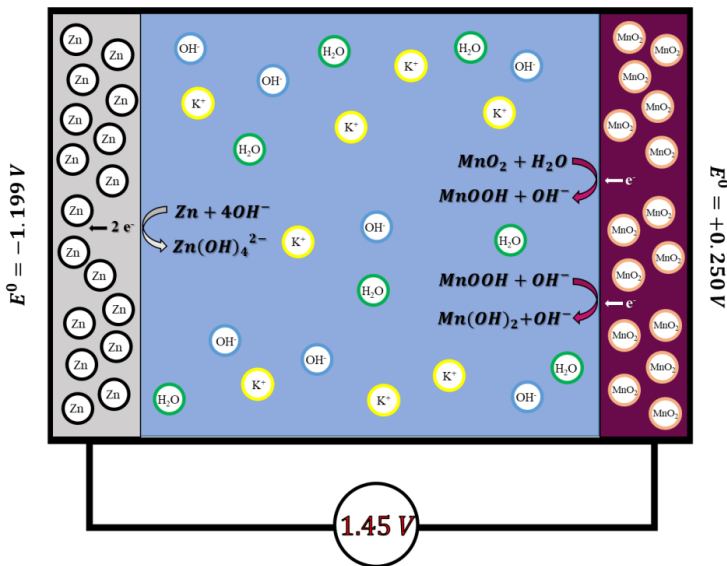
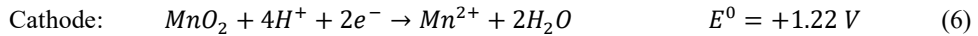


Fig. 1.1. Schematic operating mechanism of Zn-MnO₂ batteries with an alkaline aqueous electrolyte.

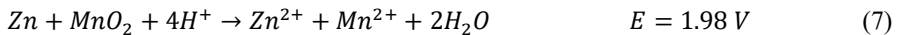
1.2. Neutral and acidic electrolyte Zn-MnO₂ batteries

The modification of the electrolyte in Zn-MnO₂ batteries has been further advanced by reducing the pH of the electrolyte from alkaline to neutral and even acidic, thereby altering the overall reactions occurring in the battery, as illustrated in the schematic representation of the Zn-MnO₂ battery with an acidic aqueous electrolyte (Fig. 1.2). In these systems, the alkaline electrolyte composed of KOH, NaOH, and LiOH [97], [98], [103]–[105] has been replaced with solutions of ZnSO₄, MnSO₄, K₂SO₄, Na₂SO₄ [106]–[111] and/or a diluted acid electrolyte [52], [53]. As shown in the Pourbaix diagram of manganese compounds (Fig. 1.3 a), which depicts the changes in the standard potential of the element in an aqueous electrolyte depending on the pH, at higher pH values, the electrochemical reaction of MnO₂ occurs at a standard potential of 0.250 V, with the possibility of forming the electrochemically inactive Mn₂O₃ phase. However, when the electrolyte pH is lowered to an acidic level, the oxygen atom in the MnO₂ cathode can bind with H⁺ ions from the electrolyte, forming water molecules. Consequently, Mn⁴⁺ ions can be reduced to Mn²⁺ ions, which dissolve into the electrolyte solution without forming the electrochemically inactive Mn₂O₃ phase. Moreover, this MnO₂ reaction in an acidic medium occurs at a standard potential above 1.2 V. However, this reduction in electrolyte pH increases the electrochemical reaction potential of the Zn anode. As seen in the Pourbaix diagram of zinc compounds (Fig. 1.3 b), the standard potential of the reaction increases from –1.199 V in an alkaline medium to –0.762 V in an acidic medium.

Despite the increase in the standard potential of the Zn anode, the overall battery design results in a higher operating voltage of up to 2 V, according to Reactions (5)–(7) [112]:



Overall reaction:



However, in an acidic medium, a parasitic reaction occurs – Zn anode corrosion. During this process, the Zn anode dissociates into Zn²⁺ ions in the electrolyte, releasing H₂ gas. This parasitic reaction not only reduces the capacity of the battery but can also lead to the rupture of the battery cell [113]. The occurrence of the parasitic reaction at the anode can be mitigated by coating the Zn anode with fumed silica and polyethylene glycol (with a molecular weight of 300 g/mol) [114]. To prevent potential MnO₂ dissolution, 0.1 M MnSO₄ is added to the electrolyte [107]–[110]. However, even in this type of battery, the formation of the ZnMn₂O₄ phase has been observed, which is chemically inactive and leads to capacity fading by increasing reaction irreversibility [115]. This suggests that both alkaline and neutral-acidic aqueous electrolyte Zn-MnO₂ batteries face similar challenges.

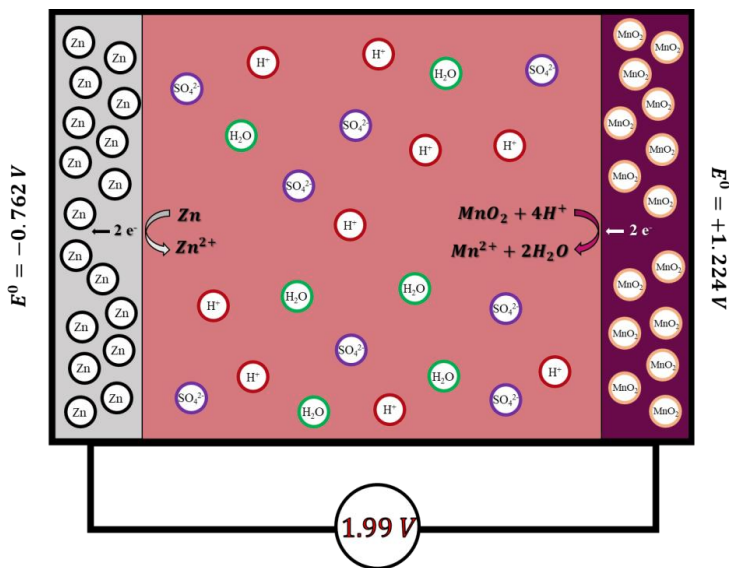


Fig. 1.2. Schematic operating mechanism of Zn-MnO₂ batteries with an acidic aqueous electrolyte.

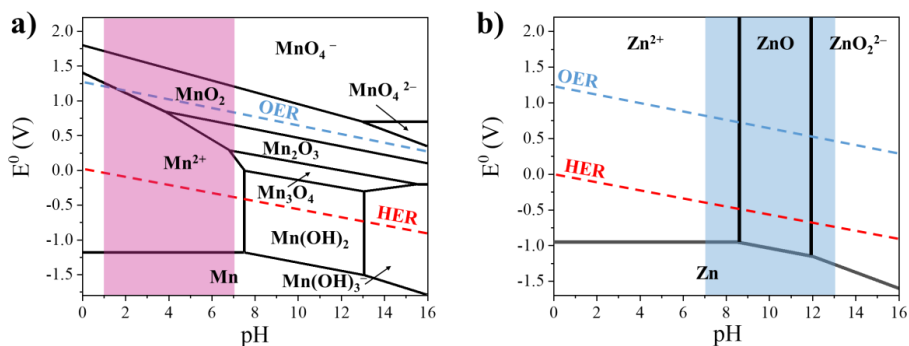
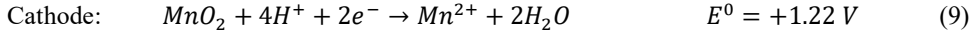
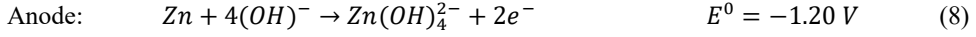


Fig. 1.3. Pourbaix diagrams with marked water decomposition potentials: a) for manganese compounds, and b) for zinc compounds [116].

1.3. Dual/amphoteric electrolyte Zn-MnO₂ batteries

To combine the beneficial properties of both alkaline and acidic aqueous electrolytes, a new type of cell has been developed, enabling an increase in the water decomposition voltage above 2 V. The structure of this cell consists of two electrolytes with different pH mediums, allowing the Zn anode to operate in an alkaline electrolyte while the MnO₂ cathode functions in an acidic electrolyte. This unique battery design, whose operating principle is illustrated in Fig. 1.4,

enhances the open-circuit voltage (OCV) of the cell up to 2.45 V, according to Reactions (8)–(10) [54], [113], [114].



Overall reaction:

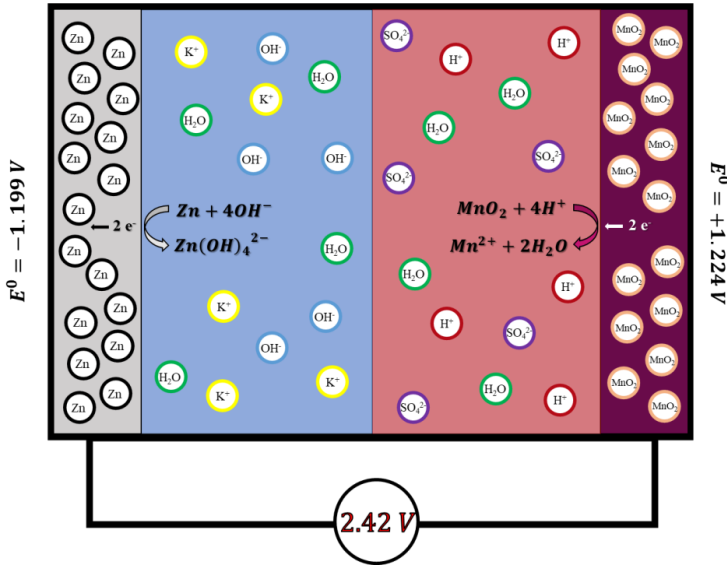
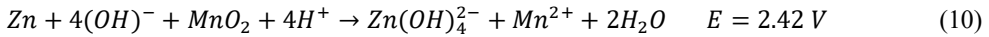


Fig. 1.4. Schematic operating mechanism of Zn-MnO₂ batteries with dual/amphoterous aqueous electrolyte.

The expanded water decomposition voltage window can also be explained using the Pourbaix diagram. As shown in Fig. 1.5, when the battery cell consists of a single electrolyte with a constant pH, the water decomposition voltage is 1.23 V. Consequently, using an aqueous electrolyte battery within a wider voltage window can lead to undesirable OER and HER. However, by employing a dual/amphoterous electrolyte system, it is possible to achieve a stable electrochemical voltage window for the aqueous electrolyte exceeding 2 V. Moreover, considering that, according to the Tafel equation, hydrogen evolution on Zn exhibits a high overpotential [117], [118], while oxygen evolution has a high overpotential [56] and slow reaction kinetics [119], the usable voltage range of the aqueous electrolyte can be extended up to 3 V.

Overall, the concept of a dual-electrolyte system and an expanded water stability voltage window has been described since 2005 [55]–[57]. Later, this dual-electrolyte concept was also applied to various battery systems, including Al-air [120]–[123], Zn-air [121], [124], [125], Mg-air [121], [126], Zn-PbO₂ [127]–[129], Zn-Br₂ [130], and Zn-MnO₂ [54], [58], [131].

However, the operational lifespan and efficiency of all these batteries are limited by neutralization reactions and ion diffusion within the electrolyte.

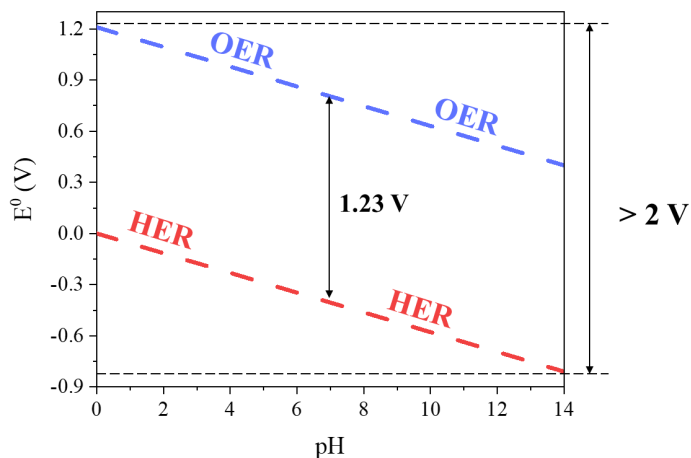


Fig. 1.5. Water Pourbaix diagram [116].

2. Main results about the improvement of MnO_2 cathode performance in acidic electrolyte

This chapter describes the improvement of MnO_2 cathode performance in a highly acidic ($\text{pH} < 2$) aqueous electrolyte by doping MnO_2 with Bi and Mo ions. The effect of the dopant ions is evaluated by investigating the impact of Bi and Mo ion concentration on the structural and electrochemical properties of MnO_2 , with concentrations ranging from 0 mol% to 10 mol%. Additionally, the mechanical role of Bi and Mo in stabilizing MnO_2 during the charge-discharge cycles is also examined.

2.1. Methodology

Bi- and Mo-doped MnO_2 powders were synthesized via a hydrothermal method using KMnO_4 as the manganese precursor. BiCl_3 was used as the bismuth precursor and introduced in concentrations ranging from 0 mol% to 10 mol%, while Na_2MoO_4 was used for Mo-doped samples in concentrations from 0 mol% to 5 mol%. The required salts for each synthesis were dissolved in distilled water, with a fixed amount of CB additionally introduced. The resulting solution was placed in an autoclave and kept in an oven at $120\text{ }^{\circ}\text{C}$ for either 12 h or 24 h. After the hydrothermal synthesis, all obtained powder samples were thoroughly washed with distilled water and dried in an oven at $60\text{ }^{\circ}\text{C}$ for 24 h.

Additionally, a commercially obtained MnO_2 (in the pyrolusite phase or $\beta\text{-MnO}_2$) sample was studied as a reference for the synthesized samples. To fabricate the cathodes, pyrolusite

and obtained powder samples were mixed with additional CB in a 13 : 5 ratio to improve the conductivity of the cathode. A cathode slurry was then prepared from the powder mixture by adding a polyvinylidene fluoride solution in N-methyl-2-pyrrolidone (NMP) in a 1 : 9 ratio. The resulting slurry was applied onto carbon paper using a doctor blade, followed by NMP evaporation and cutting the electrodes to the required dimensions.

2.2. Results

2.2.1. Bi-doped MnO₂ cathode

According to the XRD results shown in Fig. 2.1 a, the synthesized samples exhibited a two-phase mixture consisting of δ -MnO₂ (Mn₇O₁₃·5 H₂O – birnessite) and α -MnO₂ (K_{2-x}Mn₈O₁₆ – hollandite). Additionally, at higher dopant concentrations, the formation of a BiOCl phase was observed. Increasing the Bi ion concentration in the samples resulted in a decrease in the intensity of the δ -MnO₂ phase peak at 24.6° and an increase in the intensity of the α -MnO₂ phase peaks at 29° and 42°. This suggests that the introduction of Bi ions promotes the formation of the α -MnO₂ phase, which exhibits a 2 × 2 tunnel-like crystal structure. In this case, Bi ions occupy the vacant sites in the MnO₂ 2 × 2 tunnel structure as a filler. This prevents MnO₂ from adopting the layered δ -MnO₂ structure [70], [72], [132]–[134]. The formation of the tunnel-like α -phase is preferable in this context, as its tunnel structure facilitates ion transport through the crystal lattice, thereby enhancing electrochemical kinetics. In contrast, MnO₂ without dopant ions predominantly exhibited a phase more susceptible to dissolution in acidic environments. Scanning electron microscopy (SEM) images of the samples, shown in Fig. 2.1 b, reveal that the synthesized powders consist of aggregates of smaller and larger needle-like structures, which are characteristic of different MnO₂ polymorphs [135]–[137]. In comparison, the pyrolusite reference sample consists of rounded particle aggregates.

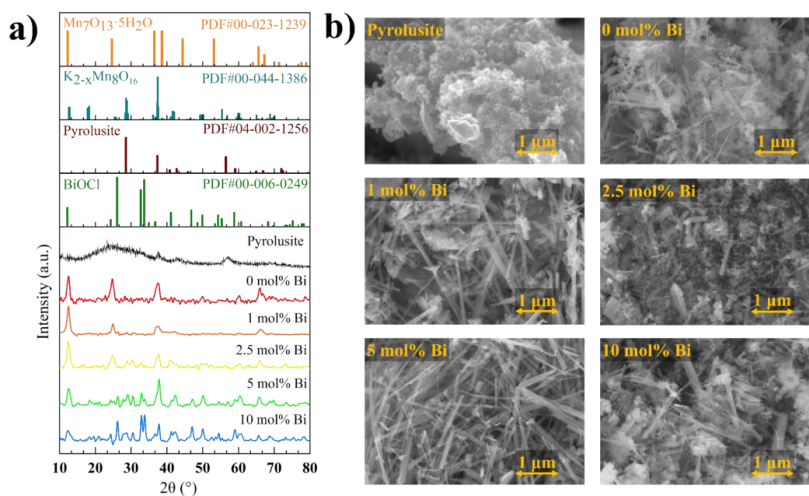


Fig. 2.1. Bi-doped MnO₂ sample and pyrolusite: a) XRD diffractograms, and b) SEM images.

To further characterize the synthesized samples, X-ray photoelectron spectroscopy (XPS) analysis was performed. In the normalized Mn 2p XPS spectra (Fig. 2.2 a), a peak shift towards the Mn³⁺ binding energy is observed, which becomes more pronounced with increasing Bi³⁺ concentration in the sample. Additionally, the differential spectra of the normalized XPS signals (Fig. 2.2 b) show a decrease in the Mn⁴⁺ signal and an increase in the Mn³⁺ signal as the Bi³⁺ concentration increases. Similar observations regarding the formation of Mn³⁺ and Mn⁴⁺ oxidation states under comparable synthesis conditions in various metal oxide systems have been reported in the literature [138], [139]. These studies explain the role of heteroatoms introduced into the MnO₂ crystal structure in stabilizing metastable Mn³⁺ ions, which typically undergo disproportionation in oxide crystal lattices [140]. In the normalized O 1s spectra (Fig. 2.2 c), an increase in hydroxyl groups and adsorbed water on the surface is observed with higher Bi³⁺ concentrations in the sample. According to literature data, binding energies in the range of 531–535 eV are closely associated with surface hydroxyl groups, water, or oxygen-containing organic byproducts [141]. Examining the Bi 4f XPS spectra (Fig. 2.2 d), no Bi signal is detected in the 0 mol% Bi sample. However, as the Bi³⁺ concentration increases, the Bi signal becomes more pronounced, confirming that all Bi-containing samples have Bi atoms in the 3+ oxidation state [142], [143].

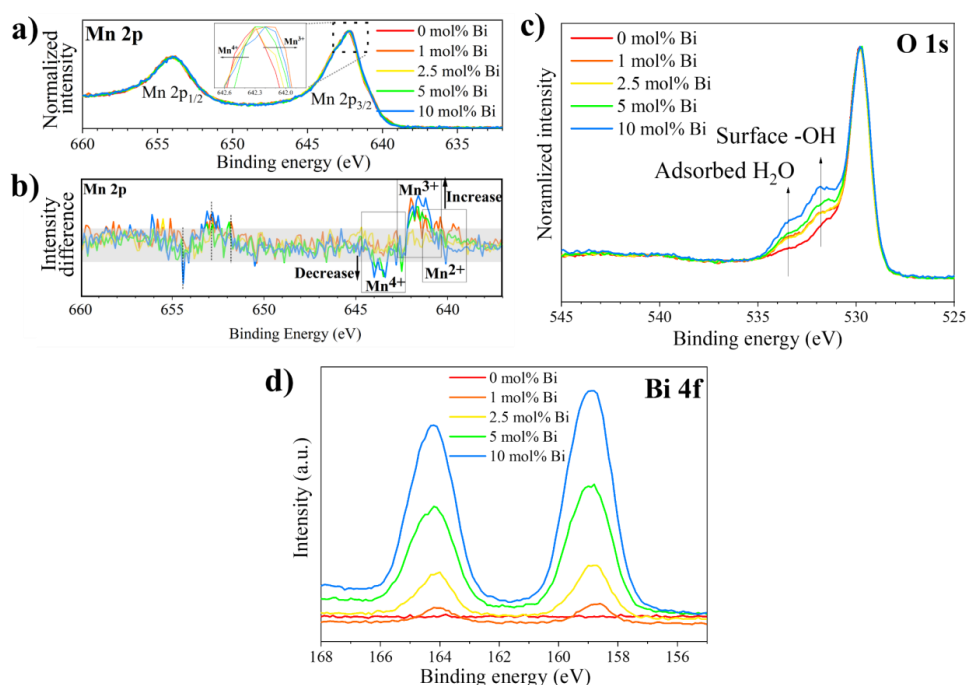


Fig. 2.2. Bi-doped MnO₂ sample and pyrolusite: a) normalized Mn 2p XPS spectra, and b) difference thereof; c) Bi 4f spectra, and d) normalized O 1s spectra.

Cyclic voltammetry (CV) measurements were performed on the prepared cathodes, and the specific capacities of each cathode were calculated based on the obtained data, as shown in Fig. 2.3 a. From these results, at slower scan rates, the cathode with 5 mol% Bi ion content exhibits the highest specific capacity of 130 mAh/g, while the cathode without Bi ions reaches only 120 mAh/g, and the pyrolusite cathode achieves 90 mAh/g.

To evaluate the capacity retention, galvanostatic charge-discharge (GCD) measurements were performed at varying current densities, as shown in Fig. 2.3 b. During the first five cycles, material activation and cathode stabilization take place. The pyrolusite cathode and the cathode without Bi ions require all five cycles to fully stabilize. In contrast, samples containing Bi ions stabilize within 2–3 cycles. In the following 15 cycles, as the current density increases from 0.25 A/g to 1.0 A/g, the pyrolusite cathode exhibits a similar capacity to the cathodes containing 0–5 mol% Bi ions. However, when the current density is reduced back to the initial 0.25 A/g, cathode materials with a higher Bi ion content demonstrate better capacity retention.

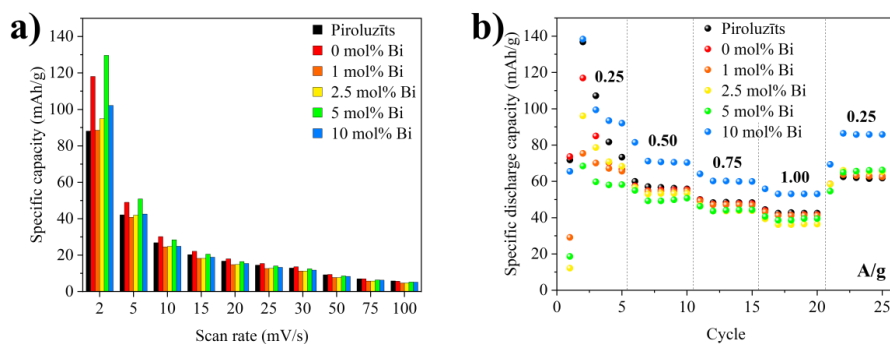


Fig. 2.3. Specific capacities of Bi-doped MnO_2 samples and pyrolusite: a) specific capacities obtained from CV measurements at different scan rates, and b) specific discharge capacities from GCD measurements at different current densities.

The electrochemical impedance spectroscopy (EIS) results for all samples after CV measurements are shown in the EIS diagrams in Fig. 2.4 a, where two compressed semicircles can be observed – one at high frequencies and the other at low frequencies. Additionally, fitted curves are shown based on the equivalent circuit in Fig. 2.4 b. The circuit consists of resistances – R_s , R_1 , and R_2 – and constant phase elements – CPE_1 and CPE_2 – parallel to their respective resistances. The values of all these components are listed in Table 2.1. The ohmic resistance of the electrolyte corresponds to component R_s and is approximately 22–23 Ω for all samples. The resistance R_1 and constant phase element CPE_1 represent the charge transfer resistance between the electrode and electrolyte as well as the double-layer capacitance. The fitted values indicate that the hydrothermally synthesized cathode materials exhibit a reduced double-layer capacitance, with the most significant reduction observed for the 10 mol% Bi MnO_2 sample. This observation correlates with the increase in surface hydroxyl groups shown in Fig. 2.2 c. The variation in surface hydroxyl group content influences the wetting properties of the

electrode and affects the interaction between the electrode surface and the electrolyte, thereby impacting the charge transfer resistance. The second set of parallel components – resistance R_2 and constant phase element CPE_2 – corresponds to the overall resistance and capacitance between individual cathode particles, since the cathode consists of a mixture of individual semiconductor MnO_2 and CB particles. According to the fitted values, the synthesized samples exhibit significantly lower resistance between individual particles. Comparing the pyrolusite and 0 mol% Bi samples, the CB added during synthesis reduces the particle-to-particle resistance by more than nine times.

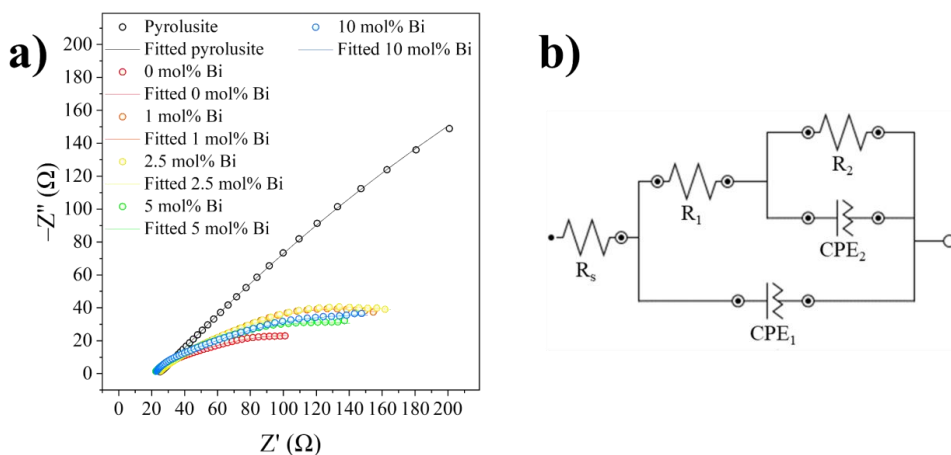


Fig. 2.4. Bi-doped MnO_2 sample and pyrolusite: a) measured EIS diagrams with fitted data according to b) equivalent circuit.

Table 2.1

Equivalent Circuit Parameters of the EIS Fitted Data

Sample	R_s Ω	R_1 Ω	CPE_1		R_2 Ω	CPE_2		χ^2
			Y^0	N		Y^0	N	
			$mS \cdot s^N$			$mS \cdot s^N$		
Pyrolusite	23.82	5.05	1.13	0.54	1474.8	1.93	0.52	0.00039
0 mol% Bi	21.66	9.49	0.29	0.68	161.94	6.30	0.34	0.00045
1 mol% Bi	23.75	49.03	1.52	0.52	162.74	3.32	0.45	0.00106
2.5 mol% Bi	23.74	39.57	1.38	0.53	195.00	3.54	0.40	0.00148
5 mol% Bi	21.71	6.23	0.16	0.74	204.60	4.68	0.36	0.00208
10 mol% Bi	22.37	8.04	0.13	0.77	242.74	4.80	0.35	0.00210

2.3.2. Mo-doped MnO₂ cathode

Also, XRD diffractograms shown in Fig. 2.5 for the Mo-doped samples reveal the presence of two phases: δ -MnO₂ (Mn₇O₁₃·5H₂O – birnessite) and α -MnO₂ (K_{2-x}Mn₈O₁₆ – hollandite). Similar to the Bi-doped samples, an increase in Mo concentration leads to a decrease in the δ -MnO₂ phase and an increase in the α -MnO₂ phase. This indicates that the addition of Mo dopant promotes the formation of the α -MnO₂ phase. Additionally, the synthesis time influences the crystallinity of the samples, as evidenced by more pronounced diffraction peaks in the samples synthesized for 24 hours with Mo concentration up to 2.5 mol%. This suggests the formation of larger crystallites [144], which is also consistent with the SEM images shown in Fig. 2.6 a. In these images, the samples synthesized for longer durations exhibit more defined structures, whereas the 12-hour samples consist of randomly shaped agglomerates.

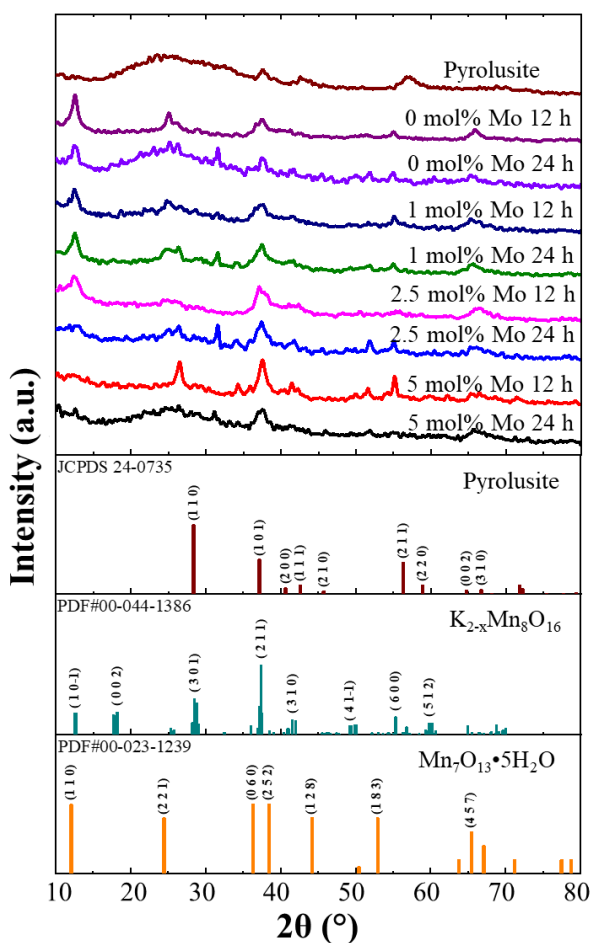


Fig. 2.5. XRD diffractograms of Mo-doped MnO₂ samples and pyrolusite.

XPS analysis was also performed to determine the oxidation states of the elements present, with the spectra shown in Fig. 2.6 b. All samples contain Mn^{4+} ions, and the synthesized samples also exhibit carbon-oxygen bonds due to the addition of CB during the synthesis process. Furthermore, the Mo-doped MnO_2 samples contain Mo^{6+} ions and metastable Mn^{3+} ions, indicating that the addition of Mo ions also stabilizes Mn^{3+} ions [145].

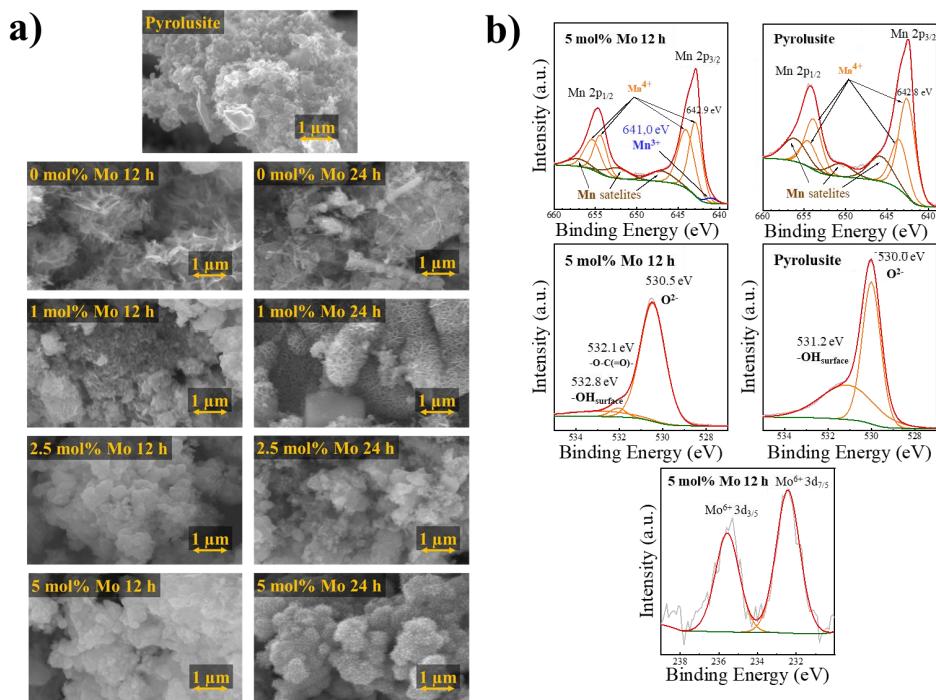


Fig. 2.6. Mo-doped MnO_2 sample and pyrolusite: a) SEM images, and b) Mn 2p, O 1s and Mo 3d spectra.

Further cathodes were prepared from Mo-doped MnO_2 samples, and CV measurements were performed to calculate the specific capacities of each cathode, which are summarized in Fig. 2.7 a. All synthesized samples show a higher specific capacity than the pyrolusite sample, with the specific capacity of the synthesized samples increasing as Mo atoms are added. The general increase in specific capacity between the pyrolusite and synthesized samples may be related to phase differences, as seen in the XRD results (Fig. 2.5), where the synthesized samples contain both $\delta\text{-MnO}_2$ and $\alpha\text{-MnO}_2$ phases. The highest specific capacity, 415 mAh/g at 0.002 V/s, was obtained from the 2.5 mol% Mo-doped MnO_2 sample synthesized for 12 hours. However, further tests reveal that the 1 mol% Mo-doped sample, synthesized for 12 hours, retains its specific capacity better as the scan rate increases. Overall, the CV measurements indicate that Mo-doped samples show an increase in specific capacity up to a Mo concentration of 2.5 mol%.

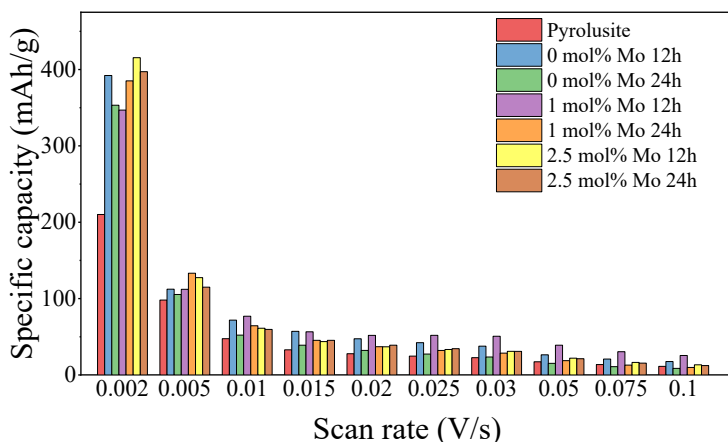


Fig. 2.7. Specific capacities of Mo-doped MnO₂ samples and pyrolusite.

3. Main results about improving the performance of the Zn anode in alkaline electrolyte

This chapter describes the improvement of the electrochemical properties of the zinc anode achieved by irradiating the Zn surface with a pulsed laser. The effect of laser irradiation on the structural and morphological properties of the Zn anode was evaluated. The electrochemical properties of the obtained anode materials, such as surface-specific capacity and charge transfer resistance, were examined. Possible mechanisms for the influence of laser modification on the performance of Zn anodes are discussed.

3.1. Methodology

Zinc plates with 99.95 % purity were modified using a nanosecond pulsed Nd: YAG laser at two wavelengths (266 nm and 1064 nm) in air and deionized water environments. A schematic of the irradiation process is shown in Fig. 3.1. The main laser parameters – energy fluence (ranging from 0.32 J/cm² to 2.66 J/cm²), which varies depending on the irradiation process, and pulse duration (6 ns) – were systematically varied and are summarized in Table 3.1. The resulting Zn anode samples were tested in an electrochemical half-cell with a 1 M KOH electrolyte, a Pt counter electrode, and an Ag/AgCl (3M KCl) reference electrode following surface examination.

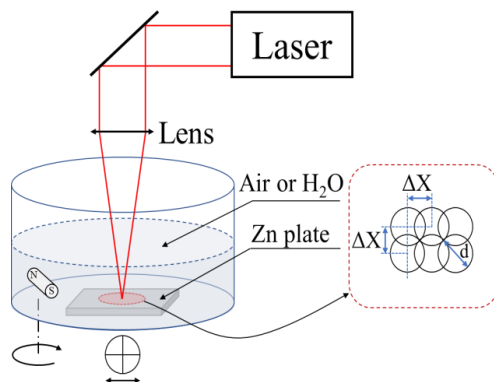


Fig. 3.1. Schematic representation of the laser irradiation process.

Table 3.1

Laser Irradiation Parameters			
Sample*	Laser wavelength, nm	Irradiation medium	Energy fluence, J/cm ²
Zn	un-irradiated	–	–
Zn-A-2.66*	266	Air	2.66
Zn-A-0.38	1064	Air	0.38
Zn-A-0.59	1064	Air	0.59
Zn-A-0.64	1064	Air	0.64
Zn-A-0.71	1064	Air	0.71
Zn-W-0.32*	266	Deionized water	0.32
Zn-W-0.53*	266	Deionized water	0.53
Zn-W-0.69	1064	Deionized water	0.69
Zn-W-1.29	1064	Deionized water	1.29
Zn-W-1.42	1064	Deionized water	1.42
Zn-W-1.60	1064	Deionized water	1.60

*A – air medium, W – water medium.

3.2. Results

Irradiation of samples with a pulsed laser caused significant morphological changes on the surface, as seen in SEM micrographs (Fig. 3.2). The untreated zinc sample exhibits a smooth surface with cold rolling marks characteristic of the manufacturing process, while the laser-treated samples display various surface morphologies depending on the irradiation environment. Samples irradiated in air with a 1064 nm laser show intense melting during irradiation, resulting in frozen droplet-like structures on the surface. In contrast, samples

irradiated in water with the same wavelength reveal wrinkled structures with homogeneously distributed droplets underneath. Samples irradiated in air with a 266 nm laser exhibit a moderately melted surface with a more uniform texture, whereas irradiation in water induces ZnO growth and forms a wrinkled melt structure.

XRD (Theta/2theta) diffractograms of untreated Zn plates (Fig. 3.3 a) show a polycrystalline Zn pattern with a dominant (002) basal plane parallel to the surface of the sheet. This is related to deformations caused during rolling in the production process [146]. However, Laser treatment of the samples reduces the intensity of the dominant (002) basal plane in the diffractograms. This is due to the surface melting caused by the laser, revealing the underlying polycrystalline structure where the (101) plane dominates. These changes promote more uniform zinc deposition during electrochemical processes. However, Raman spectra shown in Fig. 3.3 b confirm the formation of hexagonal ZnO on the surfaces of the irradiated samples. Additionally, Raman spectra reveal various ZnO defects: oxygen vacancies ($A_1(LO)$ peak at 574 cm^{-1}), interstitial Zn atoms (broad peak between $250\text{--}300\text{ cm}^{-1}$), and nitrogen-related defects (peak at 275 cm^{-1}) [147], [148].

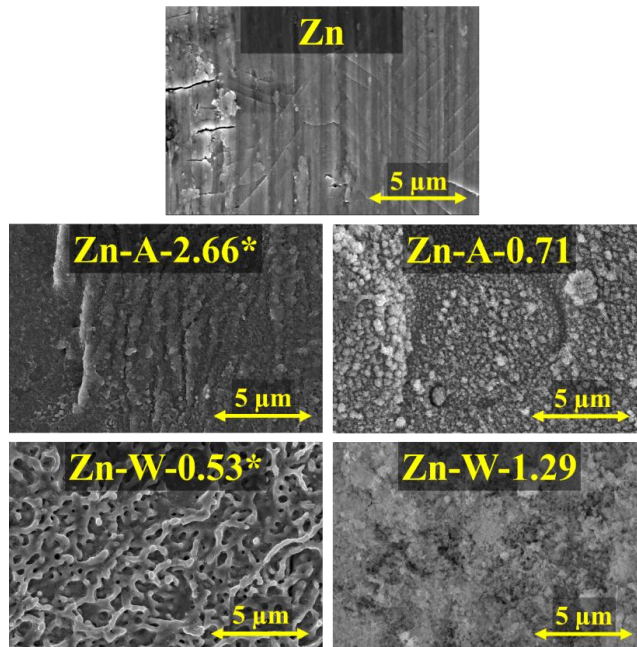


Fig. 3.2. SEM micrographs of untreated and pulsed laser irradiated Zn samples at different energy fluxes (A – in air medium, and W – in water medium).

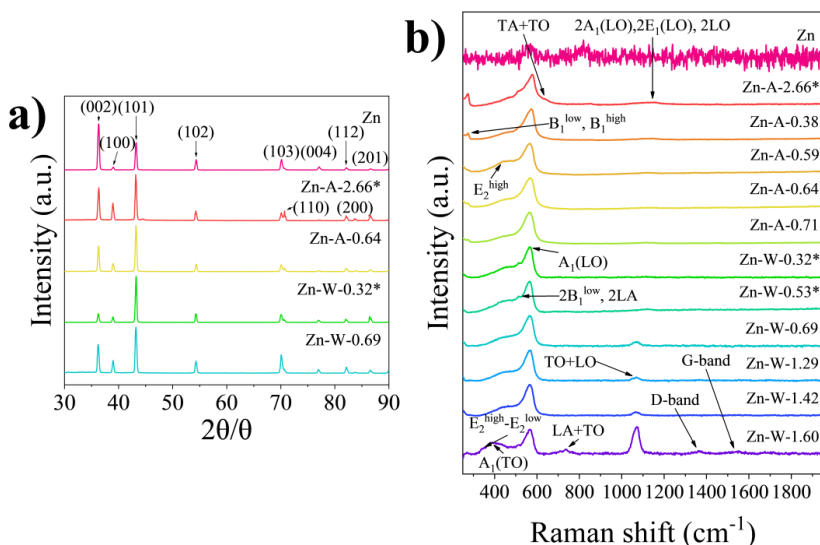


Fig. 3.3. Untreated and laser-irradiated Zn samples: a) XRD diffractograms; b) Raman spectra.

In CV measurements shown in Fig. 3.4 a and b, significant improvements in electrochemical properties are observed for laser-irradiated samples. During anodic oxidation (in accordance with reaction (1)), the Zn sample dissolves electrochemically until the electrolyte can no longer access the active Zn surface for further reaction. During this reaction, $\text{Zn}(\text{OH})_4^{2-}$ is formed, which immediately turns into ZnO and covers the anode surface. In turn, during the cathodic reduction reaction, a rapid increase in current is observed at -1.3 V [149], [150]. In this potential region, when ZnO is reduced back to Zn, the previously unreacted Zn surface is exposed to the electrolyte. This appears as a sharp current increase, indicating resumed Zn oxidation. Notably, this phenomenon is less pronounced in laser-treated samples, suggesting that oxidation is more controlled and ZnO grows more uniformly, despite that oxidation is at a higher maximum current. This implies that laser surface treatment improves the overall cyclic performance of the Zn electrode, and treated surfaces show higher oxidation and reduction currents, indicating enhanced reaction kinetics.

Specific surface capacities determined from CV measurements are summarized in Fig. 3.4 c and d. At a scan rate of 0.005 V/s, samples irradiated in air show slightly higher specific surface capacity (1.35 – 1.50 mAh/cm²) compared to those irradiated in water (1.25 – 1.35 mAh/cm²), and significantly higher than untreated Zn (1.15 mAh/cm²). Overall, laser-irradiated samples exhibit an 8–30 % increase in capacity depending on the treatment parameters. This increase is attributed to enhanced surface roughness and more active reaction sites caused by laser-induced melting and re-solidification.

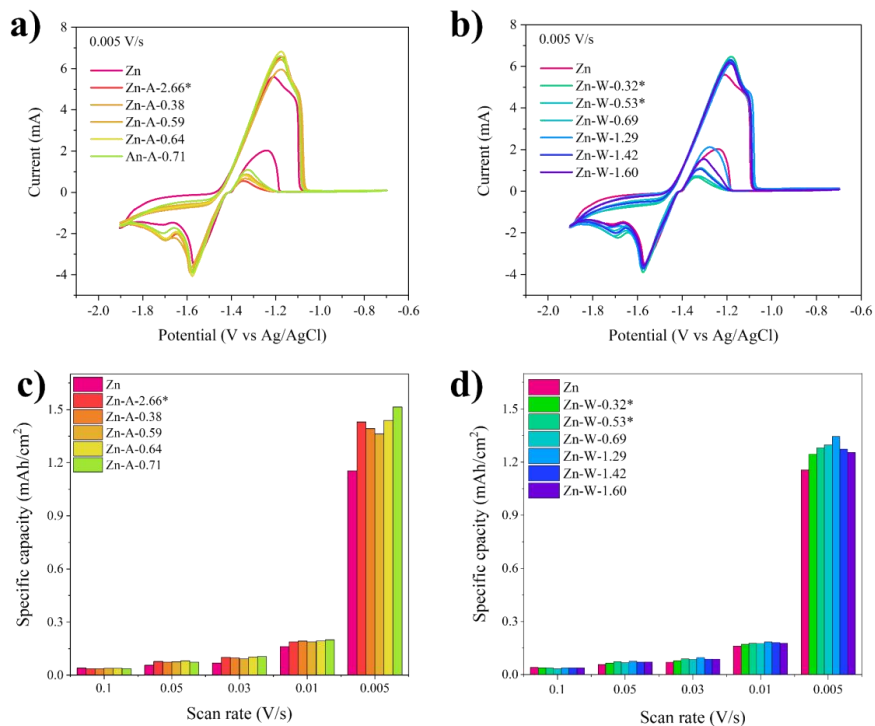


Fig. 3.4. Untreated and air-irradiated Zn samples: a) CV measurements; c) specific surface capacities. Untreated and water-irradiated Zn samples: b) CV measurements; d) specific surface capacities.

After electrochemical measurements, samples were re-examined using SEM (Fig. 3.5) to assess surface changes. The irradiated samples show grain structures with pronounced hexagonal Zn crystal facets. In contrast, the untreated Zn sample surface lacks defined crystal facets and shows random growth features.

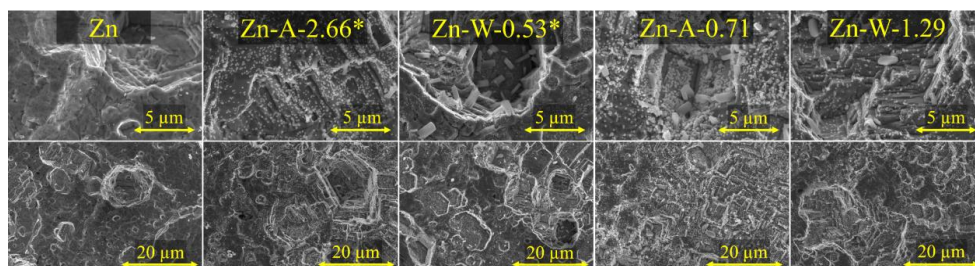


Fig. 3.5. SEM micrographs of untreated and laser-irradiated Zn samples after CV measurements.

Raman spectra of irradiated samples after electrochemical measurements, shown in Fig. 3.6 a, exhibit increased background, and characteristic ZnO peaks are difficult to identify. Conversely, untreated Zn samples still display ZnO peaks at 382 cm^{-1} , 441 cm^{-1} and 585 cm^{-1} , indicating that laser treatment improves Zn anode electrochemical reactions by promoting more uniform ZnO growth and more complete reversion to metallic Zn. However, untreated Zn samples only undergo partial charging (ZnO reduction to Zn), leading to increased ZnO content and a stronger ZnO Raman signal. This observation correlates with CV results of untreated Zn (Fig. 3.4 a and b), which show a more pronounced phenomenon at -1.3 V , linked to increased ZnO formation on the surface.

XRD (Theta/2theta) diffractograms were also repeatedly taken for the sample surfaces after CV measurements, which are shown in Fig. 3.6 b. The untreated Zn sample shows increased intensity of the (002) plane and reduced intensity of the (101) plane, indicating preferential growth in the (002) direction. A slight increase in the (100) plane suggests dendrite-like and porous structure formation [151]. In contrast, irradiated samples retain a polycrystalline (101) structure after CV. An increase in the (002) c-plane direction suggests a more horizontal structure formation. A slight decrease in (100) and (200) plane intensities indicates better resistance to dendrite formation. As illustrated schematically in Fig. 3.6 c, the growth directions of characteristic Zn planes influence potential surface structures. Growth in the (002) plane corresponds to smooth horizontal structures, while growth in (110) and (100) planes indicates dendritic and porous structures.

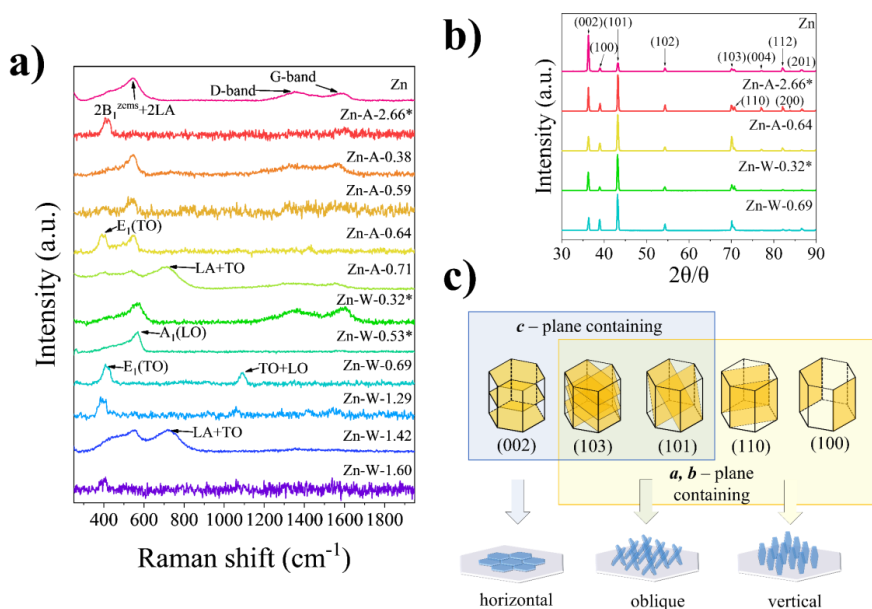


Fig. 3.6. Post-CV measurement results for untreated and laser-irradiated Zn samples: a) Raman spectra; b) XRD diffractograms; c) schematic of hexagonal Zn characteristic crystal planes and growth models.

To further characterize the electrode-electrolyte interface, EIS analysis was performed. EIS spectra at a negative DC offset of -150 mV from OCV are shown in Fig. 3.7 a, and spectra at a positive offset of $+150$ mV from OCV are in Fig. 3.7 b. Additionally, EIS spectra were fitted using equivalent circuits shown in the graphs, and component values are summarized in Table 3.2. At negative voltage, resistance R_1 is about 27Ω for all samples, corresponding to the ohmic resistance of the electrolyte. Resistance R_2 represents the charge transfer resistance of the faradaic process and is lower for laser-treated samples. However, CPE value (representing the double-layer capacitance) is increased for irradiated samples, indicating a macroscopically increased surface area. At low frequencies, all spectra transition into a sloped line, corresponding to Warburg impedance related to diffusion-limited processes.

An extended equivalent circuit model was applied to the obtained EIS diagrams at a positive voltage bias, where Zn oxidation and ZnO formation occur. As before, R_s represents the electrolyte resistance and is about 27Ω . The first R_1 and CPE_1 parallel connection characterizes the state of the electric double layer: R_1 is the ion polarization resistance, and CPE_1 is the double-layer capacitance. Capacitance values are similar, indicating that the macro-surface does not change during the electrochemical reaction. The second parallel circuit of CPE_2 and R_2 describes the faradaic process, where R_2 corresponds to charge transfer resistance. For untreated Zn, this value is 38Ω ; however, for laser-treated samples, it increases to about 200Ω . This increase is associated with laser-induced defects, also observed in Raman spectra after electrochemical measurements (Fig. 3.6 a). This increases the charge transfer resistance in the irradiated samples and reduces the reaction rate for Zn oxidation. CPE_2 reflects the Zn oxidation process capacitance and is several orders of magnitude higher than the double-layer capacitance. This decrease in capacitance is related to the slowed reaction due to the increased resistance of irradiated samples.

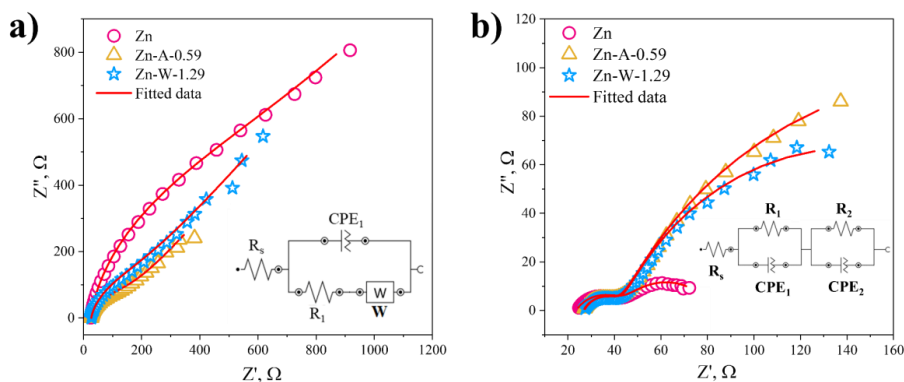


Fig. 3.7. EIS spectra of untreated and laser-irradiated Zn samples: a) at -150 mV DC offset from OCV; b) at $+150$ mV DC offset from OCV.

Table 3.2

Parameters of the Equivalent Circuit of EIS Fitted Data

Sample	R_s	R_1	CPE ₁		R_2	CPE ₂	
			Y^0	N		Y^0	N
	Ω	Ω	$\mu S \cdot s^N$		Ω	$\mu S \cdot s^N$	
at a negative DC offset from OCV							
Zn	24.7	668	70	0.90	–	–	–
Zn-A-0.59	26.5	185	103	0.87	–	–	–
Zn-W-1.29	26.5	132	124	0.84	–	–	–
at a positive DC offset from OCV							
Zn	23.6	20.5	369	0.63	38	6.35	0.67
Zn-A-0.59	26.7	15.5	292	0.70	304	3.95	0.72
Zn-W-1.29	27.0	16.0	290	0.70	200	3.79	0.72

4. Main results about the development of amphoteric batteries using hydrogels with different pH environments

This chapter describes the development of an innovatively designed aqueous Zn-MnO₂ battery and the evaluation of its electrochemical properties. The basis of this innovative design is an elevated OCV above that of the commercially available 1.5 V alkaline Zn-MnO₂ battery. This is achieved without the use of membranes, utilizing hydrogel electrolytes with differing pH environments, where the Zn anode is located in an alkaline (KOH) hydrogel electrolyte and the MnO₂ cathode in an acidic (H₂SO₄) electrolyte. Additionally, the use of a neutral (K₂SO₄) hydrogel as an interfacial layer between the two electrolytes is evaluated. This dual-environment approach minimizes unwanted side reactions, such as Zn anode corrosion in acidic electrolyte and the formation of electrochemically inactive Mn compounds in alkaline electrolyte.

4.1. Methodology

For battery fabrication, 30 wt% Pluronic F-127 micellar solutions were used as electrolytes, dissolved respectively in acidic (0.5 M H₂SO₄), alkaline (1 M KOH) and neutral salt (0.5 M K₂SO₄) solutions. pH indicators were added to the electrolyte solutions to allow visual identification of pH changes. A Zn plate of defined diameter was used as the anode. The cathode consisted of carbon felt impregnated with a mixture of MnO₂ (pyrolusite phase) and CB in a 13 : 5 ratio, further mixed with the acidic hydrogel to form a homogeneous mass.

To evaluate the performance of each electrode and its corresponding hydrogel, half-cell measurements were performed, where the cathode or anode was the working electrode, one platinum electrode was the counter electrode, and the other platinum electrode was the reference electrode. Afterwards, the battery was assembled in a syringe body (Fig. 4.1), allowing

observation of electrolyte changes during operation. First, the MnO_2 cathode felt was inserted at the syringe tip, followed by the 0.5 M H_2SO_4 acidic hydrogel, the 0.4–0.6 M K_2SO_4 neutral hydrogel (only for three-layer batteries), the 1 M KOH alkaline hydrogel, and finally the Zn anode, attached to the syringe plunger. In all battery configurations, the total electrolyte volume was fixed at 3 mL.

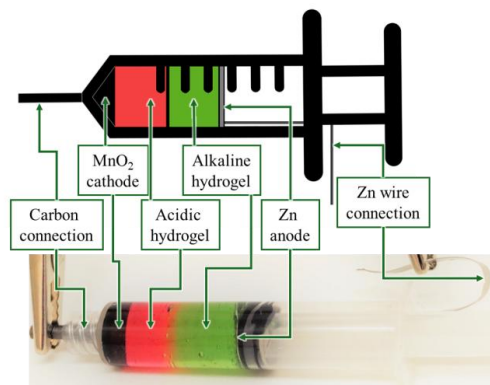


Fig. 4.1. Schematic and photograph of the constructed battery with labelled components.

4.2. Results

To determine the theoretical behaviour of the cathode and anode during battery operation, half-cell CV measurements were conducted. The MnO_2 cathode half-cell with acidic (0.5 M H_2SO_4) hydrogel and Zn anode half-cell with alkaline (1 M KOH) hydrogel were tested against a Pt counter electrode and Pt reference electrode. According to the combined data shown in Fig. 4.2 a, the OCV of the amphoteric battery is approximately 2.3 V. Measurements from several assembled Zn- MnO_2 amphoteric batteries (Fig. 4.2 a) confirm that the voltage ranges from 2.3 V to 2.4 V.

The expected minimum discharge voltage, based on the combined data, should be around 1.6 V. To assess this theoretical value, a complete discharge of the amphoteric Zn- MnO_2 battery was performed (Fig. 4.2 b) with a discharge current of 10 mA/s. Before discharge, the OCV was 2.4 V, the initial discharge plateau was around 2.0 V, and the end-of-discharge voltage was 1.7 V – consistent with observations from the half-cell CV measurements. Additionally, under a lower discharge current of 0.1 mA/s (Fig. 4.2 c), the initial voltage was 2.34 V, decreasing to 2.2 V over 10 hours.

During all measurements, the formation of a visibly neutral pH layer between the two hydrogels was observed. This can be explained by H^+ and OH^- ion diffusion from the acidic and alkaline electrolytes, where they neutralize in the interface, forming water, further diluting both hydrogel electrolytes and increasing internal resistance. To assess the influence of this neutral layer, OCV measurements were also carried out using an additional neutral hydrogel between the acidic and alkaline layers. The neutral electrolyte concentration (K_2SO_4) was varied relative to the acid/base concentration at 0.4 M, 0.5 M, and 0.6 M. According to the

measurements shown in Fig. 4.2 d, three-layer hydrogel electrolyte batteries maintained a stable voltage for over 45 h – longer than two-layer batteries, which dropped to 1.7 V after ~ 27 h due to the neutralization reaction. Among the three concentrations, the balanced 0.5 M hydrogel exhibited the longest voltage stability (~ 52 h), while both the lower and higher concentrations maintained stability only up to ~ 45 h. Overall, the pH gradient stability of the three-layer hydrogel electrolyte battery is more pronounced than that of the two-layer system.

To evaluate internal resistances, EIS measurements were performed on a fully assembled amphoteric Zn-MnO₂ battery, and the fitted data according to the equivalent circuit are shown in Fig. 4.3. The obtained parameter values are summarized in Table 4.1. The series resistance R_s of 30.5 Ω corresponds to the electrolyte resistance and is relatively high due to limited ion mobility hindered by micellar structures. The first semicircle at high frequencies represents the electrolyte-electrode interface, which is noted in the equivalent circuit as R_1 and CPE_1 parallel connection. Fitted R_1 was found to be 17 Ω , and the equivalent capacitance of CPE_1 is 102 mF. Both these parameters are sensitive to electrolyte composition [152] and electrode surface porosity [153], [154]. The second semicircle at low frequencies reflects charge-transfer processes, where R_{ct} is the charge transfer resistance with a fitted value of 6.7 Ω , and CPE_2 represents the double-layer capacitance with a fitted value of 39 mF.

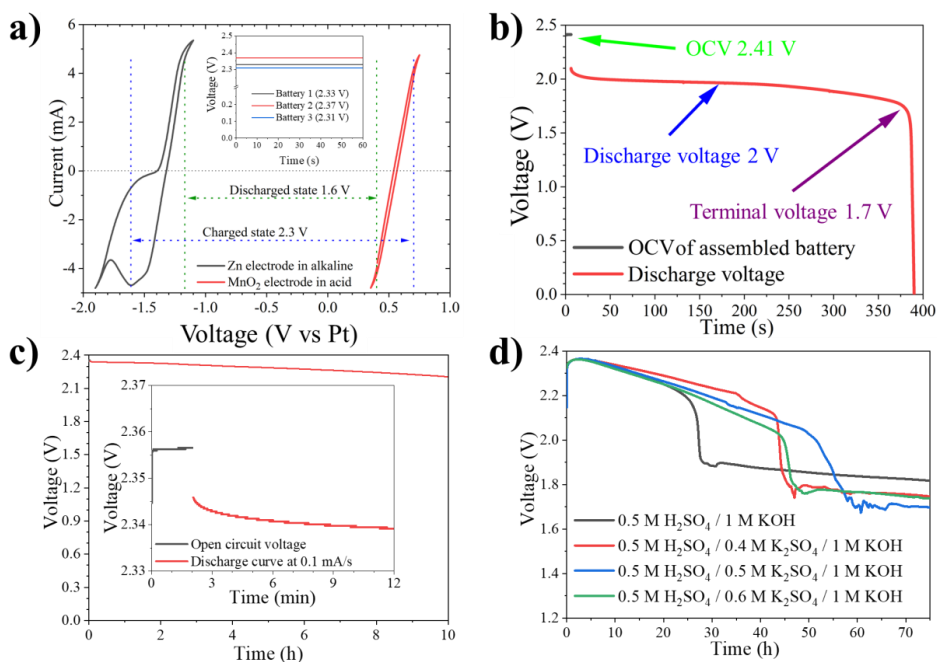


Fig. 4.2. Properties of the amphoteric battery: a) CV measurements of the half-cells in corresponding electrolytes (scan rate 0.01 V/s) and OCV measurements of the prepared batteries; b) OCV and discharge voltage at 10 mA/s discharge current; c) OCV and discharge voltage at 0.1 mA/s; d) OCV measurements for two-layer and three-layer electrolyte batteries with varying neutral layer concentrations.

Table 4.1

Fitted Parameter Values from EIS Measurements Based on the Equivalent Circuit

Parameter	Value	Error, %
R_s	30.5 Ω	0.2
R_1	17.2 Ω	6
CPE_1	106 mF	3
R_{ct}	6.7 Ω	7
CPE_2	39 mF	4

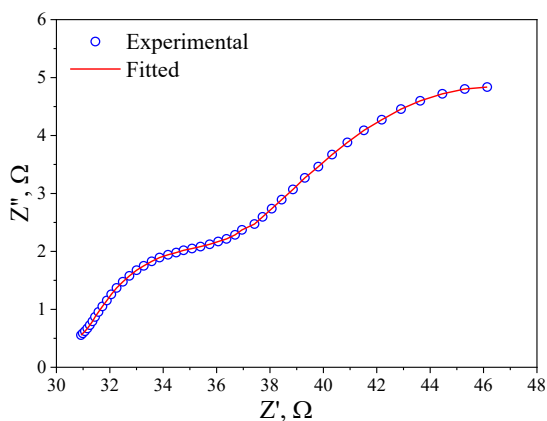


Fig. 4.3. EIS spectrum with fitted model and equivalent circuit.

Chronopotentiometry results for the amphoteric Zn-MnO₂ rechargeable battery with two-layer hydrogels (1 M KOH and 0.5 M H₂SO₄) are shown in Fig. 4.4 a, and OCV measurements before discharge, after 100 cycles, and after 200 cycles are shown in Fig. 4.4 b. The upper charge voltage of the battery was around 2.7 V, and the lowest discharge voltage ranged from 2.2–2.3 V. Additional OCV measurements show that the voltage of 2.34 V remained stable throughout 14 hours of cycling. During the measurements, ion diffusion was observed with a visible formation of a neutral pH layer between the hydrogels due to H⁺ and OH⁻ ion migration and their neutralization, forming water. This further diluted both electrolytes, increasing internal resistance. Additionally, K⁺ and SO₄²⁻ ions (counterions of the base and acid, respectively, and responsible for ion conductivity) also migrated toward the battery centre, forming crystalline potassium sulphate. This is explained by the limited solubility of K₂SO₄ in water (120 g/L at 25 °C), further contributing to internal resistance.

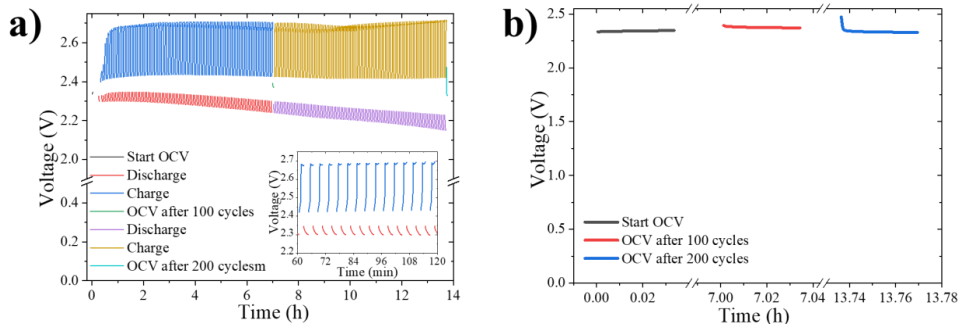


Fig. 4.4. Chronopotentiometry of the two-layer (acidic and alkaline) hydrogel Zn-MnO₂ amphoteric battery: a) charge/discharge curves; and b) OCV before discharge, after 100 and 200 charge/discharge cycles. Charge-discharge current: ± 1 mA/s.

To assess the effect of the neutral layer in the battery structure, additional chronopotentiometry and OCV measurements were conducted for batteries with a three-layer electrolyte – 1 M KOH, 0.5 M K₂SO₄ and 0.5 M H₂SO₄ – shown in Fig. 4.5 a and b. The charge voltage of the three-layer hydrogel battery was 0.5 V higher, and the discharge voltage was 0.5 V lower than in the two-layer battery (Fig. 4.4 a). This charge/discharge voltage discrepancy is due to the higher resistance of the hydrogel electrolyte in the three-layer configuration. While the conductivity of the acidic (0.5 M H₂SO₄) hydrogel is 83.6 mS/cm (at 23 °C) and the basic (1 M KOH) hydrogel is 78.6 mS/cm (at 23 °C), the neutral (0.5 M K₂SO₄) hydrogel conductivity is more than 6 times lower – 12.6 mS/cm (at 23 °C). This results in a significantly higher total resistance in the three-layer system, causing the observed charge–discharge voltage mismatch. However, the OCV of 2.32 V for the three-layer hydrogel battery (Fig. 4.5 b) remained stable, similarly to the two-layer battery (Fig. 4.4 b).

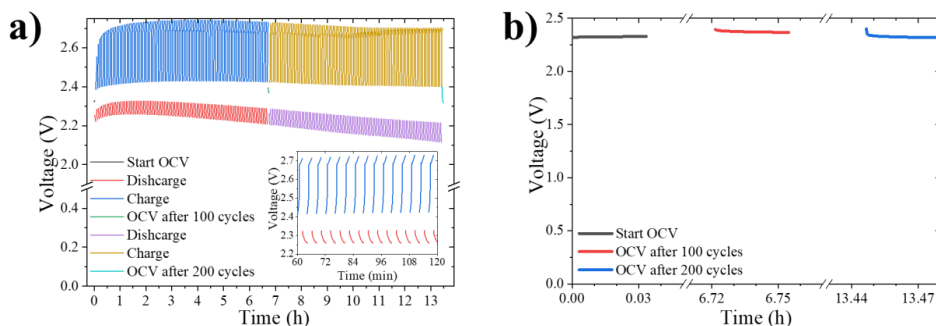


Fig. 4.5. Chronopotentiometry of the three-layer (acidic, neutral, alkaline) hydrogel Zn-MnO₂ amphoteric battery: a) charge/discharge curves; and b) OCV before discharge, after 100 and 200 charge/discharge cycles. Charge–discharge current: ± 1 mA/s.

CONCLUSIONS

1. Using a pH gradient electrolyte system, where the Zn anode operates in an alkaline environment, and the MnO₂ cathode operates in an acidic environment, shifts the hydrogen evolution reaction to a lower potential (to -0.81 V) and the oxygen evolution reaction to a higher potential (to +1.2 V), increasing the electrochemical window of water.
2. By doping the MnO₂ cathode with Bi³⁺ and Mo⁶⁺ ions, Mn³⁺ ions are stabilized in the material, which promotes the formation of the electrochemically more active α -MnO₂ phase structure. The optimal concentrations have been determined: 5–10 mol% Bi and 2.5 mol% Mo.
3. Irradiating the Zn anode with a pulsed laser increases the specific surface capacity by 30 % and reduces the charge transfer resistance, which improves the kinetics of the electrochemical reaction in a 1 M KOH electrolyte solution.
4. Using Pluronic F-127 micelle hydrogels, a rechargeable amphoteric aqueous electrolyte Zn-MnO₂ battery is obtained, where the Zn anode is in a 1 M KOH electrolyte solution, and the MnO₂ cathode is in a 0.5 M H₂SO₄ electrolyte solution.
5. The open-circuit voltage of the amphoteric aqueous electrolyte Zn-MnO₂ battery is 2.4 V, the pH gradient stability is maintained for more than 25 hours, the discharge voltage at 0.1 mA/s is 2.34 V, and it is stable for 200 charge–discharge cycles at 1 mA/s.

REFERENCES

- [1] J. L. Holechek, H. M. E. Geli, M. N. Sawalhah, R. Valdez. A Global Assessment: Can Renewable Energy Replace Fossil Fuels by 2050? *Sustainability*, 14 (2022), 4792. <https://doi.org/10.3390/su14084792>.
- [2] Q. Jiang, S. I. Khattak, M. Ahmad, P. Lin. Mitigation pathways to sustainable production and consumption: Examining the impact of commercial policy on carbon dioxide emissions in Australia, *Sustain. Prod. Consum.*, 25 (2021), 390–403. <https://doi.org/10.1016/j.spc.2020.11.016>.
- [3] T.-Y. Chen, C.-J. Huang. A Two-Tier Scenario Planning Model of Environmental Sustainability Policy in Taiwan, *Sustainability*, 11 (2019), 2336. <https://doi.org/10.3390/su11082336>.
- [4] I. Kougias, N. Taylor, G. Kakoulaki, A. Jäger-Waldau. The role of photovoltaics for the European Green Deal and the recovery plan, *Renewable and Sustainable Energy Reviews*, 144 (2021), 111017. <https://doi.org/10.1016/j.rser.2021.111017>.
- [5] S. García-Freites, C. Gough, M. Röder. The greenhouse gas removal potential of bioenergy with carbon capture and storage (BECCS) to support the UK’s net-zero emission target, *Biomass Bioenergy*, 151 (2021), 106164. <https://doi.org/10.1016/j.biombioe.2021.106164>.
- [6] J. Collins, G. Gourdin, D. Qu. Modern Applications of Green Chemistry, in: *Green Chemistry*, Elsevier, 2018: pp. 771–860. <https://doi.org/10.1016/B978-0-12-809270-5.00028-5>.
- [7] T. Placke, R. Kloepsch, S. Dühnen, M. Winter. Lithium ion, lithium metal, and alternative rechargeable battery technologies: the odyssey for high energy density, *Journal of Solid State Electrochemistry*, 21 (2017), 1939–1964. <https://doi.org/10.1007/s10008-017-3610-7>.
- [8] Y. Sui, C. Liu, R. C. Masse, Z. G. Neale, M. Atif, M. AlSalhi, G. Cao. Dual-ion batteries: The emerging alternative rechargeable batteries, *Energy Storage Mater.*, 25 (2020), 1–32. <https://doi.org/10.1016/j.ensm.2019.11.003>.
- [9] M. S. Ziegler, J. M. Mueller, G. D. Pereira, J. Song, M. Ferrara, Y.-M. Chiang, J. E. Trancik. Storage Requirements and Costs of Shaping Renewable Energy Toward Grid Decarbonization, *Joule*, 3 (2019), 2134–2153. <https://doi.org/10.1016/j.joule.2019.06.012>.
- [10] J. Y. Lee, A. K. Ramasamy, K. H. Ong, R. Verayah, H. Mokhlis, M. Marsadek. Energy storage systems: A review of its progress and outlook, potential benefits, barriers and solutions within the Malaysian distribution network, *J. Energy Storage*, 72 (2023), 108360. <https://doi.org/10.1016/j.est.2023.108360>.
- [11] T.-Z. Ang, M. Salem, M. Kamarol, H. S. Das, M. A. Nazari, N. Prabaharan. A comprehensive study of renewable energy sources: Classifications, challenges and suggestions, *Energy Strategy Reviews*, 43 (2022), 100939. <https://doi.org/10.1016/j.esr.2022.100939>.

- [12] J. Escudero-González, P. A. López-Jiménez. Iron redox battery as electrical energy storage system in the Spanish energetic framework, *International Journal of Electrical Power & Energy Systems*, 61 (2014), 421–428. <https://doi.org/10.1016/j.ijepes.2014.03.067>.
- [13] L. Kong, C. Li, J. Jiang, M. G. Pecht. Li-Ion Battery Fire Hazards and Safety Strategies, *Energies (Basel)*, 11 (2018), 2191. <https://doi.org/10.3390/en11092191>.
- [14] Y. Liu, Y. Liu, B. Zhu, Z. Wang, X. Zhang, X. Wu. Multilayer Ti₃C₂T_x-loaded CoOHf composite structures for high-performance lithium-ion batteries, *Mater. Res. Bull.*, 179 (2024), 112986. <https://doi.org/10.1016/j.materresbull.2024.112986>.
- [15] S. Siriroj, J. Padchasri, A. Montreeupatham, S. Sonsupap, S. Maensiri, S. Kheawhom, P. Kidkhunthod. Glass-sulfur composite cathodes: A new strategy for improving the performance of lithium-sulfur batteries, *Mater. Res. Bull.*, 178 (2024), 112919. <https://doi.org/10.1016/j.materresbull.2024.112919>.
- [16] S. Xu, S. Liu, Y. Zhou, R. Xiao, X. Ke. Study on the electrochemical process of Li⁺/Na⁺ mixed organic dual-cation battery system, *Mater. Res. Bull.*, 177 (2024), 112858. <https://doi.org/10.1016/j.materresbull.2024.112858>.
- [17] J. Wu, Y. Cao, H. Zhao, J. Mao, Z. Guo. The critical role of carbon in marrying silicon and graphite anodes for high-energy lithium-ion batteries, *Carbon Energy*, 1 (2019), 57–76. <https://doi.org/10.1002/cey2.2>.
- [18] J. Yang, X. Liu, J. Tian, X. Ma, B. Wang, W. Li, Q. Wang. Adhesive nanocomposites of hypergravity-induced Co₃O₄ nanoparticles and natural gels as Li-ion battery anode materials with high capacitance and low resistance, *RSC Adv.*, 7 (2017), 21061–21067. <https://doi.org/10.1039/c7ra02725g>.
- [19] M. B. Lim, T. N. Lambert, B. R. Chalamala. Rechargeable alkaline zinc–manganese oxide batteries for grid storage: Mechanisms, challenges and developments, *Materials Science and Engineering: R: Reports*, 143 (2021), 100593. <https://doi.org/10.1016/j.mser.2020.100593>.
- [20] J. Park, M. Kim, J. Choi, S. Lee, J. Kim, D. Han, H. Jang, M. Park. Recent Progress in High-voltage Aqueous Zinc-based Hybrid Redox Flow Batteries, *Chem. Asian J.*, 18 (2023). <https://doi.org/10.1002/asia.202201052>.
- [21] W. M. Seong, K.-Y. Park, M. H. Lee, S. Moon, K. Oh, H. Park, S. Lee, K. Kang. Abnormal self-discharge in lithium-ion batteries, *Energy Environ. Sci.*, 11 (2018), 970–978. <https://doi.org/10.1039/C8EE00186C>.
- [22] T. Or, S. W. D. Gourley, K. Kaliyappan, A. Yu, Z. Chen. Recycling of mixed cathode lithium-ion batteries for electric vehicles: Current status and future outlook, *Carbon Energy*, 2 (2020), 6–43. <https://doi.org/10.1002/cey2.29>.
- [23] H. Wang, Y. Liu, Y. Li, Y. Cui. Lithium Metal Anode Materials Design: Interphase and Host, *Electrochemical Energy Reviews*, 2 (2019), 509–517. <https://doi.org/10.1007/s41918-019-00054-2>.
- [24] W. Xu, J. Wang, F. Ding, X. Chen, E. Nasybulin, Y. Zhang, J.-G. Zhang. Lithium metal anodes for rechargeable batteries, *Energy Environ. Sci.*, 7 (2014), 513–537. <https://doi.org/10.1039/C3EE40795K>.

- [25] Y. S. Duh, K. H. Lin, C. S. Kao, Experimental investigation and visualization on thermal runaway of hard prismatic lithium-ion batteries used in smart phones, *J. Therm. Anal. Calorim.*, 132 (2018), 1677–1692. <https://doi.org/10.1007/s10973-018-7077-2>.
- [26] N. Nitta, F. Wu, J. T. Lee, G. Yushin. Li-ion battery materials: Present and future, *Materials Today*, 18 (2015), 252–264. <https://doi.org/10.1016/j.mattod.2014.10.040>.
- [27] W. Zaman, K. B. Hatzell, Processing and manufacturing of next-generation lithium-based all-solid-state batteries, *Curr. Opin. Solid. State Mater. Sci.*, 26 (2022), 101003. <https://doi.org/10.1016/j.cossms.2022.101003>.
- [28] H. Wang, W. Shi, F. Hu, Y. Wang, X. Hu, H. Li. Over-heating triggered thermal runaway behavior for lithium-ion battery with high nickel content in positive electrode, *Energy*, 224 (2021). <https://doi.org/10.1016/j.energy.2021.120072>.
- [29] S. Chen, Z. Gao, T. Sun. Safety challenges and safety measures of Li-ion batteries, *Energy Sci. Eng.*, 9 (2021), 1647–1672. <https://doi.org/10.1002/ese3.895>.
- [30] A. Zeng, W. Chen, K. D. Rasmussen, X. Zhu, M. Lundhaug, D. B. Müller, J. Tan, J. K. Keiding, L. Liu, T. Dai, A. Wang, G. Liu. Battery technology and recycling alone will not save the electric mobility transition from future cobalt shortages, *Nat. Commun.*, 13 (2022). <https://doi.org/10.1038/s41467-022-29022-z>.
- [31] J. Zhang, Y. Lei, Z. Lin, P. Xie, H. Lu, J. Xu. A novel approach to recovery of lithium element and production of holey graphene based on the lithiated graphite of spent lithium ion batteries, *Chemical Engineering Journal*, 436 (2022). <https://doi.org/10.1016/j.cej.2022.135011>.
- [32] B. Liu, Q. Zhang, J. Liu, Y. Hao, Y. Tang, Y. Li. The impacts of critical metal shortage on China's electric vehicle industry development and countermeasure policies, *Energy*, 248 (2022). <https://doi.org/10.1016/j.energy.2022.123646>.
- [33] T. Wu, W. Zhang, J. Yang, Q. Lu, J. Peng, M. Zheng, F. Xu, Y. Liu, Y. Liang. Architecture engineering of carbonaceous anodes for high-rate potassium-ion batteries, *Carbon Energy*, 3 (2021), 554–581. <https://doi.org/10.1002/cey2.99>.
- [34] M. Minakshi, D. R. G. Mitchell. The influence of bismuth oxide doping on the rechargeability of aqueous cells using MnO₂ cathode and LiOH electrolyte, *Electrochim. Acta*, 53 (2008), 6323–6327. <https://doi.org/10.1016/j.electacta.2008.04.013>.
- [35] N. Zhang, F. Cheng, J. Liu, L. Wang, X. Long, X. Liu, F. Li, J. Chen. Rechargeable aqueous zinc-manganese dioxide batteries with high energy and power densities, *Nat. Commun.*, 8 (2017), 405. <https://doi.org/10.1038/s41467-017-00467-x>.
- [36] H. Zhang, W. Lu, X. Li. Progress and Perspectives of Flow Battery Technologies, *Electrochemical Energy Reviews*, 2 (2019), 492–506. <https://doi.org/10.1007/s41918-019-00047-1>.
- [37] H. Luo, B. Liu, Z. Yang, Y. Wan, C. Zhong. The Trade-Offs in the Design of Reversible Zinc Anodes for Secondary Alkaline Batteries, *Electrochemical Energy Reviews*, 5 (2022), 187–210. <https://doi.org/10.1007/s41918-021-00107-5>.
- [38] G. G. Yadav, X. Wei, J. Huang, D. Turney, M. Nyce, S. Banerjee, Accessing the second electron capacity of MnO₂ by exploring complexation and intercalation reactions in

- energy dense alkaline batteries, *Int. J. Hydrogen Energy*, 43 (2018), 8480–8487. <https://doi.org/10.1016/j.ijhydene.2018.03.061>.
- [39] Y. Liao, H.-C. Chen, C. Yang, R. Liu, Z. Peng, H. Cao, K. Wang. Unveiling performance evolution mechanisms of MnO₂ polymorphs for durable aqueous zinc-ion batteries, *Energy Storage Mater.*, 44 (2022), 508–516. <https://doi.org/10.1016/j.ensm.2021.10.039>.
- [40] S. Yao, R. Zhao, S. Wang, Y. Zhou, R. Liu, L. Hu, A. Zhang, R. Yang, X. Liu, Z. Fu, D. Wang, Z. Yang, Y.-M. Yan. Ni-doping induced structure distortion of MnO₂ for highly efficient Na⁺ storage, *Chemical Engineering Journal*, 429 (2022), 132521. <https://doi.org/10.1016/j.cej.2021.132521>.
- [41] X. Zhang, J. Hu, N. Fu, W. Zhou, B. Liu, Q. Deng, X. Wu. Comprehensive review on <sc>zinc-ion</sc> battery anode: Challenges and strategies, *Info. Mat.*, 4 (2022). <https://doi.org/10.1002/inf2.12306>.
- [42] C. Nie, G. Wang, D. Wang, M. Wang, X. Gao, Z. Bai, N. Wang, J. Yang, Z. Xing, S. Dou. Recent Progress on Zn Anodes for Advanced Aqueous Zinc-Ion Batteries, *Adv. Energy Mater.*, 13 (2023). <https://doi.org/10.1002/aenm.202300606>.
- [43] C. Zhu, P. Li, G. Xu, H. Cheng, G. Gao. Recent progress and challenges of Zn anode modification materials in aqueous Zn-ion batteries, *Coord. Chem., Rev.* 485 (2023), 215142. <https://doi.org/10.1016/j.ccr.2023.215142>.
- [44] Y. Xie, Y. Yu, X. Gong, Y. Guo, Y. Guo, Y. Wang, G. Lu. Effect of the crystal plane figure on the catalytic performance of MnO₂ for the total oxidation of propane, *Cryst. Eng. Comm.*, 17 (2015), 3005–3014. <https://doi.org/10.1039/C5CE00058K>.
- [45] S. Jana, S. Basu, S. Pande, S. K. Ghosh, T. Pal. Shape-Selective Synthesis, Magnetic Properties, and Catalytic Activity of Single Crystalline β -MnO₂ Nanoparticles, *The Journal of Physical Chemistry C*, 111 (2007), 16272–16277. <https://doi.org/10.1021/jp074803l>.
- [46] J. K. Seo, J. Shin, H. Chung, P. Y. Meng, X. Wang, Y. S. Meng. Intercalation and Conversion Reactions of Nanosized β -MnO₂ Cathode in the Secondary Zn/MnO₂ Alkaline Battery, *The Journal of Physical Chemistry C*, 122 (2018), 11177–11185. <https://doi.org/10.1021/acs.jpcc.7b11685>.
- [47] H.-W. Zhu, J. Ge, Y.-C. Peng, H.-Y. Zhao, L.-A. Shi, S.-H. Yu. Dip-coating processed sponge-based electrodes for stretchable Zn-MnO₂ batteries, *Nano Res.*, 11 (2018), 1554–1562. <https://doi.org/10.1007/s12274-017-1771-4>.
- [48] X. Guo, J. Zhou, C. Bai, X. Li, G. Fang, S. Liang, Zn/MnO₂ battery chemistry with dissolution-deposition mechanism, *Mater. Today Energy*, 16 (2020), 100396. <https://doi.org/10.1016/j.mtener.2020.100396>.
- [49] L. Wu, Z. Li, Y. Xiang, W. Dong, X. Qi, Z. Ling, Y. Xu, H. Wu, M. D. Levi, N. Shpigel, X. Zhang. Revisiting the Charging Mechanism of α -MnO₂ in Mildly Acidic Aqueous Zinc Electrolytes, *Small* 20 (2024). <https://doi.org/10.1002/smll.202404583>.
- [50] H. Chen, C. Dai, F. Xiao, Q. Yang, S. Cai, M. Xu, H. J. Fan, S. Bao. Reunderstanding the Reaction Mechanism of Aqueous Zn-Mn Batteries with Sulfate Electrolytes: Role of

- the Zinc Sulfate Hydroxide, *Advanced Materials*, 34 (2022). <https://doi.org/10.1002/adma.202109092>.
- [51] L. Li, T. K. A. Hoang, J. Zhi, M. Han, S. Li, P. Chen. Functioning Mechanism of the Secondary Aqueous Zn- β -MnO₂ Battery, *ACS Appl. Mater. Interfaces.*, 12 (2020), 12834–12846. <https://doi.org/10.1021/acscami.9b22758>.
- [52] D. Chao, W. Zhou, C. Ye, Q. Zhang, Y. Chen, L. Gu, K. Davey, S. Qiao. An Electrolytic Zn-MnO₂ Battery for High-Voltage and Scalable Energy Storage, *Angewandte Chemie International Edition*, 58 (2019), 7823–7828. <https://doi.org/10.1002/anie.201904174>.
- [53] S. J. Kim, D. Wu, L. M. Housel, L. Wu, K. J. Takeuchi, A. C. Marschilok, E. S. Takeuchi, Y. Zhu, Toward the Understanding of the Reaction Mechanism of Zn/MnO₂ Batteries Using Non-alkaline Aqueous Electrolytes, *Chemistry of Materials*, 33 (2021), 7283–7289. <https://doi.org/10.1021/acs.chemmater.1c01542>.
- [54] C. Zhong, B. Liu, J. Ding, X. Liu, Y. Zhong, Y. Li, C. Sun, X. Han, Y. Deng, N. Zhao, W. Hu. Decoupling electrolytes towards stable and high-energy rechargeable aqueous zinc–manganese dioxide batteries, *Nat. Energy*, 5 (2020), 440–449. <https://doi.org/10.1038/s41560-020-0584-y>.
- [55] S. Hasegawa, K. Shimotani, K. Kishi, H. Watanabe. Electricity Generation from Decomposition of Hydrogen Peroxide, *Electrochemical and Solid-State Letters*, 8 (2005), A119. <https://doi.org/10.1149/1.1849112>.
- [56] J. L. Cohen, D. J. Volpe, D. A. Westly, A. Pechenik, H. D. Abruña. A Dual Electrolyte H₂/O₂ Planar Membraneless Microchannel Fuel Cell System with Open Circuit Potentials in Excess of 1.4 V, *Langmuir*, 21 (2005), 3544–3550. <https://doi.org/10.1021/la0479307>.
- [57] E. R. Choban, J. S. Spendelow, L. Gancs, A. Wieckowski, P. J. A. Kenis. Membraneless laminar flow-based micro fuel cells operating in alkaline, acidic, and acidic/alkaline media, *Electrochim. Acta*, 50 (2005), 5390–5398. <https://doi.org/10.1016/j.electacta.2005.03.019>.
- [58] G. G. Yadav, D. Turney, J. Huang, X. Wei, S. Banerjee. Breaking the 2 V Barrier in Aqueous Zinc Chemistry: Creating 2.45 and 2.8 V MnO₂–Zn Aqueous Batteries, *ACS Energy Lett.*, 4 (2019), 2144–2146. <https://doi.org/10.1021/acscenergylett.9b01643>.
- [59] C. Liu, X. Chi, Q. Han, Y. Liu, A High Energy Density Aqueous Battery Achieved by Dual Dissolution/Deposition Reactions Separated in Acid-Alkaline Electrolyte, *Adv. Energy Mater.*, 10 (2020), 1903589. <https://doi.org/10.1002/aenm.201903589>.
- [60] J. Liu, J. Bao, X. Zhang, Y. Gao, Y. Zhang, L. Liu, Z. Cao. MnO₂-based materials for supercapacitor electrodes: challenges, strategies and prospects, *RSC Adv.*, 12 (2022), 35556–35578. <https://doi.org/10.1039/D2RA06664E>.
- [61] S. Devaraj, N. Munichandraiah. Effect of Crystallographic Structure of MnO₂ on Its Electrochemical Capacitance Properties, *The Journal of Physical Chemistry C*, 112 (2008), 4406–4417. <https://doi.org/10.1021/jp7108785>.
- [62] B. Yin, S. Zhang, H. Jiang, F. Qu, X. Wu. Phase-controlled synthesis of polymorphic MnO₂ structures for electrochemical energy storage, *J. Mater. Chem. A Mater.*, 3 (2015), 5722–5729. <https://doi.org/10.1039/C4TA06943A>.

- [63] Z. Zhang, W. Li, Y. Shen, R. Wang, H. Li, M. Zhou, W. Wang, K. Wang, K. Jiang. Issues and opportunities of manganese-based materials for enhanced Zn-ion storage performances, *J. Energy Storage*, 45 (2022), 103729. <https://doi.org/10.1016/j.est.2021.103729>.
- [64] C. Chen, M. Shi, Y. Zhao, C. Yang, L. Zhao, C. Yan. Al-Intercalated MnO₂ cathode with reversible phase transition for aqueous Zn-Ion batteries, *Chemical Engineering Journal*, 422 (2021), 130375. <https://doi.org/10.1016/j.cej.2021.130375>.
- [65] J. Yao, J. Ji, H. Wan, J. Duan, X. Wang, L. Lv, G. Ma, L. Tao, H. Wang, J. Zhang, H. Wang. Highly stable Co-doped MnO₂ nanoarrays as enhanced cathode materials for aqueous zinc-ion batteries, *Oxford Open Energy*, 1 (2022). <https://doi.org/10.1093/ooenergy/oiab003>.
- [66] S. Yang, L. Zhang, M. Luo, Y. Cui, J. Wang, D. Zhao, C. Yang, X. Wang, B. Cao. Synergistic combination of a Co-doped σ -MnO₂ cathode with an electrolyte additive for a high-performance aqueous zinc-ion battery, *Chem. Phys. Mater.*, 2 (2023), 77–82. <https://doi.org/10.1016/j.chphma.2022.04.007>.
- [67] S. Liu, J. Wang, Z. Zhou, Y. Li, W. Zhang, C. Wang. Cobalt-doped δ -MnO₂ /CNT composites as cathode material for aqueous zinc-ion batteries, *Inorg. Chem. Front.*, 10 (2023), 5167–5177. <https://doi.org/10.1039/D3QI01010D>.
- [68] X. Xia, Y. Zhao, Y. Zhao, M. Xu, W. Liu, X. Sun. Mo doping provokes two-electron reaction in MnO₂ with ultrahigh capacity for aqueous zinc ion batteries, *Nano Res.*, 16 (2023), 2511–2518. <https://doi.org/10.1007/s12274-022-5057-0>.
- [69] Y. Liu, W. Chen, J. Su, X. Zhao, X. Pan. Inhibition of phase transition from δ -MnO₂ to α -MnO₂ by Mo-doping and the application of Mo-doped MnO₂ in aqueous zinc-ion batteries, *Physical Chemistry Chemical Physics*, 25 (2023), 30663–30669. <https://doi.org/10.1039/D3CP04182D>.
- [70] Y. Ma, M. Xu, R. Liu, H. Xiao, Y. Liu, X. Wang, Y. Huang, G. Yuan. Molecular tailoring of MnO₂ by bismuth doping to achieve aqueous zinc-ion battery with capacitor-level durability, *Energy Storage Mater.*, 48 (2022), 212–222. <https://doi.org/10.1016/j.ensm.2022.03.024>.
- [71] D. Im, A. Manthiram. Role of Bismuth and Factors Influencing the Formation of Mn₃O₄ in Rechargeable Alkaline Batteries Based on Bismuth-Containing Manganese Oxides, *J. Electrochem. Soc.*, 150 (2003), A68. <https://doi.org/10.1149/1.1524611>.
- [72] K. Ma, Q. Li, C. Hong, G. Yang, C. Wang. Bi Doping-Enhanced Reversible-Phase Transition of α -MnO₂ Raising the Cycle Capability of Aqueous Zn–Mn Batteries, *ACS Appl. Mater. Interfaces*, 13 (2021), 55208–55217. <https://doi.org/10.1021/acsami.1c17677>.
- [73] L. Gou, Y. Yang, Y. Zhang, J. Li, X. Fan, D. Li. In situ synthesis of Bi³⁺-doped δ -MnO₂ cathode to enhance the cycle stability for aqueous zinc-ion batteries, *Journal of Solid State Electrochemistry*, 27 (2023), 1443–1450. <https://doi.org/10.1007/s10008-023-05501-1>.

- [74] L. Kang, M. Cui, F. Jiang, Y. Gao, H. Luo, J. Liu, W. Liang, C. Zhi. Nanoporous CaCO₃ Coatings Enabled Uniform Zn Stripping/Plating for Long-Life Zinc Rechargeable Aqueous Batteries, *Adv. Energy Mater.*, 8 (2018). <https://doi.org/10.1002/aenm.201801090>.
- [75] X. Xie, S. Liang, J. Gao, S. Guo, J. Guo, C. Wang, G. Xu, X. Wu, G. Chen, J. Zhou. Manipulating the ion-transfer kinetics and interface stability for high-performance zinc metal anodes, *Energy Environ. Sci.*, 13 (2020), 503–510. <https://doi.org/10.1039/C9EE03545A>.
- [76] X. Hu, J. Borowiec, Y. Zhu, X. Liu, R. Wu, A. M. Ganose, I. P. Parkin, B. D. Boruah. Dendrite-Free Zinc Anodes Enabled by Exploring Polar-Face-Rich 2D ZnO Interfacial Layers for Rechargeable Zn-Ion Batteries, *Small*, 20 (2024). <https://doi.org/10.1002/smll.202306827>.
- [77] Q. Ren, X. Tang, K. He, C. Zhang, W. Wang, Y. Guo, Z. Zhu, X. Xiao, S. Wang, J. Lu, Y. Yuan. Long-cycling Zinc Metal Anodes Enabled by an In Situ Constructed ZnO Coating Layer, *Adv. Funct. Mater.*, 34 (2024). <https://doi.org/10.1002/adfm.202312220>.
- [78] P. Liang, J. Yi, X. Liu, K. Wu, Z. Wang, J. Cui, Y. Liu, Y. Wang, Y. Xia, J. Zhang. Highly Reversible Zn Anode Enabled by Controllable Formation of Nucleation Sites for Zn-Based Batteries, *Adv. Funct. Mater.*, 30 (2020). <https://doi.org/10.1002/adfm.201908528>.
- [79] S. Sun, Y. Wen, A. Billings, R. Rajabi, B. Wang, K. Zhang, K. Huang. Protecting Zn anodes by atomic layer deposition of ZrO₂ to extend the lifetime of aqueous Zn-ion batteries, *Energy Advances*, 3 (2024), 299–306. <https://doi.org/10.1039/D3YA00400G>.
- [80] Y. Liu, T. Guo, Q. Liu, F. Xiong, M. Huang, Y. An, J. Wang, Q. An, C. Liu, L. Mai. Ultrathin ZrO₂ coating layer regulates Zn deposition and raises long-life performance of aqueous Zn batteries, *Mater. Today Energy*, 28 (2022), 101056. <https://doi.org/10.1016/j.mtener.2022.101056>.
- [81] K. Zhao, C. Wang, Y. Yu, M. Yan, Q. Wei, P. He, Y. Dong, Z. Zhang, X. Wang, L. Mai. Ultrathin Surface Coating Enables Stabilized Zinc Metal Anode, *Adv. Mater. Interfaces*, 5 (2018). <https://doi.org/10.1002/admi.201800848>.
- [82] B. Li, J. Xue, X. Lv, R. Zhang, K. Ma, X. Wu, L. Dai, L. Wang, Z. He. A facile coating strategy for high stability aqueous zinc ion batteries: Porous rutile nano-TiO₂ coating on zinc anode, *Surf. Coat. Technol.*, 421 (2021), 127367. <https://doi.org/10.1016/j.surfcoat.2021.127367>.
- [83] N. Naresh, S. Eom, S. Hwan Jeong, S. Jun Lee, S. Hyeon Park, J. Park, J.-H. Ahn, J.-H. Kim, Y. Hwa Jung. Dendrite-free Zn anodes enabled by a hierarchical zincophilic TiO₂ layer for rechargeable aqueous zinc-ion batteries, *Appl. Surf. Sci.*, 606 (2022), 154932. <https://doi.org/10.1016/j.apsusc.2022.154932>.
- [84] P. Ye, X. Li, K. He, A. Dou, X. Wang, A. Naveed, Y. Zhou, M. Su, P. Zhang, Y. Liu. A semi-interpenetrating network polymer coating for dendrite-free Zn anodes, *J. Power Sources*, 558 (2023), 232622. <https://doi.org/10.1016/j.jpowsour.2022.232622>.

- [85] X. Cai, W. Tian, Z. Zhang, Y. Sun, L. Yang, H. Mu, C. Lian, H. Qiu. Polymer Coating with Balanced Coordination Strength and Ion Conductivity for Dendrite-Free Zinc Anode, *Advanced Materials*, 36 (2024). <https://doi.org/10.1002/adma.202307727>.
- [86] P. Chen, X. Yuan, Y. Xia, Y. Zhang, L. Fu, L. Liu, N. Yu, Q. Huang, B. Wang, X. Hu, Y. Wu, T. van Ree. An Artificial Polyacrylonitrile Coating Layer Confining Zinc Dendrite Growth for Highly Reversible Aqueous Zinc-Based Batteries, *Advanced Science*, 8 (2021). <https://doi.org/10.1002/advs.202100309>.
- [87] Z. Hu, X. Wang, W. Du, Z. Zhang, Y. Tang, M. Ye, Y. Zhang, X. Liu, Z. Wen, C. C. Li. Crowding Effect-Induced Zinc-Enriched/Water-Lean Polymer Interfacial Layer Toward Practical Zn-Iodine Batteries, *ACS Nano*, 17 (2023), 23207–23219. <https://doi.org/10.1021/acsnano.3c10081>.
- [88] J. Shin, J. K. Seo, R. Yaylian, A. Huang, Y. S. Meng. A review on mechanistic understanding of MnO₂ in aqueous electrolyte for electrical energy storage systems, *International Materials Reviews*, 65 (2020), 356–387. <https://doi.org/10.1080/09506608.2019.1653520>.
- [89] D. Akinyele, J. Belikov, Y. Levron, Battery Storage Technologies for Electrical Applications: Impact in Stand-Alone Photovoltaic Systems, *Energies (Basel)*, 10 (2017), 1760. <https://doi.org/10.3390/en10111760>.
- [90] J. Song, K. Xu, N. Liu, D. Reed, X. Li. Crossroads in the renaissance of rechargeable aqueous zinc batteries, *Materials Today*, 45 (2021), 191–212. <https://doi.org/10.1016/j.mattod.2020.12.003>.
- [91] L. Urry. Alkaline deferred action cell, US2970180 (A), 1959.
- [92] T. Takamura. PRIMARY BATTERIES – AQUEOUS SYSTEMS | Alkaline Manganese–Zinc, in: *Encyclopedia of Electrochemical Power Sources*, Elsevier, 2009: pp. 28–42. <https://doi.org/10.1016/B978-044452745-5.00098-8>.
- [93] SAFETY DATA SHEET, (2014).
- [94] G. G. Yadav, J. W. Gallaway, D. E. Turney, M. Nyce, J. Huang, X. Wei, S. Banerjee. Regenerable Cu-intercalated MnO₂ layered cathode for highly cyclable energy dense batteries, *Nat. Commun.*, 8 (2017), 14424. <https://doi.org/10.1038/ncomms14424>.
- [95] L. Bai, D. Y. Qu, B. E. Conway, Y. H. Zhou, G. Chowdhury, W. A. Adams. Rechargeability of a Chemically Modified MnO₂/Zn Battery System at Practically Favorable Power Levels, *J. Electrochem. Soc.*, 140 (1993), 884–889. <https://doi.org/10.1149/1.2056222>.
- [96] B. B. Owens, P. Reale, B. Scrosati. PRIMARY BATTERIES | Overview, in: *Encyclopedia of Electrochemical Power Sources*, Elsevier, 2009: pp. 22–27. <https://doi.org/10.1016/B978-044452745-5.00096-4>.
- [97] M. J. D’Ambrose, D. E. Turney, G. G. Yadav, M. Nyce, S. Banerjee. Material Failure Mechanisms of Alkaline Zn Rechargeable Conversion Electrodes, *ACS Appl. Energy Mater.*, 4 (2021), 3381–3392. <https://doi.org/10.1021/acsaem.0c03144>.
- [98] B. J. Hertzberg, A. Huang, A. Hsieh, M. Chamoun, G. Davies, J. K. Seo, Z. Zhong, M. Croft, C. Erdonmez, Y. S. Meng, D. Steingart. Effect of Multiple Cation Electrolyte

- Mixtures on Rechargeable Zn–MnO₂ Alkaline Battery, *Chemistry of Materials*, 28 (2016), 4536–4545. <https://doi.org/10.1021/acs.chemmater.6b00232>.
- [99] A. M. Bruck, M. A. Kim, L. Ma, S. N. Ehrlich, J. S. Okasinski, J. W. Gallaway. Bismuth Enables the Formation of Disordered Birnessite in Rechargeable Alkaline Batteries, *J. Electrochem. Soc.*, 167 (2020), 110514. <https://doi.org/10.1149/1945-7111/aba075>.
- [100] E. D. Rus, G. D. Moon, J. Bai, D. A. Steingart, C. K. Erdonmez. Electrochemical Behavior of Electrolytic Manganese Dioxide in Aqueous KOH and LiOH Solutions: A Comparative Study, *J. Electrochem. Soc.*, 163 (2016), A356–A363. <https://doi.org/10.1149/2.1011602jes>.
- [101] M. Kelly, J. Duay, T.N. Lambert, R. Aidun. Impact of Triethanolamine as an Additive for Rechargeable Alkaline Zn/MnO₂ Batteries under Limited Depth of Discharge Conditions, *J. Electrochem. Soc.*, 164 (2017), A3684–A3691. <https://doi.org/10.1149/2.0641714jes>.
- [102] M. Minakshi, P. Singh. Synergistic effect of additives on electrochemical properties of MnO₂ cathode in aqueous rechargeable batteries, *Journal of Solid State Electrochemistry*, 16 (2012), 1487–1492. <https://doi.org/10.1007/s10008-011-1547-9>.
- [103] N. D. Ingale, J. W. Gallaway, M. Nyce, A. Couzis, S. Banerjee. Rechargeability and economic aspects of alkaline zinc-manganese dioxide cells for electrical storage and load leveling, *J. Power Sources*, 276 (2015), 7–18. <https://doi.org/10.1016/j.jpowsour.2014.11.010>.
- [104] A. Poosapati, S. Vadnala, K. Negrete, Y. Lan, J. Hutchison, M. Zupan, D. Madan. Rechargeable Zinc-Electrolytic Manganese Dioxide (EMD) Battery with a Flexible Chitosan-Alkaline Electrolyte, *ACS Appl. Energy Mater.*, 4 (2021), 4248–4258. <https://doi.org/10.1021/acsam.1c00675>.
- [105] M. Minakshi, D. Ralph. A Novel Sodium-Ion Rechargeable Battery, *ECS Trans.*, 45 (2013), 95–102. <https://doi.org/10.1149/04529.0095ecst>.
- [106] Z. Wei, J. Cheng, R. Wang, Y. Li, Y. Ren. From spent Zn–MnO₂ primary batteries to rechargeable Zn–MnO₂ batteries: A novel directly recycling route with high battery performance, *J. Environ. Manage.*, 298 (2021), 113473. <https://doi.org/10.1016/j.jenvman.2021.113473>.
- [107] V. Soundharajan, B. Sambandam, S. Kim, S. Islam, J. Jo, S. Kim, V. Mathew, Y. Sun, J. Kim. The dominant role of Mn²⁺ additive on the electrochemical reaction in ZnMn₂O₄ cathode for aqueous zinc-ion batteries, *Energy Storage Mater.*, 28 (2020), 407–417. <https://doi.org/10.1016/j.ensm.2019.12.021>.
- [108] C. Wang, Y. Zeng, X. Xiao, S. Wu, G. Zhong, K. Xu, Z. Wei, W. Su, X. Lu. γ -MnO₂ nanorods/graphene composite as efficient cathode for advanced rechargeable aqueous zinc-ion battery, *Journal of Energy Chemistry*, 43 (2020), 182–187. <https://doi.org/10.1016/j.jechem.2019.08.011>.
- [109] J.-W. Lee, S.-D. Seo, D.-W. Kim. Comparative study on ternary spinel cathode Zn–Mn–O microspheres for aqueous rechargeable zinc-ion batteries, *J. Alloys Compd.*, 800 (2019), 478–482. <https://doi.org/10.1016/j.jallcom.2019.06.051>.

- [110] D. Xu, B. Li, C. Wei, Y.-B. He, H. Du, X. Chu, X. Qin, Q.-H. Yang, F. Kang. Preparation and Characterization of MnO₂/acid-treated CNT Nanocomposites for Energy Storage with Zinc Ions, *Electrochim. Acta*, 133 (2014), 254–261. <https://doi.org/10.1016/j.electacta.2014.04.001>.
- [111] K. Han, F. An, F. Yan, H. Chen, Q. Wan, Y. Liu, P. Li, X. Qu. High-performance aqueous Zn–MnO₂ batteries enabled by the coupling engineering of K⁺ pre-intercalation and oxygen defects, *J. Mater. Chem. A Mater.*, 9 (2021), 15637–15647. <https://doi.org/10.1039/D1TA03994F>.
- [112] M. Wang, X. Zheng, X. Zhang, D. Chao, S. Qiao, H. N. Alshareef, Y. Cui, W. Chen. Opportunities of Aqueous Manganese-Based Batteries with Deposition and Stripping Chemistry, *Adv. Energy Mater.*, 11 (2021), 2002904. <https://doi.org/10.1002/aenm.202002904>.
- [113] J. Yang, J. Cao, Y. Peng, W. Yang, S. Barg, Z. Liu, I. A. Kinloch, M. A. Bissett, R. A. W. Dryfe. Unravelling the Mechanism of Rechargeable Aqueous Zn–MnO₂ Batteries: Implementation of Charging Process by Electrodeposition of MnO₂, *Chem. Sus. Chem.*, 13 (2020), 4103–4110. <https://doi.org/10.1002/cssc.202001216>.
- [114] A. Mitha, H. Mi, W. Dong, I. S. Cho, J. Ly, S. Yoo, S. Bang, T. K. A. Hoang, P. Chen. Thixotropic gel electrolyte containing poly(ethylene glycol) with high zinc ion concentration for the secondary aqueous Zn/LiMn₂O₄ battery, *Journal of Electroanalytical Chemistry*, 836 (2019), 1–6. <https://doi.org/10.1016/j.jelechem.2019.01.014>.
- [115] C. Qiu, X. Zhu, L. Xue, M. Ni, Y. Zhao, B. Liu, H. Xia. The function of Mn²⁺ additive in aqueous electrolyte for Zn/δ-MnO₂ battery, *Electrochim. Acta*, 351 (2020), 136445. <https://doi.org/10.1016/j.electacta.2020.136445>.
- [116] Marcel Pourbaix. *Atlas of Electrochemical Equilibria in Aqueous Solutions*, 2nd ed., National Association of Corrosion, 1974.
- [117] C. Li, X. Xie, S. Liang, J. Zhou. Issues and Future Perspective on Zinc Metal Anode for Rechargeable Aqueous Zinc-ion Batteries, *Energy & Environmental Materials*, 3 (2020), 146–159. <https://doi.org/10.1002/eem2.12067>.
- [118] M. A. Ibrahim. Improving the throwing power of acidic zinc sulfate electroplating baths, *Journal of Chemical Technology & Biotechnology*, 75 (2000), 745–755. [https://doi.org/10.1002/1097-4660\(200008\)75:8<745::AID-JCTB274>3.0.CO;2-5](https://doi.org/10.1002/1097-4660(200008)75:8<745::AID-JCTB274>3.0.CO;2-5).
- [119] J. Li. Oxygen Evolution Reaction in Energy Conversion and Storage: Design Strategies Under and Beyond the Energy Scaling Relationship, *Nanomicro Lett.*, 14 (2022), 112. <https://doi.org/10.1007/s40820-022-00857-x>.
- [120] H. Wen, Z. Liu, J. Qiao, R. Chen, G. Qiao, J. Yang. Ultrahigh voltage and energy density aluminum-air battery based on aqueous alkaline-acid hybrid electrolyte, *Int. J. Energy Res.*, 44 (2020), 10652–10661. <https://doi.org/10.1002/er.5707>.
- [121] Y. Wang, W. Pan, S. Luo, X. Zhao, H. Y. H. Kwok, X. Xu, D. Y. C. Leung. High-performance solid-state metal-air batteries with an innovative dual-gel electrolyte, *Int. J. Hydrogen Energy*, 47 (2022), 15024–15034. <https://doi.org/10.1016/j.ijhydene.2022.03.011>.

- [122] L. Wang, R. Cheng, C. Liu, M. C. Ma, W. Wang, G. Yang, M. K. H. Leung, F. Liu, S. P. Feng. Trielectrolyte aluminum-air cell with high stability and voltage beyond 2.2 V, *Materials Today Physics*, 14 (2020), 100242. <https://doi.org/10.1016/j.mtphys.2020.100242>.
- [123] B. Chen, D. Y. C. Leung, J. Xuan, H. Wang. A mixed-pH dual-electrolyte microfluidic aluminum-air cell with high performance, *Appl. Energy*, 185 (2017), 1303–1308. <https://doi.org/10.1016/j.apenergy.2015.10.029>.
- [124] P. Cai, Y. Li, J. Chen, J. Jia, G. Wang, Z. Wen. An Asymmetric-Electrolyte Zn–Air Battery with Ultrahigh Power Density and Energy Density, *Chem. Electro. Chem.*, 5 (2018), 589–592. <https://doi.org/10.1002/celec.201701269>.
- [125] S. Zhao, T. Liu, Y. Dai, Y. Wang, Z. Guo, S. Zhai, J. Yu, C. Zhi, M. Ni. All-in-one and bipolar-membrane-free acid-alkaline hydrogel electrolytes for flexible high-voltage Zn-air batteries, *Chemical Engineering Journal*, 430 (2022), 132718. <https://doi.org/10.1016/j.cej.2021.132718>.
- [126] K. W. Leong, Y. Wang, W. Pan, S. Luo, X. Zhao, D. Y. C. Leung. Doubling the power output of a Mg-air battery with an acid-salt dual-electrolyte configuration, *J. Power Sources*, 506 (2021), 230144. <https://doi.org/10.1016/j.jpowsour.2021.230144>.
- [127] Y. Xu, P. Cai, K. Chen, Y. Ding, L. Chen, W. Chen, Z. Wen. High-Voltage Rechargeable Alkali–Acid Zn–PbO₂ Hybrid Battery, *Angewandte Chemie International Edition*, 59 (2020), 23593–23597. <https://doi.org/10.1002/anie.202012017>.
- [128] T. Gao, Y. Sun, L. Gong, C. Ma, J. Wang, L. Su. 2.8 V Aqueous Lead Dioxide–Zinc Rechargeable Battery Using H₂ SO₄–K₂ SO₄–KOH Three Electrolytes, *J. Electrochem. Soc.*, 167 (2020), 020552. <https://doi.org/10.1149/1945-7111/ab6f58>.
- [129] H. Wu, S.-J. Liu, K. Lian. Aqueous based dual-electrolyte rechargeable Pb–Zn battery with a 2.8 V operating voltage, *J. Energy Storage*, 29 (2020), 101305. <https://doi.org/10.1016/j.est.2020.101305>.
- [130] F. Yu, L. Pang, X. Wang, E. R. Waclawik, F. Wang, K. (Ken) Ostrikov, H. Wang. Aqueous alkaline–acid hybrid electrolyte for zinc-bromine battery with 3V voltage window, *Energy Storage Mater.*, 19 (2019), 56–61. <https://doi.org/10.1016/j.ensm.2019.02.024>.
- [131] L. Chen, Z. Guo, Y. Xia, Y. Wang. High-voltage aqueous battery approaching 3 V using an acidic-alkaline double electrolyte, *Chemical Communications*, 49 (2013), 2204. <https://doi.org/10.1039/c3cc00064h>.
- [132] N. Vilas Bôas, J. B. Souza Junior, L. C. Varanda, S. A. S. Machado, M. L. Calegari. Bismuth and cerium doped cryptomelane-type manganese dioxide nanorods as bifunctional catalysts for rechargeable alkaline metal-air batteries, *Appl. Catal. B*, 258 (2019), 118014. <https://doi.org/10.1016/j.apcatb.2019.118014>.
- [133] X. Zhang, W. Yang, J. Yang, D. G. Evans. Synthesis and characterization of α -MnO₂ nanowires: Self-assembly and phase transformation to β -MnO₂ microcrystals, *J. Cryst. Growth*, 310 (2008), 716–722. <https://doi.org/10.1016/j.jcrysgro.2007.11.113>.

- [134] X. Zhang, P. Yu, D. Wang, Y. Ma. Controllable Synthesis of α -MnO₂ Nanostructures and Phase Transformation to β -MnO₂ Microcrystals by Hydrothermal Crystallization, *J. Nanosci. Nanotechnol.*, 10 (2010) 898–904. <https://doi.org/10.1166/jnn.2010.1893>.
- [135] Y. Khan, S. K. Durrani, M. Mehmood, M. R. Khan. Mild hydrothermal synthesis of γ -MnO₂ nanostructures and their phase transformation to α -MnO₂ nanowires, *J. Mater. Res.*, 26 (2011), 2268–2275. <https://doi.org/10.1557/jmr.2011.138>.
- [136] K. Li, C. Chen, H. Zhang, X. Hu, T. Sun, J. Jia. Effects of phase structure of MnO₂ and morphology of δ -MnO₂ on toluene catalytic oxidation, *Appl. Surf. Sci.*, 496 (2019), 143662. <https://doi.org/10.1016/j.apsusc.2019.143662>.
- [137] H. Song, H. Zhao, X. Zhang, Y. Xu, X. Cheng, S. Gao, L. Huo. A hollow urchin-like α -MnO₂ as an electrochemical sensor for hydrogen peroxide and dopamine with high selectivity and sensitivity, *Microchimica Acta*, 186 (2019), 210. <https://doi.org/10.1007/s00604-019-3316-x>.
- [138] M. Wang, K. Chen, J. Liu, Q. He, G. Li, F. Li. Efficiently Enhancing Electrocatalytic Activity of α -MnO₂ Nanorods/N-Doped Ketjenblack Carbon for Oxygen Reduction Reaction and Oxygen Evolution Reaction Using Facile Regulated Hydrothermal Treatment, *Catalysts*, 8 (2018), 138. <https://doi.org/10.3390/catal8040138>.
- [139] Z. Huang, W. Zhou, C. Ouyang, J. Wu, F. Zhang, J. Huang, Y. Gao, J. Chu. High performance of Mn-Co-Ni-O spinel nanofilms sputtered from acetate precursors, *Sci. Rep.*, 5 (2015), 10899. <https://doi.org/10.1038/srep10899>.
- [140] Z. Morgan Chan, D. A. Kitchaev, J. Nelson Weker, C. Schnedermann, K. Lim, G. Ceder, W. Tumas, M. F. Toney, D. G. Nocera. Electrochemical trapping of metastable Mn³⁺ ions for activation of MnO₂ oxygen evolution catalysts, *Proceedings of the National Academy of Sciences*, 115 (2018). <https://doi.org/10.1073/pnas.1722235115>.
- [141] H. Idriss, On the wrong assignment of the XPS O1s signal at 531–532 eV attributed to oxygen vacancies in photo- and electro-catalysts for water splitting and other materials applications, *Surf. Sci.*, 712 (2021), 121894. <https://doi.org/10.1016/j.susc.2021.121894>.
- [142] L. Jia, F. Li, C. Yang, X. Yang, B. Kou, Y. Xing, J. Peng, G. Ni, Z. Cao, S. Zhang, T. Zhao, X. Jin. Direct Z-Scheme Heterojunction α -MnO₂/BiOI with Oxygen-Rich Vacancies Enhanced Photoelectrocatalytic Degradation of Organic Pollutants under Visible Light, *Catalysts*, 12 (2022), 1596. <https://doi.org/10.3390/catal12121596>.
- [143] T. Hishida, K. Ohbayashi, M. Kobata, E. Ikenaga, T. Sugiyama, K. Kobayashi, M. Okawa, T. Saitoh. Empirical relationship between x-ray photoemission spectra and electrical conductivity in a colossal magnetoresistive manganite La_{1-x} Sr_x MnO₃, *J. Appl. Phys.*, 113 (2013). <https://doi.org/10.1063/1.4811372>.
- [144] P. Umek, R. C. Korošec, A. Gloter, U. Pirnat. The control of the diameter and length of α -MnO₂ nanorods by regulation of reaction parameters and their thermogravimetric properties, *Mater. Res. Bull.*, 46 (2011), 278–284. <https://doi.org/10.1016/j.materresbull.2010.10.012>.
- [145] Z. Zheng, G. Yang, J. Yao, J. Li, J. Zheng, Z. Wu, Y. Gan, C. Wang, L. Lv, H. Wan, C. Chen, H. Wang, L. Tao, J. Zhang, H. Wang. High-valence molybdenum promoted proton

- migration and inhibited dissolution for long-life aqueous Zn-MnO₂ batteries, *Appl. Surf. Sci.*, 592 (2022), 153335. <https://doi.org/10.1016/j.apsusc.2022.153335>.
- [146] M. Zhou, S. Guo, J. Li, X. Luo, Z. Liu, T. Zhang, X. Cao, M. Long, B. Lu, A. Pan, G. Fang, J. Zhou, S. Liang. Surface-Preferred Crystal Plane for a Stable and Reversible Zinc Anode, *Advanced Materials*, 33 (2021). <https://doi.org/10.1002/adma.202100187>.
- [147] Y. Song, S. Zhang, C. Zhang, Y. Yang, K. Lv. Raman Spectra and Microstructure of Zinc Oxide irradiated with Swift Heavy Ion, *Crystals (Basel)*, 9 (2019), 395. <https://doi.org/10.3390/cryst9080395>.
- [148] F. Friedrich, N. H. Nickel. Resonant Raman scattering in hydrogen and nitrogen doped ZnO, *Appl. Phys. Lett.*, 91 (2007). <https://doi.org/10.1063/1.2783222>.
- [149] C. Mele, B. Bozzini, Spectroelectrochemical investigation of the anodic and cathodic behaviour of zinc in 5.3 M KOH, *J. Appl. Electrochem.*, 45 (2015), 43–50. <https://doi.org/10.1007/s10800-014-0755-2>.
- [150] S. Hosseini, A. Abbasi, L.-O. Uginet, N. Haustraete, S. Praserthdam, T. Yonezawa, S. Kheawhom. The Influence of Dimethyl Sulfoxide as Electrolyte Additive on Anodic Dissolution of Alkaline Zinc-Air Flow Battery, *Sci. Rep.*, 9 (2019), 14958. <https://doi.org/10.1038/s41598-019-51412-5>.
- [151] P. He, J. Huang. Detrimental Effects of Surface Imperfections and Unpolished Edges on the Cycling Stability of a Zinc Foil Anode, *ACS Energy Lett.*, 6 (2021), 1990–1995. <https://doi.org/10.1021/acsenergylett.1c00638>.
- [152] C. Hitz, A. Lasia. Experimental study and modeling of impedance of the her on porous Ni electrodes, *Journal of Electroanalytical Chemistry*, 500 (2001), 213–222. [https://doi.org/10.1016/S0022-0728\(00\)00317-X](https://doi.org/10.1016/S0022-0728(00)00317-X).
- [153] L. Birry, A. Lasia. Studies of the Hydrogen Evolution Reaction on Raney Nickel–Molybdenum Electrodes, *J. Appl. Electrochem.*, 34 (2004), 735–749. <https://doi.org/10.1023/B:JACH.0000031161.26544.6a>.
- [154] C. F. Bischoff, O. S. Fitz, J. Burns, M. Bauer, H. Gentischer, K. P. Birke, H.-M. Henning, D. Biro. Revealing the Local pH Value Changes of Acidic Aqueous Zinc Ion Batteries with a Manganese Dioxide Electrode during Cycling, *J. Electrochem. Soc.*, 167 (2020), 020545. <https://doi.org/10.1149/1945-7111/ab6c57>.

Appendix 1

1. pielikums

R. Durena, A. Zukuls

**A Short Review: Comparison of Zinc–Manganese Dioxide Batteries with Different pH
Aqueous Electrolytes**

Batteries, 2023, 9(6), 311

DOI: [10.3390/batteries9060311](https://doi.org/10.3390/batteries9060311)

Review

A Short Review: Comparison of Zinc–Manganese Dioxide Batteries with Different pH Aqueous Electrolytes

Ramona Durena * and Anzelms Zukuls

Institute of Materials and Surface Engineering, Faculty of Materials Science and Applied Chemistry,
P. Valdena 3/7, LV-1010 Riga, Latvia; anzels.zukuls@rtu.lv

* Correspondence: ramona.durena@rtu.lv

Abstract: As the world moves towards sustainable and renewable energy sources, there is a need for reliable energy storage systems. A good candidate for such an application could be to improve secondary aqueous zinc–manganese dioxide (Zn–MnO₂) batteries. For this reason, different aqueous Zn–MnO₂ battery technologies are discussed in this short review, focusing on how electrolytes with different pH affect the battery. Improvements and achievements in alkaline aqueous Zn–MnO₂ batteries the recent years have been briefly reviewed. Additionally, mild to acidic aqueous electrolyte employment in Zn–MnO₂ batteries has been described, acknowledging their potential success, as such a battery design can increase the potential by up to 2 V. However, we have also recognized a novel battery electrolyte type that could increase even more scientific interest in aqueous Zn–MnO₂ batteries. Consisting of an alkaline electrolyte in the anode compartment and an acidic electrolyte in the cathode compartment, this dual (amphoteric) electrolyte system permits the extension of the battery cell potential above 2 V without water decomposition. In addition, papers describing pH immobilization in aqueous zinc–manganese compound batteries and the achieved results are reported and discussed.

Keywords: Zn anode; MnO₂ cathode; energy storage; dual electrolyte; amphoteric electrolyte; anolyte; catholyte



Citation: Durena, R.; Zukuls, A. A Short Review: Comparison of Zinc–Manganese Dioxide Batteries with Different pH Aqueous Electrolytes. *Batteries* **2023**, *9*, 311. <https://doi.org/10.3390/batteries9060311>

Academic Editor: Alice Lee-Sie Eh

Received: 12 May 2023

Revised: 23 May 2023

Accepted: 29 May 2023

Published: 5 June 2023



Copyright: © 2023 by the authors. Licensee MDPI, Basel, Switzerland. This article is an open access article distributed under the terms and conditions of the Creative Commons Attribution (CC BY) license (<https://creativecommons.org/licenses/by/4.0/>).

1. Introduction

Effective and reliable battery technology is highly desired as the world leans toward sustainable energy sources, such as hydro, solar, and wind energies. However, all these options suffer from uneven energy production patterns throughout the day and year and cannot supply the energy on demand [1]. One way to overcome these shortcomings is to store the excess energy in batteries or create more everyday appliances with accumulators. This would allow us to charge up these devices when energy is available, such as in the daytime, from solar panels and use electricity-powered devices in the evening [2].

Li-ion batteries (LIBs) in recent decades have found wide applications in consumer electronics [3], such as computers, cell phones [4], and now also electric and hybrid vehicles [5]. The extensive use of LIBs can be attributed to their high energy density (up to 500 Wh/L), power density (up to 300 W/kg), high theoretical lithium storage capacity (890 mA h/g), operating voltage (>3.7 V), excellent cycling performance (over 10,000 cycles), and low self-discharge (<5% of the stored capacity over 1 month) [6–9]. However, the optimal operating range of LIBs is 15–35 °C. Furthermore, battery overheating can induce the melting of the separator, which causes an internal short circuit. In this short-circuit spot, a rapid self-heating begins at a rate of around 2592.0 to 11,860.0 °C min^{−1} [10], resulting in a thermal runaway [11,12]. This means that once the process has started, no cooling application can stop it. Unfortunately, this process results in a fire or an explosion, thus creating a considerable safety risk for consumers [4,13,14]. Furthermore, another significant drawback has emerged: a material shortage of commonly used metals in LIBs could be on the rise [15–17]; thus, this suggests that new or improved battery technology is needed.

One such technology could be improved aqueous Zn-MnO₂ batteries. They do not pose large safety risks; the two-electron reaction of Zn²⁺/Zn has a high theoretical capacity of 820 mAh/g, Zn has low toxicity, and is earth-abundant [18,19]. Moreover, MnO₂ as a cathode has an attractive total theoretical capacity of 617 mAh/g. Thus, making Zn-MnO₂ cells with an energy density of >400 W h/L and >500 Wh/kg [20], which is comparable to some LIBs, is an interesting technology to improve large-scale rechargeable battery applications.

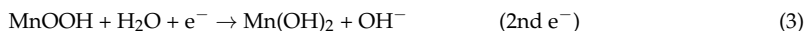
The origin of aqueous Zn-MnO₂ batteries can be traced back to 1866 when the French scientist Georges-Lionel Leclanché created and patented the first Zn-MnO₂ battery, which was called the Leclanché cell [21]. Improving the electrolyte composition and design of this battery cell has led to the creation of commercialized dry cells. Further development of Zn-MnO₂ batteries took place in the 1950s when the Canadian engineer Lewis Urry improved and rebuilt the battery cell known at that time. In 1960, a patent was granted for aqueous alkaline Zn-MnO₂ batteries [22–24]. These batteries have continued their development until now, improving the composition and shelf life, and replacing harmful elements inside the batteries, such as mercury. This has led aqueous alkaline Zn-MnO₂ batteries to be the longest and most widely used primary battery technology that still dominates the global market as the primary battery source nowadays [25].

Aqueous alkaline Zn-MnO₂ batteries consist of a zinc metal anode, a manganese dioxide powder mixture with finely dispersed carbon as the cathode, and concentrated potassium hydroxide (>30 wt%) aqueous solution as the electrolyte. In this electrode pairing (as depicted in Figure 1), Zn acts as an anode with a standard potential of −1.199 V vs. SHE (standard hydrogen electrode) and undergoes reaction (1), whereas MnO₂ acts as an active material in the cathode with a standard potential of +0.250 V vs. SHE and undergoes reactions (2) and (3) in the primary cells. As MnO₂ is non-conductive, usually a small amount of finely dispersed carbon is added to ensure the conductivity of the cathode. This results in an overall reaction (4) [1,26–28]. The calculated open circuit potential (OCP) for this system of 1.45 V is in discrepancy with the actual commercially available battery OCP of 1.55–1.6 V. This effect can be attributed to the fact that reactions (1)–(4) are very general and the actual system is quite complex [29–32]. Additionally, the total theoretical capacity of the MnO₂ cathode consists of a two-stage (two-electron) reaction. The first electron reaction (2) of the MnO₂ cathode in an alkaline medium corresponds to the intercalation of hydrogen in the solid phase with a theoretical capacity of 309 mAh/g. As the discharge continues, the second electron reaction (3) can also occur. A dissolution–precipitation heterogeneous process with a theoretical capacity of 308 mAh/g continues to enter the deep discharge stage of the cathode [20,28,33].

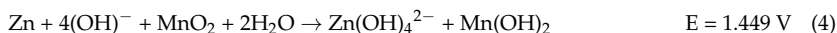
Anode:



Cathode:



Overall:



Although researched for a very long time now, alkaline Zn-MnO₂ batteries are still of great interest to scientists. Aqueous alkaline electrolyte Zn-MnO₂ batteries have proven to be a great source for primary batteries; however, their secondary battery performance is very limited due to the formation of insoluble compounds (usually in the second electron reaction of the cathode). For this reason, many scientists are devoting their research activi-

ties to developing rechargeable aqueous Zn-MnO₂ secondary batteries with higher specific capacities and OCP. In this short review, we discuss improvements and achievements in recent years for different aqueous Zn-MnO₂ battery types, as shown in Figure 2. We have discussed alkaline and acidic/mild aqueous electrolyte rechargeable Zn-MnO₂ battery types and also recognized a dual (amphoteric) aqueous electrolyte battery concept that could increase research interest in aqueous Zn-MnO₂ batteries.

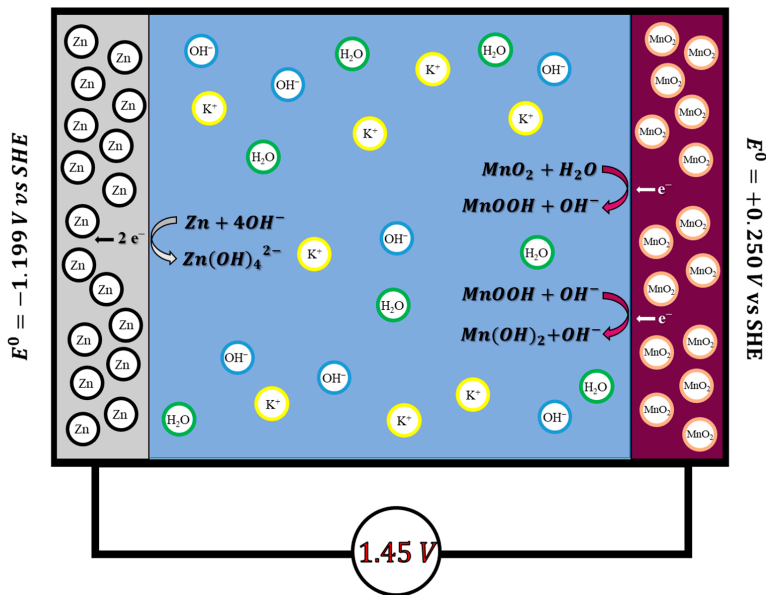


Figure 1. The schematic working mechanism of alkaline Zn-MnO₂ batteries.

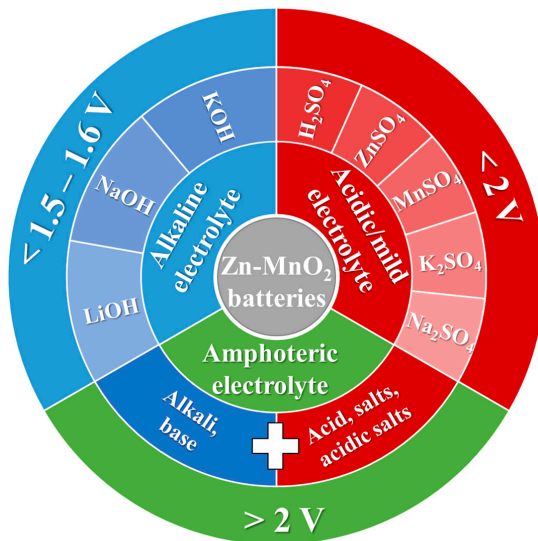


Figure 2. Different types of Zn-MnO₂ batteries with their possible potentials and the most commonly used electrolytes.

2. Alkaline Electrolyte Zn-MnO₂ Batteries

Many authors have attributed the poor rechargeability of alkaline Zn-MnO₂ batteries to the formation of electrochemically inactive manganese oxides such as Mn₃O₄ and ZnMn₂O₄. These oxides form during deep discharge that takes place while accessing the second electron capacity of MnO₂ [22,34]. After several charge/discharge cycles, the irreversible manganese oxides coated the active MnO₂ particles, preventing them from undergoing further reactions. N. D. Ingale with co-authors [35] investigated this problem and provided proof for the connection between insoluble compound formation and the depth of discharge (DOD). They experimentally obtained 3000 cycles for alkaline (45 wt% KOH water solution) Zn-MnO₂ batteries at 10% DOD. However, at 20% DOD, only ~500 cycles could be obtained. For these experiments, the DOD was based on the first theoretical electron capacitance of the MnO₂ cathode (308 mAh/g).

Other scientists have tried to improve the rechargeability of aqueous alkaline Zn-MnO₂ batteries by using additives to electrolytes and/or MnO₂ cathodes [7,34]. A.M. Bruck with co-workers [36] investigated the effects of Bi₂O₃ addition to the MnO₂ electrode. They found that Bi³⁺ occupies an interstitial position in the layered MnO₂ phase—birnessite—limiting the Mn³⁺ ion diffusion in the lattice. Thus, Bi³⁺ promotes the conversion from the MnO₂ birnessite phase directly to Mn(OH)₂ and prevents Mn₂O₃ phase formation during the battery charge/discharge process. A similar technique has been employed by G.G. Yadav with co-authors [28]. They used Cu-intercalated birnessite mixed with Bi₂O₃ as a cathode in alkaline Zn batteries and obtained capacity reversibility (from the second electron capacity of the MnO₂ cathode—617 mAh/g) for more than 6000 cycles. However, the tested cathode material contained only ~19% of the active MnO₂ material.

Other authors have investigated the possibility of improving the alkaline aqueous Zn-MnO₂ battery system by modifying the electrolytes [34,37–39]. For example, B.J. Hertzberg with co-authors [34] researched the effects of mixing KOH electrolyte with LiOH addition. They found that the insertion of lithium or a combined lithium proton is the dominant reduction mechanism for MnO₂. This prevents Zn poisoning reactions and increases the battery cycle lifetime up to 60 cycles with negligible capacity loss (cycling around 360 mAh/g). However, despite their rechargeability improvements, aqueous alkaline Zn-MnO₂ batteries still have limited applications due to their low cell potential of ~1.4 V. For this reason, other scientists have gone one step ahead and changed the electrolyte even further, excluding hydroxides entirely.

3. Mild to Acidic Electrolyte Zn-MnO₂ Batteries

To overcome the low cell potential of 1.4 V and improve the cyclability of aqueous Zn-MnO₂ batteries, other scientists have changed the pH of the electrolyte, thus altering the reaction mechanism of the cell (as depicted in Figure 3). This was achieved by replacing standard hydroxide solutions such as KOH, NaOH, and LiOH [27,34,35,40,41] with ZnSO₄, MnSO₄ (K₂SO₄; Na₂SO₄) [42–47] salts, and/or diluted acid (H₂SO₄) [48,49]. As shown in the Pourbaix diagram of manganese oxide compounds (Figure 4a), at higher pH values, MnO₂ goes through a low potential reaction (0.250 V vs. SHE) with the possibility of transforming into electrochemically inactive manganese oxides such as Mn₃O₄. However, by lowering the pH value well into the acidic medium, the oxygen atom from the MnO₂ cathode can combine with the hydrogen ions to create water; thus, Mn⁴⁺ ions can be reduced to Mn²⁺ and dissolved in an acidic medium without electrochemically inactive manganese oxide creation. Additionally, the reaction potential of the cathode is significantly improved above 1.2 V vs. SHE by placing MnO₂ in an acidic medium. On the other hand, this change in the pH of the electrolyte also increases the reaction potential of the Zn anode, which lowers the overall potential of the cell. As seen in the Pourbaix diagram of zinc oxide compounds (Figure 4b), this potential increase is quite notable, from −1.199 V vs. SHE in an alkaline medium to −0.762 V vs. SHE in an acidic medium.

Overall:



However, this increased cell potential comes with a considerable drawback. In an acidic environment, a parasitic reaction can take place at the Zn anode. A corrosion reaction can occur, the Zn anode dissociates into the electrolyte as Zn^{2+} , and a hydrogen gas H_2 is produced. This corrosion reaction can not only decrease the capacity but also lead to cell rupture [53]. A. Mitha with co-workers [54] designed Zn-LiMn₂O₄ batteries with mildly acidic (pH 4) aqueous electrolyte. To overcome gas production on the anode, fumed silica and polyethylene glycol (MW 300 g/mol) were added. Both additives acted as Zn anode corrosion inhibitors and dendrite suppressors. Thus, this led to achieving a 27–40% lower corrosion current density on the Zn anode and performing 1000 charge–discharge cycles, cycling at a capacity of ~140 mAh/g and retaining ~65% of its initial capacity after 1000 cycles.

H. Pan with co-authors [55] also reported mild electrolyte aqueous Zn-MnO₂ batteries with 5000 charge–discharge cycles and a capacity retention of 92% (based on the first electron capacity of the MnO₂ cathode—308 mAh/g). The high battery cyclability and capacity retention were attributed to the addition of 0.1 M MnSO₄ to 2 M ZnSO₄ electrolyte. The Mn²⁺ ion suppresses MnO₂ dissolution into the electrolyte, thus improving the stability of the cathode and the utilization of the MnO₂ active material. This idea has been well adapted in the literature [43–46]. However, C. Qiu with co-authors [56] addressed the possibility of adding Mn²⁺ deposition to the MnO₂ cathode while cycling and adding extra capacity to the cathode. Cells with different Mn²⁺ concentrations were tested, and as expected, all the cells showed a stable capacity for a certain number of cycles, followed by fast capacity fading due to the consumption of Mn²⁺ ions from the electrolyte. Although effective for a number of cycles, the Mn²⁺ additive may not be an effective strategy for improving the charge–discharge stability. Furthermore, C. Qiu with co-authors again provided proof for the formation of ZnMn₂O₄ at the cathode during discharge, which is attributed to the battery capacity fading and poor cyclability. This indicates that the same rechargeability issues exist in mild aqueous Zn-MnO₂ cells under alkaline conditions. Nonetheless, there could be other methods to improve aqueous Zn-MnO₂ batteries and extend the water decomposition potential window over 1.23 V [57] by combining scientific advances made in aqueous alkaline and acid electrolyte systems.

4. Dual/Amphoteric Electrolyte Zn-MnO₂ Batteries

Recently, another type of Zn-MnO₂ battery has been adapted, which takes advantage of the increased MnO₂ potential in acidic electrolytes without creating drawbacks to the Zn anode. This has been realized by placing the Zn anode in an alkaline electrolyte and the MnO₂ cathode in an acidic electrolyte, as shown in Figure 5. By creating such a unique battery cell type, it is possible to increase the OCP to 2.45 V according to reactions (8)–(10) [32,58,59].

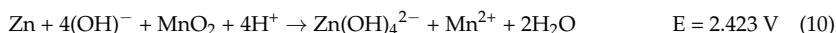
Anode:



Cathode:



Overall:



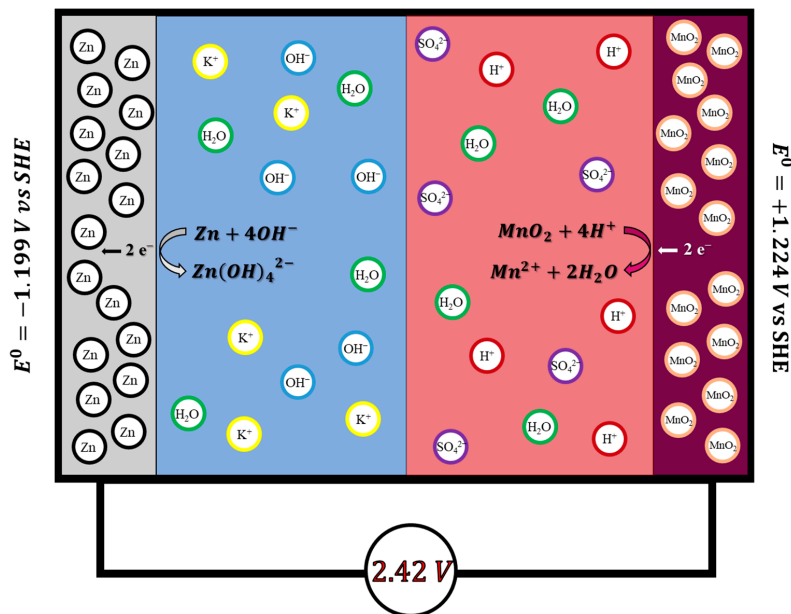


Figure 5. The schematic working mechanism of dual/amphoteric electrolyte Zn-MnO₂ batteries.

The increased theoretical battery potential and widened water decomposition window can also be explained with Pourbaix diagrams. As shown in Figure 6, by operating the battery in a constant pH electrolyte, the maximum water–electrolyte operation potential window is $\sim 1.23 \text{ V}$. By operating a water-based electrolyte battery in a wider potential window, oxygen evolution reaction (OER) and hydrogen evolution reaction (HER) can take place. If a dual-electrolyte system is used and the cathode is operated at lower pH values and the anode at higher pH values, as shown in Figure 6, the stable electrochemical window of water could be increased to $\sim 2 \text{ V}$. However, the HER has a high overpotential for zinc, which can be explained by the Tafel Equation (11):

$$\eta = \alpha + b \log i \quad (11)$$

where η is the HER overpotential, α is the transfer coefficient (overpotential when current density i is equal to the unit current density), b is the Tafel slope (a constant), and i is the current density [60,61]. In addition, OER has a significant intrinsic overpotential of at least 0.37 V due to the complex reaction mechanism [62] and slow reaction kinetics [63]. This way, the water–electrolyte operating potential significantly improves up to 3 V , and the OER and HER reactions are prohibited, thus paving the way for high-voltage aqueous batteries.

Overall, this idea of creating electrolytes with different pH values and increasing the supposed half-reaction potentials as well as the origin of the water decomposition potential origin can be found described in 2005 by three non-related articles. S. Hasegawa with co-authors [64] demonstrated an H₂O₂ fuel cell with acidic (H₂SO₄) catholyte and alkaline (NaOH) anolyte. J.L. Cohen with co-authors [65] published findings on H₂/O₂ fuel cells, where acidic (0.1 M H₂SO₄) and alkaline (0.1 M KOH) electrolytes were used. Additionally, in the same year, E.R. Choban with co-authors [66] presented a methanol/O₂ fuel cell with acidic (0.5 M H₂SO₄) and alkaline (1 M KOH) electrolytes. Later this dual-electrolyte (acidic and alkaline) idea was adapted to different electrode batteries such as Al-air [67–70], Zn-air [68,71,72], Mg-air [68,73], Zn-PbO₂ [74–76], Zn-Br₂ [77], etc. However, the battery working time and efficiency of this battery cell type are limited by both the electrolyte

neutralization reaction and ion diffusion. Scientists have tried to overcome this limitation by using membranes and/or gelation of electrolytes.

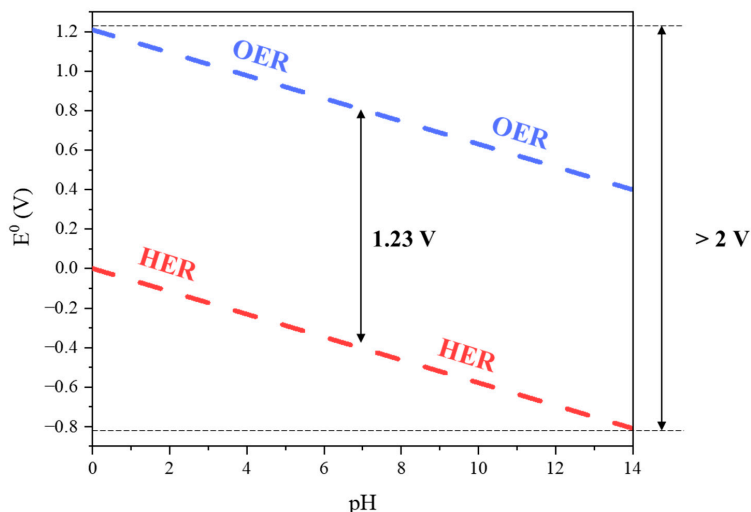


Figure 6. Pourbaix diagram of water.

The first zinc–manganese compound-based battery using an acid–alkaline dual electrolyte was presented by L. Chen with co-authors [78]. The battery cell consisted of a Zn metal sheet placed in an alkaline anolyte (KOH + LiOH solution) against Ti mesh (current collector) placed in an acidic KMnO_4 (active cathode material) catholyte. The battery exhibited an astonishing OCP of 2.8 V and a capacity of up to 750 mAh/g (discharge current density of 375 mA/g). However, no charge–discharge cycles were observed. Later, G. G. Yadav with co-authors [79] showed a two-compartment Zn– MnO_2 cell in 2019. The Zn anode compartment electrolyte consisted of a 45% KOH aqueous solution gelled in potassium polyacrylate. The MnO_2 cathode compartment electrolyte consisted of either KMnO_4 or MnSO_4 in a diluted H_2SO_4 solution. Both compartments were separated using a cellophane membrane, as shown in Figure 7a. This approach enabled achieving cell potential up to 2.45 V (MnSO_4) and 2.8 V (KMnO_4). Battery cells with KMnO_4 in the catholyte were stable, with capacity retention for 35 charge/discharge cycles when utilized at 20% (~62 mAh/g) of MnO_2 one-electron capacity. Moreover, the battery cells with MnSO_4 in the catholyte were stable for 120 charge/discharge cycles when utilized at a capacity of 20% (~62 mAh/g). Unfortunately, this article does not present measurements that would exceed the 35 h mark. A similar approach to Zn– MnO_2 cells has been shown by C. Liu with co-authors [80] in 2020. As depicted in Figure 7b, the cell consisted of two electrolyte compartments: 2.4 M KOH + 0.1 M $\text{Zn}(\text{CH}_3\text{COO})_2$ anolyte and 0.5 M H_2SO_4 + 1.0 M MnSO_4 catholyte. A bipolar membrane was used to prevent ion migration. With this design, a cell potential of ~2.4 V was demonstrated, a Coulombic efficiency of 98.4% was reached, and 1500 cycles were performed while utilizing 0.4 mAh/cm² areal capacity.

Other authors have tried to improve this concept by adding one more (neutral) compartment between the alkaline and acidic electrolytes. C. Zhong with co-authors [32] in 2020 showed a rechargeable Zn– MnO_2 battery as shown in Figure 7c. The battery cell consisted of three electrolyte compartments: (1) acidic 3M H_2SO_4 + 0.1 M MnSO_4 catholyte; (2) neutral 0.1 M K_2SO_4 electrolyte; (3) alkaline 6 M KOH + 0.2 M ZnO + 5 mM vanillin anolyte. The acidic and alkaline compartments were separated from the neutral compartment using anion- and cation-exchange membranes. In this system, an astonishing OCP of 2.83 V was recorded. Additionally, deep discharge (616 mAh/g) cycling was performed

for over 200 h, with 2% capacity fading. However, it should be noted that ion-selective membranes are quite expensive.

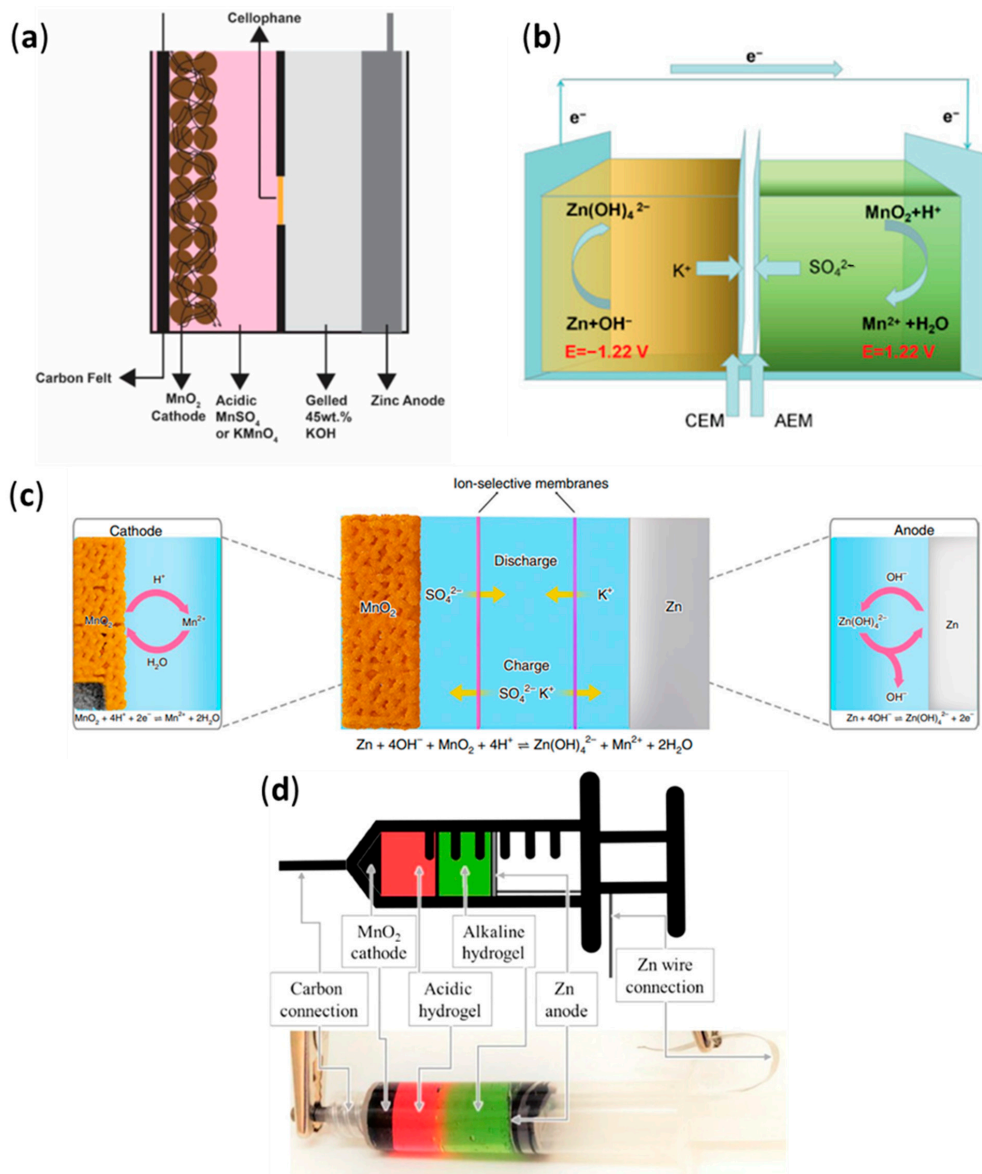


Figure 7. Design schemes of different aqueous amphoteric (dual) electrolyte Zn-MnO₂ batteries: (a) experimental setup of G. G. Yadav (Reprinted with permission from Ref. [79]. Copyright 2019 American Chemical Society.); (b) experimental setup of C. Liu (Reproduced with permission from Ref. [80]; published by John Wiley & Sons, Inc., Hoboken, NJ, USA, 2020); (c) experimental setup of C. Zhong (Reproduced with permission from Ref. [32]; published by Springer Nature Limited, 2020); (d) experimental setup of A. Zukuls (Reproduced with permission from Ref. [59]; published by Elsevier B.V, 2022).

More recently, in 2022, A. Zukuls with co-authors [59] demonstrated a rechargeable aqueous Zn-MnO₂ battery in which the mixing of anolyte and catholyte was prevented by gelling both electrolytes. As shown in Figure 7d, the battery consisted of an acidic (0.5 M H₂SO₄) Pluronic® F-127 aqueous catholyte and an alkaline (1.0 M KOH) Pluronic® F-127 aqueous anolyte. No specific membranes were used in this design, only a porous paper separator was used for visual purposes. With this design, 200 charge–discharge cycles were performed (cycling ~10% of MnO₂ one-electron capacity) while maintaining a high and stable OCP of ~2.4 V. Additionally, the impact of a neutral layer (0.5 M K₂SO₄ + Pluronic® F-127) between the catholyte and anolyte was tested. With this configuration, 200 cycles (cycling ~10% of MnO₂ one-electron capacity) were also performed while maintaining a high and stable OCP of ~2.4 V. However, the discharge and charge potentials were 0.5 V lower and higher, respectively. Although in the design with the neutral layer, a larger internal resistance was observed due to an increase and decrease in the charge–discharge potential, the battery was overall more stable. In a two-layer electrolyte, the battery was stable only for 25 h; however, in a three-layer electrolyte, the battery was stable for 30 h. After this time, a rapid neutralization reaction took place and battery failure was observed. Even though this battery design did not use expensive ion-exchange membranes, thus reducing the expected price, the design did not provide long-term use. Other studies describing zinc–manganese compound-based batteries with dual (amphoteric) electrolytes are listed in Table 1.

Table 1. List of papers investigating zinc–manganese compound-based batteries with dual electrolytes.

Ref.	Year of Publishing	Anode Material	Cathode Material	Anolyte	Catholyte	Membrane	Potential	Cycling	Maximum Capacity	Capacity Retention	Stability
[78]	2013	Zn-plate	KMnO ₄ dissolved in catholyte (Ti mesh as a current collector)	2 M KOH + 2 M LiOH	1 M H ₂ SO ₄ + KMnO ₄	Li-ion exchange membrane (Li _{1+x+y} Al _x Ti _{2-x} Si _y P _{3-y} O ₁₂)	2.8 V OCP	-	from 510 mAh/g (discharge current density of 37.5 mA/g) to 750 mAh/g (discharge current density of 375 mA/g)	-	~110 h (with an intermittent supply of KMnO ₄)
[79]	2019	Zn-foil	85 wt% electrolytic manganese dioxide + 15 wt% multiwalled carbon nanotubes on carbon felt	~45 wt% KOH solution in potassium polyacrylate	1 M MnSO ₄ + 0.5 M H ₂ SO ₄ mixed in ratio of 4:1	Four-layers of cellophane	2.45 OCP	120 cycles (capacity 62 mAh/g) at C/2	308 mAh/g at C/2	100%	35 h
		Zn-foil	85 wt% electrolytic manganese dioxide + 15 wt% multiwalled carbon nanotubes on carbon felt	~45 wt% KOH solution in potassium polyacrylate	1 M MnSO ₄ + 0.5 M H ₂ SO ₄ mixed in ratio of 1:3	Four-layers of cellophane	2.8 OCP	35 cycles (capacity 62 mAh/g) at C/2	308 mAh/g at C/2	100%	35 h
[80]	2020	Zn-foil	potentiostatic electrodeposited MnO ₂ on carbon cloth	2.4 M KOH + 0.1 M Zn(CH ₃ COO)	0.5 M H ₂ SO ₄ + 1.0 M MnSO ₄	bipolar membrane (Fumasep FBM)	2.42 V at 2 mA/cm ²	1500 cycles (capacity of 0.4 mAh/cm ²) at the current density of 2 mA/cm ²	0.4 mAh/cm ² at the current density of 2 mA/cm ²	~90%	200 h

Table 1. Cont.

Ref.	Year of Publishing	Anode Material	Cathode Material	Anolyte	Catholyte	Membrane	Potential	Cycling	Maximum Capacity	Capacity Retention	Stability
[58]	2020	Zn-foil	carbon-felt as a cathode-less current-collector	3 M NaOH + 0.3 M ZnO	3 M MnSO ₄ + 0.3 M H ₂ SO ₄ + 0.06 M NiSO ₄	Selective membrane (no more information provided)	2.44 at 1 mA/cm (1C)	450 cycles (capacity of 1.0 mAh/cm ² at 2C)	1.0 mAh/cm ² (or ~270 mAh/g) at 1C	99.9%	140 h
[81]	2020	Zn-foil	MnO ₂ + acetylene black + PTFE (70:20:10)	1 M NaOH + 0.01 M Zn(CH ₃ CO ₂) ₂	2 M ZnSO ₄ + 0.1 M MnSO ₄	Nafion 115	2.2 V	90 cycles (capacity 282.2–428.6 mAh/g) at 200 mA/g	300 mAh/g at (not specified)	~100%	Not shown
[82]	2021	Zn-foil	MnO ₂ powder coated on Ti foil	2 M ZnSO ₄ + H ₂ SO ₄ gelled in polyacrylamide	2 M ZnSO ₄ (with adjusted pH = 7) gelled in polyacrylamide	Neutral layer: 2 M ZnSO ₄ gelled in sodium polyacrylate	1.8 V at 5 A/g	5000 cycles (capacity of 150 mAh/g) at 5 A/g	516 mAh/g at 0.05 A/g	93.18%	>6 months
[59]	2022	Zn-foil	MnO ₂ + carbon black (13:5) on carbon felt	1 M KOH Pluronic® F-127 hydrogel	0.5 M H ₂ SO ₄ Pluronic® F-127 hydrogel	-	2.4 V OCP	200 cycles (discharge for 120 s) at 1 mA/s	25 mAh/g at 20 mA/g	-	>25 h
[83]	2022	Zn-foil	MoS-MnO ₂ heterostructure + conductive carbon + PVDF (80:15:5) on carbon cloth	1 M Zn(ClO ₄) ₂ + acetonitrile + water + H ₂ SO ₄	1 M Zn(ClO ₄) ₂ + acetonitrile + water + KOH	PVA+PVP crosslinked membrane	1.9 V (at the start of discharge at 0.2 A/g)	5000 cycles (160 mAh/g) at 10 A/g	464 mAh/g at 0.2 A/g	74%	Not shown
[84]	2022	Zn-foil	potentiostatic electrodeposited MnO ₂ from catholyte on carbon cloth	0.3 M ZnO + 3 M NaOH	3 M MnSO ₄ + 0.3 M H ₂ SO ₄	agar with Na ₂ SO ₄	2.5 V at 0.1 C	350 cycles (capacity ~550 mAh/g) at 1 C	577.8 mAh/g at 1C	94%	>350 h

Table 1. Cont.

Ref.	Year of Publishing	Anode Material	Cathode Material	Anolyte	Catholyte	Membrane	Potential	Cycling	Maximum Capacity	Capacity Retention	Stability
[85]	2022	Zn-foil	electrochemically deposited MnO ₂ on carbon paper	0.5 M ZnSO ₄ + 1 M LiTFSI (bis(trifluoromethane)sulfonimide lithium salt)	1 M MnSO ₄ + 1 M HTFSI (bis(trifluoromethanesulfonyl)imide)	dual-hydrophobic-induced membrane (consisting of polymer/ionic liquid/graphene mixture)	2.05 V at 1 mA/cm	2000 cycles (fixed area capacity of 1 mAh/cm ² at 1 mA/cm ²)	18 mAh/cm ² at 1 mA/cm ²	98%	2275 h
[86]	2023	Zn-foil	carbon cloth	2.4 M KOH + 0.1 M Zn(CH ₃ COO) ₂	1.0 M H ₂ SO ₄ + 0.3 M CuSO ₄ + 1.0 M MnSO ₄	Cu foil	1.84 V at 2.5 mA/cm ²	3500 (capacity ~0.5 mAh/cm ² at 2.5 mA/cm ²)	0.5 mAh/cm ² at 2.5 mA/cm ²	~125% (Coulombic efficiency after 3500 cycles)	>107 h

5. Challenges and Outlook

Primary aqueous alkaline Zn-MnO₂ battery technology already dominates the primary battery market. This technology has proven itself as safe, affordable, and reliable. As the world moves towards renewable energy sources, we are in need of safe, affordable, and reliable secondary battery technology with a high-power density and excellent capacity retention during charge/discharge cycles. A good candidate for this application could be aqueous Zn-MnO₂ battery technology. However, several improvements and new technological approaches are needed. A very new approach has been demonstrated by G. G. Yadav with co-authors [79] and by others [32,59,80]. In the literature, dual (amphoteric) electrolyte aqueous cells have been demonstrated that result in a significant increase in cell potential over 2 V. This voltage increase has been achieved in these new aqueous cell types by placing a Zn anode in an alkaline medium and an MnO₂ cathode in an acidic medium. To prevent neutralization reactions from occurring, different approaches have been used, such as the usage of ion exchange membranes or other types of membranes, gelation of electrolytes, or both. However, when put to the test, this cell design presents several problems that should be addressed in the near future by researchers. Different recyclability problems continue to exist for the Zn anode in an alkaline medium and the MnO₂ cathode in an acidic medium. For aqueous Zn-MnO₂ batteries to compete with LIBs, full utilization of the MnO₂ cathode capacity should be achieved with high-capacity retention over a large number of charge–discharge cycles. Additionally, the economic aspects should be taken into account when considering new types of chemical energy storage systems. Although ion exchange membranes provide excellent immiscibility with the electrolyte pH, they are quite expensive. Different hydrogels such as Pluronic® F-127 are economically disadvantageous as well. Thus, effective methods for pH immobilization should be more thoughtfully considered.

6. Conclusions

In this short review, aqueous Zn-MnO₂ batteries with different pH electrolytes have been acknowledged. The historical origins of alkaline Zn-MnO₂ batteries can be traced back to the middle of the 20th century. Although they have been successfully utilized in the primary battery market and research has been carried out to tackle the rechargeability challenges, little to no secondary aqueous Zn-MnO₂ batteries are seen in the market. Another type of Zn-MnO₂ battery discussed is a mild to acidic aqueous electrolyte battery. If an alkaline-type battery suffers from electrochemically inactive and insoluble compound formations, such as Mn₃O₄ and ZnMn₂O₄, then, in an acidic electrolyte, this problem is partially solved since these compounds are soluble in acid. Moreover, by decreasing the pH value of the electrolyte, the cathode goes through a higher potential reaction and increases the overall potential of the cell from 1.4–1.6 V in the alkaline electrolyte to 1.9–2.0 V in the mild/acidic electrolyte. However, more recently, the scientific community has shown a new and innovative battery cell type that combines the positive effects of alkaline and acidic electrolytes and advances the possibility of creating a water-electrolyte battery with a potential of up to 3 V. This has been accomplished by operating the anode in an alkaline medium and cathode in an acidic medium. Thus, increasing the potential of this aqueous dual/amphoteric electrolyte Zn-MnO₂ battery up to 2.4 V improves the reachability of the cell. However, this unique battery cell imposes new challenges, such as neutralization reactions between both electrolytes.

Author Contributions: Conceptualization, R.D. and A.Z.; methodology, R.D. and A.Z.; validation, A.Z.; formal analysis, R.D. and A.Z.; investigation, R.D.; writing—original draft preparation, R.D.; writing—review and editing, A.Z.; visualization, R.D.; supervision, A.Z.; funding acquisition, R.D. All authors have read and agreed to the published version of the manuscript.

Funding: Ramona Durena acknowledges that this work has been supported by the European Social Fund within Project No 8.2.2.0/20/1/008 «Strengthening of PhD students and academic personnel of Riga Technical University and BA School of Business and Finance in the strategic fields of specialization» of the Specific Objective 8.2.2 «To Strengthen Academic Staff of Higher Education Institutions in Strategic Specialization Areas» of the Operational Programme «Growth and Employment».

Institutional Review Board Statement: Not applicable.

Informed Consent Statement: Not applicable.

Data Availability Statement: Not applicable.

Conflicts of Interest: The authors declare that they have no known competing financial interests or personal relationships that could have appeared to influence the work reported in this paper.

References

1. Collins, J.; Gourdin, G.; Qu, D. Modern Applications of Green Chemistry. In *Green Chemistry*; Elsevier: Amsterdam, The Netherlands, 2018; pp. 771–860.
2. Ziegler, M.S.; Mueller, J.M.; Pereira, G.D.; Song, J.; Ferrara, M.; Chiang, Y.-M.; Trancik, J.E. Storage Requirements and Costs of Shaping Renewable Energy Toward Grid Decarbonization. *Joule* **2019**, *3*, 2134–2153. [[CrossRef](#)]
3. Lu, L.; Han, X.; Li, J.; Hua, J.; Ouyang, M. A Review on the Key Issues for Lithium-Ion Battery Management in Electric Vehicles. *J. Power Sources* **2013**, *226*, 272–288. [[CrossRef](#)]
4. Chen, Y.; Kang, Y.; Zhao, Y.; Wang, L.; Liu, J.; Li, Y.; Liang, Z.; He, X.; Li, X.; Tavajohi, N.; et al. A Review of Lithium-Ion Battery Safety Concerns: The Issues, Strategies, and Testing Standards. *J. Energy Chem.* **2021**, *59*, 83–99. [[CrossRef](#)]
5. Galushkin, N.E.; Yazvinskaya, N.N.; Galushkin, D.N. Mechanism of Thermal Runaway in Lithium-Ion Cells. *J. Electrochem. Soc.* **2018**, *165*, A1303–A1308. [[CrossRef](#)]
6. Yang, J.; Liu, X.; Tian, J.; Ma, X.; Wang, B.; Li, W.; Wang, Q. Adhesive Nanocomposites of Hypergravity Induced Co_3O_4 Nanoparticles and Natural Gels as Li-Ion Battery Anode Materials with High Capacitance and Low Resistance. *RSC Adv.* **2017**, *7*, 21061–21067. [[CrossRef](#)]
7. Lim, M.B.; Lambert, T.N.; Chalamala, B.R. Rechargeable Alkaline Zinc–Manganese Oxide Batteries for Grid Storage: Mechanisms, Challenges and Developments. *Mater. Sci. Eng. R Rep.* **2021**, *143*, 100593. [[CrossRef](#)]
8. Park, J.; Kim, M.; Choi, J.; Lee, S.; Kim, J.; Han, D.; Jang, H.; Park, M. Recent Progress in High-voltage Aqueous Zinc-based Hybrid Redox Flow Batteries. *Chem. Asian J.* **2023**, *18*, e202201052. [[CrossRef](#)]
9. Seong, W.M.; Park, K.-Y.; Lee, M.H.; Moon, S.; Oh, K.; Park, H.; Lee, S.; Kang, K. Abnormal Self-Discharge in Lithium-Ion Batteries. *Energy Environ. Sci.* **2018**, *11*, 970–978. [[CrossRef](#)]
10. Duh, Y.S.; Lin, K.H.; Kao, C.S. Experimental Investigation and Visualization on Thermal Runaway of Hard Prismatic Lithium-Ion Batteries Used in Smart Phones. *J. Therm. Anal. Calorim.* **2018**, *132*, 1677–1692. [[CrossRef](#)]
11. Nitta, N.; Wu, F.; Lee, J.T.; Yushin, G. Li-Ion Battery Materials: Present and Future. *Mater. Today* **2015**, *18*, 252–264. [[CrossRef](#)]
12. Zaman, W.; Hatzell, K.B. Processing and Manufacturing of next Generation Lithium-Based All Solid-State Batteries. *Curr. Opin. Solid State Mater. Sci.* **2022**, *26*, 101003. [[CrossRef](#)]
13. Wang, H.; Shi, W.; Hu, F.; Wang, Y.; Hu, X.; Li, H. Over-Heating Triggered Thermal Runaway Behavior for Lithium-Ion Battery with High Nickel Content in Positive Electrode. *Energy* **2021**, *224*, 120072. [[CrossRef](#)]
14. Chen, S.; Gao, Z.; Sun, T. Safety Challenges and Safety Measures of Li-Ion Batteries. *Energy Sci. Eng.* **2021**, *9*, 1647–1672. [[CrossRef](#)]
15. Zeng, A.; Chen, W.; Rasmussen, K.D.; Zhu, X.; Lundhaug, M.; Müller, D.B.; Tan, J.; Keiding, J.K.; Liu, L.; Dai, T.; et al. Battery Technology and Recycling Alone Will Not Save the Electric Mobility Transition from Future Cobalt Shortages. *Nat. Commun.* **2022**, *13*, 1341. [[CrossRef](#)]
16. Zhang, J.; Lei, Y.; Lin, Z.; Xie, P.; Lu, H.; Xu, J. A Novel Approach to Recovery of Lithium Element and Production of Holey Graphene Based on the Lithiated Graphite of Spent Lithium Ion Batteries. *Chem. Eng. J.* **2022**, *436*, 135011. [[CrossRef](#)]
17. Liu, B.; Zhang, Q.; Liu, J.; Hao, Y.; Tang, Y.; Li, Y. The Impacts of Critical Metal Shortage on China's Electric Vehicle Industry Development and Countermeasure Policies. *Energy* **2022**, *248*, 123646. [[CrossRef](#)]
18. Zhang, H.; Lu, W.; Li, X. Progress and Perspectives of Flow Battery Technologies. *Electrochem. Energy Rev.* **2019**, *2*, 492–506. [[CrossRef](#)]
19. Luo, H.; Liu, B.; Yang, Z.; Wan, Y.; Zhong, C. The Trade-Offs in the Design of Reversible Zinc Anodes for Secondary Alkaline Batteries. *Electrochem. Energy Rev.* **2022**, *5*, 187–210. [[CrossRef](#)]
20. Yadav, G.G.; Wei, X.; Huang, J.; Turney, D.; Nyce, M.; Banerjee, S. Accessing the Second Electron Capacity of MnO_2 by Exploring Complexation and Intercalation Reactions in Energy Dense Alkaline Batteries. *Int. J. Hydrogen Energy* **2018**, *43*, 8480–8487. [[CrossRef](#)]
21. Placke, T.; Kloepsch, R.; Dühnen, S.; Winter, M. Lithium Ion, Lithium Metal, and Alternative Rechargeable Battery Technologies: The Odyssey for High Energy Density. *J. Solid State Electrochem.* **2017**, *21*, 1939–1964. [[CrossRef](#)]
22. Shin, J.; Seo, J.K.; Yaylian, R.; Huang, A.; Meng, Y.S. A Review on Mechanistic Understanding of MnO_2 in Aqueous Electrolyte for Electrical Energy Storage Systems. *Int. Mater. Rev.* **2020**, *65*, 356–387. [[CrossRef](#)]

23. Akinyele, D.; Belikov, J.; Levron, Y. Battery Storage Technologies for Electrical Applications: Impact in Stand-Alone Photovoltaic Systems. *Energies* **2017**, *10*, 1760. [[CrossRef](#)]
24. Song, J.; Xu, K.; Liu, N.; Reed, D.; Li, X. Crossroads in the Renaissance of Rechargeable Aqueous Zinc Batteries. *Mater. Today* **2021**, *45*, 191–212. [[CrossRef](#)]
25. Takamura, T. PRIMARY BATTERIES—AQUEOUS SYSTEMS | Alkaline Manganese–Zinc. In *Encyclopedia of Electrochemical Power Sources*; Elsevier: Amsterdam, The Netherlands, 2009; pp. 28–42.
26. Owens, B.B.; Reale, P.; Scrosati, B. PRIMARY BATTERIES | Overview. In *Encyclopedia of Electrochemical Power Sources*; Elsevier: Amsterdam, The Netherlands, 2009; pp. 22–27.
27. D’Ambrose, M.J.; Turney, D.E.; Yadav, G.G.; Nyce, M.; Banerjee, S. Material Failure Mechanisms of Alkaline Zn Rechargeable Conversion Electrodes. *ACS Appl. Energy Mater.* **2021**, *4*, 3381–3392. [[CrossRef](#)]
28. Yadav, G.G.; Gallaway, J.W.; Turney, D.E.; Nyce, M.; Huang, J.; Wei, X.; Banerjee, S. Regenerable Cu-Intercalated MnO₂ Layered Cathode for Highly Cyclable Energy Dense Batteries. *Nat. Commun.* **2017**, *8*, 14424. [[CrossRef](#)] [[PubMed](#)]
29. Liu, X.; Yi, J.; Wu, K.; Jiang, Y.; Liu, Y.; Zhao, B.; Li, W.; Zhang, J. Rechargeable Zn–MnO₂ Batteries: Advances, Challenges and Perspectives. *Nanotechnology* **2020**, *31*, 122001. [[CrossRef](#)] [[PubMed](#)]
30. Faegh, E.; Omasta, T.; Hull, M.; Ferrin, S.; Shrestha, S.; Lechman, J.; Bolintineanu, D.; Zuraw, M.; Mustain, W.E. Understanding the Dynamics of Primary Zn–MnO₂ Alkaline Battery Gassing with Operando Visualization and Pressure Cells. *J. Electrochem. Soc.* **2018**, *165*, A2528–A2535. [[CrossRef](#)]
31. Perez-Antolin, D.; Sáez-Bernal, I.; Colina, A.; Ventosa, E. Float-Charging Protocol in Rechargeable Zn–MnO₂ Batteries: Unraveling the Key Role of Mn²⁺ Additives in Preventing Spontaneous PH Changes. *Electrochem. Commun.* **2022**, *138*, 107271. [[CrossRef](#)]
32. Zhong, C.; Liu, B.; Ding, J.; Liu, X.; Zhong, Y.; Li, Y.; Sun, C.; Han, X.; Deng, Y.; Zhao, N.; et al. Decoupling Electrolytes towards Stable and High-Energy Rechargeable Aqueous Zinc–Manganese Dioxide Batteries. *Nat. Energy* **2020**, *5*, 440–449. [[CrossRef](#)]
33. Bai, L.; Qu, D.Y.; Conway, B.E.; Zhou, Y.H.; Chowdhury, G.; Adams, W.A. Rechargeability of a Chemically Modified MnO₂/Zn Battery System at Practically Favorable Power Levels. *J. Electrochem. Soc.* **1993**, *140*, 884–889. [[CrossRef](#)]
34. Hertzberg, B.J.; Huang, A.; Hsieh, A.; Chamoun, M.; Davies, G.; Seo, J.K.; Zhong, Z.; Croft, M.; Erdonmez, C.; Meng, Y.S.; et al. Effect of Multiple Cation Electrolyte Mixtures on Rechargeable Zn–MnO₂ Alkaline Battery. *Chem. Mater.* **2016**, *28*, 4536–4545. [[CrossRef](#)]
35. Ingale, N.D.; Gallaway, J.W.; Nyce, M.; Couzis, A.; Banerjee, S. Rechargeability and Economic Aspects of Alkaline Zinc–Manganese Dioxide Cells for Electrical Storage and Load Leveling. *J. Power Sources* **2015**, *276*, 7–18. [[CrossRef](#)]
36. Bruck, A.M.; Kim, M.A.; Ma, L.; Ehrlich, S.N.; Okasinski, J.S.; Gallaway, J.W. Bismuth Enables the Formation of Disordered Birnessite in Rechargeable Alkaline Batteries. *J. Electrochem. Soc.* **2020**, *167*, 110514. [[CrossRef](#)]
37. Rus, E.D.; Moon, G.D.; Bai, J.; Steingart, D.A.; Erdonmez, C.K. Electrochemical Behavior of Electrolytic Manganese Dioxide in Aqueous KOH and LiOH Solutions: A Comparative Study. *J. Electrochem. Soc.* **2016**, *163*, A356–A363. [[CrossRef](#)]
38. Kelly, M.; Duay, J.; Lambert, T.N.; Aidun, R. Impact of Triethanolamine as an Additive for Rechargeable Alkaline Zn/MnO₂ Batteries under Limited Depth of Discharge Conditions. *J. Electrochem. Soc.* **2017**, *164*, A3684–A3691. [[CrossRef](#)]
39. Minakshi, M.; Singh, P. Synergistic Effect of Additives on Electrochemical Properties of MnO₂ Cathode in Aqueous Rechargeable Batteries. *J. Solid State Electrochem.* **2012**, *16*, 1487–1492. [[CrossRef](#)]
40. Pooapat, A.; Vadnala, S.; Negrete, K.; Lan, Y.; Hutchison, J.; Zupan, M.; Madan, D. Rechargeable Zinc-Electrolytic Manganese Dioxide (EMD) Battery with a Flexible Chitosan-Alkaline Electrolyte. *ACS Appl. Energy Mater.* **2021**, *4*, 4248–4258. [[CrossRef](#)]
41. Minakshi, M.; Ralph, D. A Novel Sodium-Ion Rechargeable Battery. *ECS Trans.* **2013**, *45*, 95–102. [[CrossRef](#)]
42. Wei, Z.; Cheng, J.; Wang, R.; Li, Y.; Ren, Y. From Spent Zn–MnO₂ Primary Batteries to Rechargeable Zn–MnO₂ Batteries: A Novel Directly Recycling Route with High Battery Performance. *J. Environ. Manag.* **2021**, *298*, 113473. [[CrossRef](#)]
43. Soundharajan, V.; Sambandam, B.; Kim, S.; Islam, S.; Jo, J.; Kim, S.; Mathew, V.; Sun, Y.; Kim, J. The Dominant Role of Mn²⁺ Additive on the Electrochemical Reaction in ZnMn₂O₄ Cathode for Aqueous Zinc-Ion Batteries. *Energy Storage Mater.* **2020**, *28*, 407–417. [[CrossRef](#)]
44. Wang, C.; Zeng, Y.; Xiao, X.; Wu, S.; Zhong, G.; Xu, K.; Wei, Z.; Su, W.; Lu, X. γ-MnO₂ Nanorods/Graphene Composite as Efficient Cathode for Advanced Rechargeable Aqueous Zinc-Ion Battery. *J. Energy Chem.* **2020**, *43*, 182–187. [[CrossRef](#)]
45. Lee, J.-W.; Seo, S.-D.; Kim, D.-W. Comparative Study on Ternary Spinel Cathode Zn–Mn–O Microspheres for Aqueous Rechargeable Zinc-Ion Batteries. *J. Alloy. Compd.* **2019**, *800*, 478–482. [[CrossRef](#)]
46. Xu, D.; Li, B.; Wei, C.; He, Y.-B.; Du, H.; Chu, X.; Qin, X.; Yang, Q.-H.; Kang, F. Preparation and Characterization of MnO₂/Acid-Treated CNT Nanocomposites for Energy Storage with Zinc Ions. *Electrochim. Acta* **2014**, *133*, 254–261. [[CrossRef](#)]
47. Han, K.; An, F.; Yan, F.; Chen, H.; Wan, Q.; Liu, Y.; Li, P.; Qu, X. High-Performance Aqueous Zn–MnO₂ Batteries Enabled by the Coupling Engineering of K⁺ Pre-Intercalation and Oxygen Defects. *J. Mater. Chem. A Mater.* **2021**, *9*, 15637–15647. [[CrossRef](#)]
48. Chao, D.; Zhou, W.; Ye, C.; Zhang, Q.; Chen, Y.; Gu, L.; Davey, K.; Qiao, S. An Electrolytic Zn–MnO₂ Battery for High-Voltage and Scalable Energy Storage. *Angew. Chem. Int. Ed.* **2019**, *58*, 7823–7828. [[CrossRef](#)]
49. Kim, S.J.; Wu, D.; Housel, L.M.; Wu, L.; Takeuchi, K.J.; Marschilok, A.C.; Takeuchi, E.S.; Zhu, Y. Toward the Understanding of the Reaction Mechanism of Zn/MnO₂ Batteries Using Non-Alkaline Aqueous Electrolytes. *Chem. Mater.* **2021**, *33*, 7283–7289. [[CrossRef](#)]
50. Boytsova, O.V.; Shekunova, T.O.; Baranchikov, A.E. Nanocrystalline Manganese Dioxide Synthesis by Microwave-Hydrothermal Treatment. *Russ. J. Inorg. Chem.* **2015**, *60*, 546–551. [[CrossRef](#)]

51. Krežel, A.; Maret, W. The Biological Inorganic Chemistry of Zinc Ions. *Arch. Biochem. Biophys.* **2016**, *611*, 3–19. [[CrossRef](#)]
52. Wang, M.; Zheng, X.; Zhang, X.; Chao, D.; Qiao, S.; Alshareef, H.N.; Cui, Y.; Chen, W. Opportunities of Aqueous Manganese-Based Batteries with Deposition and Stripping Chemistry. *Adv. Energy Mater.* **2021**, *11*, 2002904. [[CrossRef](#)]
53. Yang, J.; Cao, J.; Peng, Y.; Yang, W.; Barg, S.; Liu, Z.; Kinloch, I.A.; Bissett, M.A.; Dryfe, R.A.W. Unravelling the Mechanism of Rechargeable Aqueous Zn–MnO₂ Batteries: Implementation of Charging Process by Electrodeposition of MnO₂. *ChemSusChem* **2020**, *13*, 4103–4110. [[CrossRef](#)]
54. Mitha, A.; Mi, H.; Dong, W.; Cho, I.S.; Ly, J.; Yoo, S.; Bang, S.; Hoang, T.K.A.; Chen, P. Thixotropic Gel Electrolyte Containing Poly(Ethylene Glycol) with High Zinc Ion Concentration for the Secondary Aqueous Zn/LiMn₂O₄ Battery. *J. Electroanal. Chem.* **2019**, *836*, 1–6. [[CrossRef](#)]
55. Pan, H.; Shao, Y.; Yan, P.; Cheng, Y.; Han, K.S.; Nie, Z.; Wang, C.; Yang, J.; Li, X.; Bhattacharya, P.; et al. Reversible Aqueous Zinc/Manganese Oxide Energy Storage from Conversion Reactions. *Nat. Energy* **2016**, *1*, 16039. [[CrossRef](#)]
56. Qiu, C.; Zhu, X.; Xue, L.; Ni, M.; Zhao, Y.; Liu, B.; Xia, H. The Function of Mn²⁺ Additive in Aqueous Electrolyte for Zn/ δ -MnO₂ Battery. *Electrochim. Acta* **2020**, *351*, 136445. [[CrossRef](#)]
57. Demir-Cakan, R.; Palacin, M.R.; Croguennec, L. Rechargeable Aqueous Electrolyte Batteries: From Univalent to Multivalent Cation Chemistry. *J. Mater. Chem. A Mater.* **2019**, *7*, 20519–20539. [[CrossRef](#)]
58. Chao, D.; Ye, C.; Xie, F.; Zhou, W.; Zhang, Q.; Gu, Q.; Davey, K.; Gu, L.; Qiao, S. Atomic Engineering Catalyzed MnO₂ Electrolysis Kinetics for a Hybrid Aqueous Battery with High Power and Energy Density. *Adv. Mater.* **2020**, *32*, 2001894. [[CrossRef](#)]
59. Dürren, R.; Zukuls, A.; Vanags, M.; Šutka, A. How to Increase the Potential of Aqueous Zn–MnO₂ Batteries: The Effect of PH Gradient Electrolyte. *Electrochim. Acta* **2022**, *434*, 141275. [[CrossRef](#)]
60. Li, C.; Xie, X.; Liang, S.; Zhou, J. Issues and Future Perspective on Zinc Metal Anode for Rechargeable Aqueous Zinc-ion Batteries. *Energy Environ. Mater.* **2020**, *3*, 146–159. [[CrossRef](#)]
61. Ibrahim, M.A. Improving the Throwing Power of Acidic Zinc Sulfate Electroplating Baths. *J. Chem. Technol. Biotechnol.* **2000**, *75*, 745–755. [[CrossRef](#)]
62. Li, J. Oxygen Evolution Reaction in Energy Conversion and Storage: Design Strategies Under and Beyond the Energy Scaling Relationship. *Nanomicro. Lett.* **2022**, *14*, 112. [[CrossRef](#)]
63. Zhang, G.-R.; Shen, L.-L.; Mei, D. Enhanced Electrocatalysis at Ionic Liquid Modified Solid–Liquid Interfaces. In *Reference Module in Chemistry, Molecular Sciences and Chemical Engineering*; Elsevier: Amsterdam, The Netherlands, 2023.
64. Hasegawa, S.; Shimotani, K.; Kishi, K.; Watanabe, H. Electricity Generation from Decomposition of Hydrogen Peroxide. *Electrochem. Solid-State Lett.* **2005**, *8*, A119. [[CrossRef](#)]
65. Cohen, J.L.; Volpe, D.J.; Westly, D.A.; Pechenik, A.; Abruña, H.D. A Dual Electrolyte H₂/O₂ Planar Membraneless Microchannel Fuel Cell System with Open Circuit Potentials in Excess of 1.4 V. *Langmuir* **2005**, *21*, 3544–3550. [[CrossRef](#)] [[PubMed](#)]
66. Choban, E.R.; Spendelow, J.S.; Gancs, L.; Wieckowski, A.; Kenis, P.J.A. Membraneless Laminar Flow-Based Micro Fuel Cells Operating in Alkaline, Acidic, and Acidic/Alkaline Media. *Electrochim. Acta* **2005**, *50*, 5390–5398. [[CrossRef](#)]
67. Wen, H.; Liu, Z.; Qiao, J.; Chen, R.; Qiao, G.; Yang, J. Ultrahigh Voltage and Energy Density Aluminum–air Battery Based on Aqueous Alkaline-acid Hybrid Electrolyte. *Int. J. Energy Res.* **2020**, *44*, 10652–10661. [[CrossRef](#)]
68. Wang, Y.; Pan, W.; Luo, S.; Zhao, X.; Kwok, H.Y.H.; Xu, X.; Leung, D.Y.C. High-Performance Solid-State Metal–Air Batteries with an Innovative Dual-Gel Electrolyte. *Int. J. Hydrog. Energy.* **2022**, *47*, 15024–15034. [[CrossRef](#)]
69. Wang, L.; Cheng, R.; Liu, C.; Ma, M.C.; Wang, W.; Yang, G.; Leung, M.K.H.; Liu, F.; Feng, S.P. Trielectrolyte Aluminum–Air Cell with High Stability and Voltage beyond 2.2 V. *Mater. Today Phys.* **2020**, *14*, 100242. [[CrossRef](#)]
70. Chen, B.; Leung, D.Y.C.; Xuan, J.; Wang, H. A Mixed-PH Dual-Electrolyte Microfluidic Aluminum–Air Cell with High Performance. *Appl. Energy* **2017**, *185*, 1303–1308. [[CrossRef](#)]
71. Cai, P.; Li, Y.; Chen, J.; Jia, J.; Wang, G.; Wen, Z. An Asymmetric-Electrolyte Zn–Air Battery with Ultrahigh Power Density and Energy Density. *ChemElectroChem* **2018**, *5*, 589–592. [[CrossRef](#)]
72. Zhao, S.; Liu, T.; Dai, Y.; Wang, Y.; Guo, Z.; Zhai, S.; Yu, J.; Zhi, C.; Ni, M. All-in-One and Bipolar-Membrane-Free Acid–Alkaline Hydrogel Electrolytes for Flexible High-Voltage Zn–Air Batteries. *Chem. Eng. J.* **2022**, *430*, 132718. [[CrossRef](#)]
73. Leong, K.W.; Wang, Y.; Pan, W.; Luo, S.; Zhao, X.; Leung, D.Y.C. Doubling the Power Output of a Mg–Air Battery with an Acid–Salt Dual-Electrolyte Configuration. *J. Power Sources* **2021**, *506*, 230144. [[CrossRef](#)]
74. Xu, Y.; Cai, P.; Chen, K.; Ding, Y.; Chen, L.; Chen, W.; Wen, Z. High-Voltage Rechargeable Alkali–Acid Zn–PbO₂ Hybrid Battery. *Angew. Chem. Int. Ed.* **2020**, *59*, 23593–23597. [[CrossRef](#)]
75. Gao, T.; Sun, Y.; Gong, L.; Ma, C.; Wang, J.; Su, L. 2.8 V Aqueous Lead Dioxide–Zinc Rechargeable Battery Using H₂SO₄–K₂SO₄–KOH Three Electrolytes. *J. Electrochem. Soc.* **2020**, *167*, 020552. [[CrossRef](#)]
76. Wu, H.; Liu, S.-J.; Lian, K. Aqueous Based Dual-Electrolyte Rechargeable Pb–Zn Battery with a 2.8 V Operating Voltage. *J. Energy Storage* **2020**, *29*, 101305. [[CrossRef](#)]
77. Yu, F.; Pang, L.; Wang, X.; Waclawik, E.R.; Wang, F.; Ostrikov, K.; Wang, H. Aqueous Alkaline–Acid Hybrid Electrolyte for Zinc–Bromine Battery with 3V Voltage Window. *Energy Storage Mater.* **2019**, *19*, 56–61. [[CrossRef](#)]
78. Chen, L.; Guo, Z.; Xia, Y.; Wang, Y. High-Voltage Aqueous Battery Approaching 3 V Using an Acidic–Alkaline Double Electrolyte. *Chem. Commun.* **2013**, *49*, 2204. [[CrossRef](#)] [[PubMed](#)]
79. Yadav, G.G.; Turney, D.; Huang, J.; Wei, X.; Banerjee, S. Breaking the 2 V Barrier in Aqueous Zinc Chemistry: Creating 2.45 and 2.8 V MnO₂–Zn Aqueous Batteries. *ACS Energy Lett.* **2019**, *4*, 2144–2146. [[CrossRef](#)]

80. Liu, C.; Chi, X.; Han, Q.; Liu, Y. A High Energy Density Aqueous Battery Achieved by Dual Dissolution/Deposition Reactions Separated in Acid-Alkaline Electrolyte. *Adv Energy Mater.* **2020**, *10*, 1903589. [[CrossRef](#)]
81. Fan, W.; Liu, F.; Liu, Y.; Wu, Z.; Wang, L.; Zhang, Y.; Huang, Q.; Fu, L.; Wu, Y. A High Voltage Aqueous Zinc–Manganese Battery Using a Hybrid Alkaline-Mild Electrolyte. *Chem. Commun.* **2020**, *56*, 2039–2042. [[CrossRef](#)] [[PubMed](#)]
82. Shen, Z.; Tang, Z.; Li, C.; Luo, L.; Pu, J.; Wen, Z.; Liu, Y.; Ji, Y.; Xie, J.; Wang, L.; et al. Precise Proton Redistribution for Two-Electron Redox in Aqueous Zinc/Manganese Dioxide Batteries. *Adv Energy Mater.* **2021**, *11*, 2102055. [[CrossRef](#)]
83. Samanta, P.; Ghosh, S.; Bolar, S.; Kolya, H.; Kang, C.-W.; Samanta, P.; Chandra Murmu, N.; Kuila, T. Acid–Alkaline Electrolyte for the Development of High-Energy Density Zn-Ion Batteries through Structural Modification of MoS₂ by MnO₂. *ACS Appl. Energy Mater.* **2022**, *5*, 8581–8591. [[CrossRef](#)]
84. Xu, Q.; Xie, Q.-X.; Xue, T.; Cheng, G.; Wu, J.-D.; Ning, L.; Yan, X.-H.; Lu, Y.-J.; Zou, Z.-L.; Wang, B.-P.; et al. Salt Bridge-Intermediated Three Phase Decoupling Electrolytes for High Voltage Electrolytic Aqueous Zinc-Manganese Dioxides Battery. *Chem. Eng. J.* **2023**, *451*, 138775. [[CrossRef](#)]
85. Cui, Y.; Zhuang, Z.; Xie, Z.; Cao, R.; Hao, Q.; Zhang, N.; Liu, W.; Zhu, Y.; Huang, G. High-Energy and Long-Lived Zn–MnO₂ Battery Enabled by a Hydrophobic-Ion-Conducting Membrane. *ACS Nano* **2022**, *16*, 20730–20738. [[CrossRef](#)] [[PubMed](#)]
86. Liu, C.; Chi, X.; Yang, C.; Liu, Y. High-Voltage Aqueous Zinc Batteries Achieved by Tri-functional Metallic Bipolar Electrodes. *Energy Environ. Mater.* **2023**, *6*, e12300. [[CrossRef](#)]

Disclaimer/Publisher's Note: The statements, opinions and data contained in all publications are solely those of the individual author(s) and contributor(s) and not of MDPI and/or the editor(s). MDPI and/or the editor(s) disclaim responsibility for any injury to people or property resulting from any ideas, methods, instructions or products referred to in the content.

Appendix 2

2. pielikums

R. Durena, N. Griscenko, L. Orlova, M. Bertins, A. Viksna, M. Iesalnieks, A. Zukuls

Synthesis, structure, and electrochemical performance of Bi-induced stabilization of MnO₂ cathodes for use in highly acidic aqueous electrolytes (pH <2)

Journal of Alloys and Compounds, 1010, 2025, 177904.

DOI: 10.1016/j.jallcom.2024.177904



Synthesis, structure, and electrochemical performance of Bi-induced stabilization of MnO₂ cathodes for use in highly acidic aqueous electrolytes (pH < 2)

Ramona Durena^a, Nikita Griscenko^a, Liga Orlova^a, Maris Bertins^b, Arturs Viksna^b, Mairis Iesalnieks^a, Anzelms Zukuls^{a,*}

^a Institute of Materials and Surface Engineering, Faculty of Natural Sciences and Technology, Riga Technical University, Paula Valdena Street 7, Riga LV-1048, Latvia

^b Faculty of Chemistry, University of Latvia, Jelgavas 1, Riga LV-1004, Latvia

ARTICLE INFO

Keywords:

MnO₂ cathode
Acidic electrolyte
Bi³⁺ ion doping
Capacity retention
Mn³⁺ stabilisation
Capacity fading

ABSTRACT

MnO₂ cathode materials are widely studied in alkaline and neutral aqueous electrolytes. In these mediums, the MnO₂ cathode shows suboptimal performance limited by dissolution and electrochemically inactive compound formation, leading to capacity fading. This study explores the enhancement of MnO₂ cathode performance through Bi³⁺ ion doping (0, 1, 2.5, 5, and 10 mol%) in a highly acidic electrolyte (pH < 2). By incorporating up to 10 mol% Bi ions into the MnO₂ structure, we significantly improved specific capacity and capacity retention stability. Energy-dispersive X-ray spectroscopy (EDX) analysis revealed a uniform dispersion of Bi³⁺ ions throughout the MnO₂ cathode after electrochemical cycling, contributing to performance enhancements. X-ray photoelectron spectroscopy (XPS) results indicated that Bi³⁺ ion concentration from 1 to 10 mol% stabilises Mn³⁺ within the MnO₂ lattice. Also, Bi³⁺ ion doping promotes the formation of a 2 × 2 tunnel structured α-MnO₂ phase. Electrochemical impedance spectroscopy results demonstrated a reduction in double-layer and overall bulk capacitance. These findings suggest that Bi³⁺ ion doping effectively enhances MnO₂ electrochemical performance and could enhance its use in aqueous metal-ion batteries.

1. Introduction

As the world faces more severe climate change, innovative and advanced solutions are essential to tackle the associated challenges. Transitioning to green energy is a critical step already underway. However, a significant drawback of green energy is its production inconsistency. To mitigate this issue, storing excess energy in energy storage systems, such as rechargeable batteries, is a promising approach [1–5].

Currently, Li-ion batteries (LIBs) dominate the rechargeable battery market due to their long-lasting performance and high operating voltage [6–9]. However, the rapid increase in global lithium consumption and production suggests that demand for LIBs could surpass supply within the next decade [10], potentially leading to a production crisis [11]. One approach to mitigate potential LIB shortages is to promote the recovery of critical components [12]. Nonetheless, recycling LIBs possess significant hazards, including thermal runaway, toxic gas emissions, electrolyte leakage, and heavy metal pollution [13–16]. Introducing an

alternative or complementary system to LIBs could help address these challenges [17,18]. A great candidate to supplement the current rechargeable battery market is various metal-ion batteries [19–23], dual-electrolyte batteries (where the cathode is operated in an acidic medium and anode in an alkaline medium) [24–26], and flow batteries [27–30].

The MnO₂ cathode paired with a metal-ion anode could potentially be implemented in the secondary-type (rechargeable) battery market, as the MnO₂ and Zn metal combination already dominates the primary (non-rechargeable) battery market [31]. The MnO₂ cathode offers several promising properties, including the abundance of Mn compounds [32], relatively high reaction potential of 1.23 V vs SHE (standard hydrogen electrode) in acidic electrolyte [33,34], the high theoretical specific capacity of 308 mAh/g (for one electron transfer) and 616 mAh/g (for two-electron transfer) [35–37], and overall lower environmental impact compared to LIBs [38]. Additionally, the ability of Mn to exhibit multiple valence states leads to the formation of diverse polymorphic modifications, such as α-, β-, δ-, γ-, and λ-MnO₂, which vary

* Corresponding author.

E-mail address: anzelms.zukuls@rtu.lv (A. Zukuls).

<https://doi.org/10.1016/j.jalcom.2024.177904>

Received 18 September 2024; Received in revised form 26 November 2024; Accepted 30 November 2024

Available online 2 December 2024

0925-8388/© 2024 Elsevier B.V. All rights are reserved, including those for text and data mining, AI training, and similar technologies.

in tunnel and interlayer sizes. These polymorphs comprise $[\text{MnO}_6]$ octahedra that connect through shared edges [39–41]. For example, birnessite, $\delta\text{-MnO}_2$, forms a layered structure with an interlayer spacing as large as 7 Å. Differently arranged hollandite, $\alpha\text{-MnO}_2$, the structure forms tunnels with dimensions around 4.6 Å, creating combinations of (1 × 1) and (2 × 2) tunnel spaces. Another form is the densely packed pyrolusite, $\beta\text{-MnO}_2$, which forms smaller (1 × 1) tunnels with a size of 1.89 Å [42,43]. Such variable structural properties of polymorphs have an outcome on their thermal stability, and it can be arranged in descending order in the following row: $\beta > \alpha > \gamma > \delta \approx \lambda$ [44]. The differences in crystalline structures of MnO_2 polymorphs also play a significant role in the electrochemical behaviour of cathode materials. As mentioned in the literature, the specific capacity, comparing different polymorphs, fades in the following order: $\alpha > \delta > \beta$ [45].

Despite the potential electrochemical value of the MnO_2 cathode, the structure tends to destabilise and lose integrity during cycling [46], gradually converting into lower-capacity compounds [39]. Another significant issue is the dissolution of MnO_2 during cycling due to the Jahn-Teller distortion effect [47], leading to the loss of the cathode active mass and decreased capacity [48]. Introducing heteroatoms into the electrode structure is a potential solution to these problems [49], thus enhancing the electrochemical properties. For example, doping with Co ions can stabilise the structure [50–52], and adding Mo ions can induce lattice defects for improved performance [53–55]. Also, introducing Bi^{3+} ions into the MnO_2 structure offers several benefits. Bi^{3+} ion additives tighten the band gap, boosting conductivity [56] and improving the reversibility of dissolution/deposition processes by enlarging lattice spacing with Bi^{3+} ions [31,56–59]. Furthermore, bismuth is considered a relatively “green” heavy metal [60].

Although MnO_2 cathode properties have been widely investigated in alkaline [61–64] and neutral to mildly acidic conditions [65–68], little to no investigation has been performed about the MnO_2 characteristics in highly acidic electrolytes. This is primarily because previous research has focused on single-electrolyte systems coupled with metal anodes, which tend to corrode in highly acidic conditions. However, at such low pH values, MnO_2 cathodes can achieve higher potential [69,70] and also offer the possibility of enhanced performance of the cathode for use in dual-electrolyte batteries, where the MnO_2 cathode is placed in acidic electrolyte and anode in alkaline [24–26]. Therefore, this article investigated the performance of Bi-doped MnO_2 cathodes at very low pH values ($\text{pH} < 2$).

In this paper, we report the improvement of hydrothermally synthesised MnO_2 cathode by doping with Bi^{3+} ions. The doping concentrations were set at 0, 0.5, 1, 2.5, 5, and 10 mol% Bi. The morphology and phase composition of the obtained powders were analysed. Furthermore, cathodes were assembled from these powders, and their electrochemical performance was tested. According to MnO_2 Pourbaix diagrams in acidic electrolytes under cathodic potentials, MnO_2 forms the pyrolusite phase; therefore, the results were compared to a commercially available pyrolusite MnO_2 [71,72]. The results indicated increased cycling stability and capacity for the Bi-doped samples. Moreover, Bi^{3+} ion doping decreased the charge transfer resistance between individual particles of the cathode material. This study will help advance the development of dual-electrolyte and flow battery cathode materials for new energy storage devices.

2. Materials and methods

2.1. Raw materials

All chemicals were purchased from Sigma Aldrich and used without further purification. Commercially available MnO_2 was utilised as a reference cathode active material and, according to the datasheet, consisted of $\beta\text{-MnO}_2$ (pyrolusite). To prepare Bi-doped MnO_2 samples, KMnO_4 and BiCl_3 were used. The electrolyte was prepared from H_2SO_4 and MnSO_4 . Cathode electrode ink was prepared by adding

polyvinylidene fluoride (PVDF) (MW ~530,000) and N-Methyl-2-pyrrolidone (NMP) to the obtained samples. Vulcan XC72 Carbon Black (CB) was employed and purchased from Nanografi as a synthesis and conductivity-enhancing additive. Also, 0.05 mm thick graphite paper (RERAS, China) was used as a conductive carbon substrate.

2.2. Synthesis of Bi-doped MnO_2 powders

Bi-doped MnO_2 powders were prepared using the hydrothermal synthesis method, which is well-known in the literature for obtaining nanosized structures [73–76]. Bi-doping concentrations were set at 0, 1, 2.5, 5, and 10 mol%. KMnO_4 and BiCl_3 were used as precursors, and the total Mn+Bi molar amount was kept constant (0.0035 mol). Additionally, 0.042 g of CB was used as a conductivity-enhancing additive. When the calculated values of all ingredients were combined, an additional 0.7 mL of 10 % H_2SO_4 solution and the necessary amount of deionised water was added to reach 35 mL total volume of synthesis solution. The obtained mixture was magnetically stirred for 1 h. Then, the solution was transferred to a 50 mL Teflon-lined stainless-steel autoclave and heated in the oven for 12 h to obtain cathode active material. Centrifugation (three times) using deionised water as a solvent was utilised to purify the obtained materials further. The precipitate was dried at 80 °C for 24 h and then was ground using a pestle and mortar. The obtained material was compared with the purchased MnO_2 (pyrolusite). Powder of MnO_2 was mixed with CB in a mass ratio of 13:5 and ball milled (Retsch PM100) at 200 rpm for 2 h to homogenise the sample. Previously mentioned prepared samples were further utilised for cathode ink preparation.

2.3. Preparation of cathodes

Cathode material slurry was prepared by adding additional CB to powder samples to reach a mass ratio of 13:5 (MnO_2 :CB). During mixing NMP/PVDF (mass ratio 9:1), a solution was added to a weight ratio 1:1 (cathode powder: PVDF solution). To obtain homogenous spreadable ink, additional NMP was added, reaching MnO_2 to NMP ratio around 1:1.8. Homogenous inks were used to create cathode coatings onto graphite paper using a 25 μm size manual doctor blade coating applicator. Coatings were dried in the air overnight to evaporate excess NMP. Obtained coatings were used for further measurements.

2.4. Characterization

Crystallographic sample characterisation was done by Rigaku Ultima+ X-ray diffractometer (XRD) using a $\text{Cu-K}\alpha$ ($\lambda = 0.154056$ nm) radiation source. A scanning speed of 2° min^{-1} at a 2 θ angle range from 5° to 80° at 40 kV and 20 mA was used to characterise obtained samples. Results were analysed using the PDF 4 + database.

Renishaw In-ViaV727 Raman spectrometer was used to study obtained samples at room temperature before and after cyclic voltammetry (CV) measurements under 500x magnification in a backscattering geometry. Ar^+ green laser (wavelength $\lambda = 514.5$ nm, grating – 1200 mm^{-1} , power – 10 mW) with an exposure time of 10 s was utilised to obtain the Raman spectra.

FEI Nova NanoSEM 650 scanning electron microscope (SEM) was utilised for the surface morphology study. An acceleration voltage of 15 kV was used to characterise the samples. The atomic composition of the cathode materials was evaluated by the energy-dispersive X-ray spectroscopy (EDX) using an Apollo X-SDD detector.

Inductively coupled plasma mass spectrometry (ICP-MS) analysis was performed to determine the molar ratio of atoms in the obtained samples. A full description of the preparation and analysis procedure is given in our previous work [55].

X-ray photoelectron spectroscopy (XPS) was used to study and compare synthesised and fully charged/discharged cathode materials. A 500 μm spot size with a monochromatic $\text{Al K}_1\alpha$ anode source for the

sample characterisation was utilised. The carbon peak at 248.8 eV was used as a calibration reference, and Avantage 5.9925 software was applied for data analysis.

2.5. Electrochemical testing

The electrochemical investigation was performed using Potentiostat-Galvanostat Autolab PGSTAT302N. Measurement cell "TSC Surface" (from rhd instruments) was used for CV measurements in a 3-electrode system. The electrode configuration consisted of an Ag/AgCl (3 M KCl) reference electrode, platinum rod counter electrode, and graphite paper-coated MnO₂ sample as a working electrode. A 1 mL mixture of 0.5 M H₂SO₄ and 0.1 M MnSO₄ solution (pH = 0.7) was used as an electrolyte. To characterise samples, CV measurements with multiple scan speeds (from 2 mV/s to 100 mV/s) were performed in a potential window of 0.7 V to 1.6 V. At the start of each CV measurement, 10 stabilisation or cathode forming cycles were performed at a scan speed of 75 mV/s and for each scan speed minimum of 10 cycles were performed to reach a stabilisation. Thus, each cathode performed no less than 110 cycles. Electrochemical impedance spectroscopy (EIS) was used to study electrode parameters further. A small perturbation voltage (+/-150 mV) in the 10 kHz to 0.1 Hz frequency range was applied to characterise prepared electrodes. For data evaluation and equivalent scheme analysis, NOVA 2.1 software was used. A galvanostatic charge-discharge (GCD) rate study was performed to evaluate cathode performance. The prepared MnO₂ cathodes were tested against the carbon paper electrode in the two-electrode setup. A glass fibre filter paper was used as a separator and electrolyte holder. A 200 μ L solution of 0.5 M H₂SO₄ and 0.1 M MnSO₄ was used as the electrolyte. The charge/discharge potential was limited to 0 – 1.3 V, and the measurements were carried out at different current densities.

3. Results and discussion

In this work, MnO₂ samples were hydrothermally synthesised for 12 hours and doped with Bi ions. The Bi³⁺ ion dopant concentrations in the samples were set at 0, 1, 2.5, 5, and 10 mol%. In addition, all synthesised samples were compared with commercially available MnO₂ powder, which, according to the supplier, is in the pyrolusite crystalline phase. XRD measurements show that the commercially available

pyrolusite contains this phase, and it also has a fine polycrystalline structure with small crystallites, which appear as broad peaks in obtained XRD spectra. The XRD results for all powder samples are shown in Fig. 1a. The results indicate that the synthesised samples comprise a two-phase mixture – δ -MnO₂ (Mn₇O₁₃·5 H₂O) and α -MnO₂ (K₂·xMn₈O₁₆). In the XRD spectrum, δ -MnO₂ peaks appear at 12.2° (110), 24.6° (221), and 65.5° (457), while merged peaks at 36.4° (060) and 38.6° (252) overlap with those of α -MnO₂. Also, overlapping α -MnO₂ peak groups can be seen around 12° corresponding to *hkl* planes (10 $\bar{1}$), (101) overlapping with δ -MnO₂; around 29° corresponding to (30 $\bar{1}$), (301), (10 $\bar{3}$), (103); around 37° corresponding to (21 $\bar{1}$), (11 $\bar{2}$), (211), (112) overlapping with δ -MnO₂; around 42° corresponding to (310), (204), (013); around 60° corresponding to (51 $\bar{2}$), (512), (215); individual peaks at 65.0° (020) overlapping with δ -MnO₂ and at 68.8° (51 $\bar{4}$), 70.0° (415) can be seen. In addition, a small amount of BiOCl is seen in all Bi-doped samples, becoming more distinct in the highly doped samples of 5 mol% Bi³⁺ and 10 mol% Bi³⁺ with characteristic peaks at 25.8°, 32.4°, 33.4°, 46.6°, 49.6°, 54.0°, and 58.6° corresponding to *hkl* planes (101), (110), (102), (200), (113), (211), and (212). Overall, for sample without Bi³⁺ ion doping, peaks corresponding to the δ -MnO₂ phase are the most pronounced, while for samples with Bi³⁺ ion doping, these peaks are reduced, for example, the peak at 24.6°. However, by introducing 2.5 mol% to 10 mol% Bi³⁺ ion doping, broad peaks appear at around 29° and 42°, corresponding to the α -MnO₂ phase. This indicates that Bi³⁺ ion doping decreases layer structured δ -MnO₂ phase formation and promotes α -MnO₂, which exhibits a 2 × 2 tunnel structure. As Bi³⁺ ions are much larger than Mn⁴⁺ ions (represented in Fig. 1c), incorporating Bi³⁺ ions into the MnO₂ structure leads to lattice distortion, causing an expansion and thus opening up the tunnel structures. In these tunnel structures, Bi³⁺ ions act as pillars in the middle of the tunnels, as shown in [56,58,77], and prevent structural collapse to β -MnO₂ [78,79]. A similar phenomenon with Bi³⁺ ions and other larger ions has also been observed elsewhere in the literature [80–82].

Also, in Raman results (Fig. 1b), the signals corresponding to MnO₂ can be seen. No additional Raman signals corresponding to BiOCl are visible. Otherwise, the Raman results of the synthesised samples indicate the same as XRD results – the samples consist of α - and δ -MnO₂ mixture [83–88]. Three peaks can be distinguished for all the samples at 180, 570, and 640 cm⁻¹. The most intensive 640 cm⁻¹ peak is assigned to

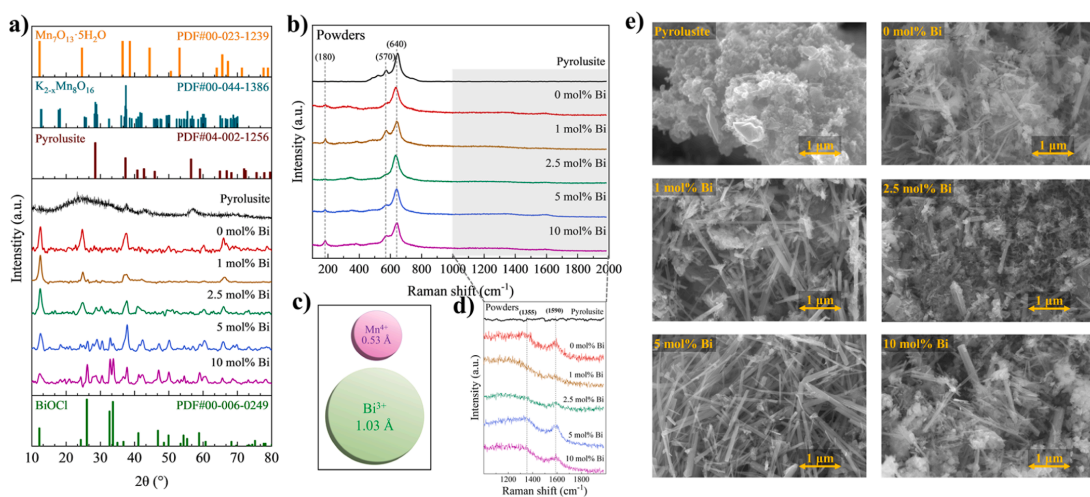


Fig. 1. Results of pyrolusite, undoped, and Bi-doped MnO₂ powder samples: a) XRD, b) Raman results, c) comparison of ion size in solution; e) expanded Raman results of the carbon D and G bands, and d) SEM images.

symmetric Mn–O stretching vibration (ν_1) in $[\text{MnO}_6]$ octahedral. Similarly, a 570 cm^{-1} peak is assigned to the deformation modes of the metal-oxygen chain of Mn–O–Mn in the MnO_2 octahedral lattice [83–86]. The Raman band at 180 cm^{-1} in MnO_2 is generally attributed to $\alpha\text{-MnO}_2$ (hollandite-type) and $\beta\text{-MnO}_2$ (rutile-type) vibrational modes due to variations in crystal symmetry and Mn oxidation states [84, 87–89]. This band is also associated with the foreign cations intercalated in the $\alpha\text{-MnO}_2$ tunnels [56]. From the XRD results mentioned above, we also observe that K^+ ions are present in the obtained crystal structure. For the pyrolusite sample, peaks at $450\text{--}550\text{ cm}^{-1}$ and 740 cm^{-1} indicate the presence of crystals with multiple orientations [90] correlating with the polycrystalline morphology observations of pyrolusite in the XRD. Also, small peaks from carbon D and G bands (Fig. 1d) can be observed at 1355 and 1590 cm^{-1} , attributable to the carbon powder added to the synthesis mixture [91]. Consequently, carbon signals are not visible in the spectrum of the pyrolusite powder as no carbon was added to the sample in this stage.

SEM images were obtained to investigate the morphology of the samples further. Fig. 1e and Figure S1 show that all the synthesised samples contain clusters of larger and smaller needles typical of different MnO_2 polymorphs [92–94]. However, the pyrolusite sample consists of clusters of rounded-shaped particles. In addition, EDX analyses were carried out for the synthesised samples by analysing 3 points in each sample. The mean results are represented in Table 1. The Mn:Bi ratio, according to EDX results, is lower than expected because only part of Bi^{3+} ions are incorporated into the MnO_2 structure. However, the other part is precipitated separately as BiOCl . Moreover, this aligns with XRD results, which show that two phases can be separated at higher doping levels. These findings are also confirmed by ICP-MS measurements (Table 1) of the synthesised samples, which show that the amount of Mn: Bi mol% introduced correlates with the theoretically expected ratio. The results of ICP-MS show a more accurate ratio of all samples compared to EDX, as a larger quantity of the test sample is dissolved and analysed.

To determine the oxidation states of elements, XPS measurements were performed for obtained Bi-doped MnO_2 powders and pyrolusite MnO_2 . The most noticeable changes in the survey spectra (Fig. 2a) can be observed at $158\text{--}165$, 530 , and $640\text{--}656\text{ eV}$, corresponding to Bi 4f, O 1s, and Mn 2p binding energy regions. Also, from the Bi 4f spectrum (Fig. 2b), it can be seen that increasing the Bi^{3+} ion amount in MnO_2 increases the binding energy spectra intensity, confirming the presence of Bi^{3+} ions in the obtained samples. Additionally, valence-band XPS spectra (Fig. 2c) reveal that by increasing the Bi-ion amount, the valence band shifts towards a lower binding energy region, also shifting the Fermi edge. A similar shift can be observed in an $\alpha\text{-MnO}_2/\text{BiOI}$ mixed system [95]. According to the literature, this shift is closely related to material conductivity and is influenced by the introduction of additional ions [96]. Looking at the normalised high-resolution and subtracted spectra of Mn 2p (Fig. 2d and e), a shift of the peak towards the formation of the Mn^{3+} ions can be observed, which becomes much more pronounced as the concentration of Bi^{3+} ion amount increases. Subtracted normalised intensity spectra (Fig. 2e) show that by adding the Bi^{3+} ions, the Mn^{4+} ion signal intensity decreases, however, the Mn^{3+} ion signal increases. Similar observations about Mn^{3+} and Mn^{4+} valence state formation in an almost identical synthesis process and different metal oxide systems are discussed in the literature [97,98]. The ions

introduced into the obtained MnO_2 crystal structure stabilise the metastable Mn^{3+} ions, which are typically disproportionate in the oxide crystal lattice [99]. In the normalised spectra of O 1s (Fig. 2f), as the concentration of Bi^{3+} ions increases, the amount of hydroxyl groups and adsorbed water on the sample surface also increases. According to the literature, binding energy located at $531\text{--}535\text{ eV}$ is closely related to surface hydroxyl groups, water, or organic contaminants containing oxygen atoms [100]. In addition, all Bi^{3+} ions found in the MnO_2 structure have a 3+ oxidation state (Fig. 2f and h-k). Increasing the concentration of Bi^{3+} ions, according to subtracted normalised Bi 4f intensity spectra, increases the amount of BiOCl and Bi_2O_3 in the crystalline structure compared to the 1 mol% Bi^{3+} ion sample. Literature suggests that BiOCl can also be identified in other systems [101,102]. Additional peaks located at $291\text{--}296\text{ eV}$ can be observed for the synthesised samples (Figure S2) and can be attributed to the K 2p binding energy of potassium. This suggests that the K^+ ions, even after sample washing, remain and take part in stabilising the obtained MnO_2 structure and confirm XRD results (Fig. 1a). Similar findings were made in our previous work [55]. A small peak for the samples with higher Bi^{3+} ion amount is also observed in the $198\text{--}199\text{ eV}$ region (Figure S2), corresponding to the binding energy of Cl 2p [103], further confirming the presence of BiOCl observed in the XPS and XRD results.

CV tests were performed on prepared cathodes (denoted by the abbreviation C-x mol% Bi) in a highly acidic electrolyte ($\text{pH} = 0.7$) from previously characterised powder samples. The resulting graphs after electrode stabilisation are shown in Fig. 3. During the charge/discharge of MnO_2 , the oxidation state of manganese changes from Mn^{2+} to Mn^{4+} , and solid MnO_2 dissolves into electrolyte as Mn^{2+} ions and water, according to reaction (1) [104].



Two electrons interact in this process; thus, two oxidation and reduction peaks should be visible in the graphs. However, only one peak for each process can be seen at the given scan rate. The influence of the scan rate can explain the absence of redox peaks. The results show that the shape and peak location of the redox reaction change with the scan rate. It can be assumed that the peak of the first electron transition is stable at lower speeds. Also, as the scan rate increases, the differences between the transitions merge and the second peak, or the combination of the two electrons, becomes more pronounced. Another reason for the inseparability of CV peaks could be attributed to the involvement of Bi^{3+} in the redox process. However, a similar picture is also observed between samples without Bi^{3+} addition. This suggests that the influence of Bi^{3+} ions on MnO_2 in the electrochemical process cannot be verified. In addition, the same CV test was also conducted in a $0.5\text{ M H}_2\text{SO}_4$ electrolyte for the cathode material, containing only BiOCl as the active material. As shown in Figure S3, no distinct oxidation or reduction peaks are observed, indicating capacitor-like characteristics. This suggests that BiOCl does not participate in the electrochemical reaction, with only MnO_2 reactions visible in Fig. 3.

At consistent scan rates across all samples (Figure S4), a noticeable trend in the effect of Bi^{3+} ions on electrochemical MnO_2 deposition is observed. During slower scan rates, the Bi^{3+} ions containing samples exhibit higher charging currents than the undoped and pyrolusite samples. Notably, the sample doped with 5 mol% Bi^{3+} ions demonstrates the highest charging current. However, as the scan rate increases, the presence of Bi^{3+} ions begins to impede MnO_2 deposition, as evidenced by the CV curves. At high CV scan rates, the diffusion of Mn^{2+} ions to the cathode becomes increasingly restricted due to the additional Bi^{3+} ions. This limitation arises from the complex interactions between the ions, which slow down the diffusion process, particularly at faster scanning rates [105]. The presence of Bi^{3+} ions during charging allows them to be successfully incorporated into the MnO_2 structure, as can be seen in the evaluation of SEM and EDX measurement results discussed further.

To quantitatively assess the resulting cathodes, previously obtained

Table 1
 Bi^{3+} ion content in the samples, according to ICP-MS and EDX results.

Sample	According to synthesis, mol%	ICP-MS, mol%	EDX, mol%
Pyrolusite	0.0	0.0	0.0
0 mol% Bi	0.0	0.0	0.0
1 mol% Bi	1.0	1.0	0.4 ± 0.11
2.5 mol% Bi	2.5	2.4	1.9 ± 1.06
5 mol% Bi	5.0	5.1	2.8 ± 2.36
10 mol% Bi	10.0	10.5	6.9 ± 1.72

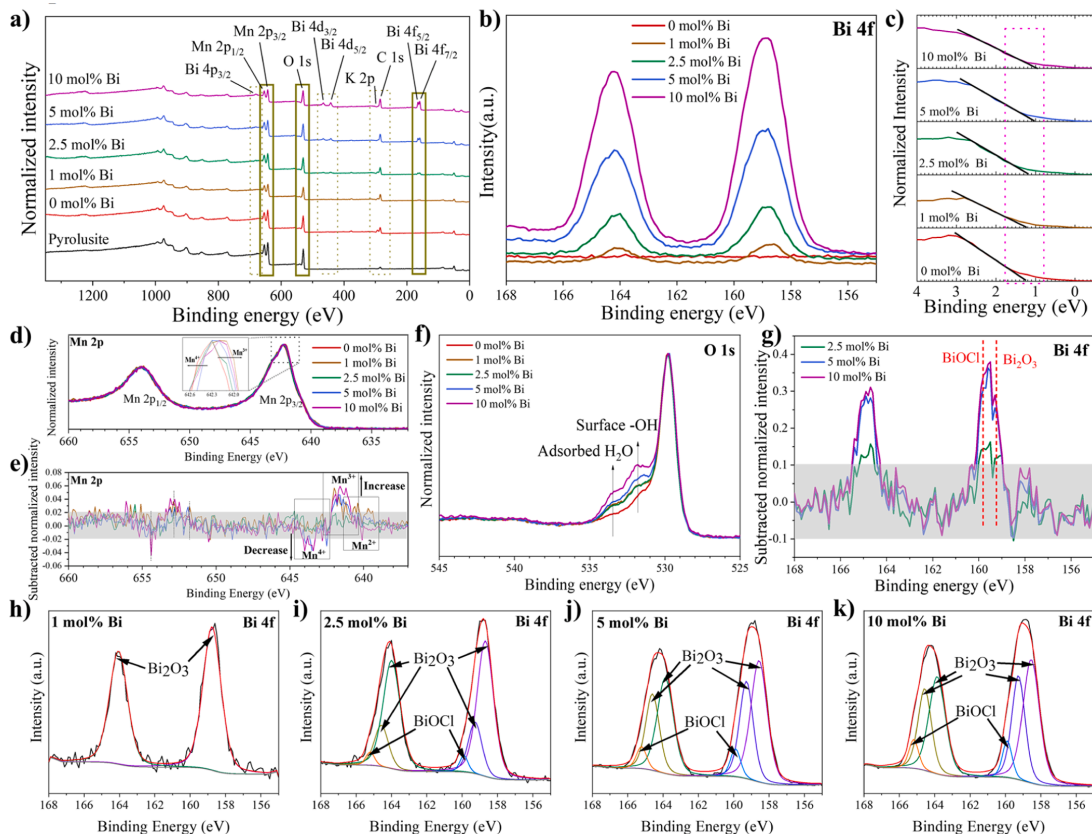


Fig. 2. XPS results for synthesised Bi-doped MnO_2 samples: a) survey spectra, b) Bi 4f comparison, c) valence-band, d) normalised and e) subtracted normalised Mn2p, f) normalised O 1s, f) subtracted normalised Bi 4f and h-k) varying Bi^{3+} amount Bi 4f; high-resolution spectra.

CV plots were integrated and used to calculate the specific capacity of each cathode. The obtained results are shown in Fig. 4a. The best specific capacity result and highest peak current were demonstrated by the C-5 mol% Bi sample at a scan rate of 2 mV/s. The effect of Bi-doping is more noticeable at low scan rates, as the specific capacity of all the synthesised material cathodes exceeds the specific capacity of the pyrolusite MnO_2 material cathode. However, increasing the scan rate decreases the specific capacity, and almost no difference is observed between the cathodes of the pyrolusite, undoped, and Bi-doped materials. This can be explained by the limited ion diffusion rate in the electrolyte at higher scan rates. Thus, the value of capacity begins to be determined by ion diffusion rather than the characteristics of the cathode material.

Specific discharge capacities at various current densities obtained from GCD measurements can be seen in Fig. 4b (more detailed in Figures S5 and S6). In the first 5 cycles, material activation and cathode stabilisation occur. For pyrolusite and 0 mol% Bi samples, this stabilisation requires all 5 cycles to stabilise fully. In contrast, samples with added Bi^{3+} ions achieve stabilisation more quickly, within 2–3 cycles. In the subsequent 15 cycles, increasing the current density from 0.25 to 1.0 A/g, the cathode made of pyrolusite MnO_2 shows a similar capacity to the 0–5 mol% Bi-doped cathodes. On the other hand, by reducing the current density to the initial 0.25 A/g, cathode materials with a higher Bi^{3+} content show a more successful capacity recovery capability. Moreover, the sample with the significantly higher amount of Bi^{3+} ions –

10 mol% indicates approximately 25% higher capacity at all current densities.

Raman analysis was carried out on the cathode materials before and after CV to examine whether the cathode preparation process has altered the MnO_2 phase and how cycling has affected it. As seen in Fig. 4d, all the cathodes prepared from hydrothermally synthesised samples exhibit peaks at 180, 570, and 640 cm^{-1} , as in Fig. 1b. However, the pyrolusite MnO_2 cathode exhibits one peak at 640 cm^{-1} . This indicates that the $\alpha\text{-MnO}_2$ phase of hydrothermally synthesised samples and the $\beta\text{-MnO}_2$ phase of pyrolusite were preserved in the cathode formation process. In addition, two additional peaks at 1355 and 1590 cm^{-1} can be seen. Both peaks correspond to the disordered (D) and graphitic (G) bands of CB [107–109], respectively, which were added during MnO_2 synthesis and the cathode preparation process to increase the cathode conductivity. After CV measurements, the D and G bands of CB cannot be seen in Raman spectra. During CV measurements, as MnO_2 cyclically dissolves and Mn^{2+} oxidises, the involved CB particles are uniformly covered with a layer of MnO_2 . This MnO_2 layer covers the CB in the charged cathode state and inhibits Raman signals of carbon. Moreover, three peaks associated with $\alpha\text{-MnO}_2$ can be seen at 520, 570, and 640 cm^{-1} for all the cathode samples after CV measurements. The Raman peaks at 520 cm^{-1} are associated with $\alpha\text{-MnO}_2$. This mode can vary slightly in frequency based on the symmetry and the specific oxidation state of manganese present in the sample. The peak at 570 cm^{-1} is typically associated with the symmetric stretching mode of Mn-O bonds within the MnO_6

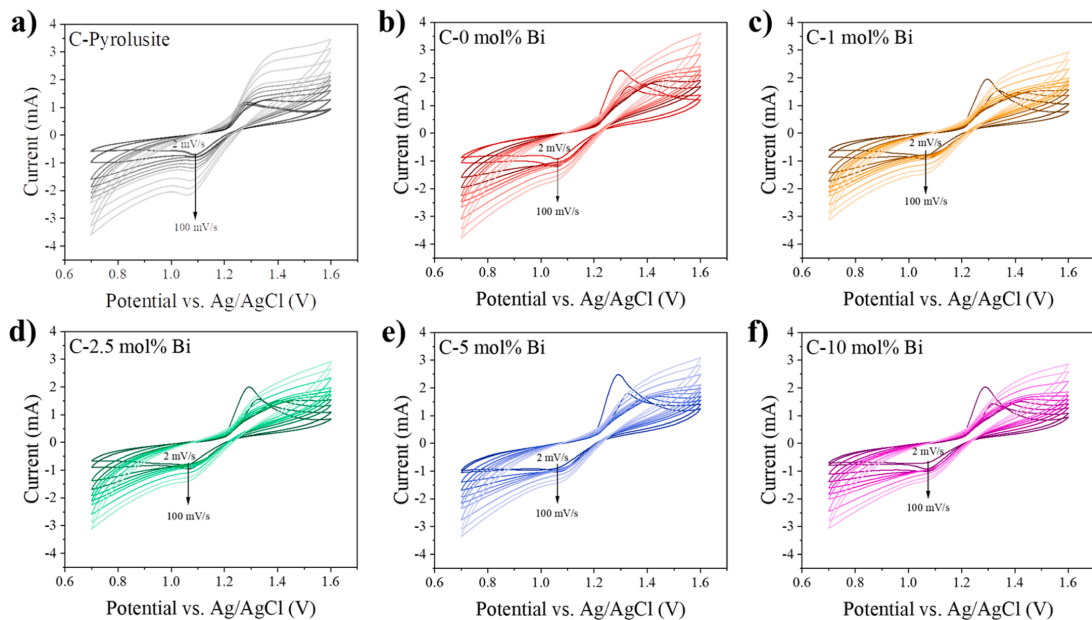


Fig. 3. CV plots for a) pyrolusite, b) undoped, and c) – f) Bi-doped MnO_2 cathode samples at scan rates 2, 5, 10, 15, 20, 25, 30, 50, 75, and 100 mV/s [106].

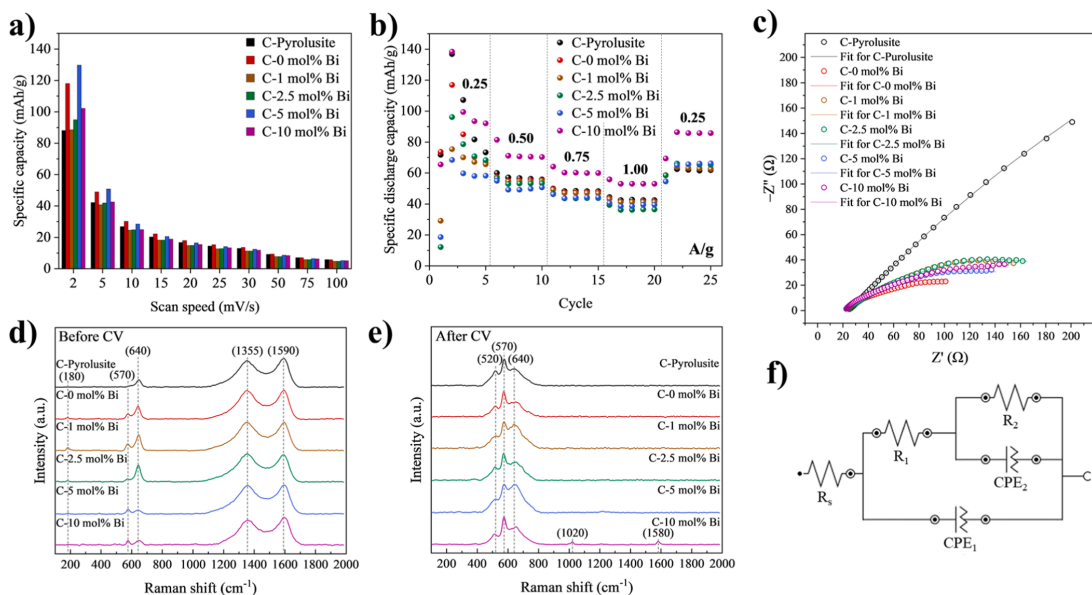


Fig. 4. Results of pyrolusite, undoped, and Bi-doped MnO_2 cathode samples: a) specific capacities from CV measurements at various scan speeds; b) discharge capacities from GCD measurements at various current densities; c) Nyquist plots of measured and fitted data; Raman spectroscopy results d) before and e) after CV; f) equivalent circuit scheme.

octahedral and is observed in $\alpha\text{-MnO}_2$. This specific mode reflects the bond strength and symmetry within the crystal lattice. Meanwhile, the peak at 640 cm^{-1} is sensitive to the manganese oxidation state, with variations in frequency reflecting different structural distortions. This

peak can often indicate the presence of phases with higher Mn^{3+} concentrations that impact the vibrational bands differently from other MnO_2 forms. The absence of the 180 cm^{-1} mode is due to the formation of polycrystalline structured particles on the entire electrode surface.

This mode usually defines a longer-range structural vibration and arises from the bending of the overall octahedral structure [90].

To confirm the growth and dissolution of MnO_2 during GCD measurement according to reaction (1), the cycled samples in the charged and discharged states were also analysed by Raman spectroscopy measurements (Figure S7). The results of discharged samples (Figure S7a) show distinct C and G bands of carbon. However, peaks corresponding to MnO_2 are almost not visible. On the other hand, samples within a charged state (Figure S7b) show only MnO_2 peaks at 640 and 570 cm^{-1} , and carbon bands are suppressed due to MnO_2 redeposition, which also confirms the findings of Raman results (Fig. 4e) and SEM images (Fig. 5) after CV measurements. This indicates that both the synthesised and the pyrolusite MnO_2 samples undergo a phase transition to the $\alpha\text{-MnO}_2$ structure. During the discharge process, MnO_2 dissolves into the electrolyte and, upon charging, redeposits as the $\alpha\text{-MnO}_2$, demonstrating the phase change while cycling according to the reaction (1).

Fig. 4c represents the Nyquist plots of all sample impedance after CV measurements. With a 10 mV sinusoidal excitation signal in the frequency range from 0.1 Hz to 10 kHz , the imaginary part of the resistance is plotted against its real component. The Nyquist plots show that the measured impedance spectrum consists of a small depressed arc at high frequencies and a larger one at low frequencies. The obtained impedance results were also analysed with NOVA 2 software, and fitted curves according to the equivalent scheme depicted in Fig. 4f were obtained. The scheme consists of resistances – R_s , R_1 , and R_2 – and constant phase elements – CPE_1 and CPE_2 – parallel to the corresponding resistances. The values of equivalent scheme components are shown in Table 2. The ohmic resistance of electrolyte corresponds to component R_s , and for all the samples, is around $22 - 23\ \Omega$, indicating that all the half-cells were constructed fairly similarly and no poor electrical contacts were made. Resistance R_1 and constant phase element CPE_1 correspond to charge transfer resistance between electrode and electrolyte and double-layer capacitance. The fitted values suggest that synthesising the cathode active material can decrease the double-layer capacitance with the most significant decrease for a 10 mol\% Bi -doped MnO_2 sample. These observations are related to the increase in surface hydroxyl groups visible in the XPS O1s spectra (Fig. 2f). Changes in the surface hydroxyl group

amount determine electrode wettability properties and affect the interaction between the electrode surface and the electrolyte, thus changing the charge transfer resistance. However, the charge transfer resistance remains similar for all samples, with some changes in samples with lower Bi^{3+} doping levels.

The other parallel components – resistance R_2 and constant phase element CPE_2 – correspond to resistance between individual cathode particles and bulk capacitance. According to the fitted values, the synthesised samples have significantly lower resistance between individual particles. Comparing the pyrolusite and 0 mol\% synthesised samples, the CB added during the synthesis reduces the resistance of individual particles by more than 9 times. These observations are in good agreement with the valence band measurement results discussed above (Fig. 2c). Among the synthesised products, the samples with a small amount of Bi^{3+} doping have the same resistance as the undoped sample. However, increasing the amount of Bi^{3+} doping slightly increases the resistance. The formation of BiOCl might cause this resistance increase.

To evaluate the distribution of the Bi^{3+} on the investigated electrode samples before and after their electrochemical cycling, the electrode was examined by SEM (Fig. 5) and EDX (Fig. 6). The SEM images of the prepared cathode material show the presence of the synthesised products on their surface. The pyrolusite-containing sample consists of small-sized polycrystalline particles dispersed in the carbon matrix. In contrast, the other Bi-doped samples consist of needle-shaped particles, visible in the obtained sample images of Fig. 1e. The size and shape of the particles have not changed during the production of electrodes. This also confirms the tendency of the peaks observed in the Raman measurements (Fig. 4d) to be preserved for the obtained cathode materials. Concerning the obtained particle shape and size seen in Fig. 1 correlation to CV results (Fig. 3), no direct relation can be drawn, as all the cathodes were previously cycled to reach stabilisation, and as seen in Fig. 5, different particle shapes and sizes are deposited on the surface of the cathode.

After CV measurements, a completely different observation can be made from the obtained sample surfaces. The structures formed after charging (Fig. 5) no longer depict the shape of the particles placed in the cathode material, however, are polycrystalline agglomerates for both

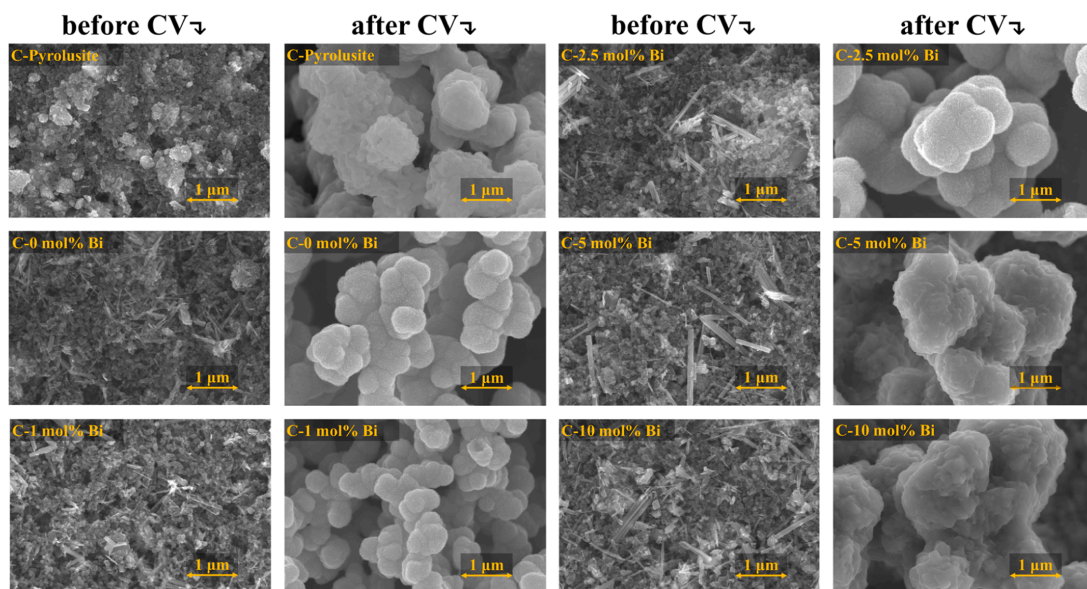


Fig. 5. SEM of cathode materials before and after CV measurements.

Table 2
Equivalent circuit parameters of fitted data.

Sample	R_s	R_1	CPE_1		R_2	CPE_2		χ^2
	Ω	Ω	Y_0 $mS \cdot s^N$	N	Ω	Y_0 $mS \cdot s^N$	N	
C-Pyrolusite	23.82	5.05	1.13	0.54	1474.80	1.93	0.52	0.00039
C-0 mol% Bi	21.66	9.49	0.29	0.68	161.94	6.30	0.34	0.00045
C-1 mol% Bi	23.75	49.03	1.52	0.52	162.74	3.32	0.45	0.00106
C-2.5 mol% Bi	23.74	39.57	1.38	0.53	195.00	3.54	0.40	0.00148
C-5 mol% Bi	21.71	6.23	0.16	0.74	204.60	4.68	0.36	0.00208
C-10 mol% Bi	22.37	8.04	0.13	0.77	242.74	4.80	0.35	0.00210

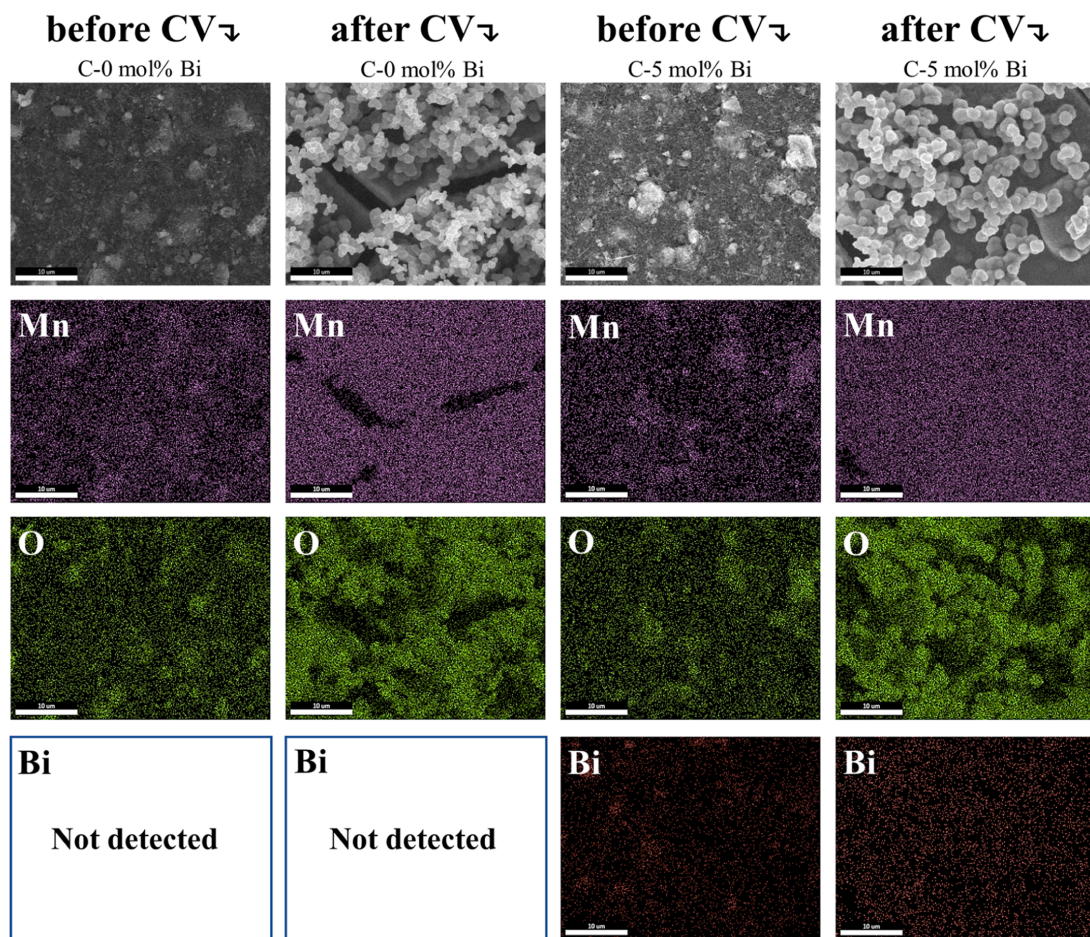


Fig. 6. SEM and EDX investigation of cathode samples before and after CV measurements.

pyrolusite and Bi^{3+} ion doped samples. The polycrystallinity of these samples was also observed in the Raman measurements (Fig. 4e). Moreover, the surface of the charged samples reveals a size difference of the pyrolusite, 0 and 1 mol% Bi^{3+} doped samples compared to the 2.5 – 10 mol% Bi^{3+} doped samples. The polycrystalline formations on the surfaces of conducting carbon electrodes with higher doping levels (2.5 – 10 mol% Bi^{3+}) are notably larger. To confirm the presence of Bi^{3+} in samples after cycling, an EDX measurement was performed (Fig. 6). After the electrochemical cycling, Bi^{3+} ions are evenly distributed across

the entire polycrystalline surface, indicating that the presence of Bi^{3+} contributes to the observed electrochemical changes. There are no concentrated points of Bi^{3+} ions or the formation of a secondary phase, indicating that these ions are effectively incorporated into the electrode structure during charging. SEM observation and EIS findings suggest that introducing Bi^{3+} ions increases the size of the polycrystalline agglomerates, which in turn increases the bulk capacitance of MnO_2 .

Due to the rapid Mn^{2+}/MnO_2 dissolution/deposition process during CV measurements, a more thorough investigation of the surfaces was

performed after the slower GCD process. The XPS measurements for samples containing 0 and 10 mol% Bi^{3+} ions were characterised at charged and discharged states (Fig. 7). Results confirm that MnO_2 is growing deeper inside the conductive electrode substrate (Fig. 7b), and for the sample with 10 mol% Bi, the stabilised form of Mn^{3+} is observed alongside Bi^{3+} (Fig. 7c and d) [102,110]. In addition, during the slower charging and discharging process (1 A/g) compared to CV, Mn ions are slowly diffusing closer to the most conductive part of the electrode substrate, resulting in gradient formation in the upper layer of the electrode. This is confirmed by fluorine F 1s spectra, where depth profile surveys were measured. In Figs. 7e and 7f, the surface of the electrode dominant part contains fluorine ions from the PVDF binder. When survey spectra are taken from deeper electrode layers, changes in the F:Mn ion ratio suggest that the surface of the electrode has less MnO_2 . This indicates that electrode formation primarily occurs in the deeper, more conductive regions of the substrate. Taking into account that the characteristic peaks of Mn are visible in both the discharged and charged spectra, it is not objective to judge the discharge state of MnO_2 , as the signals can also be collected from the "dead" part of the cathode material.

4. Conclusions

In this study, MnO_2 was hydrothermally synthesised and doped with 0, 1, 2.5, 5, and 10 mol% Bi, as the incorporation of Bi^{3+} ions is expected to narrow the band gap, enhance electrical conductivity, and improve the reversibility of the dissolution/deposition processes by increasing the lattice spacing [31,56–59]. The resulting powders consisted of polycrystalline agglomerated and rod/needle-like structured particles with a diameter of 20–200 nm and a length of 100–5000 nm. ICP-MS analysis confirmed that the measured dopant amounts align well with the theoretically added Bi-ion molar values of 0, 1; 2.5, 5, and 10 mol%. According to XRD data, the synthesised powders consist of α - and δ - MnO_2 phases. As Bi^{3+} ions are roughly twice the size of Mn^{4+} ions, their presence in the structure of MnO_2 leads to the creation of 2×2 tunnels – a characteristic crystal lattice formation of the α - MnO_2 phase. Thus, adding Bi^{3+} ions enhances the stability of the α - MnO_2 structure, which is more electrochemically active than other MnO_2 polymorphs. XPS measurements for synthesised samples indicate the presence of

Mn^{3+} and Bi^{3+} at 1–10 mol% Bi^{3+} doping levels, suggesting that Bi^{3+} ions stabilise Mn^{3+} within the MnO_2 structure.

In highly acidic electrolytes ($\text{pH} < 2$), Bi-doped MnO_2 cathodes were compared with pyrolusite MnO_2 cathode, which, according to the literature [71,72], should form during electrochemical deposition of MnO_2 . Based on CV measurements, Bi^{3+} doped samples exhibit a higher specific capacity. The cathode with 5 mol% Bi^{3+} achieves a specific capacity of 130 mAh/g, outperforming both the undoped cathode at 120 mAh/g and the pyrolusite MnO_2 cathode at 90 mAh/g. In addition, the sample with 10 mol% Bi^{3+} has improved capacity retention compared with the pyrolusite sample and approximately 25 % higher capacity at all current densities. SEM measurements show that the initial cathode particles undergo electrochemical dissolution and subsequently redeposit as polycrystalline particle agglomerates, reaching sizes up to 2 μm . At Bi^{3+} concentrations ranging from 2.5 to 10 mol%, these agglomerates reach their maximum size, suggesting that Bi^{3+} doping leads to an increase in electrical conductivity. This improved conductivity facilitates the growth of larger α - MnO_2 structures, thereby increasing the bulk capacitance. EDX analysis of electrochemically cycled cathodes shows a uniform distribution of Bi and Mn atoms across the cathode surface. This indicates that MnO_2 electrochemically dissolves (reduces to Mn^{2+}) and uniformly deposits (oxidises to MnO_2). However, Bi^{3+} ions are not involved in electrochemical reactions and are present at the cathode where Mn^{2+} ion oxidation/deposition processes occur. XPS analysis of a charged electrode surface doped with 10 mol% Bi^{3+} after GCD cycling reveals the presence of Mn^{3+} and Bi^{3+} , suggesting possible ion charge compensation within the MnO_2 crystal structure. Additionally, Raman spectroscopy confirms that the α - MnO_2 phase remains stable after CV and GCD measurements. EIS results indicate a decrease in double-layer capacitance at the electrode-electrolyte interface by approximately an order of magnitude, along with a ~ 30 % decrease in overall bulk capacitance for samples with added Bi^{3+} ions. This leads to the main conclusion: the enhanced MnO_2 reversibility of the dissolution/deposition processes in highly acidic electrolyte is achieved by Bi^{3+} ion incorporation, which narrows the MnO_2 band gap and improves electrical conductivity.

Overall, this work demonstrates the successful enhancement of the electrochemical properties of the MnO_2 cathode in strongly acidic electrolytes by Bi^{3+} ion doping. These results provide a basis for further

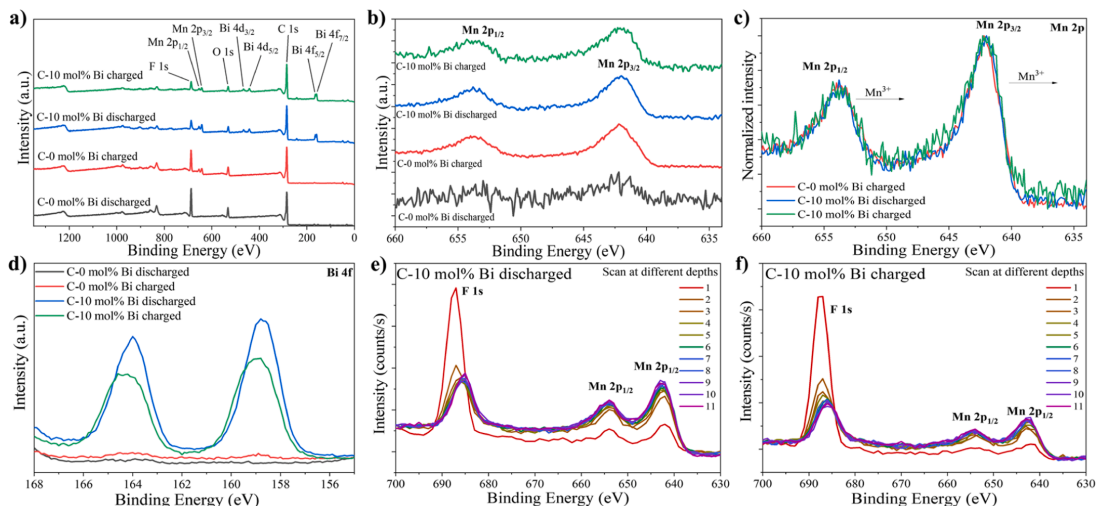


Fig. 7. XPS results for cathode material after GCD at charged and discharged states: a) survey spectra, b) normal and c) normalised Mn 2p spectra, d) Bi 4f spectra and depth profile survey spectra of F 1s and Mn 2p at e) discharged and f) charged states.

research of Bi-MnO₂ cathodes in acidic electrolytes, intending to improve the performance of dual-electrolyte batteries in which the MnO₂ cathode is used in a strongly acidic electrolyte and the anode is in an alkaline one. Further dual-electrolyte battery system exploration is crucial as it extends the water-splitting potential window and increases the use of water-based electrolytes. Further research on Bi-doped MnO₂ cathodes should focus on optimising the Bi³⁺ ion content, the composition of the electrolyte, as well as long-term cycling stability and performance. Additionally, investigation of other doping ions should be conducted to explore the possibility of MnO₂ cathode electrochemical property tunability for various energy storage applications.

CRedit authorship contribution statement

Ramona Durena: Writing – review & editing, Writing – original draft, Visualization, Validation, Methodology, Investigation, Formal analysis, Conceptualization. **Nikita Griscenko:** Writing – original draft, Visualization, Validation, Methodology, Investigation, Formal analysis. **Liga Orlova:** Methodology, Investigation, Formal analysis. **Maris Bertins:** Methodology, Investigation, Formal analysis. **Arturs Viksna:** Writing – review & editing, Methodology, Investigation, Formal analysis. **Mairis Iesalnieks:** Methodology, Investigation, Formal analysis. **Anzelms Zukuls:** Writing – review & editing, Writing – original draft, Visualization, Validation, Supervision, Methodology, Investigation, Formal analysis, Conceptualization.

Declaration of Competing Interest

The authors declare that they have no known competing financial interests or personal relationships that could have appeared to influence the work reported in this paper.

Acknowledgements

Nikita Griscenko acknowledges the financial support from the grant: “Strengthening the capacity of Riga Technical University scientific staff” project No. ZM-2024/14.

Appendix A. Supporting information

Supplementary data associated with this article can be found in the online version at [doi:10.1016/j.jallcom.2024.177904](https://doi.org/10.1016/j.jallcom.2024.177904).

Data Availability

Data will be made available on request.

References

- A.R. Dehghani-Sanji, E. Tharumalingam, M.B. Dusseault, R. Fraser, Study of energy storage systems and environmental challenges of batteries, *Renew. Sustain. Energy Rev.* 104 (2019) 192–208, <https://doi.org/10.1016/j.rser.2019.01.023>.
- Q. Li, Y. Liu, S. Guo, H. Zhou, Solar energy storage in the rechargeable batteries, *Nano Today* 16 (2017) 46–60, <https://doi.org/10.1016/j.nantod.2017.08.007>.
- D. Di Lecce, R. Verrelli, J. Hassoun, Lithium-ion batteries for sustainable energy storage: recent advances towards new cell configurations, *Green. Chem.* 19 (2017) 3442–3467, <https://doi.org/10.1039/c7gc01328k>.
- F. Zhou, M. Wu, W. Hu, Z.-G. Jiang, D. Noréus, Alpha nickel hydroxide electrodes improve aqueous rechargeable batteries capacity, *Mater. Res. Bull.* 179 (2024) 112967, <https://doi.org/10.1016/j.materresbull.2024.112967>.
- Y.-L. Zhang, X.-W. Wang, K. Ma, X.-R. Wen, Z.-Q. He, Z.-H. Yuan, Efficiently catalyzed sea urchin-like mixed phase SmMn2O5/MnO2 for oxygen reduction reaction in zinc-air battery, *Mater. Res. Bull.* 149 (2022) 111744, <https://doi.org/10.1016/j.materresbull.2022.111744>.
- L. Kong, C. Li, J. Jiang, M.G. Pecht, Li-ion battery fire hazards and safety strategies, *Energy (Basel)* 11 (2018), <https://doi.org/10.3390/en11092191>.
- Y.-L. Liu, B. Zhu, Z. Wang, X. Zhang, X. Wu, Multilayer Ti3C2Tx-loaded CoOHf composite structures for high-performance lithium-ion batteries, *Mater. Res. Bull.* 179 (2024) 112986, <https://doi.org/10.1016/j.materresbull.2024.112986>.
- S. Siroj, J. Padchhari, A. Montreupatham, S. Sonsupap, S. Maensiri, S. Kheawhom, P. Kikkunthod, Glass-sulfur composite cathodes: a new strategy for improving the performance of lithium-sulfur batteries, *Mater. Res. Bull.* 178 (2024) 112919, <https://doi.org/10.1016/j.materresbull.2024.112919>.
- S. Xu, S. Liu, Y. Zhou, R. Xiao, X. Ke, Study on the electrochemical process of Li⁺/Na⁺ mixed organic dual-cation battery system, *Mater. Res. Bull.* 177 (2024) 112858, <https://doi.org/10.1016/j.materresbull.2024.112858>.
- H. Li, T. Zhu, X. Chen, H. Liu, G. He, Improving China's global lithium resource development capacity, *Front. Environ. Sci.* 10 (2022), <https://doi.org/10.3389/fenvs.2022.938534>.
- M. Arribas-Ibar, P.A. Nylund, A. Brem, The risk of dissolution of sustainable innovation ecosystems in times of crisis: the electric vehicle during the covid-19 pandemic, *Ecosyst. (Switz.)* 13 (2021) 1–14, <https://doi.org/10.3390/su13031319>.
- K. Giza, B. Pospiech, J. Gega, Future technologies for recycling spent lithium-ion batteries (LIBs) from electric vehicles—overview of latest trends and challenges, *Energy (Basel)* 16 (2023), <https://doi.org/10.3390/en16155777>.
- X. Yu, W. Li, V. Gupta, H. Gao, D. Tran, S. Sarwar, Z. Chen, Current challenges in efficient lithium-ion batteries' recycling: a perspective, *Glob. Chall.* 6 (2022), <https://doi.org/10.1002/gch2.202200099>.
- Z. Dobo, T. Dinh, T. Kulcsár, A review on recycling of spent lithium-ion batteries, *Energy Rep.* 9 (2023) 6362–6395, <https://doi.org/10.1016/j.egyrs.2023.05.264>.
- V.M. Leal, J.S. Ribeiro, E.L.D. Coelho, M.B.J.G. Freitas, Recycling of spent lithium-ion batteries as a sustainable solution to obtain raw materials for different applications, *J. Energy Chem.* 79 (2023) 118–134, <https://doi.org/10.1016/j.jechem.2022.08.005>.
- K.K. Jena, A. Alfantazi, A.T. Mayyas, Comprehensive review on concept and recycling evolution of lithium-ion batteries (LIBs), *Energy Fuels* 35 (2021) 18257–18284, <https://doi.org/10.1021/acs.energyfuels.1c02489>.
- F. Duffner, N. Kronenmeyer, J. Tübke, J. Leker, M. Winter, R. Schmuch, Post-lithium-ion battery cell production and its compatibility with lithium-ion cell production infrastructure, *Nat. Energy* 6 (2021) 123–134, <https://doi.org/10.1038/s41560-020-00748-8>.
- X. Lou, Y. Liu, H. Wan, H. Chen, W. Zhou, Constructing δ-MnO₂ nano-flower microspheres for high-voltage and long-life aqueous ammonium-ion battery, *Mater. Res. Bull.* 179 (2024) 112947, <https://doi.org/10.1016/j.materresbull.2024.112947>.
- J. Pross-Brakhage, O. Fitz, C. Bischoff, D. Biro, K.P. Birke, Post-lithium batteries with zinc for the energy transition, *Batteries* 9 (2023) 367, <https://doi.org/10.3390/batteries9070367>.
- F. Lionetto, N. Arianpouya, B. Bozzini, A. Maffezzoli, M. Nematollahi, C. Mele, Advances in zinc-ion structural batteries, *J. Energy Storage* 84 (2024) 110849, <https://doi.org/10.1016/j.est.2024.110849>.
- D. Singh, Y. Hu, S.S. Meena, R. Vengarathody, M. Fichtner, P. Barpanda, Iron-based fluorophosphate Na₂FePO₄F as a cathode for aqueous zinc-ion batteries, *Chem. Commun.* 59 (2023) 14391–14394, <https://doi.org/10.1039/D3CC004940J>.
- H. Hong, X. Guo, J. Zhu, Z. Wu, Q. Li, C. Zhi, Metal/covalent organic frameworks for aqueous rechargeable zinc-ion batteries, *Sci. China Chem.* 67 (2024) 247–259, <https://doi.org/10.1007/s11426-023-1558-2>.
- A. Feng, L. Liu, P. Liu, Y. Zu, F. Han, X. Li, S. Ding, Y. Chen, Interfacial nanoparticles of Co₂P/Co₃Fe₇ encapsulated in N-doped carbon nanotubes as bifunctional oxygen electrocatalysts for rechargeable zinc-air batteries, *Mater. Today Energy* 44 (2024) 101626, <https://doi.org/10.1016/j.mtener.2024.101626>.
- R. Durena, A. Zukuls, M. Vanags, A. Šutka, How to increase the potential of aqueous Zn-MnO₂ batteries: the effect of pH gradient electrolyte, *Electro Acta* 434 (2022) 141275, <https://doi.org/10.1016/j.electacta.2022.141275>.
- G.G. Yadav, D. Turney, J. Huang, X. Wei, S. Banerjee, Breaking the 2 V barrier in aqueous zinc chemistry: creating 2.45 and 2.8 V MnO₂-Zn aqueous batteries, *ACS Energy Lett.* 4 (2019) 2144–2146, <https://doi.org/10.1021/acscenergylett.9b01643>.
- T. Xue, H.J. Fan, From aqueous Zn-ion battery to Zn-MnO₂ flow battery: a brief story, *J. Energy Chem.* 54 (2021) 194–201, <https://doi.org/10.1016/j.jechem.2020.05.056>.
- T.M. Narayanan, Y.G. Zhu, E. Gençer, G. McKinley, Y. Shao-Horn, Low-cost manganese dioxide semi-solid electrode for flow batteries, *Joule* 5 (2021) 2934–2954, <https://doi.org/10.1016/j.joule.2021.07.010>.
- G. Li, W. Chen, H. Zhang, Y. Gong, F. Shi, J. Wang, R. Zhang, G. Chen, Y. Jin, T. Wu, Z. Tang, Y. Cui, Membrane-free Zn/MnO₂ flow battery for large-scale energy storage, *Adv. Energy Mater.* 10 (2020), <https://doi.org/10.1002/aem.201902085>.
- N. Liu, M. K. J. Pan, Y. Hu, Y. Sun, X. Liu, A facile preparation of λ-MnO₂ as cathode material for high-performance zinc-manganese redox flow battery, *J. Electrochem Soc.* 167 (2020) 040517, <https://doi.org/10.1149/1945-7111/ab75c2>.
- G. Shu, Z. Song, W. Wang, H. Tian, Review of emerging multiple ion-exchange membrane electrochemical systems for effective energy conversion and storage, *Sustain. Energy Technol. Assess.* 70 (2024) 103926, <https://doi.org/10.1016/j.seta.2024.103926>.
- M. Minakshi, D.R.G. Mitchell, The influence of bismuth oxide doping on the rechargeability of aqueous cells using MnO₂ cathode and LiOH electrolyte, *Electro Acta* 53 (2008) 6323–6327, <https://doi.org/10.1016/j.electacta.2008.04.013>.
- Y. Yang, X. Huang, Y. Yang, C. Wu, B. Lei, Q. Peng, G. Wang, Improving the rate performance of manganese dioxide by doping with Cu²⁺, Co²⁺ and Ni²⁺ ions,

- Int J. Electrochem Sci. 14 (2019) 3673–3683, <https://doi.org/10.20964/2019.04.30>.
- [33] M. Wang, X. Zheng, X. Zhang, D. Chao, S.Z. Qiao, H.N. Alshareef, Y. Cui, W. Chen, Opportunities of aqueous manganese-based batteries with deposition and stripping chemistry, *Adv. Energy Mater.* 11 (2021), <https://doi.org/10.1002/aenm.202002904>.
- [34] W. Li, D. Wang, Conversion-type cathode materials for aqueous Zn metal batteries in nonalkaline aqueous electrolytes: progress, challenges, and solutions, *Adv. Mater.* (2023), <https://doi.org/10.1002/adma.202304983>.
- [35] L. Liu, Y.C. Wu, L. Huang, K. Liu, B. Duployer, P. Rozier, P.L. Taberna, P. Simon, Alkali ions pre-intercalated layered MnO₂ nanosheet for zinc-ions storage, *Adv. Energy Mater.* 11 (2021), <https://doi.org/10.1002/aenm.202101287>.
- [36] J. Yang, J. Cao, Y. Peng, W. Yang, S. Barg, Z. Liu, L.A. Kinloch, M.A. Bissett, R.A. W. Dryfe, Unravelling the mechanism of rechargeable aqueous Zn–MnO₂ batteries: implementation of charging process by electrodeposition of MnO₂, *ChemSusChem* 13 (2020) 4103–4110, <https://doi.org/10.1002/cssc.202001216>.
- [37] Q. Zhang, H. Fan, Q. Liu, Y. Wu, E. Wang, Fe-doped α -MnO₂ GO cathode material for zinc ion batteries with long lifespan and high areal capacity, *J. Mater. Chem. A Mater.* 12 (2024) 8167–8174, <https://doi.org/10.1039/D3TA07587G>.
- [38] M. Iturrondobaita, O. Akizu-Gardoki, O. Amondarain, R. Minguez, E. Lizundia, Environmental impacts of aqueous zinc ion batteries based on life cycle assessment, *Adv. Sustain Syst.* 6 (2022), <https://doi.org/10.1002/adus.202100308>.
- [39] Y. Liao, H.-C. Chen, C. Yang, R. Liu, Z. Peng, H. Cao, K. Wang, Unveiling performance evolution mechanisms of MnO₂ polymorphs for durable aqueous zinc-ion batteries, *Energy Storage Mater.* 44 (2022) 508–516, <https://doi.org/10.1016/j.ensm.2021.10.039>.
- [40] Y. Dai, J. Zhang, X. Yan, G. Zhao, M. Yang, J. Xiong, R. Li, N. Miao, H. Yu, M. Hu, J. Liu, J. Yang, Investigating the electrochemical performance of MnO₂ polymorphs as cathode materials for aqueous proton batteries, *Chem. Eng. J.* 471 (2023) 144158, <https://doi.org/10.1016/j.cej.2023.144158>.
- [41] D.A. Kitchaev, H. Peng, Y. Liu, J. Sun, J.P. Perdew, G. Ceder, Energetics of MnO₂ polymorphs in density functional theory, *Phys. Rev. B* 93 (2016), <https://doi.org/10.1103/PhysRevB.93.045132>.
- [42] S. Dey, V.V. Praveen Kumar, The performance of highly active manganese oxide catalysts for ambient conditions carbon monoxide oxidation, *Curr. Res. Green. Sustain. Chem.* 3 (2020), <https://doi.org/10.1016/j.crgsc.2020.100012>.
- [43] M. Wang, S. Yagi, Layered birnessite MnO₂ with enlarged interlayer spacing for fast Mg-ion storage, *J. Alloy. Compd.* 820 (2020) 153135, <https://doi.org/10.1016/j.jallcom.2019.153135>.
- [44] T. Hatakeyama, N.L. Okamoto, T. Ichitsubo, Thermal stability of MnO₂ polymorphs, *J. Solid State Chem.* 305 (2022) 122683, <https://doi.org/10.1016/j.jssc.2021.122683>.
- [45] B. Yin, S. Zhang, H. Jiang, F. Qu, X. Wu, Phase-controlled synthesis of polymorphic MnO₂ structures for electrochemical energy storage, *J. Mater. Chem. A Mater.* 3 (2015) 5722–5729, <https://doi.org/10.1039/C4TA06943A>.
- [46] S. Yao, R. Zhao, S. Wang, Y. Zhou, R. Liu, L. Hu, A. Zhang, R. Yang, X. Liu, Z. Fu, D. Wang, Z. Yang, Y.M. Yan, Ni-doping induced structure distortion of MnO₂ for highly efficient Na⁺ storage, *Chem. Eng. J.* 429 (2022), <https://doi.org/10.1016/j.cej.2021.132521>.
- [47] Z. Zhang, W. Li, Y. Shen, R. Wang, H. Li, M. Zhou, W. Wang, K. Wang, K. Jiang, Issues and opportunities of manganese-based materials for enhanced Zn-ion storage performances, *J. Energy Storage* 45 (2022) 103729, <https://doi.org/10.1016/j.est.2021.103729>.
- [48] N. Becknell, P.P. Lopes, T. Hatakeyama, X. Zhou, Y. Liu, B. Fisher, D.Y. Chung, M. G. Kanatzidis, N.M. Markovic, S. Tepavcic, V.R. Stamenkovic, Employing the dynamics of the electrochemical interface in aqueous zinc-ion battery cathodes, *Adv. Funct. Mater.* 31 (2021), <https://doi.org/10.1002/adfm.202102135>.
- [49] C. Chen, M. Shi, Y. Zhao, C. Yang, L. Zhao, C. Yan, Al-Intercalated MnO₂ cathode with reversible phase transition for aqueous Zn-ion batteries, *Chem. Eng. J.* 422 (2021), <https://doi.org/10.1016/j.cej.2021.130375>.
- [50] Y. Jia, J. Jie, W. Houzhao, D. Jinxia, W. Xunying, L. Lin, M. Guokun, T. Li, W. Hanbin, Z. Jun, W. Hao, Highly stable Co-doped MnO₂ nanoarrays as enhanced cathode materials for aqueous zinc-ion batteries, *Oxf. Open Energy* 1 (2022), <https://doi.org/10.1093/oenenergy/oiab003>.
- [51] S. Yang, L. Zhang, M. Luo, Y. Cui, J. Wang, D. Zhao, C. Yang, X. Wang, B. Cao, Synergistic combination of a Co-doped α -MnO₂ cathode with an electrolyte additive for a high-performance aqueous zinc-ion battery, *ChemPhysMater* 2 (2023) 77–82, <https://doi.org/10.1016/j.cphma.2022.04.007>.
- [52] S. Liu, J. Wang, Z. Zhou, Y. Li, W. Zhang, C. Wang, Cobalt-doped δ -MnO₂/CNT composites as cathode material for aqueous zinc-ion batteries, *Inorg. Chem. Front* 10 (2023) 5167–5177, <https://doi.org/10.1039/D3QO1010D>.
- [53] X. Xia, Y. Zhao, Y. Zhao, M. Xu, W. Liu, X. Sun, Mo doping provokes two electron reaction in MnO₂ with ultrahigh capacity for aqueous zinc ion batteries, *Nano Res.* 16 (2023) 2511–2518, <https://doi.org/10.1007/s12274-022-5057-0>.
- [54] Y. Liu, W. Chen, J. Su, X. Zhao, X. Pan, Inhibition of phase transition from δ -MnO₂ to α -MnO₂ by Mo-doping and the application of Mo-doped MnO₂ in aqueous zinc-ion batteries, *Phys. Chem. Chem. Phys.* 25 (2023) 30663–30669, <https://doi.org/10.1039/D3CP04182D>.
- [55] R. Grisenko, M. Durena, M. Iesalnieks, A. Bertsins, A. Viksna, Zukuls, Improvement of manganese dioxide cathode by molybdenum doping in highly acidic electrolyte, *J. Energy Storage* 76 (2024) 109847, <https://doi.org/10.1016/j.est.2023.109847>.
- [56] Y. Ma, M. Xu, R. Liu, H. Xiao, Y. Liu, X. Wang, Y. Huang, G. Yuan, Molecular tailoring of MnO₂ by bismuth doping to achieve aqueous zinc-ion battery with capacitor-level durability, *Energy Storage Mater.* 48 (2022) 212–222, <https://doi.org/10.1016/j.ensm.2022.03.024>.
- [57] D. Im, A. Manthiram, Role of bismuth and factors influencing the formation of Mn₃O₄ in rechargeable alkaline batteries based on bismuth-containing manganese oxides, *J. Electrochem Soc.* 150 (2003) A68, <https://doi.org/10.1149/1.1524611>.
- [58] K. Ma, Q. Li, C. Hong, G. Yang, C. Wang, Bi doping-enhanced reversible-phase transition of α -MnO₂ raising the cycle capability of aqueous Zn–Mn batteries, *ACS Appl. Mater. Interfaces* 13 (2021) 55208–55217, <https://doi.org/10.1021/acsaami.1c17677>.
- [59] L. Gou, Y. Yang, Y. Zhang, J. Li, X. Fan, D. Li, In situ synthesis of Bi³⁺-doped δ -MnO₂ cathode to enhance the cycle stability for aqueous zinc-ion batteries, *J. Solid State Electrochem.* 27 (2023) 1443–1450, <https://doi.org/10.1007/s10008-023-05501-1>.
- [60] R. Wang, H. Li, H. Sun, Bismuth: Environmental pollution and health effects. Encyclopedia of Environmental Health, Elsevier, 2019, pp. 415–423, <https://doi.org/10.1016/B978-0-12-409548-9.11870-6>.
- [61] M.B. Lim, T.N. Lambert, B.R. Chalamala, Rechargeable alkaline zinc–manganese oxide batteries for grid storage: Mechanisms, challenges and developments, *Mater. Sci. Eng. R: Rep.* 143 (2021) 100593, <https://doi.org/10.1016/j.mser.2020.100593>.
- [62] J.K. Seo, J. Shin, H. Chung, P.Y. Meng, X. Wang, Y.S. Meng, Intercalation and conversion reactions of nanosized β -MnO₂ cathode in the secondary Zn/MnO₂Alkaline battery, *J. Phys. Chem. C* 122 (2018) 11177–11185, <https://doi.org/10.1021/acs.jpcc.7b11685>.
- [63] G.G. Yadav, X. Wei, J. Huang, D. Turney, M. Nyce, S. Banerjee, Accessing the second electron capacity of MnO₂ by exploring coexplanation and intercalation reactions in energy dense alkaline batteries, *Int. J. Hydrog. Energy* 43 (2018) 8480–8487, <https://doi.org/10.1016/j.ijhydene.2018.03.061>.
- [64] H.-W. Zhu, J. Ge, Y.-C. Peng, H.-Y. Zhao, L.-A. Shi, S.-H. Yu, Dip-coating processed sponge-based electrodes for stretchable Zn–MnO₂ batteries, *Nano Res.* 11 (2018) 1554–1562, <https://doi.org/10.1007/s12274-017-1771-4>.
- [65] X. Guo, J. Zhou, C. Bai, X. Li, G. Fang, S. Liang, Zn/MnO₂ battery chemistry with dissolution-deposition mechanism, *Mater. Today Energy* 16 (2020), <https://doi.org/10.1016/j.mtener.2020.100396>.
- [66] L. Wu, Z. Li, Y. Xiang, W. Dong, X. Qi, Z. Ling, Y. Xu, H. Wu, M.D. Levi, N. Shpigel, X. Zhang, Revisiting the charging mechanism of α -MnO₂ in mildly acidic aqueous zinc electrolytes, *Small* (2024), <https://doi.org/10.1002/smll.202404583>.
- [67] H. Chen, C. Dai, F. Xiao, Q. Yang, S. Cai, M. Xu, H. J. Fan, S. Bao, Reunderstanding the reaction mechanism of aqueous Zn–Mn batteries with sulfate electrolytes: role of the zinc sulfate hydroxide, *Adv. Mater.* 34 (2022), <https://doi.org/10.1002/adma.202109092>.
- [68] L. Li, T.K.A. Hoang, J. Zhi, M. Han, S. Li, P. Chen, Functioning mechanism of the secondary aqueous Zn- β -MnO₂ battery, *ACS Appl. Mater. Interfaces* 12 (2020) 12834–12846, <https://doi.org/10.1021/acsaami.9b22758>.
- [69] M.H. Alfaruqi, S. Islam, J. Lee, J. Jo, V. Mathew, J. Kim, First principles calculations study of α -MnO₂ as a potential cathode for Al-ion battery application, *J. Mater. Chem. A Mater.* 7 (2019) 26966–26974, <https://doi.org/10.1039/C9TA09321D>.
- [70] J. Ambrose, A.K. Covington, H.R. Thirsk, Standard electrode potential of γ -manganese dioxide and its relation to other properties, *Trans. Faraday Soc.* 65 (1969) 1897, <https://doi.org/10.1039/tf9696501897>.
- [71] E. Gydesen, H. Tkker, Groundwater Chemistry and Treatment: Application to Danish Waterworks. Water Treatment, InTech, 2013, <https://doi.org/10.5772/54166>.
- [72] A.A. Rodríguez-Díaz, C. Canet, R.E. Villanueva-Estrada, E. Chacón, F. Gervilla, F. Velasco-Tapia, E.M. Cruz-Gómez, E. González-Partida, R. Casas-García, C. Linares-López, D. Pérez-Zárata, Recent Mn-Ag deposits in coastal hydrothermal springs in the Baja California Peninsula, Mexico, *Min. Depos.* 54 (2019) 849–866, <https://doi.org/10.1007/s00126-018-0846-9>.
- [73] T. Zhao, D. Lan, Z. Jia, Z. Gao, G. Wu, Hierarchical porous molybdenum carbide synergic morphological engineering towards broad multi-band tunable microwave absorption, *Nano Res.* (2024), <https://doi.org/10.1007/s12274-024-6938-1>.
- [74] G. Ma, D. Lan, Y. Zhang, X. Sun, Z. Jia, G. Wu, G. Bu, P. Yin, Microporous cobalt ferrite with bio-carbon loosely decorated to construct multi-functional composite for dye adsorption, anti-bacteria and electromagnetic protection, *Small* (2024), <https://doi.org/10.1002/smll.202404449>.
- [75] X. Xie, H. Wang, H. Kimura, C. Ni, W. Du, G. Wu, NiCoZn/C/melamine sponge-derived carbon composites with high-performance electromagnetic wave absorption, *Int. J. Miner., Metall. Mater.* 31 (2024) 2274–2286, <https://doi.org/10.1007/s12613-024-2880-1>.
- [76] S. Zhang, D. Lan, J. Zheng, A. Feng, Y. Pei, S. Cai, S. Du, X. Chen, G. Wu, Z. Jia, Rational construction of heterointerfaces in biomass sugarcane-derived carbon for superior electromagnetic wave absorption, *Int. J. Miner., Metall. Mater.* 31 (2024) 2749–2759, <https://doi.org/10.1007/s12613-024-2875-y>.
- [77] N. Vilas Boas, J.B. Souza Junior, L.C. Varanda, S.A.S. Machado, M.L. Calegario, Bismuth and cerium doped cryptomelane-type manganese dioxide nanorods as bifunctional catalysts for rechargeable alkaline metal-air batteries, *Appl. Catal. B* 258 (2019) 118014, <https://doi.org/10.1016/j.apcatb.2019.118014>.
- [78] X. Zhang, W. Yang, J. Yang, D.G. Evans, Synthesis and characterization of α -MnO₂ nanowires: self-assembly and phase transformation to β -MnO₂ microcrystals, *J. Cryst. Growth* 310 (2008) 716–722, <https://doi.org/10.1016/j.jcrysgro.2007.11.113>.
- [79] X. Zhang, P. Yu, D. Wang, Y. Ma, Controllable synthesis of α -MnO₂ nanostructures and phase transformation to β -MnO₂ microcrystals by

- hydrothermal crystallization, *J. Nanosci. Nanotechnol.* 10 (2010) 898–904, <https://doi.org/10.1166/jnn.2010.1893>.
- [80] D. Jampaiah, V.K. Velisaju, P. Venkateswamy, V.E. Coyle, A. Nafady, B.M. Reddy, S.K. Bhargava, Nanowire morphology of Mono- and bidoped α -MnO₂ catalysts for remarkable enhancement in soot oxidation, *ACS Appl. Mater. Interfaces* 9 (2017) 32652–32666, <https://doi.org/10.1021/acsami.7b07656>.
- [81] K. Selvakumar, V. Duraisamy, S. Venkateshwaran, N. Arumugam, A.I. Almansour, Y. Wang, T. Xiaoteng Liu, S. Murugesan Senthil Kumar, Development of α -MnO₂ nanowire with Ni- and (Ni, Co)-cation doping as an efficient bifunctional oxygen evolution and oxygen reduction reaction catalyst, *ChemElectroChem* 9 (2022), <https://doi.org/10.1002/celec.202101303>.
- [82] T. Uematsu, Y. Miyamoto, Y. Ogasawara, K. Suzuki, K. Yamaguchi, N. Mizuno, Molybdenum-doped α -MnO₂ as an efficient reusable heterogeneous catalyst for aerobic sulfide oxygenation, *Catal. Sci. Technol.* 6 (2016) 222–233, <https://doi.org/10.1039/C5CY01552A>.
- [83] Y. Xin, H. Gao, C. Liu, J. Chen, P. Liu, Y. Lu, Z. Ling, A systematic spectroscopic study of laboratory synthesized manganese oxides relevant to Mars, *J. Raman Spectrosc.* 53 (2022) 340–355, <https://doi.org/10.1002/jrs.6231>.
- [84] B. Zhang, G. Cheng, B. Lan, X. Zheng, M. Sun, F. Ye, L. Yu, X. Cheng, Crystallization design of MnO₂: Via acid towards better oxygen reduction activity, *CrystEngComm* 18 (2016) 6895–6902, <https://doi.org/10.1039/C6CE01131D>.
- [85] Y. Xie, Y. Yu, X. Gong, Y. Guo, Y. Guo, Y. Wang, G. Lu, Effect of the crystal plane figure on the catalytic performance of MnO₂ for the total oxidation of propane, *CrystEngComm* 17 (2015) 3005–3014, <https://doi.org/10.1039/C5CE00058K>.
- [86] T. Gao, H. Fjellvåg, P. Norby, A comparison study on Raman scattering properties of α - and β -MnO₂, *Anal. Chim. Acta* 648 (2009) 235–239, <https://doi.org/10.1016/j.aca.2009.06.059>.
- [87] B. Zhang, D. Chen, H. Liu, X. Zou, T. Chen, Selective catalytic reduction of NO with NH₃ over high purity palygorskite-supported MnO₂ with different crystal structures, *Aerosol Air Qual. Res* 20 (2020) 1155–1165, <https://doi.org/10.4209/aaqr.2020.03.0099>.
- [88] H. Chen, Y. Wang, Y.-K. Lv, Catalytic oxidation of NO over MnO₂ with different crystal structures, *RSC Adv.* 6 (2016) 54032–54040, <https://doi.org/10.1039/C6RA10103H>.
- [89] J.E. Post, D.A. McKeown, P.J. Heaney, Raman spectroscopy study of manganese oxides: layer structures, *Am. Mineral.* 106 (2021) 351–366, <https://doi.org/10.2138/am-2021-7666>.
- [90] J.E. Post, D.A. McKeown, P.J. Heaney, Raman spectroscopy study of manganese oxides: Tunnel structures, *Am. Mineral.* 105 (2020) 1175–1190, <https://doi.org/10.2138/am-2020-7390>.
- [91] Y. Wang, D.C. Alsmeyer, R.L. McCreery, Raman spectroscopy of carbon materials: structural basis of observed spectra, *Chem. Mater.* 2 (1990) 557–563, <https://doi.org/10.1021/cm00011a018>.
- [92] Y. Khan, S.K. Durrani, M. Mehmood, M.R. Khan, Mild hydrothermal synthesis of γ -MnO₂ nanostructures and their phase transformation to α -MnO₂ nanowires, *J. Mater. Res.* 26 (2011) 2268–2275, <https://doi.org/10.1557/jmr.2011.138>.
- [93] H. Song, H. Zhao, X. Zhang, Y. Xu, X. Cheng, S. Gao, L. Huo, A hollow urchin-like α -MnO₂ as an electrochemical sensor for hydrogen peroxide and dopamine with high selectivity and sensitivity, *Microchim. Acta* 186 (2019), <https://doi.org/10.1007/s00604-019-3316-x>.
- [94] K. Li, C. Chen, H. Zhang, X. Hu, T. Sun, J. Jia, Effects of phase structure of MnO₂ and morphology of δ -MnO₂ on toluene catalytic oxidation, *Appl. Surf. Sci.* 496 (2019), <https://doi.org/10.1016/j.apsusc.2019.143662>.
- [95] L. Jia, F. Li, C. Yang, X. Yang, B. Kou, Y. Xing, J. Peng, G. Ni, Z. Cao, S. Zhang, T. Zhao, X. Jin, Direct Z-Scheme Heterojunction α -MnO₂/BiOI with Oxygen-Rich Vacancies Enhanced Photoelectrocatalytic Degradation of Organic Pollutants under Visible Light, *Catalysts* 12 (2022) 1596, <https://doi.org/10.3390/catal12121596>.
- [96] T. Hishida, K. Ohbayashi, M. Kobata, E. Ikenaga, T. Sugiyama, K. Kobayashi, M. Okawa, T. Saitoh, Empirical relationship between x-ray photoemission spectra and electrical conductivity in a colossal magnetoresistive manganite La_{1-x}Sr_xMnO₃, *J. Appl. Phys.* 113 (2013), <https://doi.org/10.1063/1.4811372>.
- [97] M. Wang, K. Chen, J. Liu, Q. He, G. Li, F. Li, Efficiently Enhancing Electrocatalytic Activity of α -MnO₂ Nanorods/N-Doped Ketjenblack Carbon for Oxygen Reduction Reaction and Oxygen Evolution Reaction Using Facile Regulated Hydrothermal Treatment, *Catalysts* 8 (2018) 138, <https://doi.org/10.3390/catal8040138>.
- [98] Z. Huang, W. Zhou, C. Ouyang, J. Wu, F. Zhang, J. Huang, Y. Gao, J. Chu, High performance of Mn-Co-Ni-O spinel nanofilms sputtered from acetate precursors, *Sci. Rep.* 5 (2015) 10899, <https://doi.org/10.1038/srep10899>.
- [99] Z. Morgan Chan, D.A. Kitchev, J. Nelson Weker, C. Schneidermann, K. Lim, G. Ceder, W. Tumas, M.F. Toney, D.G. Nocera, Electrochemical trapping of metastable Mn³⁺ ions for activation of MnO₂ oxygen evolution catalysts, *Proc. Natl. Acad. Sci.* 115 (2018), <https://doi.org/10.1073/pnas.1722235115>.
- [100] H. Idriss, On the wrong assignment of the XPS O1s signal at 531–532 eV attributed to oxygen vacancies in photo- and electro-catalysts for water splitting and other materials applications, *Surf. Sci.* 712 (2021) 121894, <https://doi.org/10.1016/j.susc.2021.121894>.
- [101] X. Cao, Y. You, D. Sha, H. Xia, H. Wang, J. Zhang, R. Hu, Y. Wei, Z. Bao, Y. Xu, L. Pan, C. Lu, W. He, M. Zhou, Z. Sun, Ultralong Cycle Life for Deep Potassium Storage Enabled by BiOCl/MKene van der Waals Heterostructures, *Adv. Funct. Mater.* 33 (2023), <https://doi.org/10.1002/adfm.202303275>.
- [102] S. Wang, D. Song, L. Liao, B. Wang, Z. Li, M. Li, W. Zhou, Bi/Mn-Doped BiOCl nanosheets self-assembled microspheres toward optimized photocatalytic performance, *Nanomaterials* 13 (2023) 2408, <https://doi.org/10.3390/nano13172408>.
- [103] M. Zhang, C. Shao, X. Zhang, Y. Liu, Bismuth oxychloride/carbon nanofiber heterostructures for the degradation of 4-nitrophenol, *CrystEngComm* 17 (2015) 7276–7282, <https://doi.org/10.1039/C5CE01012H>.
- [104] R. Durena, A. Zukuls, A short review: comparison of zinc-manganese dioxide batteries with different pH aqueous electrolytes, *Batteries* 9 (2023) 311, <https://doi.org/10.3390/batteries9060311>.
- [105] X. Xiao, Z. Liu, L. Baggetto, G.M. Veith, K.L. More, R.R. Unocic, Unraveling manganese dissolution/deposition mechanisms on the negative electrode in lithium ion batteries, *Phys. Chem. Chem. Phys.* 16 (2014) 10398, <https://doi.org/10.1039/c4cp00833b>.
- [106] Z. Zhang, K. Shen, Y. Zhou, X. Hou, Q. Ru, Q. He, C. Su, L. Sun, S.H. Aung, F. Chen, The composite electrode of Bi@carbon-texture derived from metal-organic frameworks for aqueous chloride ion battery, *Ion. (Kiel.)* 26 (2020) 2395–2403, <https://doi.org/10.1007/s11581-019-03389-4>.
- [107] C.C. Zhang, S. Hartlaub, I. Petrovic, B. Yilmaz, Raman spectroscopy characterization of amorphous coke generated in industrial processes, *ACS Omega* 7 (2022) 2565–2570, <https://doi.org/10.1021/acsomega.1c03456>.
- [108] A.Y. Lee, K. Yang, N.D. Anh, C. Park, S.M. Lee, T.G. Lee, M.S. Jeong, Raman study of D* band in graphene oxide and its correlation with reduction, *Appl. Surf. Sci.* 536 (2021), <https://doi.org/10.1016/j.apsusc.2020.147990>.
- [109] Z. Li, L. Deng, I.A. Kinloch, R.J. Young, Raman spectroscopy of carbon materials and their composites: graphene, nanotubes and fibres, *Prog. Mater. Sci.* 135 (2023), <https://doi.org/10.1016/j.pmatsci.2023.101089>.
- [110] H. Fan, G. Wang, L. Hu, Infrared, Raman and XPS spectroscopic studies of Bi₂O₃-B₂O₃-Ga₂O₃ glasses, *Solid State Sci.* 11 (2009) 2065–2070, <https://doi.org/10.1016/j.solidstatesciences.2009.09.007>.

Appendix 3

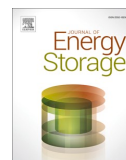
3. pielikums

Ņ. Griščenko, R. Dūrena, M. Iesalnieks, M. Bērtiņš, A. Vīksna, A. Zukuls

Improvement of manganese dioxide cathode by molybdenum doping in highly acidic electrolyte

Journal of Energy Storage, 76, 2024, 109847

DOI: [10.1016/j.est.2023.109847](https://doi.org/10.1016/j.est.2023.109847)



Research Papers

Improvement of manganese dioxide cathode by molybdenum doping in highly acidic electrolyte

Nikita Griščenko^a, Ramona Dūrena^{a,*}, Mairis Iesalnieks^a, Māris Bērtiņš^b, Arturs Viksna^b, Anzelms Zukuls^a

^a Institute of Materials and Surface Engineering, Faculty of Materials Science and Applied Chemistry, Riga Technical University, P. Valdena 3 and 7, Riga LV-1048, Latvia

^b Faculty of Chemistry, University of Latvia, Jelgavas 1, Riga LV-1004, Latvia



ARTICLE INFO

Keywords:

MnO₂
High capacity materials
Mo-doped
Hydrothermal synthesis
Aqueous medium

ABSTRACT

To address the increased demand for rechargeable batteries such as Li-ion, the market must introduce an alternative to Li-ion technology. Rechargeable Zn-MnO₂ battery technology is one feasible option, yet it has struggled to dominate the market due to low cathode cyclic stability and potential. To look into this problem, the characteristics of the cathode material were altered in this work through Mo-doping and modification of the resulting material morphology. KMnO₄ was used as a precursor in the hydrothermal synthesis of the active material, which was produced at 120 °C for 12 or 24 h with Mo doping at varied concentrations. The phase composition and morphology of the produced samples were determined using X-ray diffraction (XRD), scanning electron microscopy (SEM), and energy-dispersive X-ray spectroscopy (EDX). Moreover, the electrochemical characteristics were determined using a galvanostat. It was found that the synthesised powders consist of α-MnO₂ and δ-MnO₂ crystalline phases and the phase does not change after cyclic voltammetry (CV) measurements. In addition, the distribution of doped Mo before and after CV measurements was even throughout the sample surface. Furthermore, the addition of up to 2.5 mol% Mo to MnO₂ increases the specific capacity of the cathode in a highly acidic (pH = 1.5) electrolyte, in addition, improved capacity retention for faster discharge rates is observed by increasing Mo doping up to 5 mol%.

1. Introduction

Due to Green Policies for climate change mitigation, the move from fossil fuels to green energy is encouraged [1]. Researchers are looking for innovative strategies to store surplus renewable energy in various kinds of storage systems. One of the energy storage alternatives is battery technology with the most commonly used storage method Li-ion batteries. However, this technology has limitations, such as a scarcity of lithium in the Earth's crust and highly flammable organic electrolytes [2]. Other elements, such as Ni [3] and Co, are required for the production of Li-ion batteries, but industrial mining and processing of minerals containing such elements is highly toxic to the environment and humans [4]. Moreover, rechargeable Li-ion batteries are expected to be in higher demand than the current industry can accommodate [5]. This means that alternative battery technologies will be required in the near future and aqueous rechargeable Zn-MnO₂ batteries may be one of them.

The non-rechargeable battery industry is already dominated by Zn-MnO₂ batteries [6], however, research is more drawn to secondary-type cells as they offer wider application options. Moreover, aqueous Zn-MnO₂ batteries have promising properties for large-scale applications like high safety and low cost. Without this, Mn is more abundant in the Earth's crust than Li [7]. However, no matter how good these properties may seem, aqueous Zn-MnO₂ batteries also have several disadvantages, such as poor cycle stability due to large capacity decline mainly due to the MnO₂ cathode.

The main reason for the failure of rechargeable Zn-MnO₂ alkaline batteries is the formation of an insoluble precipitate such as Mn(OH)₂, Mn₂O₃ and Mn₃O₄ which are electrochemically passive, thus leading to permanent loss of capacity [8]. Adjusting the acidity of the electrolyte medium can mitigate the influence of the insoluble phase formation by promoting the electrochemically inactive phase to dissolve [9]. Moreover, in an acidic medium, the MnO₂ cathode goes through reaction with H⁺ ions forming Mn²⁺ ions and water as shown in half-reaction (1) with

* Corresponding author.

E-mail address: ramona.durena@rtu.lv (R. Dūrena).

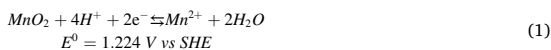
<https://doi.org/10.1016/j.est.2023.109847>

Received 25 September 2023; Received in revised form 9 November 2023; Accepted 20 November 2023

Available online 26 November 2023

2352-152X/© 2023 Elsevier Ltd. All rights reserved.

increased potential versus standard hydrogen electrode (SHE) [10]:



As H^+ ions play a key role in the functionality of MnO_2 cathode, promoting their interaction with MnO_2 is crucial. This may be achieved by adding different metals to the structure of MnO_2 , such as Al, Bi, Ni, etc. [11–14]. Moreover, Zheng and co-authors [15] in 2022 demonstrated a Mo-doped MnO_2 cathode employing mildly acidic ($\text{pH} \sim 4.8$) ZnSO_4 and MnSO_4 co-solution as electrolyte and concluded that H^+ contributes to battery stability. To further evaluate the possible improvement of elevated H^+ ion concentration on MnO_2 cathode material, Mo-doped MnO_2 cathodes should also be tested in an increased acidic medium electrolyte.

Another way to improve cathode material properties is morphology engineering since it affects the surface area and hence the available capacity [16]. There are many polymorphic modifications of MnO_2 , such as α , β , γ , δ , and λ , with different crystallographic structures. The physical and electrochemical properties of MnO_2 depend on the type of polymorph. The structures of polymorphic modifications of MnO_2 are built from MnO_6 units with shared edges. Nonetheless, these modifications differ from each other by the combinations of MnO_6 unit connections [17]. Hollandite (α - MnO_2), is a polymorphic form of MnO_2 with a monoclinic crystal structure, that consists of one-dimensional 2×2 tunnels [18]. β - MnO_2 , called pyrolusite, is another polymorph of MnO_2 with a tetragonal crystal structure, forming a structure of 1×1 dimensional tunnels [19]. Ramsdellite (γ - MnO_2), creates 2×1 tunnels [20]. Birnessite (δ - MnO_2), is a layered polymorph of MnO_2 that has a complex and variable crystal structure. It consists of layers rather than tunnels, thus various cations or water molecules can intercalate between these layers. Moreover, the layers can be separated by varying distances, resulting in various sorts of interlayer spaces. Depending on this, the layers can be at different distances from each other, leading to interlayer spaces [21]. In addition, the intergrowth MnO_2 type, λ - MnO_2 , has a unique crystal structure of three-dimensional tunnels [22]. Thus, the tunnelling structure of MnO_2 significantly affects intercalation and overall cathode performance, as the tunnels in the MnO_2 structure provide pathways for ion diffusion. The primary charge transfer process that determines the pace of electrochemical reactions within a battery is ionic conduction, which is limited by diffusion [23]. From this perspective, the δ - MnO_2 polymorph with its layered structure offers more space (7.0 Å) for ion intercalation compared, for example, to the β - MnO_2 tunnelling structure, which offers only a tunnelling space of 1.89 Å [17].

One of the most widely used methods for obtaining different polymorph MnO_2 nanoparticles is hydrothermal synthesis. This method includes the reaction of Mn precursors with oxidizing agents under high pressure and high-temperature conditions in an aqueous medium [24–27]. Various parameters can affect the properties of the product in hydrothermal synthesis, for example, altering the temperature and reaction time can change the morphology and size [28]. Also, the dimensions of the structures that develop vary depending on the duration of hydrothermal synthesis. In the case of MnO_2 nanostructures, their length is more susceptible to change than diameter. Also, adjustment in the concentration of the initial substance produces more pronounced differences in the size of structures. Therefore, by increasing the concentration of KMnO_4 , the formed nanostructures tend to decrease in size [29].

In this paper, we report the synthesis of Mo-doped MnO_2 cathode with various Mn:Mo ratios. The electrochemical properties of the MnO_2 cathode, such as CV and specific capacity, are evaluated in a highly acidic electrolyte. Moreover, the cathode material is analysed by XRD, XPS, Raman, SEM, and EDX. According to XPS observation Mo addition to MnO_2 cathode electrode tends to stabilise Mn^{3+} ion formation in cathode material. Furthermore, based on the CV results, Mo doping increases the specific capacity of the cathode material. However, as the

amount of Mo in the MnO_2 cathode increases above 2.5 mol%, the specific capacity tends to decrease.

2. Experimental section

2.1. Materials

β - MnO_2 (Pyrolusite), KMnO_4 , Na_2MoO_4 , H_2SO_4 , Polyvinylidene fluoride (PVDF) (MW $\sim 530,000$) and N-Methyl-2-pyrrolidone (NMP) were purchased from Merck; Vulcan XC72 Carbon Black (CB) were used in MnO_2 hydrothermal synthesis and 0.05 mm thick conductive graphite paper (RERAS, purchased from China and used as electrode substrate) were used to prepare cathode materials.

2.2. Preparation of MnO_2 powder samples

In total, 4 sample series of pure and molybdenum-doped MnO_2 powders were made containing 0; 1; 2.5; and 5 mol% of Mo. The total molar amount of KMnO_4 and Na_2MoO_4 sum in all samples was constant at 0.0035 mol. To prepare a sample, the necessary quantity of KMnO_4 was placed in a 50 mL conical flask. In addition, 0.042 g of CB and the required amount of Na_2MoO_4 for the doping level were added to the same flask. Afterwards, 0.7 mL of 10 % H_2SO_4 solution was added. The preparation was finished by adding the necessary amount of distilled water, resulting in a mixture with a total volume of 35 mL.

The synthesis began with stirring the obtained mixture on a magnetic stirrer for 1 h. Afterwards, the mixture was transferred to a 50 mL Teflon-coated stainless-steel autoclave and heated in an oven for 12 or 24 h. The target product in the resulting mixture was in an insoluble state, therefore, centrifugation was used to remove soluble by-products. The resulting mixture was centrifuged three times for 20 min at 6137 rpm using ethanol. Following purification, the precipitate was dried in an oven for 24 h at 60 °C before being ground with a pestle and mortar to create a powdered sample for further testing.

The purchased MnO_2 coarse powder was prepared by mixing it with CB in a mass ratio of 13:5 and milling in a steel ball mill for two hours at 200 rpm. The obtained powder was used for cathode material preparation.

2.3. Preparation of cathode materials

Additional CB was added to the synthesised samples to form a mass ratio of 13:5 (MnO_2 :CB). Further, all the obtained MnO_2 /CB samples were mixed with NMP/PVDF (mass ratio 9:1) solution in a weight ratio of 1:1 using a magnetic stirrer and ultrasonic sonication. Additional NMP was added to bring the total weight ratio of MnO_2 to NMP to 1:1.8 to obtain a cathode ink.

Then, the ink was applied onto graphite paper using a manual doctor blade coating applicator with a gap size of 50 μm and dried on a hotplate to evaporate the excess NMP. After the coated paper had dried, several cathode disks were punched out using a hollow punch.

2.4. Characterization

X-ray diffractometer (Rigaku Ultima+) with Cu-K α radiation ($\lambda = 0.154056 \text{ nm}$) measured in the 2θ angle range from 20° to 80° at a scanning speed of 2° min^{-1} , at 40 kV and 20 mA were used to obtain the diffractograms of purchased and synthesised MnO_2 samples. Obtained XRD results were analysed using the PDF 4+ database. The morphology of the cathode material was determined using a scanning electron microscope FEI Nova SEM230 operating at 15 kV. The energy-dispersive X-ray spectroscopy (EDX) with an Apollo X-SPP detector was used to determine the atomic composition of the cathode material. Raman measurements were obtained at room temperature using a Renishaw InVia727 spectrometer with a backscattering geometry. Green laser (Ar^+ , $\lambda = 514.5 \text{ nm}$, grating – 1200 cm^{-1}) was used for phonon

excitation and the sample exposure time was 10 s. X-ray photoelectron spectroscopy (XPS) spectra were acquired using 650 μm spot size with a monochromatic anode source. Samples were analysed as received without further surface cleaning. Peak fitting was performed using Avantage 5.9925 software and carbon peak at 248.8 eV was used as a calibration point. Autolab PGSTAT302N was used to determine various electrochemical properties. The CV measurement was used to analyse the oxidation and reduction of the cathode material and to determine the specific capacity. For sample characterization sample measuring cell "TSC Surface" (from rhd instruments) was used. To the sample cell, 0.6 mL of electrolyte consisting of 0.1 M MnSO_4 and 0.5 M H_2SO_4 water solution was added. Platinum electrodes were used both as a reference electrode and as a counter electrode. The CV was performed at 10 various scan rates ranging from 0.002 V/s to 0.1 V/s. The CV measurement program was designed in such a way that when starting the measurement, the open circuit potential is initially measured (5 min), from which the average open circuit potential value is taken, then the sample is cycled with a potential of ± 0.45 V relative to the measured open circuit potential. Using the same cell configuration as previously mentioned, electrochemical impedance spectroscopy (EIS) was carried out by applying a 10 mV small perturbation voltage in the 100 kHz to 0.1 Hz frequency range. An equivalent circuit software from NOVA 2.1 was used to analyse the impedance spectra.

Measurements of chronopotentiometry (CP) were conducted on samples in a half-cell configuration closed off from the atmosphere. Sample discs with 12.7 mm diameter were used in cell configuration (graphite paper/coated MnO_2 sample/filter paper with electrolyte/graphite paper) to determine the overall performance of obtained materials. As an electrolyte 100 μL of 0.1 M MnSO_4 and 0.5 M H_2SO_4 water solution was used.

Inductively coupled plasma mass spectrometry (ICP-MS) using an Agilent 8900 ICP-QQQ mass spectrometer, manufactured by Agilent Technologies in Santa Clara, CA, USA, was used to determine levels of molybdenum (Mo). The instrumental parameters were configured as follows: RF power set at 1550 W, a sampling depth of 8 mm, nebulizer gas flow at 1.1 L/min, and auxiliary gas flow at 0.9 L/min. Helium served as the collision cell gas with a flow rate of 5.0 mL/min, while oxygen acted as the reaction gas with a flow rate of 0.5 mL/min.

Samples were digested using a microwave-assisted digestion method. 9 mL HNO_3 (Fischer Scientific, TraceGrade) and 3 mL HCl (Fischer Scientific, Trace Grade) were added to 0.2 g of sample and heated in a microwave furnace (Milestone, Start E) for 30 min at 200 °C temperature. After digestion sample was diluted to the total volume of 50 mL with deionized water (Grade 1, EC < 0.055 $\mu\text{S}/\text{cm}$).

Sample solutions were introduced into the ICP-MS system through a peristaltic pump. The MicroMist nebulizer was used to generate a stable aerosol, facilitating sample vaporization in the plasma. The resulting ions were then transferred to the mass spectrometer for analysis. The collected data included intensity counts (CPS - counts per second) for specific mass-to-charge ratio (m/z) values (95 for Mo). The calibration curve was constructed using standard solutions (ICP multi-element standard solution VI, Merck) within a concentration range of 0.1 to 1000 $\mu\text{g}/\text{L}$. A blank correction was applied to account for any background interference during the measurements.

To ensure measurement stability, an internal standard solution containing Scandium (Sc) and Yttrium (Y) was added at a concentration range of 5 $\mu\text{g}/\text{L}$ to all samples, including calibration standards and test samples. Additionally, two control samples (10 $\mu\text{g}/\text{L}$ and 100 $\mu\text{g}/\text{L}$) were used to verify measurement accuracy. Results were considered acceptable if the obtained values deviated by <10 % from the known control values.

Raw data obtained from the mass spectrometer underwent processing using the Agilent MassHunter software (version B.06.00). The software's data processing functions were used to integrate the intensity counts for each target analyte (Mo) and internal standard (Sc and Y). For quantification, the calibration curve was used to determine the

concentrations of Mo in the samples. Reported concentrations were based on the calibration curve, and the relative standard deviation (RSD) of measurements was calculated to evaluate the precision and reproducibility of the analysis.

3. Results

In this work, Mo-doped MnO_2 powder samples were obtained using hydrothermal synthesis with a synthesis time of 12 or 24 h. Doping with Mo was fixed to 0; 1; 2.5 and 5 mol%. In Fig. 1 and Fig. 1S SEM images of purchased MnO_2 powder and synthesised MnO_2 samples are shown. As seen in Fig. 1b and f, samples without Mo doping are composed of different structures, such as needles, flakes and flower-cabbage structures, which is a possible result of the disproportion of the KMnO_4 raw materials reaction [30–32]. When the synthesis times of these two samples are compared, it can be seen that as the synthesis time increases, so does the particle size and the morphology of the obtained sample becomes less pronounced. By introducing Mo into the MnO_2 system, as shown in Fig. 1c and g, the synthesised powder form of MnO_2 becomes more flower-like. Moreover, by increasing the synthesis time from 12 h to 24 h, the flower-like form of MnO_2 becomes more pronounced. However, with an increased molar amount of added Mo, the formed structures became smaller. In Fig. 1d, e and h, it can be seen that any distinct shape previously seen has disappeared, only in Fig. 1i the form of the sea urchin structure can be observed. From SEM images with smaller magnification (Fig. 1S), we can conclude, that obtained powder samples are homogeneous throughout the sample and consist mainly of observed crystal shapes.

The atomic composition of synthesised products was determined using ICP-MS and EDX measurements. The quantitative results of all samples are summarized in Table 1 and Table 1S. Elements such as Mn, Mo and K were detected by ICP-MS in our samples. Also, with EDX elements such as O, Mn, Mo, K and C as well as Al are observed. Aluminium and additional carbon signals are obtained from the aluminium sample holder and adhesive carbon double-sided tape that is used for sample preparation. Considering that carbon was also added during the synthesis, it is not possible to conclude the total carbon content of the sample based on the obtained EDX results. However, with ICP-MS no carbon was detected as only soluble part of the sample can be analysed and carbon by itself if not soluble. Otherwise, both ICP-MS and EDX results are in good agreement and indicate that samples are throughout homogenous.

Furthermore, potassium is present in the sample in both ICP-MS and EDX results, which can be linked to the starting material molecule KMnO_4 , as purification of the product by multiple centrifugations failed to remove all K^+ ions. Also, taking into account the MnO_2 crystalline structure (Fig. 2a), K^+ ions are intercalated into the material, making ion removal difficult. Moreover, when the Mn:Mo ratio is compared, it roughly remains as intended by the synthesis. More deviation can be seen with higher doping levels of Mo and shorter synthesis time.

XRD analysis was performed to determine the phase composition of purchased MnO_2 and the synthesised samples (Fig. 2a). The normalised XRD results for purchased MnO_2 show broad diffraction maxima, indicating small crystallite size and corresponding to the crystalline structure of Pyrolusite ($\beta\text{-MnO}_2$). For all of the synthesised samples, two phases can be identified: $\delta\text{-MnO}_2$ ($\text{Mn}_7\text{O}_{13}\cdot 5\text{H}_2\text{O}$) and $\alpha\text{-MnO}_2$ ($\text{K}_2\cdot \text{Mn}_8\text{O}_{16}$). This supports ICP-MS and EDX finding that the K^+ ions are attached to the MnO_2 crystalline lattice. When XRD results of samples synthesised at 12 h or 24 h are compared, it can be seen that diffraction peaks became sharper with increasing synthesis time, indicating an increase in crystallinity of the sample by allowing small crystallites to grow larger and smaller crystallites to dissolve, as suggested by P. Umek et al. [29]. Samples synthesised for 24 h have additional maxima at 32° that could be assigned to $\gamma\text{-MnO}_2$ phase formation. The formation of this phase for a similar synthesis procedure, in which carbon was also added to the synthesis solution, is described in the literature [33]. However,

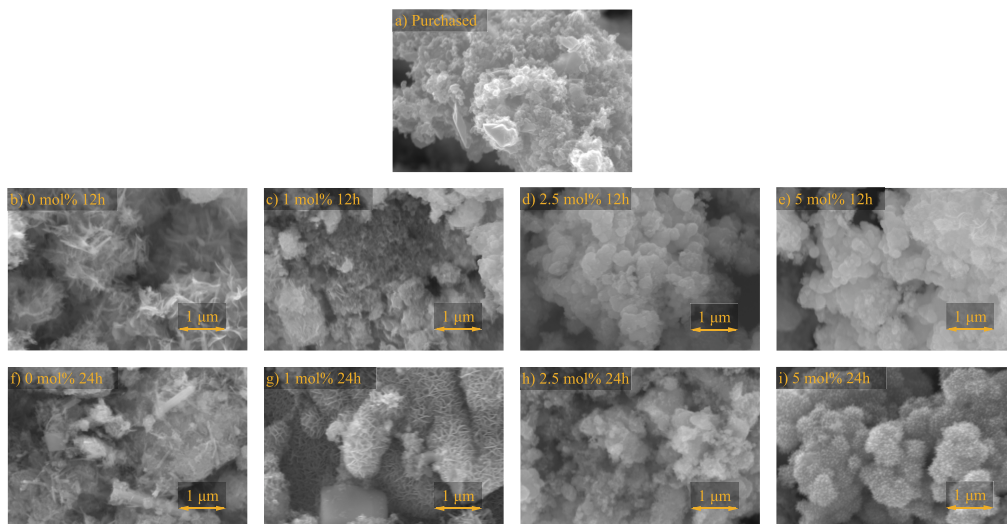


Fig. 1. SEM images of a) purchased MnO₂ powder and b) - i) synthesised Mo-doped MnO₂ powders.

Table 1
ICP-MS results of Mo-doped MnO₂ samples.

N ^o	Sample	Element mol%			Ratio, %	
		K	Mn	Mo	Mn	Mo
1	Purchased	0.06	99.94	0.00	100.0	0.0
2	0 mol% 12 h	15.78	84.22	0.00	100.0	0.0
3	0 mol% 24 h	16.67	83.33	0.00	100.0	0.0
4	1 mol% 12 h	16.11	83.08	0.81	99.0	1.0
5	1 mol% 24 h	19.12	80.08	0.80	99.0	1.0
6	2.5 mol% 12 h	15.59	82.43	1.98	97.7	2.3
7	2.5 mol% 24 h	18.19	79.87	1.94	97.6	2.4
8	5 mol% 12 h	11.93	85.26	2.81	96.8	3.2
9	5 mol% 24 h	15.45	80.77	3.79	95.5	4.5

one maxima is not enough to confirm this phase in samples. In addition, by increasing the Mo amount, a disappearance of the maxima at 12^o can be observed. The decrease for this reflection maximum is associated with (110) crystalline plane of δ-MnO₂ disappearance. This crystalline phase according to the literature [34], is attributed to rod-like structures that can be observed in SEM images (Fig. 1) as well. By increasing the molybdenum amount, rod-like structures are disappearing as well and maxima at 37^o become more intensive. This reflection maximum can be attributed to (211) crystalline plane of α-MnO₂. Thus δ-MnO₂ phase formation decreases and α-MnO₂ phase increases suggesting that Mo addition to samples promotes α-MnO₂ (K_{2-x}Mn₈O₁₆) phase formation. However, all samples exhibit broad diffraction peaks due to the small size of crystallites, which affect the shape of the maxima.

Prior to electrochemical measurements, XPS analysis (Fig. 2 b-f) was carried out to determine the oxidation states of elements in purchased and 5 mol% Mo-doped MnO₂ samples. Both samples contain Mn ions in a 4+ oxidized state, however, only synthesised MnO₂ samples contain carbon-to-oxygen bonds as CB was added during the synthesis procedure. In addition, Mo doped MnO₂ sample contains Mo in a 6+ oxidized state and Mn intermediate oxidation state of Mn³⁺. As noted by Z. Zheng and co-authors [15] Mo additive stabilizes the presence of Mn³⁺.

To analyse the electrochemical characteristics of MnO₂ samples, CV measurements were carried out. As shown in Fig. 3, the shape of the collected data results in a duck-shaped form, with the oxidation peak at the top and the reduction peak at the bottom. During discharge, MnO₂ as

a cathode undergoes a reduction reaction, changing the oxidation state of Mn from 4+ to 2+, resulting in a 2-electron discharge process. This suggests that two peaks should be visible as a result of the transfer of two electrons in both the reduction and the oxidation reactions. However, only a single peak is observed in both processes. The possible reasons for the absence of the second peak are: (1) Mo influence on the MnO₂ ox-red processes since Mo doping stabilizes the presence of Mn³⁺ [15]; (2) insufficient scanning speed, as both electron transfers could be possibly decoupled at faster scan rates [35,36]. Also, in contrast to pure and purchased MnO₂ cathode samples, the oxidation and reduction maxima for the doped samples can be seen to shift. Potential decreases when a lower concentration of Mo (1 mol%) is added to the cathode material. However, as the Mo concentration is increased (2.5 and 5 mol%), the oxidation and reduction potential maxima shift to more positive values versus the platinum electrode. Moreover, the morphology of the electrode changes after CV measurements, implying that initial particles and structures dissolve and regrow in different structures (Fig.2S). Thus, the shape of the particles obtained in the synthesis does not significantly affect the performance of the electrode during cycling. More likely, the particle size and doping agent influences the cathode material performance.

Moreover, the obtained areas of the graphs were used to calculate cathode-specific capacity at different scanning speeds using the following equation:

$$C = \frac{\int IdV}{2 \bullet m \bullet v} = \frac{[V \bullet A] \bullet [s]}{[g] \bullet [V]} \quad (2)$$

were $\int IdV$ – the area of CV graph (V•A); m – the mass of active material (g); v – scanning speed (V/s).

As seen in Fig. 4a, Fig. 3S and Fig. 4S, all synthesised samples provide a higher specific capacity than sample containing purchased MnO₂. Furthermore, the specific capacity of synthesised samples increases with the addition of Mo dopant. The reason for the overall increase in specific capacity between purchased and synthesised samples can be attributed to phase differences. As seen in XRD results (Fig. 2a) the purchased sample contains β-MnO₂ while the synthesised samples contain δ-MnO₂ and α-MnO₂. The highest specific capacity, 415 mAh/g at 0.002 V/s, was obtained from the 2.5 mol% Mo-doped MnO₂ sample with a synthesis time of 12 h. However, further testing reveals that the 1 mol% Mo-doped

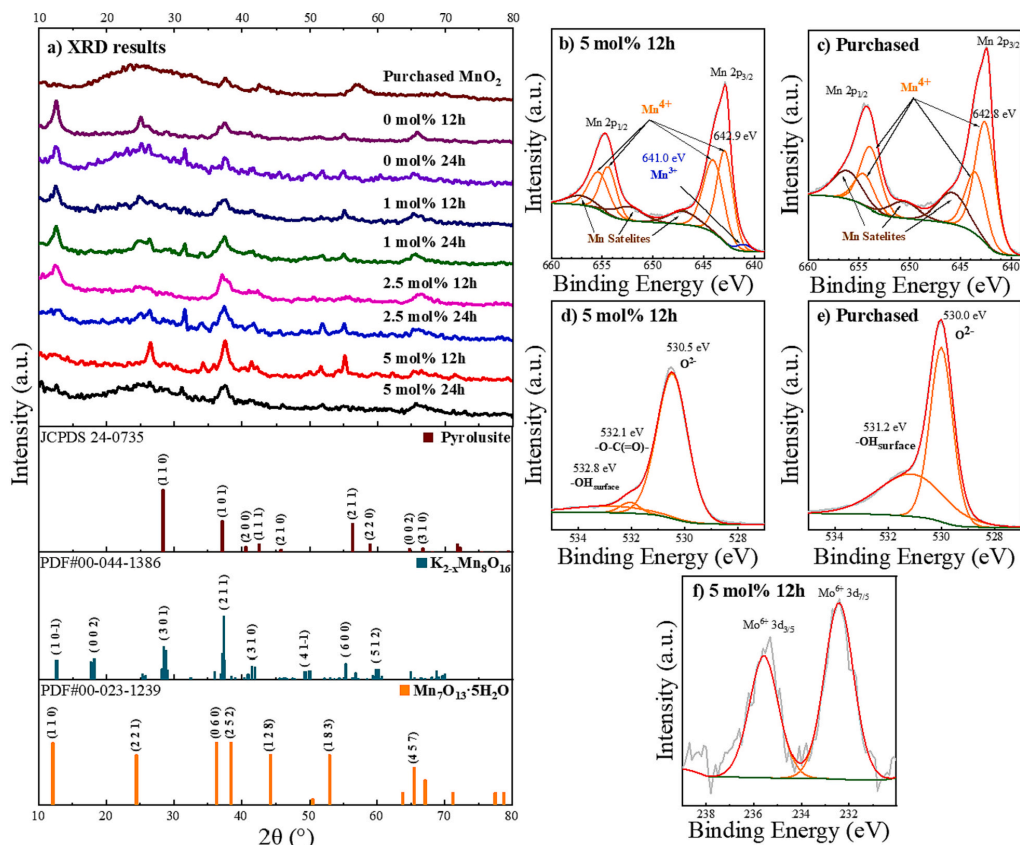


Fig. 2. Results of a) XRD spectra of purchased, pure and Mo-doped MnO_2 synthesised samples and b)-f) XPS spectra of 5 mol% Mo-doped and purchased MnO_2 .

sample synthesised for 12 h performs better than others, retaining its specific capacity at higher scanning speeds than other samples. Overall, from CV measurements (Fig. 4b) it can be seen that samples with Mo-doping show an increase in specific capacity until reaching a critical doping level of 2.5 mol%. CV results (Fig. 4) also indicate, that by increasing scan speed the capacity of more highly Mo-doped samples decreases less than for samples without Mo additive. A similar trend is also observed for CP measurements (Figs. 3S and 4S) that show better capacity retention for 5 mol% doped samples with increased cycling rates and over more performed cycles.

The Nyquist plots for each sample, obtained from electrical impedance spectroscopy, are shown in Fig. 5S. With a sinusoidal excitation signal of 10 mV, the imaginary part of the impedance is depicted versus its real component over a frequency range of 0.1 Hz to 100 kHz. By employing NOVA 2 software, an equivalent circuit was created from the Nyquist plot in order to comprehend the electrical parameters operating on the sample electrode interface. The obtained equivalent circuit [37–39] is shown in Fig. 5 and parameter values are summarized in Table 2. In the equivalent circuit, R_s is the resistance associated with solution resistance, wires, clips, etc. R_p represents the charge transfer resistance between the electrode and electrolyte interface. Combined parallel to it is Q_1 associated with the double-layer capacitance formed between the electrode and the electrolyte. In the linear circuit with R_s is the parallel circuit of R_1 and Q_2 , which is associated with resistance between individual oxide particles in the cathode layer and overall

capacitance of metal oxide, accordingly. For most of the samples, R_s value is around 10 Ω attributed mostly to the resistance of the used electrolyte. However, some loose connections and not as perfectly aligned components and sample parts of the assembled cell contributed to the increase of R_s value. Moreover, correlating with other represented data, by increasing the Mo doping level the R_1 value associated with resistance between oxide particles decreases until reaching a critical Mo doping value of 2.5 mol% and afterwards significantly increasing for 5 mol% Mo doping.

To determine the changes in cathode material after electrochemical measurements, the sample surfaces were examined using Raman spectroscopy and EDX mapping. Fig. 6 displays Raman results of samples obtained both before and after CV measurements. Peaks under 1000 cm^{-1} represent different Mn–O bonds. The peaks in the range of (630–660 cm^{-1}) and (570–580 cm^{-1}) represent the octahedral MnO_6 layer stretching modes of Mn–O bonds. The peaks located at (510–517 cm^{-1}) correspond to Mn–O–Mn deformation mode [40]. For samples examined before CV measurements (Fig. 6a), one intensive peak around 640 cm^{-1} corresponding to Mn–O bond stretching vibrations can be seen. This spectrum can be associated with $\alpha\text{-MnO}_2$ [41–43] that corresponds to XRD results (Fig. 2a). Also, two peaks of carbon are present in the range of 1300–1650 cm^{-1} : the disordered (D) band ($\approx 1350 \text{ cm}^{-1}$) and the graphitic (G) band ($\approx 1585 \text{ cm}^{-1}$) [44,45]. After CV measurements (Fig. 6b) 3 peaks associated with MnO_2 can be distinguished around 515 cm^{-1} ; 575 cm^{-1} and 640 cm^{-1} corresponding also with

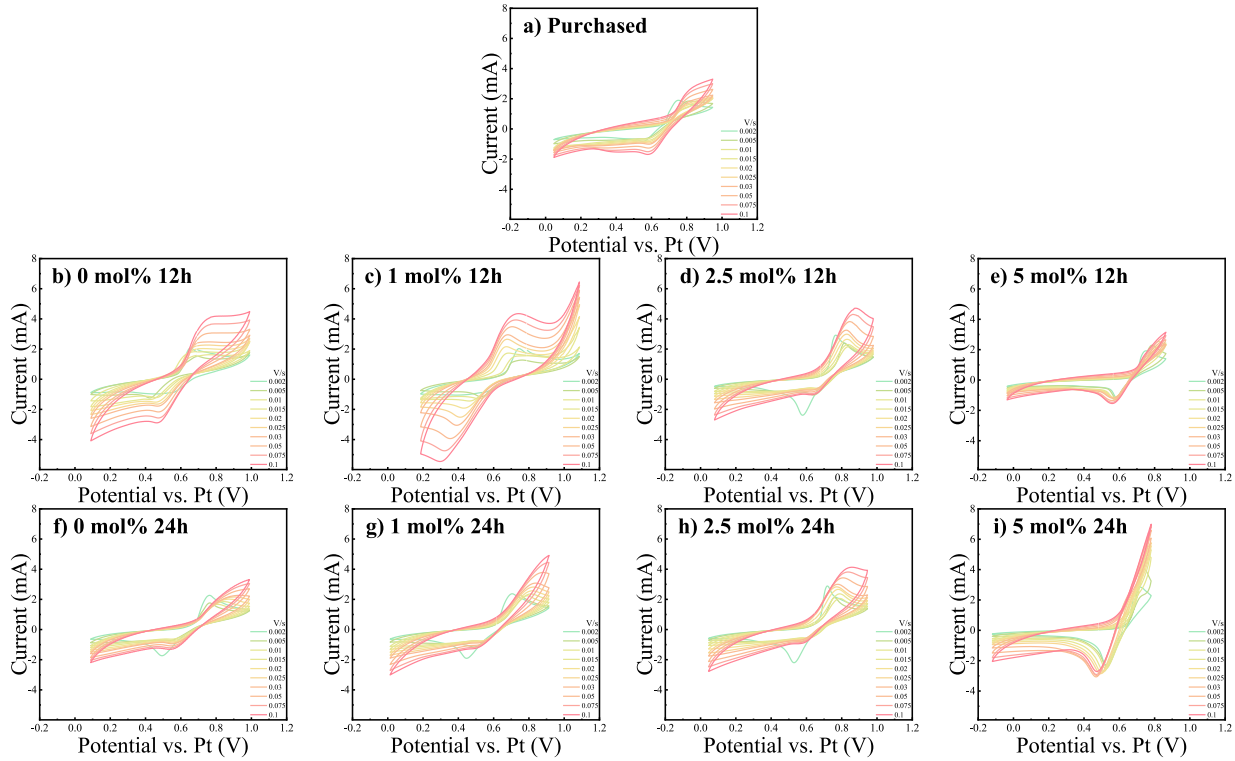


Fig. 3. CV graphs of a) purchased MnO_2 and b) - i) synthesised pure and Mo-doped MnO_2 samples.

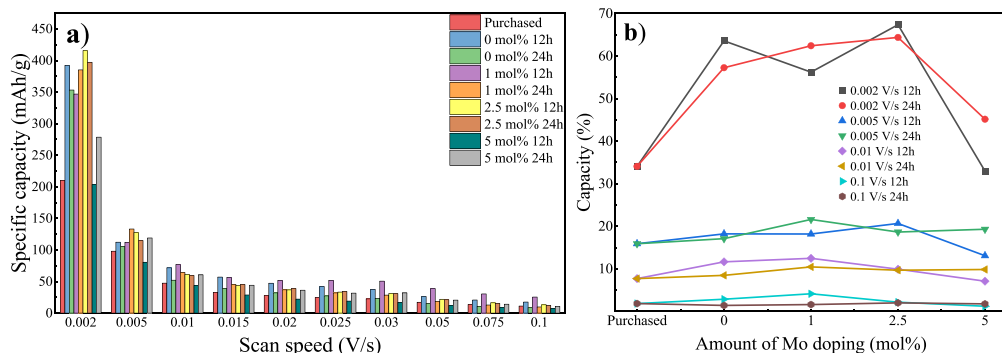


Fig. 4. a) Specific capacity of purchased and Mo-doped MnO₂ at various scan speeds from CV measurements and b) capacity of the MnO₂ theoretical maximal depending on Mo-doping amount.

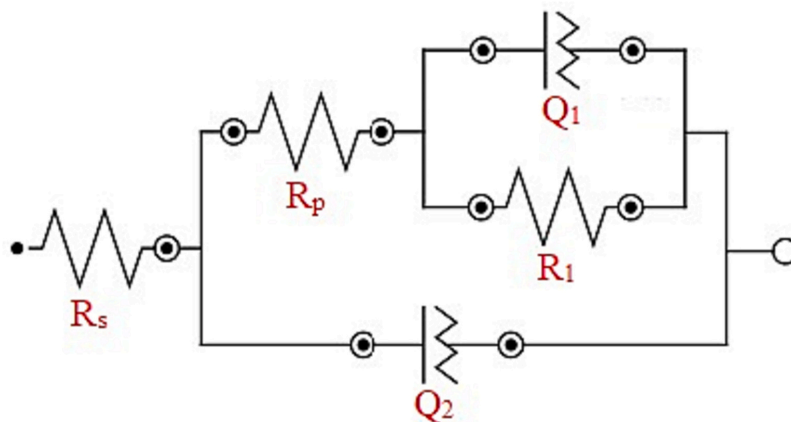


Fig. 5. Equivalent circuit model scheme for Nyquist plot fitting.

Table 2
The equivalent circuit parameters on interface electrode/electrolyte.

N ^o	Parameter	R _s	R _p	Q ₁	R ₁	Q ₂
Sample		Ω	Ω	μF	Ω	μF
1	Purchased	24.82	1.56	2540	692.54	368
2	0 mol% 12 h	12.91	0.56	33,950	473.91	922
3	0 mol% 24 h	11.46	3.37	3886	1179.20	143
4	1 mol% 12 h	9.90	2.38	16,900	389.53	2250
5	1 mol% 24 h	32.00	0.05	749	1034.30	4380
6	2.5 mol% 12 h	11.52	3.06	156	274.44	2560
7	2.5 mol% 24 h	10.62	1.42	118	164.02	1818
8	5 mol% 12 h	10.44	1.82	7	1943.50	2229
9	5 mol% 24 h	10.53	0.47	2992	652.43	61

α-MnO₂ [41,46,47]. Despite two additional peak appearances no phase changes are observed as after cathode cycling more pronounced thin layer (Fig. 2S) has grown and the expressiveness of the peaks depends on the particle morphology [48]. Moreover, no carbon bonds can be identified after electrochemically cycling the cathode as MnO₂ had grown over the CB from the initial ink during the CV measurement. The same trend can be seen in EDX mapping results (Fig. 6S) where carbon can be identified in samples before CV measurements and not in samples after CV measurements. This suggests that a dense layer of MnO₂

electrode has grown on the conductive carbon substrate surface with estimated layer thickness from SEM image (Fig. 7S) up to 2 μm. Moreover, EDX mapping results (Fig. 6S) show that Mo is evenly dispersed across all sample surfaces before and after CV measurements. Individual particles or spots with high Mo concentrations were not observed.

4. Conclusion

In this work, MnO₂ was hydrothermally synthesised for 12 or 24 h with different amounts of Mo content. Obtained samples were compared with commercially purchased MnO₂. The elemental composition investigation with XPS and EDX reveals successful Mo doping of MnO₂ samples. From XRD results we observed the δ-MnO₂ and α-MnO₂ phases formation as a form of Mn₇O₁₃·5H₂O and K₂₋₃Mn₈O₁₆. CV measurements were performed in an acidic electrolyte (pH = 1.5) to estimate the specific capacity of synthesised samples, which ranged from 220 mAh/g to 415 mAh/g with the highest capacity for 2.5 mol% Mo-doped sample synthesised for 12 h. Also, CP measurements were performed with increasing charge-discharge rates that showed improved stability of capacity for samples with larger Mo doping. The best results were for samples with 5 mol% Mo-doping suggesting that Mo additive promotes better capacity retention for faster cycling rates. Overall, all synthesised MnO₂ samples with Mo doping up to 2.5 % show an improvement in

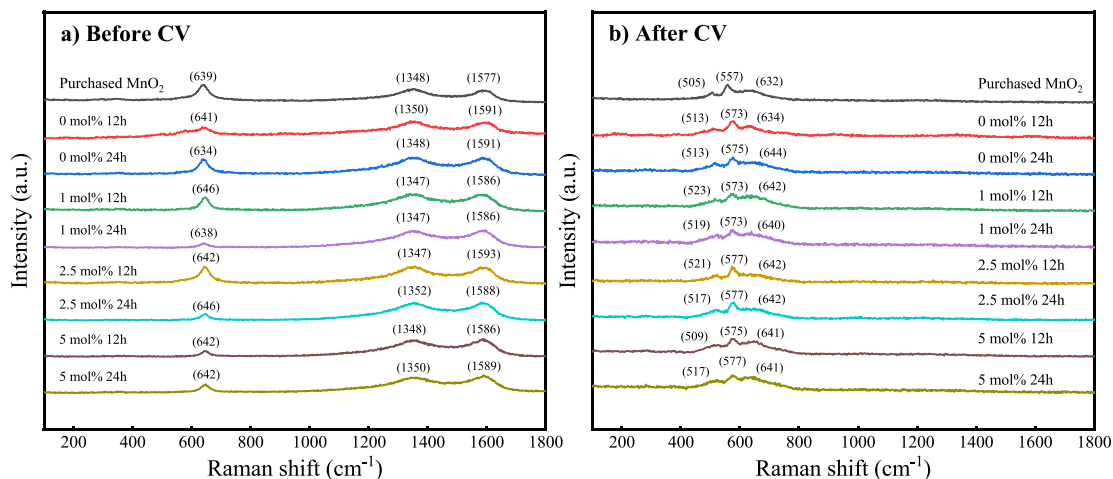


Fig. 6. Raman spectroscopy results of purchased and synthesised MnO₂ a) before and b) after CV.

specific capacity compared to the commercial MnO₂. From the Raman measurements, the α -MnO₂ phase was observed before and after CV measurements. SEM images reveal a dense MnO₂ layer (up to 2 μ m) formation that contained evenly distributed Mo ions throughout the electroactive surface of the cathode material before and after CV measurements.

CRediT authorship contribution statement

Nikita Griščenko: Methodology, Validation, Formal analysis, Investigation, Writing – original draft, Visualization. **Ramona Dūrena:** Conceptualization, Methodology, Validation, Formal analysis, Investigation, Writing – original draft, Writing – review & editing, Visualization. **Mairis Iesalnieks:** Methodology, Formal analysis, Investigation. **Māris Bērtiņš:** Methodology, Formal analysis, Investigation. **Arturs Viksna:** Methodology, Formal analysis, Investigation. **Anzelms Zukuls:** Conceptualization, Methodology, Validation, Formal analysis, Investigation, Writing – original draft, Writing – review & editing, Visualization, Supervision, Project administration, Funding acquisition.

Declaration of competing interest

The authors declare that they have no known competing financial interests or personal relationships that could have appeared to influence the work reported in this paper.

Data availability

Data will be made available on request.

Acknowledgement

This work was supported by the Latvian Council of Science in the framework of FLPP (Investigation of electrodes and electrolytes for obtaining amphoteric decoupled rechargeable batteries, lzp-2021/1-0142).

Appendix A. Supplementary data

Supplementary data to this article can be found online at <https://doi.org/10.1016/j.est.2023.109847>.

References

- [1] M. Leonard, J. Pisani-Ferry, J. Shapiro, S. Tagliapietra, G.B. Wolff, The Geopolitics of the European Green Deal Standard-Nutzungsbedingungen, n.d. <http://hdl.handle.net/10419/237660>.
- [2] T. Xue, H.J. Fan, From aqueous Zn-ion battery to Zn-MnO₂ flow battery: a brief story, *J. Energy Chem.* 54 (2021) 194–201, <https://doi.org/10.1016/j.jechem.2020.05.056>.
- [3] M. Gu, I. Belharouak, A. Genc, Z. Wang, D. Wang, K. Amine, F. Gao, G. Zhou, S. Thevuthasan, D.R. Baer, J.G. Zhang, N.D. Browning, J. Liu, C. Wang, Conflicting roles of nickel in controlling cathode performance in lithium ion batteries, *Nano Lett.* 12 (2012) 5186–5191, <https://doi.org/10.1021/nl302249v>.
- [4] L.S. Martins, L.F. Guimarães, A.B. Botelho Junior, J.A.S. Tenório, D.C.R. Espinosa, Electric car battery: an overview on global demand, recycling and future approaches towards sustainability, *J. Environ. Manag.* 295 (2021), <https://doi.org/10.1016/j.jenvman.2021.113091>.
- [5] F. Maisel, C. Neef, F. Marscheider-Weidemann, N.F. Nissen, A forecast on future raw material demand and recycling potential of lithium-ion batteries in electric vehicles, *Resour. Conserv. Recycl.* 192 (2023), <https://doi.org/10.1016/j.resconrec.2023.106920>.
- [6] N. Zhang, F. Cheng, J. Liu, L. Wang, X. Long, X. Liu, F. Li, J. Chen, Rechargeable aqueous zinc-manganese dioxide batteries with high energy and power densities, *Nat. Commun.* 8 (2017), <https://doi.org/10.1038/s41467-017-00467-x>.
- [7] L. Kavanagh, J. Keohane, G.G. Cabellos, A. Lloyd, J. Cleary, Global lithium sources-industrial use and future in the electric vehicle industry: a review, *Resources* 7 (2018), <https://doi.org/10.3390/resources7030057>.
- [8] M.B. Lim, T.N. Lambert, B.R. Chalamala, Rechargeable alkaline zinc–manganese oxide batteries for grid storage: mechanisms, challenges and developments, *Mater. Sci. Eng. R. Rep.* 143 (2021), <https://doi.org/10.1016/j.mser.2020.100593>.
- [9] M. Chamoun, Rechargeable Aqueous Batteries Based on Available Resources Investigation and Development towards Efficient Battery Performance, n.d. <http://urn.kb.se/resolve?urn=urn:nbn:se:udiva-163154>.
- [10] P. Vanýšek, *CRC Handbook of Chemistry and Physics*, 91th edition, Marcel Dekker, 1978.
- [11] J. Xu, X. Hu, M.A. Alam, G. Muhammad, Y. Lv, M. Wang, C. Zhu, W. Xiong, Al-doped α -MnO₂coated by lignin for high-performance rechargeable aqueous zinc-ion batteries, *RSC Adv.* 11 (2021) 35280–35286, <https://doi.org/10.1039/d1ra06808c>.
- [12] B.J. Hertzberg, A. Huang, A. Hsieh, M. Chamoun, G. Davies, J.K. Seo, Z. Zhong, M. Croft, C. Erdonmez, Y.S. Meng, D. Steingart, Effect of multiple cation electrolyte mixtures on rechargeable Zn-MnO₂ alkaline battery, *Chem. Mater.* 28 (2016) 4536–4545, <https://doi.org/10.1021/acs.chemmater.6b00232>.
- [13] J. Ji, J. Yao, Y. Xu, H. Wan, B. Zhang, L. Lv, J. Li, N. Wang, Z. Zheng, J. Zhang, G. Ma, L. Tao, H. Wang, Y. Wang, H. Wang, Promoting proton migration kinetics by Ni²⁺ regulating enables improved aqueous Zn-MnO₂ batteries, *Energy Environ. Mater.* (2022), <https://doi.org/10.1002/eeem.2.12340>.
- [14] Y. Zhang, Y. Liu, Z. Liu, X. Wu, Y. Wen, H. Chen, X. Ni, G. Liu, J. Huang, S. Peng, MnO₂ cathode materials with the improved stability via nitrogen doping for aqueous zinc-ion batteries, *J. Energy Chem.* 64 (2022) 23–32, <https://doi.org/10.1016/j.jechem.2021.04.046>.
- [15] Z. Zheng, G. Yang, J. Yao, J. Li, J. Zheng, Z. Wu, Y. Gan, C. Wang, L. Lv, H. Wan, C. Chen, H. Wang, L. Tao, J. Zhang, H. Wang, High-valence molybdenum promoted proton migration and inhibited dissolution for long-life aqueous Zn-MnO₂

- batteries, *Appl. Surf. Sci.* 592 (2022), <https://doi.org/10.1016/j.apsusc.2022.153335>.
- [16] J. Liu, J. Bao, X. Zhang, Y. Gao, Y. Zhang, L. Liu, Z. Cao, MnO₂-based materials for supercapacitor electrodes: challenges, strategies and prospects, *RSC Adv.* 12 (2022) 35556–35578, <https://doi.org/10.1039/d2ra06664e>.
- [17] S. Devaraj, N. Munichandraiah, Effect of crystallographic structure of MnO₂ on its electrochemical capacitance properties, *J. Phys. Chem. C* 112 (2008) 4406–4417, <https://doi.org/10.1021/jp7108785>.
- [18] A.B. Brady, K.R. Tallman, E.S. Takeuchi, A.C. Marschilok, K.J. Takeuchi, P. Liu, Transition metal substitution of hollandite α -MnO₂: enhanced potential and structural stability on lithiation from first-principles calculation, *J. Phys. Chem. C* 123 (2019) 25042–25051, <https://doi.org/10.1021/acs.jpcc.9b05376>.
- [19] B.J. Kennedy, Thermal expansion of pyrolusite, β -MnO₂; a synchrotron X-ray diffraction study, *J. Phys. Chem. Solids* 125 (2019) 131–134, <https://doi.org/10.1016/j.jpcs.2018.09.029>.
- [20] K. Galliez, P. Deniard, D. Lambertin, S. Jobic, F. Bart, Influence of MnO₂ polymorphism form on MnO₂/Ag 20 hydrogen getter, *J. Nucl. Mater.* 438 (2013) 261–267, <https://doi.org/10.1016/j.jnucmat.2013.03.053>.
- [21] S. Ching, D.J. Petrovay, M.L. Jorgensen, S.L. Suib, Sol-gel Synthesis of Layered Birnessite-type Manganese Oxides, 1997.
- [22] D.A. Kitchaev, S.T. Dacek, W. Sun, G. Ceder, Thermodynamics of phase selection in MnO₂ framework structures through alkali intercalation and hydration, *J. Am. Chem. Soc.* 139 (2017) 2672–2681, <https://doi.org/10.1021/jacs.6b11301>.
- [23] B.W. Byles, N.K.R. Palapati, A. Subramanian, E. Pomerantseva, The role of electronic and ionic conductivities in the rate performance of tunnel structured manganese oxides in Li-ion batteries, *APL Mater.* 4 (2016), <https://doi.org/10.1063/1.4948272>.
- [24] S.C. Pang, S.F. Chin, C.Y. Ling, Controlled synthesis of manganese dioxide nanostructures via a facile hydrothermal route, *J. Nanomater.* 2012 (2012), <https://doi.org/10.1155/2012/607870>.
- [25] T. Lin, J. Lin, X. Wei, L. Lu, X. Yin, Hydrothermal synthesis of nano-sized MnO₂ supported on attapulgite electrode materials for supercapacitors, *Int. J. Hydrog. Energy* 48 (2023) 10765–10777, <https://doi.org/10.1016/j.ijhydene.2022.12.151>.
- [26] D. Su, H.J. Ahn, G. Wang, Hydrothermal synthesis of α -MnO₂ and β -MnO₂ nanorods as high capacity cathode materials for sodium ion batteries, *J. Mater. Chem. A Mater.* 1 (2013) 4845–4850, <https://doi.org/10.1039/c3ta00031a>.
- [27] G. Yang, S.J. Park, Conventional and microwave hydrothermal synthesis and application of functional materials: a review, *Materials* 12 (2019), <https://doi.org/10.3390/ma12071177>.
- [28] L.Y. Meng, B. Wang, M.G. Ma, K.L. Lin, The progress of microwave-assisted hydrothermal method in the synthesis of functional nanomaterials, *Mater Today Chem.* 1–2 (2016) 63–83, <https://doi.org/10.1016/j.mtchem.2016.11.003>.
- [29] P. Umek, R.C. Korosec, A. Gloter, U. Pirnat, The control of the diameter and length of α -MnO₂ nanorods by regulation of reaction parameters and their thermogravimetric properties, *Mater. Res. Bull.* 46 (2011) 278–284, <https://doi.org/10.1016/j.materresbull.2010.10.012>.
- [30] R. Rajagopal, K.S. Ryu, Morphologically engineered cactus-like MnO₂ nanostructure as a high-performance electrode material for energy-storage applications, *J. Energy Storage* 32 (2020), <https://doi.org/10.1016/j.est.2020.101880>.
- [31] W. Xie, J. Wang, X. Long, X. Wang, S. Zou, L. Zhang, H. Xu, Y. Fu, D. Liu, Y. Li, J. Li, D. He, One-step construction of δ -MnO₂ cathodes with an interconnected nanosheet structure on graphite paper for high-performance aqueous asymmetric supercapacitors, *J. Energy Storage* 35 (2021), <https://doi.org/10.1016/j.est.2021.102308>.
- [32] H. Li, Z. Huang, B. Chen, Y. Jiang, C. Li, W. Xiao, X. Yan, A high-performance MnO₂ cathode doped with group VII metal for aqueous Zn-ion batteries: in-situ X-ray diffraction study on Zn²⁺ storage mechanism, *J. Power Sources* 527 (2022), <https://doi.org/10.1016/j.jpowsour.2022.231198>.
- [33] V.M. Tran, A.T. Ha, M.L.P. Le, Capacitance behavior of nanostructured ϵ -MnO₂/C composite electrode using different carbons matrix, *Adv. Nat. Sci. Nanosci. Nanotechnol.* 5 (2014), <https://doi.org/10.1088/2043-6262/5/2/025005>.
- [34] S.Y. Chen, W. Song, H.J. Lin, S. Wang, S. Biswas, M. Mollahosseini, C.H. Kuo, P. X. Gao, S.L. Suib, Manganese oxide Nanoarray-based monolithic catalysts: tunable morphology and high efficiency for CO oxidation, *ACS Appl. Mater. Interfaces* 8 (2016) 7834–7842, <https://doi.org/10.1021/acsami.6b00578>.
- [35] V. Climent, J.M. Feliu, Cyclic voltammetry, in: *Encyclopedia of Interfacial Chemistry: Surface Science and Electrochemistry*, Elsevier, 2018, pp. 48–74, <https://doi.org/10.1016/B978-0-12-409547-2.10764-4>.
- [36] A.W. Bott, The study of multiple electron transfer reactions by cyclic voltammetry, *Curr. Sep.* 16 (1997) 61–66, <http://www.currentseparations.com/issues/16-2/cs16-2e.pdf> (accessed July 13, 2023).
- [37] S. Khamsanga, R. Pornprasertsuk, T. Yonezawa, A.A. Mohamad, S. Kheawhom, δ -MnO₂ nanoflower/graphite cathode for rechargeable aqueous zinc ion batteries, *Sci. Rep.* 9 (2019), <https://doi.org/10.1038/s41598-019-44915-8>.
- [38] D. Qu, The Ac Impedance Studies for Porous MnO₂ Cathode by Means of Modified Transmission Line Model, n.d.
- [39] W. Choi, H.C. Shin, J.M. Kim, J.Y. Choi, W.S. Yoon, Modeling and applications of electrochemical impedance spectroscopy (Eis) for lithium-ion batteries, *J. Electrochem. Sci. Technol.* 11 (2020) 1–13, <https://doi.org/10.33961/jest.2019.00528>.
- [40] H.R. Barai, A.N. Banerjee, S.W. Joo, Improved electrochemical properties of highly porous amorphous manganese oxide nanoparticles with crystalline edges for superior supercapacitors, *J. Ind. Eng. Chem.* 56 (2017) 212–224, <https://doi.org/10.1016/j.jiec.2017.07.014>.
- [41] S. Bernardini, F. Bellatreccia, A. Casanova, M. Mucchia, G. Della Ventura, A. Sodo, Raman spectra of natural manganese oxides, *J. Raman Spectrosc.* 50 (2019) 873–888, <https://doi.org/10.1002/jrs.5583>.
- [42] H.U. Shah, F. Wang, M.S. Javed, M.A. Ahmad, M. Saleem, J. Zhan, Z.U.H. Khan, Y. Li, In-situ growth of MnO₂ nanorods forest on carbon textile as efficient electrode material for supercapacitors, *J. Energy Storage* 17 (2018) 318–326, <https://doi.org/10.1016/j.est.2018.03.015>.
- [43] X.H. Feng, W.F. Tan, F. Liu, J.B. Wang, H.D. Ruan, Synthesis of todorokite at atmospheric pressure, *Chem. Mater.* 16 (2004) 4330–4336, <https://doi.org/10.1021/cm0499545>.
- [44] M. Saravanan, M. Ganesan, S. Ambalavanan, An in situ generated carbon as integrated conductive additive for hierarchical negative plate of lead-acid battery, *J. Power Sources* 251 (2014) 20–29, <https://doi.org/10.1016/j.jpowsour.2013.10.143>.
- [45] G. Lota, P. Krawczyk, K. Lota, A. Sierczyńska, L. Kolanowski, M. Baraniak, T. Buchwald, The application of activated carbon modified by ozone treatment for energy storage, *J. Solid State Electrochem.* 20 (2016) 2857–2864, <https://doi.org/10.1007/s10008-016-3293-5>.
- [46] C.M. Julien, M. Massot, C. Poinssignon, Lattice vibrations of manganese oxides: part I. Periodic structures, *Spectrochim. Acta A Mol. Biomol. Spectrosc.* 60 (2004) 689–700, [https://doi.org/10.1016/S1386-1425\(03\)00279-8](https://doi.org/10.1016/S1386-1425(03)00279-8).
- [47] Y. Xie, Y. Yu, X. Gong, Y. Guo, Y. Wang, G. Lu, Effect of the crystal plane figure on the catalytic performance of MnO₂ for the total oxidation of propane, *CrystEngComm* 17 (2015) 3005–3014, <https://doi.org/10.1039/c5ce00058k>.
- [48] S. Jana, S. Basu, S. Pande, S.K. Ghosh, T. Pal, Shape-selective synthesis, magnetic properties, and catalytic activity of single crystalline β -MnO₂ nanoparticles, *J. Phys. Chem. C* 111 (2007) 16272–16277, <https://doi.org/10.1021/jp0748031>.

Appendix 4

4. pielikums

R. Dūrena, L. Fedorenko, Ņ. Griščenko, M. Vanags, L. Orlova, P. Onufrijevs, S. Stanionyte,
T. Malinauskas A. Zukuls

**Irradiating the Path to High-Efficiency Zn-Ion Batteries: An Electrochemical Analysis
of Laser-Modified Anodes**

Global Challenges, 8 (10), 2024, 2400105

DOI: 10.1002/gch2.202400105

Irradiating the Path to High-Efficiency Zn-Ion Batteries: An Electrochemical Analysis of Laser-Modified Anodes

Ramona Durena,* Leonid Fedorenko, Nikita Griscenko, Martins Vanags, Liga Orlova, Pavels Onufrijevs, Sandra Stanionyte, Tadas Malinauskas, and Anzelms Zukuls*

Global energy consumption is increasing yearly, yet the world is trying to move toward carbon neutrality to mitigate global warming. More research is being done on energy storage devices to advance these efforts. One well-known and widely studied technology is Zn-ion batteries (ZIBs). Therefore, this paper demonstrates how laser irradiation at wavelengths of 266 and 1064 nm, in the presence of air or water, can enhance the electrochemical performance of metallic zinc anode in alkaline electrolyte. The obtained samples are characterized using X-ray diffraction analysis, scanning electron microscopy, and Raman spectroscopy. Then, the electrochemical properties are studied by cyclic voltammetry and impedance measurements. Results indicate that the laser processing of the Zn sample increases surface-specific capacity by up to 30% compared to the non-irradiated Zn sample. Furthermore, electrochemical measurements reveal enhanced participation of metallic Zn grains in the oxidation and reduction processes in irradiated samples. In future research, integrating laser treatment into electrode preparation processes can become essential for optimizing anode battery materials.

1. Introduction

Global energy production from renewable sources continues to increase alongside that from fossil fuels. Moreover, global energy consumption increases annually. Achieving carbon neutrality necessitates reducing fossil fuel consumption while scaling up renewable energy production.^[1] A significant hurdle for the widespread adoption of renewable energy is the variability in energy production over time. Implementing diverse energy storage systems is crucial to store surplus energy for future use.^[2–4]

For now, the most used secondary battery systems are Li-ion batteries (f). They have been and will probably continue to dominate the portable device market. However, LIBs are not economically viable for battery energy storage systems due to the scarcity of the necessary metals, and the safety risks the LIBs oppose.^[5–10] Alternative to LIBs for larger energy storage facilities are Zn-ion batteries (ZIBs). Metallic Zn is more readily available, with lower costs and reduced safety risks.^[11–13] However, applying metallic Zn as an anode has several solvable drawbacks. The main problems with Zn anodes are electrochemical hydrogen evolution reaction (HER), corrosion passivation, and dendrite growth.^[14–16]

HER is a severe ZIB problem because hydrogen gas generation can lead to battery swelling or even explosion. Theoretically, HER is more thermodynamically favorable than Zn plating because its standard potential is lower. In neutral electrolytes, the equilibrium potential of Zn^{2+}/Zn is -0.76 V versus standard hydrogen electrode (SHE), and H_2O/H_2 is 0 V versus SHE; however, in alkaline electrolytes, the equilibrium potentials are -1.26 V versus SHE and -0.83 V versus SHE, respectively.^[17–20] Although HER is theoretically more favorable, the Zn plating reaction will overtake HER due to the low hydrogen ion activity and high overpotential. However, HER can still occur under certain conditions like high polarization during charging, high current density, and low potential. As a result, the Coulombic efficiency (CE) decreases, hazardous hydrogen gas is released, the pH of the electrolyte changes locally, the amount of electrolyte decreases, and the battery dries out over a more extended period of time.^[21–26]

Similar to the electrochemical HER process, a chemical reaction of Zn metal with an aqueous electrolyte can also occur, resulting in the release of gaseous hydrogen and the conversion

R. Durena, N. Griscenko, M. Vanags, L. Orlova, A. Zukuls
Institute of Materials and Surface Engineering
Faculty of Natural Sciences and Technology
Riga Technical University
Paula Valdena Street 7, Riga LV-1048, Latvia
E-mail: ramona.durena@rtu.lv; anzelm.zukuls@rtu.lv

L. Fedorenko
Lashkaryov Institute of Semiconductor Physics
National Academy of Sciences of Ukraine
Prospect Nauki 41, Kyiv 03028, Ukraine

L. Fedorenko, P. Onufrijevs
Institute of Technical Physics
Faculty of Natural Sciences and Technology
Riga Technical University
Paula Valdena Street 7, Riga LV-1048, Latvia

S. Stanionyte
Center for Physical Sciences and Technology
Sauletekio Ave. 3, Vilnius LT-10257, Lithuania

T. Malinauskas
Institute of Photonics and Nanotechnology
Vilnius University
Sauletekio Ave. 3, Vilnius LT-10257, Lithuania

 The ORCID identification number(s) for the author(s) of this article can be found under <https://doi.org/10.1002/gch2.202400105>

© 2024 The Author(s). Global Challenges published by Wiley-VCH GmbH. This is an open access article under the terms of the [Creative Commons Attribution License](#), which permits use, distribution and reproduction in any medium, provided the original work is properly cited.

DOI: 10.1002/gch2.202400105

of Zn from the metal to the solution in the form of the Zn^{2+} ion, thereby losing capacity. In addition to this corrosion process, OH^- ions are formed due to water splitting, which increases the pH of the electrolyte. Thus, inert by-products are formed because of these pH changes, which cover the surface of the anode and interfere with the further progress of the desired reaction. However, these products are not dense enough to stop the progress of side reactions.^[27–31]

The formation of dendrites in batteries on the anode surface is also common in other metal anode batteries, such as LIBs.^[32,33] The pre-conditions for their formation are widely studied and well understood. The leading cause of their formation is related to inhomogeneities of the anode surface, such as protrusions, crystallite boundaries, lattice defects, impurities, etc., which lead to an inhomogeneous electric field. This, in turn, promotes inhomogeneous deposition of Zn, forming peaks, which further contribute to various “tip” effects. Such uncontrolled growth of dendrites usually leads to separator piercing, short-circuiting, or “dead” zinc in case of dendrite breakage, which reduces anode capacity and CE.^[34–37] According to the literature, the Zn (002) plane is the most suitable for battery anodes compared to Zn (100) and Zn (101) growth planes.^[38] The Zn (002) plane has a smaller self-diffusion barrier, resulting in lower resistance to ad-atom movement on the surface of Zn. Limited ad-atom movement is the main reason for dendrite growth on Zn (100) and Zn (101) planes. The growth and dissolution of Zn/Zn^{2+} on a polycrystalline Zn surface lead to a loose and porous deposition of the Zn layer, which negatively impacts the reversibility of the anode. Additionally, side reactions, by-product accumulation, and hydrogen evolution are more pronounced on these surfaces.^[39]

All these processes are interrelated and reduce the capacity and efficiency of the Zn anode. The main directions as the scientific community tries to prevent these unwanted actions and improve the Zn anode performance are coating the electrode or modifying the electrolyte that controls and guides the stripping/plating reaction. Some coating options include $CaCO_3$,^[40] ZnO ,^[41–43] ZrO_2 ,^[44–46] and TiO_2 .^[47–49] Other scientists have used a slightly different approach to coating Zn anode by employing different polymer layers.^[50–53]

The roll-press formation of Zn sheets induces surface defects such as roughened surfaces, scratches, folds, and new edges that are prone to dendrite growth.^[39] During the manufacturing process of roll-pressed Zn, the (002) textured plane structure formation can be promoted through heating-rolling processes. However, the previously mentioned defects still occur.^[39] To eliminate the effects of introduced surface defects, surface polishing can be utilized. Studies show that polishing can increase the cycling lifespan of an electrode more than seven times.^[39] Various methods can be used for metal surface polishing, including mechanical,^[39] chemical,^[54] electrical^[55] and laser^[56] polishing.

Laser processing is cost-efficient and compatible for large-scale production compared to various chemical routes.^[57] However, this approach has received very little attention regarding Zn anode as only a few researchers have published work in this area. C. Yang et al.^[58] have modified the Zn anode with a laser-induced graphene coating, Z. Na et al.^[59] have used a laser lithography strategy, D. Yao et al.^[60] have applied femtosecond-laser filament texturing, and H. Jin et al.^[61] have employed the surface texture through a laser-micromachining method. All these works have

presented effective strategies to improve the Zn anode, highlighting the need for more attention to the laser pretreatment of metal anodes. This approach could be particularly beneficial for roll-pressed Zn substrates, as it can address surface defects and enhance Zn growth and dissolution properties. By reducing the residual stresses formed during the manufacturing of Zn sheets, oriented growth of newly plated Zn metal layers can be expected. Also, by combining it with separators, it would be possible to provide the desired uniform hexagonal zinc deposition.^[62] Therefore, in this study, the Zn anode surface was modified using pulsed laser radiation. It is well known that the effective surface area of the working electrode significantly influences charge accumulation and current flow in the anode-electrolyte system. Pulsed laser radiation, which reaches or exceeds the microablation threshold in terms of energy density (fluence – F), is recognized as highly efficient for modifying this parameter. The aim of this work was to investigate how laser processing with varying energy densities and different environments (air, water) in the active technological zone influences structural properties. Additionally, the electrochemical properties of the half-cell system consisting of a zinc plate anode and a 1 M KOH electrolyte solution were examined. This investigation revealed a surface-specific capacity increase of up to 30%, decreased charge transfer resistance, and more pronounced Zn crystal grain boundaries after electrochemical cycling.

2. Experimental Section

Zinc plates were purchased from Goodfellow Cambridge Ltd. (Zinc foil, 0.20 mm, 99.95+%), deionized waters was prepared using Adrona Crystal Sterifeed and used without further purification, KOH (pallets for analysis) was purchased from Sigma Aldrich and used without further purification. The zinc plate was washed/rinsed in deionized water/ethanol before laser irradiation to remove loose metal particles and degrease them from factory oils.

Zinc metal plates were irradiated with a nanosecond pulse Nd:YAG laser (model: NL301G, produced by Ekspla, Lithuania). Laser processing involved two different wavelengths ($\lambda_1 = 1064$ and $\lambda_2 = 266$ nm), with fluences ranging from 0.32 to 2.66 J cm⁻², under various environmental conditions (air and deionized water). The Zn surface was irradiated using pulses with a duration of $t_p = 6$ ns in scanning mode, with a repetition frequency of laser pulses in the range from 1 to 10 Hz. This setup allowed control over the overlap of the laser spot on the Zn plate surface. A schematic of the irradiation process is shown in Figure 1a, where $\Delta X = 0.125$ mm and $d = 1.2$ mm. Additionally, the laser wavelengths were varied, considering the different interactions of UV (266 nm) and infrared (IR) (1064 nm) rays with zinc oxide (ZnO) that may form during laser processing. The scanning step was selected close to the diameter of the laser spot to maximize surface heterogeneity and effective area. Detailed information about the irradiated samples can be found in Table S1 (Supporting Information).

The structural characterization of the samples before and after electrochemical measurements was performed using X-ray diffraction (XRD). Measurements were performed using the Smartlab (Rigaku, Japan) diffractometer with a 9 kW rotating Cu anode X-ray generator. Theta/2theta scans were measured with a

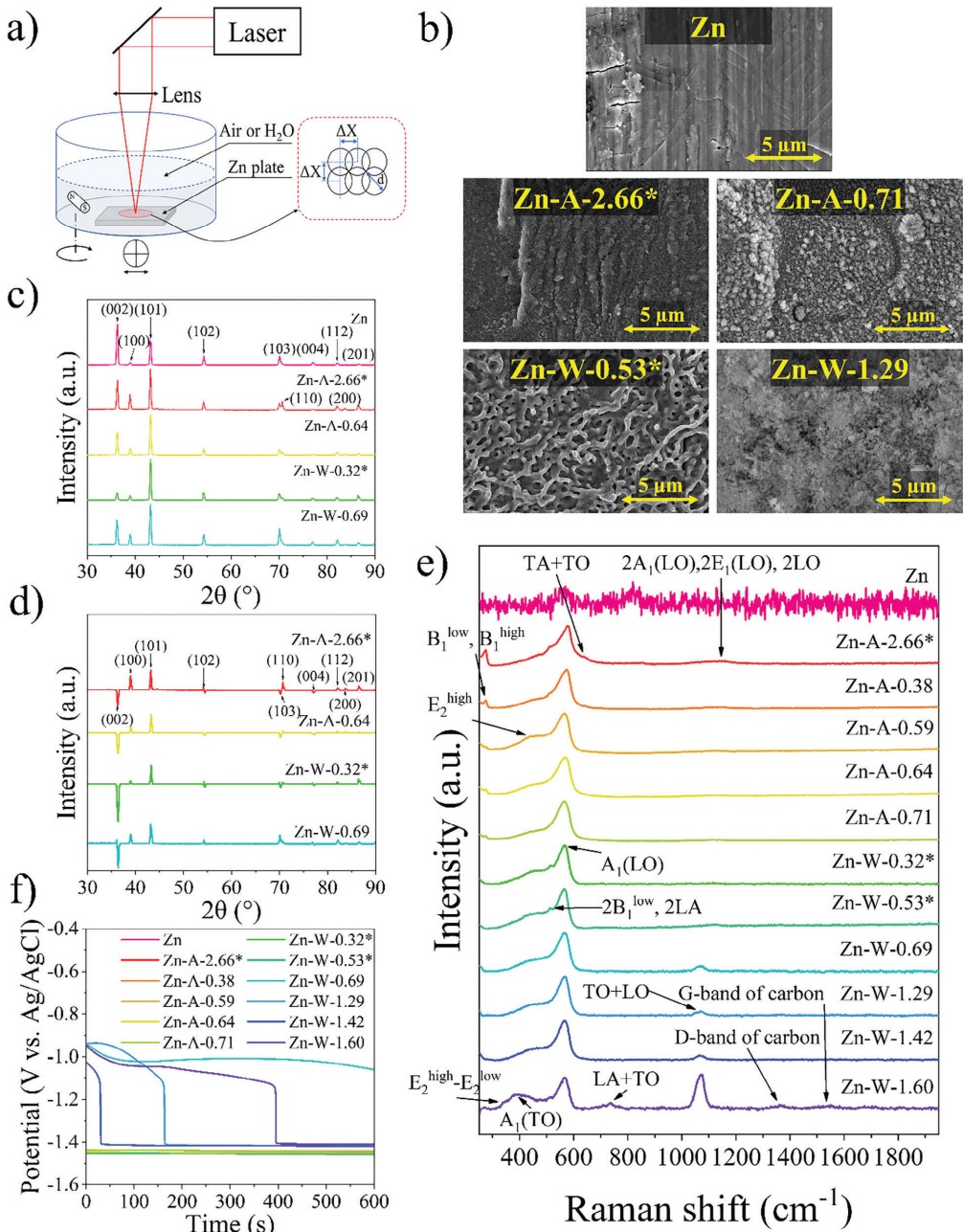


Figure 1. Pure and irradiated Zn sample characterization as prepared before electrochemical measurements: a) sample irradiation setup; b) SEM images; c) XRD diffractograms; d) difference between sample XRD and pure Zn (sample XRD spectrum minus pure Zn XRD spectrum); e) Raman analysis; f) OCP.

step size of 0.02° , with a total scan range from 30 to 90° . Obtained XRD results were analyzed using the PDF 4+ database.

Raman spectra analysis was performed for the samples before and after CV measurements at room temperature under $500\times$ magnification using a Renishaw In-ViaV727 spectrometer in backscattering geometry. The spectrometer was operated with an Ar⁺ green laser (wavelength $\lambda = 514.5$ nm, grating -1200 mm⁻¹, power -10 mW), exposure time 10 s.

FEI Nova SEM230 and Hitachi TM3000 Tabletop scanning electron microscope (SEM) with an acceleration voltage of 10 kV and 15 kV were used to characterize sample surface morphology.

Total reflectance spectra were measured with a UV-Vis-NIR optical spectrometer (Ossila Optical Spectrometer). The measurement system consisted of a light source Ocean Insight "Broad-band LED" and integrated sphere (Thorlabs, General-Purpose $\varnothing 50$ mm Integrating Spheres).

Various electrochemical properties were measured using Potentiostat-Galvanostat Autolab PGSTAT302N. Cyclic voltammetry (CV) measurements were performed in the "TSC Surface" (from rhd instruments) measuring cell using a 3-electrode system configuration. As received and laser irradiated sample zinc plates were used as working electrodes, 1 mL of 1 M KOH solution was used as an electrolyte, a platinum rod was used as a counter electrode, and a double junction configuration Ag/AgCl (3 M KCl) electrode was used as a reference electrode. For this study, no separators were used, to exclude the interference of the separator-induced growth effects on the Zn anode that has been mentioned in literature.^[62] The CV measurements were performed in a potential window of -1.9 V to -0.6 V Ag AgCl⁻¹ with variable scan rates from 0.005 to 0.1 V s⁻¹. Impedance spectroscopy (EIS) was performed by applying a ± 150 mV small perturbation voltage in the 100 kHz to 0.1 Hz frequency range. For obtained data and equivalent scheme analysis, NOVA 2.1 software was used.

3. Results and Discussion

3.1. Sample Characterization

The obtained sample abbreviations are based on the applied fluence and their irradiation parameters, and visual photos are shown in Table S1 (Supporting Information). Visual observations concluded that laser-irradiated sample surface morphology is homogeneous throughout all the irradiated 12×12 mm squares. Changes in the surface morphology and color were noticed. Diffuse reflectance measurements were performed to evaluate optical changes (Figure S1, Supporting Information) in the laser-irradiated samples. The obtained spectra show that the surface of the irradiated samples reflects less light than a pure Zn plate. This observation can be attributed to the formation of a ZnO layer on the irradiated surfaces. Similar findings of ZnO formation have also been observed when irradiating Zn samples in air and ethanol medium.^[63] The resulting ZnO layer may contain interstitials and crystal defects, which would explain the reduced relative diffuse reflectance. Additionally, possible signs of luminescence can be observed in the 350 – 400 nm range, further indicating ZnO formation.^[64]

Surface imaging was performed using SEM to investigate the obtained samples further. The SEM images are shown in

Figure 1b (images for all samples are shown in Figure S2, Supporting Information). Characteristic signs of cold metal rolling can be observed on the surface of all these samples. The surface of a Zn plate consists of pressed-down sharp-edged grains with visible stretching marks. However, following laser irradiation, the Zn surface melted to varying degrees, which, depending on the applied laser power and irradiation environment, affected either shallower or deeper surface layers. The most pronounced Zn surface melting occurred in samples irradiated in air at a wavelength of 1064 nm. As a result, droplet-like frozen structures formed on the surface of all these samples. A similar melting effect of laser-irradiated Zn has also been observed in the literature.^[65] In contrast, samples irradiated with a 1064 nm laser in an aqueous environment formed loose ZnO structures, beneath which a molten layer of uniformly frozen globular droplets developed. However, samples irradiated in air using a 266 nm laser melted more uniformly and had smoother surfaces without droplet-like structures. These samples were more similar to the unmodified Zn substrate with slight melting features, whereas samples irradiated in a water medium developed a crinkled melt structure.

The XRD measurements (Theta/2theta) for samples after laser irradiation were performed, to observe the changes in the crystallinity of the Zn surfaces perpendicularly to the growth direction (Figure 1c). For better comparison, the obtained spectra were normalized by their intensity. The diffractograms show that the Zn samples consist of a hexagonal Zn phase with peaks (PDF Card No.: 00-004-0831) located at $2\theta = 36.5, 39.2, 42.5, 54.5, 70.3, 71.0, 77.3, 82.1, 83.7,$ and 86.5° corresponding to hkl of atomic planes (002), (100), (101), (102), (103), (110), (004), (112), (200), and (201).^[66,67] The XRD results of the pristine Zn plate show a typical pattern for a polycrystalline Zn plate, with a dominant (002) basal plane that is parallel to the sheet surface due to rolling deformations induced during manufacturing.^[68] Laser treatment reduces the dominance of the (002) basal plane by re-melting the surface and revealing an underlying polycrystalline structure dominated by the (101) plane. Figure 1d, where the pure Zn substrate spectrum is subtracted from the irradiated sample spectra, shows the most noticeable changes in polycrystallinity due to the multidirectionally oriented hexagonal structure of Zn. Unfortunately, SEM images of the irradiated samples (Figure 1b) only reveal the visible melt structures, with the polycrystalline structure lying beneath the melted layer.

To obtain more information about the surface, Raman analysis was performed. The results are shown in Figure 1e. The structure of hexagonal wurtzite ZnO can be distinguished in Raman measurements by the first-order optical phonon modes. For perfect wurtzite ZnO crystals, optical phonon (Γ_{opt}) modes can be described by $\Gamma_{\text{opt}} = 1A_1 + 2B_1 + 1E_1 + 2E_2$.^[69] All visible phonon modes for Zn samples are summarized in Table 1. Observations point to hexagonal wurtzite structure ZnO growth with a space group of $P63mc$. The visible ZnO maxima at $382, 441,$ and 585 cm⁻¹ correspond to the polar $A_1(\text{TO})$, low-frequency phonon E_2^{high} , and longitudinal optical $E_1(\text{LO})$ modes, respectively. The small and broad peak at 441 cm⁻¹ of the E_2^{high} mode represents oxygen motion in hexagonal ZnO. According to the literature, the decrease and broadening of this peak indicate the breaking of translational crystal symmetry due to the formation of defects or incorporation of impurities into the Zn/ZnO lattice.^[69] This

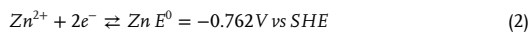
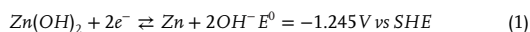
Table 1. Detectable Raman active modes of Zn samples.

Raman shift [cm ⁻¹]	Raman active modes	Indicative of	Reference
273	B ₁ ^{low} -B ₁ ^{high}	Defect formation in ZnO	[71–73]
337	E ₂ ^{high} -E ₂ ^{low}	Multi-phonon scattering modes of ZnO	[69,73]
382	A ₁ (TO)	First-order phonon modes of hexagonal ZnO	[69,73]
410	E ₁ (TO)	Optical phonon mode	[73,74]
441	E ₂ ^{high}	First-order phonon modes of hexagonal ZnO. Oxygen vibration in ZnO.	[69,73,75]
508	E ₁ (TO)+E ₂ ^{low}	Multi-phonon scattering modes of ZnO	[69,73]
536	2B ₁ ^{low} , 2LA	Overtones along L-M and H Brillouin zone points/lines	[73]
574	A ₁ (LO)	First-order phonon modes of hexagonal ZnO, assigned to the formation of oxygen vacancy-related defects.	[69,70,73]
723 – 745	LA + TO	Low-intensity modes	[73]
1044 – 1072	TO + LO	Multi-phonon scattering mode	[69,73]
1158	2A ₁ (LO); 2E ₁ (LO); 2LO	Combination of second-order LO overtones and modes	[73]
1361	D-band	Disordered band of carbon	[76–78]
1540	G-band	Graphitic band of carbon	[77–79]

shows that after laser irradiation, the structure of ZnO is polycrystalline with many small particles/crystallites, which correlates with the SEM images (Figure 1b). The peak at 333 cm⁻¹ is attributed to E₂^{high}-E₂^{low}, and the peak at 536 cm⁻¹ corresponds to 2B₁^{low} + 2LA. The most pronounced A₁(LO) peak at 574 cm⁻¹ indicates the presence of oxygen vacancies in the ZnO lattice and zinc interstitial defects.^[69] Furthermore, a broad peak at 250–300 cm⁻¹ is attributed to the formation of interstitial zinc defects. These defects are formed during the processes of metallic Zn melting (during laser irradiation) and electrode surface reforming (charge/discharge).^[70] An additional 275 cm⁻¹ peak in air-irradiated samples corresponds to nitrogen-related modes. During laser processing, N₂ gas from the air is incorporated into the ZnO structure, creating a defect.^[71] Also, the maxima located at 284 cm⁻¹ corresponds to a B₁^{low}, B₁^{high} mode, and the maxima at 536 cm⁻¹ is attributed to 2B₁^{low} and 2LA. By using water as an irradiation medium, additional modes can be observed at 1044 to 1072 cm⁻¹, referred to as TO + LO optical modes. Also, by irradiating samples in water, D and G bands of carbon appear at 1361 and 1540 cm⁻¹, possibly due to dissolved CO₂ in the water. For samples irradiated in air, an additional peak at 1158 cm⁻¹ corresponding to a 2A₁(LO), 2E₁(LO), 2LO can be observed.

The open circuit potential (OCP) measurements were also performed before electrochemical measurements (Figure 1f) to determine the cell equilibrium electrochemical potential. Freshly assembled half-cells from samples irradiated in an air atmosphere had a predicted potential of -1.44 V versus Ag/AgCl (3 m KCl) (-1.24 V vs SHE), consistent with the reaction of Zn in alkaline media 1). Samples irradiated in aqueous media using

a 266 nm laser had the same OCP. In contrast, samples irradiated in a water medium using a 1064 nm wavelength laser had a different potential and reflected a different response than expected. At the start of the measurement, the potential was -0.95 V versus Ag/AgCl (-0.75 V vs SHE) and corresponded to the reaction of a more neutral environment 2), indicating a pH change at the electrode/electrolyte interface. The concentration of OH⁻ ions should have been pH >10. However, the pH at the reaction interface was essentially pH < 10 due to ion diffusion limitations throughout the formed oxide layer on the Zn surface. Thus, the favorable equilibrium reaction (2) occurs until the imbalance is created. After some time, the electrode surface stabilizes due to electrolyte diffusion, and the concentration of OH⁻ ions increases at the interface, shifting the reaction to equilibrium (1).



3.2. Electrochemical Property Analysis

Further, CV half-cell measurements were carried out to evaluate the electrochemical properties of the irradiated sample surface. Measurements were performed with different scan speeds within a potential window of -1.9 to -0.6 V vs Ag/AgCl (3 m KCl) in an alkaline (1 m KOH) electrolyte, shown in Figure 2a (measurements for all the samples are shown in Figure S3, Supporting Information). During the oxidation (anodic) sweep of all Zn samples, the surface is oxidized to the point where the electrolyte cannot reach the active Zn surface for further reaction. However, during the reduction (cathodic) sweep, a phenomenon (≈-1.3 V vs Ag/AgCl (3 m KCl)) described in the literature^[80,81] can be observed. During a cathodic sweep in the potential range from -1.2 to -1.4 V versus Ag/AgCl (3 m KCl), an additional unreacted surface of Zn is exposed to the electrolyte, and an instant current increase can be observed due to the restored ongoing Zn oxidation process. These measurements show that the laser-treated samples have higher oxidation and reduction currents. This suggests that a greater number of reaction centers are available on the surface, resulting in more pronounced electrochemical reactions. Also, SEM images indicate (Figure 1b) that samples have a larger surface area after the laser irradiation process due to a more detailed structure. However, the previously mentioned phenomenon (≈-1.3 V vs Ag/AgCl (3 m KCl)) is less evident in laser-treated samples. This indicates that the reaction is more controlled, and ZnO grows more uniformly for the laser-treated samples despite the oxidation reaction being more pronounced. Thus, suggesting that the surface laser treatment improves the overall cycling performance of the Zn electrode.

The improved cycling performance of laser-treated samples is also evident in the specific capacity per surface area in Figure 2b,e. The results, calculated from the CV graphs, reveal that at 0.005 V s⁻¹ scan rate (C-rate of 30 C), samples that have been irradiated in an air atmosphere have a slightly larger (1.35–1.50 mAh cm⁻²) surface-specific capacity compared to samples irradiated in a water medium (1.25–1.35 mAh cm⁻²), and even higher than a pristine Zn plate (1.15 mAh cm⁻²). For samples irradiated in air with an IR laser, increasing parameter *F* also increases the specific capacity. On the other hand, to achieve similar

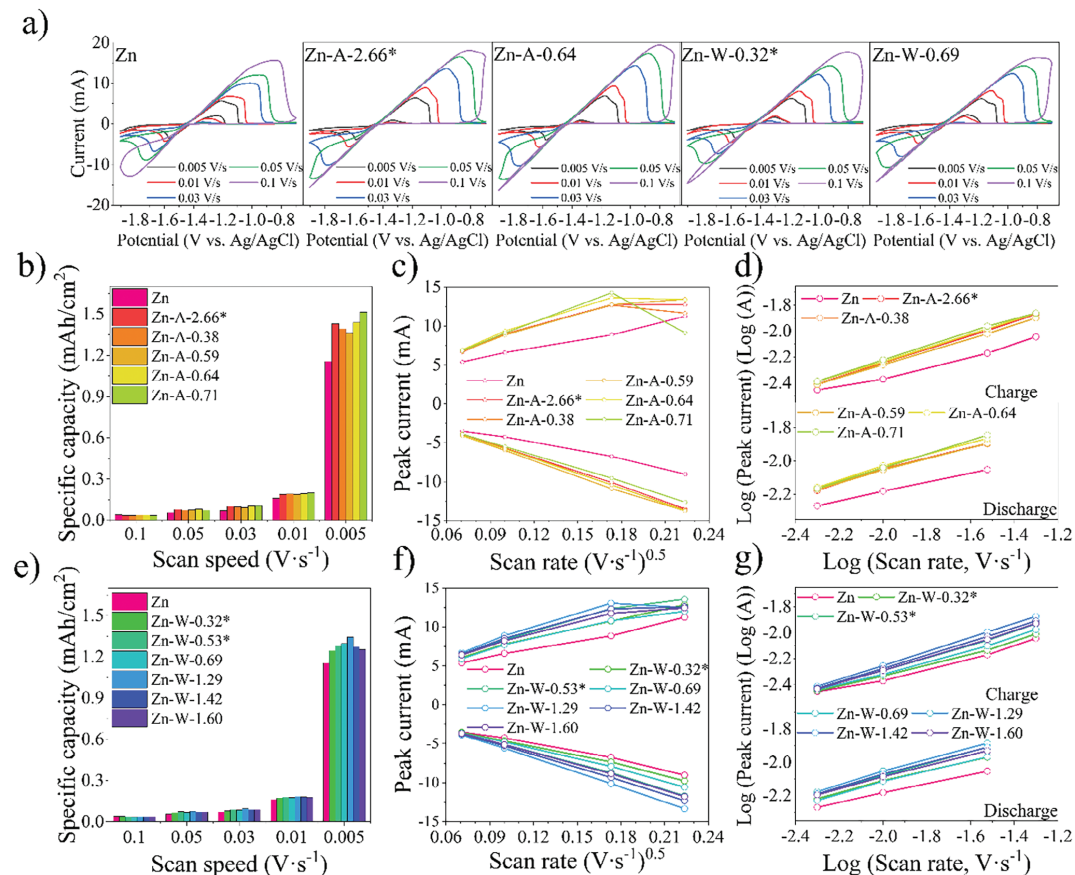


Figure 2. Electrochemical characterization of pure and irradiated Zn anodes: a) CV measurements at varying scan speeds from 0.005 V/s to 0.1 V/s; b) and e) specific capacities at different scan speeds; c) and f) Randles-Sevcik graphs; d) and g) power law relationship.

improved results with a UV laser, approximately twice the F value is required. Similar observations are made for the samples irradiated in the water medium, where increasing the parameter F also increases the specific capacity. However, at $F = 1.29$ a maximum is reached, and a further increase of F leads to a decrease in capacity. Overall observations suggest that irradiated samples have an 8–30% surface-specific capacity increase compared to the pristine Zn plate at 0.005 V s^{-1} . The highest specific capacity from samples irradiated in the air atmosphere is Zn-A-0.71, and from water samples is Zn-W-1.29. According to the SEM images (Figure 1b), samples Zn-A-0.71 and Zn-W-1.29 are characterized by smaller average sizes and higher density of surface structures, which causes the surface-specific capacity to increase. This is associated with a larger number of redox-active sites where more reactions take place. Similar observations are also described in the literature for other cathode and anode materials.^[82,83]

The Randles-Sevcik graphs (Figure 2c,f) were plotted from CV graphs and show the peak current dependency on the square root

of scanning speed. As the CV graphs show (Figure 2a), Zn plating only proceeds through a partial process at faster scanning speeds. Thus, the peak current cannot be efficiently achieved and determined from the graphs. This discrepancy is also evident in Randles-Sevcik graphs where the last point does not correlate and deviates from the others. Otherwise, the peak currents of all sample cathodic and anodic processes have a linear dependence on the square root of the scan rate. This indicates that both Zn plating and stripping are reversible and diffusion-based processes. Similar findings can be found by analyzing the anode electrochemical kinetics with the power law relationship (Figure 2g). It can be expressed by formula (3), where I_p is the peak current of anodic or cathodic reaction (mA); v is the scan rate (V/s); a represents a constant; and b is the power-law exponent. Based on the value of b , a qualitative determination of the charge storage mechanism can be made. If b is 0.5, then the process is diffusion-controlled or Faradaic, whereas if b is 1, it indicates that the current is surface-controlled and the process is non-Faradaic.

Table 2. Values of parameter *b* for all Zn samples.

Sample	Charging		Discharging	
	<i>b</i> value	R ²	<i>b</i> value	R ²
Zn	0.41	0.98611	0.28	0.99946
Zn-A-2.66*	0.53	0.99986	0.36	0.99213
Zn-A-0.38	0.55	0.99994	0.35	0.99376
Zn-A-0.59	0.51	0.99971	0.36	0.99782
Zn-A-0.64	0.53	0.99989	0.37	0.99611
Zn-A-0.71	0.53	0.99910	0.41	1.00000
Zn-W-0.32*	0.43	0.99555	0.32	0.99698
Zn-W-0.53*	0.49	0.99855	0.36	0.99997
Zn-W-0.69	0.46	0.99590	0.33	0.99606
Zn-W-1.29	0.54	0.99996	0.37	0.99803
Zn-W-1.42	0.52	0.99987	0.36	0.99805
Zn-W-1.60	0.50	0.99921	0.34	0.99911

The Equation (3) can be rewritten as (4); thus, by plotting $\log(I_p)$ versus $\log(\nu)$, the value of *b* can be found as the slope of the graph.^[84–89]

$$I_p = a \times \nu^b \quad (3)$$

$$\log(I_p) = \log(a) + b \times \log(\nu) \quad (4)$$

The Zn sample power law plots show a linear relationship between the logarithm of peak current dependence and the logarithm of scan rate. The corresponding values of *b* are listed in Table 2. The charge slopes are ≈ 0.5 , and the discharge slopes are ≈ 0.3 – 0.4 . This indicates that both cathodic and anodic processes for all samples are purely diffusion-controlled and do not have the characteristics of a capacitor.

3.3. Sample Characterization after Electrochemical Testing

After the electrochemical measurements, additional SEM imaging was performed to detect surface changes in the samples, as depicted in Figure 3a (images for all the samples are shown in Figure S2, Supporting Information). The irradiated samples exhibited visible grain structures with growth indications on distinct surfaces of the Zn hexagonal plane. Thus, the acquired SEM pictures confirm the hexagonal Zn polycrystalline structure observed in the XRD measurements (Figure 3c). In contrast, the surface of the non-irradiated Zn sample showed less pronounced grain structures. Almost half of the non-irradiated sample surface displayed visible random growth signs, interspersed between large hexagonal Zn grain regions. Overall, these observations suggest that zinc laser treatment significantly enhances the plating and stripping processes, thereby improving electrochemical performance.

To gain deeper insights into surface changes during CV measurements, Raman analysis was conducted following the electrochemical measurements. The Raman spectra of irradiated samples (Figure 3b) after electrochemical measurements are noisy, and the characteristic features of ZnO are challenging to deter-

mine. In contrast, in the irradiated samples before electrochemical measurements (Figure 1f), ZnO can be clearly distinguished from pure Zn metal. After CV measurements, the non-irradiated Zn sample showed more pronounced ZnO signals on the surface compared to the laser-irradiated samples. This suggests that the laser treatment has enhanced electrochemical reactions, facilitating a more uniform growth of ZnO on the electrode surface and a more complete conversion back to metallic Zn. However, for the pristine Zn sample, it seems that only partial charging (conversion of ZnO to Zn) is occurring, leading to an increase in the ZnO content on the surface and consequently improving the ZnO Raman signal. This observation is consistent with the CV measurements of the pristine Zn sample, where a more pronounced phenomenon (≈ -1.3 V vs Ag/AgCl (3 M KCl)) is observed, which is attributed to the formation of ZnO.

Additionally, surfaces were re-examined using XRD measurements ($\Theta/\alpha\Theta$) to observe the changes that occurred (Figure 3c). For the non-irradiated Zn sample, a distinct increase in (002) plane intensity and decrease in (101) plane intensity were observed, suggesting growth predominantly in a (002) plane direction. Additionally, a slight increase in the (100) plane was observed, indicating the formation of dendrite-like or loose structures on the surface (Figure 3g). SEM images of electrochemically cycled non-irradiated Zn sample (Figure 3a) reveal the formation of a loose structure, corresponding to the increase in the (100) plane observed in the XRD measurements, and confirming the tendency of press-rolled Zn sheets to promote dendrite formation due to induced surface defects.^[39] In contrast, irradiated samples after CV measurements retained their polycrystalline (101) crystal structure formation. A slight increase in intensity was observed for the lattices containing the c-plane, suggesting possible growth in the basal (002) plane direction of the polycrystalline surface. SEM images (Figure 3a) also confirmed more pronounced growth of crystalline structure. The slight decrease in intensities along the (100) and (200) planes may indicate that the surfaces are more resistant to vertical (dendrite-like) structure growth (Figure 1g).

From Figure 3d, where irradiated sample spectra are subtracted from the respective electrochemically cycled sample spectra, it can be concluded that growth during electrochemical cycling mostly occurs on the surfaces and along the crystal c-plane. The comparison of changes between electrochemically cycled irradiated samples and electrochemically cycled pure Zn anode can be seen in Figure 3e, where the spectrum of the cycled Zn anode has been subtracted from the laser-irradiated cycled spectra. Crystal surface growth on all surfaces and planes containing the c-plane remains dominant compared to non-irradiated Zn samples, attributable to the chaotic crystal orientation on the surface of the Zn anode.

OCP after electrochemical testing of the samples (Figure 3f) was ≈ -1.40 V vs Ag/AgCl (3 M KCl) for all the samples. This is consistent with reaction (1) indicating that there are no additional barriers for any sample that would alter the diffusion of OH⁻ ions. Further, electrochemical impedance spectroscopy was used to characterize the electrode-electrolyte interface in the frequency range from 0.1 Hz to 100 kHz. Figure 3h shows EIS spectra at a negative DC component of -150 mV from the OCP and Figure 3i shows spectra at a positive DC component of $+150$ mV from the OCP. Individual EIS spectra for all the samples are shown

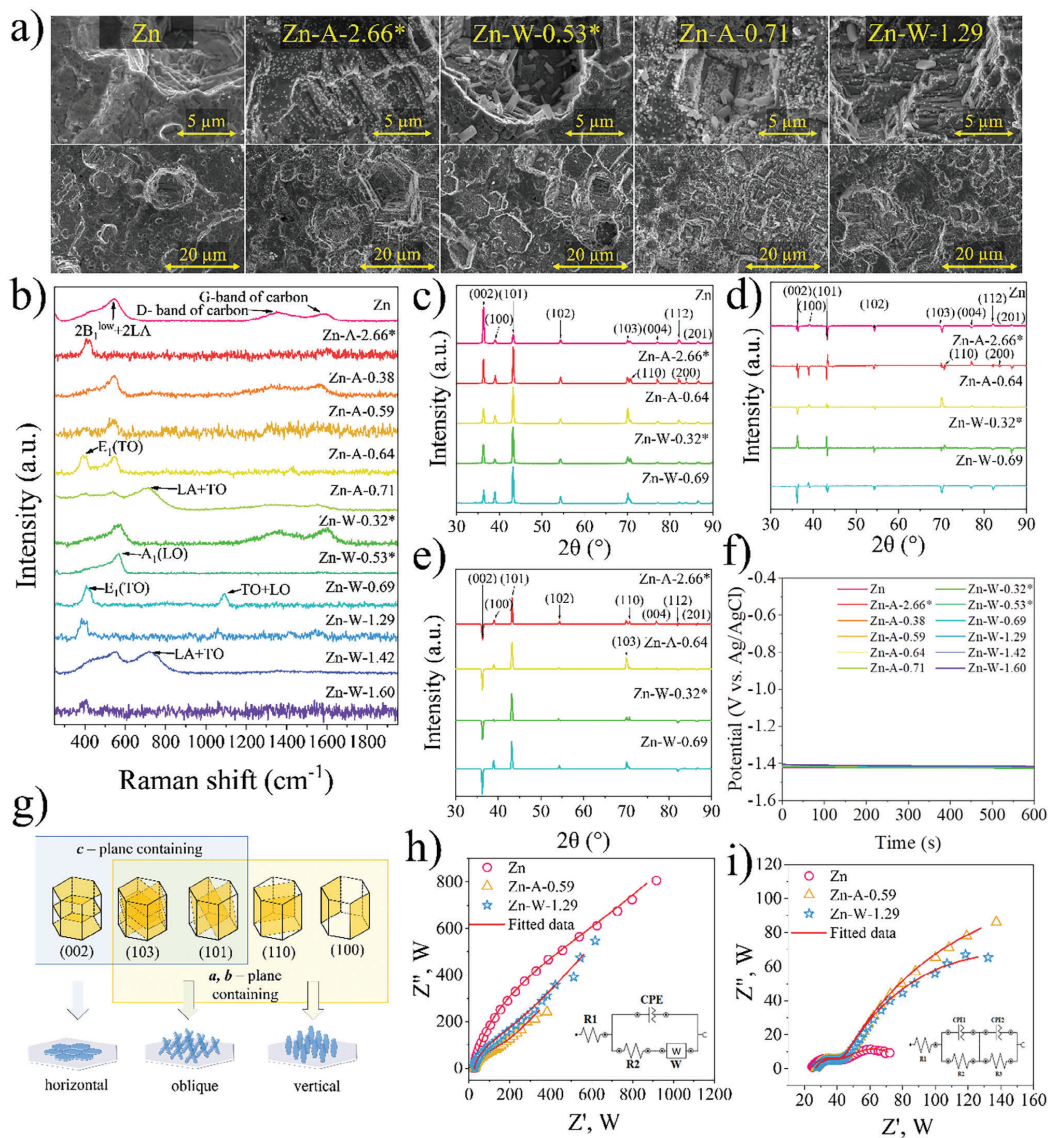


Figure 3. Pure and irradiated Zn sample characterization after electrochemical measurements: a) SEM images; b) Raman analysis; c) XRD diffractograms; d) difference between cycled sample XRD and their irradiated spectra (electrochemically cycled sample XRD spectra minus sample irradiated XRD spectrum); e) difference between cycled sample XRD and cycled pure Zn spectrum (CV sample XRD spectra minus CV pure Zn XRD spectrum); f) CV; g) hexagonal Zn planes and respective growth patterns; h) EIS measurements and equivalent circuit diagrams during negative and i) positive bias.

in Figures S4 and S5 (Supporting Information). All experimental data were analyzed using NOVA 2 software, and equivalent circuits for each fitted bias are shown next to the corresponding graphs in Figures S6–S8 (Supporting Information). The obtained values of equivalent circuit components are summarized in Tables S2 and S3 (Supporting Information). In the equiva-

lent circuit for the negative potential bias, where Zn plating takes place, the series resistance R1 for all samples is $\approx 27 \Omega$ (intersection with the real resistance axis Z'). It corresponds to the ohmic resistance of the electrolyte. A semicircle follows at high frequencies, the radius of which indicates the charge transfer resistance R2. This resistance characterizes the charge transfer resistance

of a faradaic process and is significantly reduced in laser-treated samples. This resistance is $\approx 668 \Omega$ for the pure Zn sample, while for the laser-treated samples, it is $\approx 150 \Omega$. However, the CPE element, which characterizes the capacitance of the electrical double layer, increases the analog capacitance value of the laser-treated samples. This capacitance is $\approx 45 \mu\text{F}$ for a pure Zn sample, while it is $\approx 55 \mu\text{F}$ for laser-treated samples. This slight increase indicates a macroscopic enlargement in the surface area of the laser-treated samples. At low frequencies, the spectra transition into a sloping tail corresponding to a Warburg impedance that characterizes diffusion-limiting processes.

An augmented equivalent circuit model is applied to the obtained Nyquist plots at a positive potential bias, where Zn stripping and ZnO formation occur. Two semi-circles can be seen in the Nyquist curves, indicating two parallel connections of CPE and resistance. R1, as in the previous case, describes the series resistance and is $\approx 27 \Omega$. The first parallel connection of R2 and CPE1 characterizes the condition of the electric double layer: the ion polarization resistance R2 and the electric double layer capacitance CPE1. R2 for the pure Zn sample is $\approx 20.5 \Omega$, while it is reduced to $\approx 17 \Omega$ for the laser-treated samples. The electrical double-layer capacitance of the pure Zn sample is $\approx 41.4 \mu\text{F}$ and increases to $\approx 53 \mu\text{F}$ for the laser-treated ones. The double-layer capacitance values are similar to the negative biases, indicating that the laser-treated macrosurface does not change during electrochemical cycling. The second parallel circuit of CPE2 and R3 describes a faradaic process where R3 indicates charge transfer resistance. For a pure Zn sample, this value is 38Ω , while for laser-treated samples, it is $\approx 200 \Omega$. This significant increase is due to the different defects formed during laser treatment, as observed in Raman spectra after electrochemical measurements (Figure 3b). This increases the charge transfer resistance in the bulk material and reduces the reaction rate for Zn stripping. CPE2 characterizes the capacitance of the Zn oxidation process and is several orders of magnitude larger than the capacitance of the double layer. It is $\approx 3.4 \text{ mF}$ for a pure Zn electrode, while it is reduced to $\approx 2.7 \text{ mF}$ for laser-treated samples. This capacitance reduction is due to the slowdown of the reaction, which in turn is caused by the increased bulk material resistance.

4. Conclusion

In this study, the surface of Zn metal was modified using laser irradiation at two different wavelengths (266 or 1064 nm) and irradiation environments (water or air). The results indicate that the surface of the laser-treated samples exhibits enhanced electrochemical properties. SEM images show that the surface of the modified samples has significantly more pronounced crystallinity after the electrochemical cycling compared to untreated Zn plates. This modification allows for more efficient Zn plating and dissolution during electrochemical processes. Improved Zn growth and oxidation effects were also observed in Raman spectra. It was found that laser-irradiated surfaces had significantly less unreacted ZnO residue after the electrochemical cycling than the untreated surface.

Randles-Sevcik plots indicated that the electrodes exhibit Faradaic characteristics typical of battery-type electrodes, and the power law plot showed diffusion-limited processes at the electrode/electrolyte interface. Additionally, the specific capacity of

the laser-irradiated samples was on average 8–30% higher than that of the standard Zn plate. During negative bias (Zn plating), the charge transfer resistance of the laser-irradiated samples was significantly lower than that of the untreated Zn plate, with similar findings observed during positive bias (Zn stripping). However, in positive bias measurements, an additional semicircle with increased resistance was observed for the irradiated samples. This increased resistance can be attributed to various defects formed from air or water in the Zn plate during laser treatment, as described in references.^[90,91]

Overall, samples irradiated with a 1064 nm laser in an air atmosphere exhibited superior results compared to both untreated samples and those treated with other irradiation parameters. Additionally, the ZnO content on the Zn surface after UV irradiation at 266 nm showed no significant changes compared to IR irradiation at 1064 nm. This is attributed to the high light scattering and quantum efficiency of ZnO crystals under UV laser excitation.^[92] Despite the high absorption coefficient of the UV laser beam in ZnO, its power was not enough to heat and destroy the ZnO fragments. Nonetheless, the effect of the laser with suprathreshold fluence on the Zn electrode is sufficient to enhance the electrochemical properties of the system. Laser treatment increases the effective surface area and the surface-specific capacity of the Zn electrode. This enhancement quickly reaches a saturation point with increasing laser fluence, as the surface roughness stabilizes at a certain stage of laser processing.

The overall conclusion about the fluence values used is not unambiguous, as these changes between irradiated samples are relatively small. The most noticeable changes are observed between the influence of water and air atmosphere on the irradiated sample. However, the aim of this study is to promote the understanding of the possible application of laser processing for the development of more efficient anode materials. Further experiments involving surface laser treatment are necessary to thoroughly evaluate the observed surface changes and potential improvements. Combining surface laser modification with other methods could establish a robust foundation for forming (002) basal plane surfaces in aqueous Zn-ion batteries.

Supporting Information

Supporting Information is available from the Wiley Online Library or from the author.

Acknowledgements

This work was supported by the Latvian Council of Science in the framework of FLPP (Investigation of Electrodes and Electrolytes for Obtaining Amphoteric Decoupled Rechargeable Batteries, lzp-2021/1–0142).

Conflict of Interest

The authors declare no conflict of interest.

Data Availability Statement

The data that support the findings of this study are available from the corresponding author upon reasonable request.

Keywords

Cyclic voltammetry, energy storage, Impedance spectroscopy, Laser irradiation, Raman spectroscopy, Surface morphology, Zn-ion batteries (ZIBs)

Received: April 12, 2024

Revised: July 7, 2024

Published online:

- [1] J. L. Holechek, H. M. E. Geli, M. N. Sawalhah, R. Valdez, *Sustainability* **2022**, *14*, 4792.
- [2] J. Y. Lee, A. K. Ramasamy, K. H. Ong, R. Verayiah, H. Mokhlis, M. Marsadek, *J. Energy Storage* **2023**, *72*, 108360.
- [3] T.-Z. Ang, M. Salem, M. Kamarol, H. S. Das, M. A. Nazari, N. Prabaharan, *Energy Storage Rev.* **2022**, *43*, 100939.
- [4] J. Escudero-González, P. A. López-Jiménez, *Int. J. Elec. Power* **2014**, *61*, 421.
- [5] T. Ma, D. Xu, M. Wei, H. Wu, X. He, Z. Zhang, D. Ma, S. Liu, B. Fan, C. Lin, L. Liu, F. Wang, *Solid State Ion.* **2020**, *345*, 115193.
- [6] M. Ank, T. Brehler, M. Lienkamp, *ETransportation* **2023**, *18*, 100284.
- [7] W. Kim, S. Park, G. Ko, J. Lee, K. Kwon, *Chem. Eng. J.* **2023**, *475*, 146121.
- [8] T. Punt, S. M. Bradshaw, P. van Wyk, G. Akdogan, *Minerals* **2022**, *12*, 753.
- [9] H. M. Barkholtz, Y. Preger, S. Ivanov, J. Langendorf, L. Torres-Castro, J. Lamb, B. Chalamala, S. R. Ferreira, *J. Power Sources* **2019**, *435*, 226777.
- [10] C. Liu, Y. Li, D. Lin, P. C. Hsu, B. Liu, G. Yan, T. Wu, Y. Cui, S. Chu, *Joule* **2020**, *4*, 1459.
- [11] F. Jing, J. Pei, Y. Zhou, Y. Shang, S. Yao, S. Liu, G. Chen, *J. Colloid Interface Sci.* **2022**, *609*, 557.
- [12] Y. Wang, R. Chen, T. Chen, H. Lv, G. Zhu, L. Ma, C. Wang, Z. Jin, J. Liu, *Energy Storage Mater.* **2016**, *4*, 103.
- [13] H. Jia, Z. Wang, B. Tawiah, Y. Wang, C. Y. Chan, B. Fei, F. Pan, *Nano Energy* **2020**, *70*, 104523.
- [14] X. Zhang, J. Hu, N. Fu, W. Zhou, B. Liu, Q. Deng, X. Wu, *InfoMat* **2022**, *4*, e12306.
- [15] C. Nie, G. Wang, D. Wang, M. Wang, X. Gao, Z. Bai, N. Wang, J. Yang, Z. Xing, S. Dou, *Adv. Energy Mater.* **2023**, *13*, 2300606.
- [16] C. Zhu, P. Li, G. Xu, H. Cheng, G. Gao, *Coord. Chem. Rev.* **2023**, *485*, 215142.
- [17] Q. Zhang, J. Luan, L. Fu, S. Wu, Y. Tang, X. Ji, H. Wang, *Angew. Chem., Int. Ed.* **2019**, *58*, 15841.
- [18] W. Li, H. Tian, L. Ma, Y. Wang, X. Liu, X. Gao, *Mater. Adv.* **2022**, *3*, 5598.
- [19] Y. Yu, J. Xie, H. Zhang, R. Qin, X. Liu, X. Lu, *Small Science* **2021**, *1*, 2000066.
- [20] L. Wei, Y. Chen, Z. Huang, S. Zheng, X. Guo, *Energy Storage Mater.* **2023**, *58*, 30.
- [21] L. Ma, S. Chen, N. Li, Z. Liu, Z. Tang, J. A. Zapien, S. Chen, J. Fan, C. Zhi, *Adv. Mater.* **2020**, *32*, 1908121.
- [22] H. V. Parys, G. Telias, Y. Nedashkiivskiy, B. Mollay, I. Vandendael, S. V. Damme, J. Deconinck, A. Hubin, *Electrochim. Acta* **2010**, *55*, 5709.
- [23] F. Wang, J. Tseng, Z. Liu, P. Zhang, G. Wang, G. Chen, W. Wu, M. Yu, Y. Wu, X. Feng, *Adv. Mater.* **2020**, *32*, 2000287.
- [24] Q. Zhang, Y. Hua, *Mater. Chem. Phys.* **2012**, *134*, 333.
- [25] R. C. M. Salles, G. C. G. Oliveira, S. L. Díaz, O. E. Barcia, O. R. Mattos, *Electrochim. Acta* **2011**, *56*, 7931.
- [26] J. Kim, H. Kim, W. J. Lee, B. Ruqia, H. Baik, H. S. Oh, S. M. Paek, H. K. Lim, C. H. Choi, S. I. Choi, *J. Am. Chem. Soc.* **2019**, *141*, 18256.
- [27] J. Hao, X. Li, S. Zhang, F. Yang, X. Zeng, S. Zhang, G. Bo, C. Wang, Z. Guo, *Adv. Funct. Mater.* **2020**, *30*, 2001263.
- [28] Y. Kim, Y. Park, M. Kim, J. Lee, K. J. Kim, J. W. Choi, *Nat. Commun.* **2022**, *13*, 2371.
- [29] Z. Cai, J. Wang, Y. Sun, *EScience* **2023**, *3*, 100093.
- [30] K. E. K. Sun, T. K. A. Hoang, T. N. L. Doan, Y. Yu, X. Zhu, Y. Tian, P. Chen, *ACS Appl. Mater. Interfaces* **2017**, *9*, 9681.
- [31] S. Huang, P. Pei, Z. Wang, *J. Electrochem. Soc.* **2020**, *167*, 090538.
- [32] S. Sahu, J. M. Foster, *J. Energy Storage* **2023**, *60*, 106516.
- [33] R. Zhang, X. Chen, X. Chen, X. Cheng, X. Zhang, C. Yan, Q. Zhang, *Angew. Chem., Int. Ed.* **2017**, *56*, 7764.
- [34] J. Zheng, Q. Zhao, T. Tang, J. Yin, C. D. Quilty, G. D. Renderos, X. Liu, Y. Deng, L. Wang, D. C. Bock, C. Jaye, D. Zhang, E. S. Takeuchi, K. J. Takeuchi, A. C. Marschilok, L. A. Archer, *Science* **2019**, *366*, 645.
- [35] Q. Yang, G. Liang, Y. Guo, Z. Liu, B. Yan, D. Wang, Z. Huang, X. Li, J. Fan, C. Zhi, *Adv. Mater.* **2019**, *31*, 1903778.
- [36] W. Du, Z. Zhang, F. Iacoviello, S. Zhou, R. E. Owen, R. Jervis, D. J. L. Brett, P. R. Shearing, *ACS Appl. Mater. Interfaces* **2023**, *15*, 14196.
- [37] H. Tian, G. Feng, Q. Wang, Z. Li, W. Zhang, M. Lucero, Z. Feng, Z. L. Wang, Y. Zhang, C. Zhen, M. Gu, X. Shan, Y. Yang, *Nat. Commun.* **2022**, *13*, 7922.
- [38] S. D. Pu, C. Gong, Y. T. Tang, Z. Ning, J. Liu, S. Zhang, Y. Yuan, D. Melvin, S. Yang, L. Pi, J. Marie, B. Hu, M. Jenkins, Z. Li, B. Liu, S. C. E. Tsang, T. J. Marrow, R. C. Reed, X. Gao, P. G. Bruce, A. W. Robertson, *Adv. Mater.* **2022**, *34*, 2202552.
- [39] P. He, J. Huang, *ACS Energy Lett.* **2021**, *6*, 1990.
- [40] L. Kang, M. Cui, F. Jiang, Y. Gao, H. Luo, J. Liu, W. Liang, C. Zhi, *Adv. Energy Mater.* **2018**, *8*, 1801090.
- [41] X. Xie, S. Liang, J. Gao, S. Guo, J. Guo, C. Wang, G. Xu, X. Wu, G. Chen, J. Zhou, *Energy Environ. Sci.* **2020**, *13*, 503.
- [42] X. Hu, J. Borowiec, Y. Zhu, X. Liu, R. Wu, A. M. Ganose, I. P. Parkin, B. D. Boruah, *Small* **2023**, *20*, 2306827.
- [43] Q. Ren, X. Tang, K. He, C. Zhang, W. Wang, Y. Guo, Z. Zhu, X. Xiao, S. Wang, J. Lu, Y. Yuan, *Adv. Funct. Mater.* **2023**, *34*, 2312220.
- [44] P. Liang, J. Yi, X. Liu, K. Wu, Z. Wang, J. Cui, Y. Liu, Y. Wang, Y. Xia, J. Zhang, *Adv. Funct. Mater.* **2020**, *30*, 1908528.
- [45] S. Sun, Y. Wen, A. Billings, R. Rajabi, B. Wang, K. Zhang, K. Huang, *Energy Adv.* **2024**, *3*, 299.
- [46] Y. Liu, T. Guo, Q. Liu, F. Xiong, M. Huang, Y. An, J. Wang, Q. An, C. Liu, L. Mai, *Mater. Today Energy* **2022**, *28*, 101056.
- [47] K. Zhao, C. Wang, Y. Yu, M. Yan, Q. Wei, P. He, Y. Dong, Z. Zhang, X. Wang, L. Mai, *Adv. Mater. Interfaces* **2018**, *5*, 1800848.
- [48] B. Li, J. Xue, X. Lv, R. Zhang, K. Ma, X. Wu, L. Dai, L. Wang, Z. He, *Surf. Coat. Technol.* **2021**, *421*, 127367.
- [49] N. Nareesh, S. Eom, S. H. Jeong, S. J. Lee, S. H. Park, J. Park, J. H. Ahn, J. H. Kim, Y. H. Jung, *Appl. Surf. Sci.* **2022**, *606*, 154932.
- [50] P. Ye, X. Li, K. He, A. Dou, X. Wang, A. Naveed, Y. Zhou, M. Su, P. Zhang, Y. Liu, *J. Power Sources* **2023**, *558*, 232622.
- [51] X. Cai, W. Tian, Z. Zhang, Y. Sun, L. Yang, H. Mu, C. Lian, H. Qiu, *Adv. Mater.* **2024**, *36*, 2307727.
- [52] P. Chen, X. Yuan, Y. Xia, Y. Zhang, L. Fu, L. Liu, N. Yu, Q. Huang, B. Wang, X. Hu, Y. Wu, T. Ree, *Adv. Sci.* **2021**, *8*, 2100309.
- [53] Z. Hu, X. Wang, W. Du, Z. Zhang, Y. Tang, M. Ye, Y. Zhang, X. Liu, Z. Wen, C. C. Li, *ACS Nano* **2023**, *17*, 23207.
- [54] J. Wang, Z. Cai, R. Xiao, Y. Ou, R. Zhan, Z. Yuan, Y. Sun, *ACS Appl. Mater. Interfaces* **2020**, *12*, 23028.
- [55] R. Zhu, Z. Xiong, H. Yang, T. Huang, S. Jeong, D. Kowalski, S. Kitano, Y. Aoki, H. Habazaki, C. Zhu, *Energy Storage Mater.* **2022**, *46*, 223.
- [56] B. Meylan, I. Calderon, Q. T. Le, K. Wasmer, *Procedia CIRP* **2020**, *94*, 942.
- [57] W. Pflögging, *Nanophotonics* **2018**, *7*, 549.
- [58] C. Yang, Y. Tong, Z. Yang, H. Xiao, H. Qi, F. Chen, *Nanomanufactur. Metrol.* **2023**, *6*, 16.
- [59] Z. Na, H. Qi, S. Li, Y. Wu, Q. Wang, G. Huang, *ACS Energy Lett.* **2023**, *8*, 3297.
- [60] D. Yao, D. Yu, S. Yao, Z. Lu, G. Li, H. Xu, F. Du, *ACS Appl. Mater. Interfaces* **2023**, *15*, 16584.

- [61] H. Jin, Y. Luo, B. Qi, K. Liu, Q. Wang, B. Yao, H. Li, W. Xiong, L. Huang, J. Zhou, Z. Guo, *ACS Appl. Energy Mater.* **2021**, *4*, 11743.
- [62] J. Cao, D. Zhang, C. Gu, X. Wang, S. Wang, X. Zhang, J. Qin, Z. Wu, *Adv. Energy Mater.* **2021**, *11*, 2101299.
- [63] S. Bashir, M. S. Rafique, A. A. Ajami, C. S. Nathala, W. Husinsky, K. Whitmore, *Appl. Phys. A* **2021**, *127*, 226.
- [64] I. Carlomagno, I. Lucarini, V. Secchi, F. Maita, D. Polese, S. Mirabella, G. Franzò, A. Notargiacomo, G. D. Santo, S. Gonzalez, L. Petaccia, L. Maiolo, *Appl. Surf. Sci.* **2022**, *587*, 152313.
- [65] M. Asif, A. Latif, A. Ali, M. S. Rafique, S. A. Khan, A. Haseeb, M. K. Shahid, *Physchem* **2022**, *3*, 22.
- [66] M. Aftab, A. Aftab, M. Z. Butt, D. Ali, F. Bashir, S. S. Iqbal, *Mater. Chem. Phys.* **2023**, *295*, 127117.
- [67] N. T. Mai, T. T. Thuy, D. M. Mott, S. Maenosono, *CrystEngComm* **2013**, *15*, 6606.
- [68] M. Zhou, S. Guo, J. Li, X. Luo, Z. Liu, T. Zhang, X. Cao, M. Long, B. Lu, A. Pan, G. Fang, J. Zhou, S. Liang, *Adv. Mater.* **2021**, *33*, 2100187.
- [69] M. Silambarasan, S. Saravanan, T. Soga, *Int. J. ChemTech Res. CODEN* **2014**, *7*, 1644.
- [70] Y. Song, S. Zhang, C. Zhang, Y. Yang, K. Lv, *Crystals (Basel)* **2019**, *9*, 395.
- [71] F. Friedrich, N. H. Nickel, *Appl. Phys. Lett.* **2007**, *91*, 111903.
- [72] I. Musa, N. Qamhieh, S. T. Mahmoud, *Results Phys.* **2017**, *7*, 3552.
- [73] R. Cuscó, E. A. Lladó, J. Ibáñez, L. Artús, J. Jiménez, B. Wang, M. J. Callahan, *Phys. Rev. B* **2007**, *75*, 165202.
- [74] V. I. Korepanov, S. Y. Chan, H. C. Hsu, H. Hamaguchi, *Heliyon* **2019**, *5*, e01222.
- [75] A. Sharma, B. P. Singh, S. Dhar, A. Gondorf, M. Spasova, *Surf. Sci.* **2012**, *606*, L13.
- [76] Y. Wang, D. C. Alsmeyer, R. L. McCreery, *Chem. Mater.* **1990**, *2*, 557.
- [77] G. S. Das, K. M. Tripathi, *ACS Appl. Electron. Mater.* **2024**, *6*, 1034.
- [78] G. S. Das, J. Y. Hwang, J. H. Jang, K. M. Tripathi, T. Kim, *ACS Appl. Energy Mater.* **2022**, *5*, 6663.
- [79] O. A. Maslova, M. R. Ammar, G. Guimbretière, J. N. Rouzaud, P. Simon, *Phys. Rev. B* **2012**, *86*, 134205.
- [80] C. Mele, B. Bozzini, *J. Appl. Electrochem.* **2015**, *45*, 43.
- [81] S. Hosseini, A. Abbasi, L. O. Uginet, N. Haustraete, S. Praserthdam, T. Yonezawa, S. Kheawhom, *Sci. Rep.* **2019**, *9*, 14958.
- [82] L. Tang, H. Peng, J. Kang, H. Chen, M. Zhang, Y. Liu, D. H. Kim, Y. Liu, Z. Lin, *Chem. Soc. Rev.* **2024**, *53*, 4877.
- [83] K. W. Nam, H. Kim, Y. Beldjoudi, T. Kwon, D. J. Kim, J. F. Stoddart, *J. Am. Chem. Soc.* **2020**, *142*, 2541.
- [84] Y. Liu, S. P. Jiang, Z. Shao, *Mater. Today Adv.* **2020**, *7*, 100072.
- [85] V. Adimule, V. S. Bhat, B. C. Yallur, A. H. Gowda, P. De Padova, G. Hegde, A. Toghian, *Nanomater. Nanotechno.* **2022**, *12*, 184798042110640.
- [86] J. Liu, J. Wang, C. Xu, H. Jiang, C. Li, L. Zhang, J. Lin, Z. X. Shen, *Adv. Sci.* **2018**, *5*, 1700322.
- [87] D. Y. W. Yu, C. Fietzek, W. Weydanz, K. Donoue, T. Inoue, H. Kurokawa, S. Fujitani, *J. Electrochem. Soc.* **2007**, *154*, A253.
- [88] A. S. Lakhnot, K. Bhimani, V. Mahajani, R. A. Panchal, S. Sharma, N. Koratkar, *Proc. Natl. Acad. Sci. USA* **2022**, *119*, e2205762119.
- [89] G. S. Das, R. Panigrahi, S. Ghosh, K. M. Tripathi, *Mater. Today Sustain.* **2024**, *25*, 100656.
- [90] P. Camarda, L. Vaccaro, F. Messina, M. Cannas, *Appl. Phys. Lett.* **2015**, *107*, 013103.
- [91] D. Prokuratov, A. Samokhvalov, D. Pankin, O. Vereshchagin, N. Kurganov, A. Povolotckaia, A. Shimko, A. Mikhailova, R. Balmashnov, O. Smolyanskaya, D. Redka, T. Salgals, V. Bobrovs, *J. Cult. Herit.* **2023**, *61*, 13.
- [92] L. Fedorenko, V. Litovchenko, V. Naumov, D. Korbutyak, V. Yuhymchuk, O. Gudymenko, O. Dubikovskiy, H. Mimura, A. Medvids, *Coatings* **2022**, *12*, 1705.

R. Durena, A. Zukuls, M. Vanags, A. Šutka

How to increase the potential of aqueous Zn-MnO₂ batteries: The effect of pH gradient electrolyte

Electrochimica Acta, 2022, 434, 141275

DOI: [10.1016/j.electacta.2022.141275](https://doi.org/10.1016/j.electacta.2022.141275)



How to increase the potential of aqueous Zn-MnO₂ batteries: The effect of pH gradient electrolyte

Ramona Dūrena, Anzelms Zukuls*, Mārtiņš Vanags, Andris Šutka

Faculty of Materials Science and Applied Chemistry, Riga Technical University, Institute of Materials and Surface Engineering, Paula Valdena 3/7, Riga LV-1048, Latvia

ARTICLE INFO

Keywords:

Amphoteric battery
Rechargeable
Dual electrolyte
Alkaline
Acidic

ABSTRACT

Non-rechargeable alkaline Zn-MnO₂ batteries are dominating the primary battery market and are a promising candidate for secondary battery storage systems as well. However, these batteries suffer from low potential and poor rechargeability. Here, we report a rechargeable membrane-less amphoteric aqueous Zn-MnO₂ battery with a 2.4 V open circuit potential. We have employed alkaline (KOH), acidic (H₂SO₄) and neutral (K₂SO₄) Pluronic F-127 hydrogels as electrolytes. By placing the anode in an alkaline environment but the cathode in an acidic environment, we have successfully widened the potential window in an aqueous medium avoiding hydrogen and oxygen evolution reactions. The obtained open circuit potential of as prepared amphoteric battery is stable for more than 25 h and 200 charge-discharge cycles.

1. Introduction

According to “International Energy Agency” information, the need, for batteries and energy storage devices with high power density and capacity in the global market, will multiply over the next decade [1]. Growth in the clean energy technology sector is inevitable due to various green policies [2–5], and energy independence from carbon-based energy production technologies, which will encourage renewable energy sources utilization i.e., wind, solar, tidal, wave and hydropower energy [6,7]. However, renewable energy sources suffer from uneven power generation and variable load patterns. Due to this reason rechargeable batteries are needed to provide energy on request [8,9].

Being one of the oldest battery technologies, Zn-MnO₂ primary batteries, have been studied since 1866 when they were invented by French engineer Georges-Lionel Leclanché [8] and redesigned in 1950 by Canadian engineer Lewis Urry [10–12]. A major obstacle to Zn-MnO₂ alkaline battery cells is its nominal potential of 1.5 V [13], as well as limited battery rechargeability, inhibiting its use as a secondary battery cell [14]. Different electrolytes (alkaline [15], neutral [15,16] and mildly acidic [17]) have been used to construct Zn-MnO₂ batteries with the hope to increase performance. However different electrolyte pH values induce various challenges for batteries and their construction. For example, using alkaline electrolytes, the cathode electrode during the charge/discharge cycles undergoes irreversible Mn₂O₄ and ZnMn₂O₄ phase formation [12,19]. In the neutral electrolyte, the secondary

phases of ZnMn₂O₄ and Zn₂Mn₃O₈ also limit battery performance [19]. In acidic electrolytes, a parasitic corrosion reaction occurs on the Zn anode resulting in H₂ gas release [20]. Various approaches have been implemented to mitigate these undesirable side reactions such as protective coatings on the anode surface like fumed silica and poly(ethylene glycol) [21]; additives in electrolytes like Li⁺ [19], Mn²⁺ [15]. However, the addition of Mn²⁺ additive to the aqueous electrolyte is not well understood [22]. Also, gel-solid electrolytes such as sodium polyacrylate hydrogel [23] can limit the growth of dendrites on the Zn anode surface [24].

Another route for increasing the performance of aqueous Zn-MnO₂ batteries by decoupling acidic and alkaline electrolyte mediums using membrane has been proposed by G. G. Yadav et al. in 2019 [25]. It was shown that it is possible to acquire stable open circuit potential (OCP) batteries of 2.45 and 2.8 V for 120 charge/discharge cycles in decoupled configuration separating two electrolyte mediums (alkaline and acidic) using several layers of cellophane membrane. In 2020 Zhong with co-authors [26] presented three-compartment (acidic, neutral, alkaline) Zn-MnO₂ batteries with OCP of 2.83 V and cycling stability for 200 h. For compartment separation SO₄²⁻ and K⁺ anion and cation-selective exchange membranes were used. To eliminate the need for separators and membranes another scientist group showed a membrane-less primary Zn-air battery constructed from Pluronic F-127 hydrogels with an OCP of 2 V [27].

In this work, we report a Zn-MnO₂ amphoteric rechargeable battery

* Corresponding author.

E-mail address: anzelms.zukuls@rtu.lv (A. Zukuls).

<https://doi.org/10.1016/j.electacta.2022.141275>

Received 13 July 2022; Received in revised form 6 September 2022; Accepted 28 September 2022

Available online 29 September 2022

0013-4686/© 2022 Elsevier Ltd. All rights reserved.

with an OCP of 2.4 V by employing both acidic (H_2SO_4) and alkaline (KOH) Pluronic F-127 hydrogels. The potential of this battery is much higher than that of single electrolyte (alkaline, neutral, or acidic) Zn-MnO₂ batteries, enabling a higher amount of energy to be obtained and stored. In this report, we characterize the electrochemical properties of the designed amphoteric hydrogel battery, also cathode and anode materials have been studied with X-ray diffractometer and Raman spectroscopy before use, in charged and discharged states. The reported battery design OCP is stable for more than 25 h and can be charged and discharged for at least 200 cycles while maintaining stable OCP.

2. Experimental section

2.1. Materials

For battery preparation following chemicals purchased from Sigma Aldrich were used: potassium hydroxide (KOH), sulphuric acid (H_2SO_4), carbon electrodes, Pluronic® F-127, dyes bromocresol green, methyl orange, manganese (IV) oxide (bulk density 600-800 kg m⁻³), zinc foil (0.2 mm thick), dimethylformamide (DMF). Potassium sulphate was purchased from AppliChem, carbon black (CB) (Printex XE-2) powder was purchased from Evonik Industries, carbon felt was purchased from China (Suzhou Surt Env. Protection Tech. Co., Ltd) and deionized water was obtained from Millipore Elix 3 water purification system.

2.2. Preparation of Pluronic® F-127 hydrogel electrolytes

Three types of gels were prepared – acidic, alkaline, and neutral. Firstly, aqueous solutions of 0.25 M, 0.5 M H_2SO_4 and 0.5 M, 1 M KOH and 0.4 M, 0.5 M, 0.6 M K_2SO_4 were prepared. Afterwards in the corresponding solutions, 30 mass% Pluronic® F-127 was dissolved. Dissolution of Pluronic® F-127 was carried out by placing a closed vessel in a refrigerator for two days and executing periodic stirring. For pH identification purposes saturated methyl orange water solution and saturated bromocresol green water solution were obtained. Both saturated colour solutions were accordingly added to the solutions in volume proportions against initial acid and alkaline solution volume 1:0.3:100 (methyl orange: bromocresol green: acidic/alkaline water solution). As a result, the acidic solution turned red and the alkaline solutions green, however, the neutral solution coloured yellow. Also, none of the colours affects the chemical reactions in the battery and does not affect its working parameters.

2.3. Preparation of electrodes

Zinc electrodes were pressed out as 12 mm diameter discs from 0.2 mm zinc foil sheets (weight of the electrodes around 0.16 g), cleaned with ethanol and used as follows. Two slits were cut into zinc foil and a zinc strip electrode extension was inserted and fixed. Electrodes of MnO₂ were prepared by mixing MnO₂ (Pyrolusite) with CB powder in a mass ratio of 13:5. For even mixing DMF was added to make a slurry which was then sonicated for 30 min. The obtained slurry was dried in a watch glass, afterwards, the powder was collected and grounded in a pestle. A thick slurry of cathode electrode was prepared by mixing acidic Pluronic F-127 hydrogel with the obtained MnO₂/CB powder until a spreadable consistency was reached.

2.4. Preparation of Zn-MnO₂ "syringe" batteries

Carbon felt was used as a matrix for MnO₂/CB electrode. The cathode electrode suspension was smeared on the carbon felt and placed in a syringe in which the carbon rod electrode had previously been placed. Afterwards, the necessary amount of acidic Pluronic F-127 hydrogel was pipetted. After the hydrogel was formed, a paper separator (Fig. S1) (for visual purposes only) was inserted, and alkaline hydrogel was poured onto the acidic hydrogel resulting in a two-layer electrolyte. For some

experiments, the third hydrogel with neutral pH was poured between acidic and alkaline hydrogels resulting in a three-layer electrolyte. The total amount of hydrogel used in the battery design was 3 mL; in the two-layer electrolyte, each hydrogel was 1.5 mL, and in the three-layer electrolyte, 1 mL. When the last layer was solidified into a gel, a Zn electrode with a syringe plunger was inserted. A scheme and a photo of obtained battery cell are shown in Fig. 1.

2.5. Characterization

Electrode active materials were analyzed with an X-ray diffractometer (Rigaku Ultima+ (Japan) using a Cu-K α radiation source ($\lambda = 0.154056$ nm) at 40 kV and 20 mA with a scanning rate of 2° min⁻¹. PDF -4+ database was used to analyze the obtained diffractograms. Raman scattering measurements were carried out with spectrometer Renishaw In-ViaV727 in backscattering configuration at room temperature. Samples were illuminated with Ar⁺ green laser with wavelength $\lambda = 514.5$ nm, grating -1200 mm⁻¹. Signal recording time was between 1 s and 10 s and 1 to 10 signal accumulations were collected from the sample spot. The electrode surface and morphology of the samples were determined with a scanning electron microscope (SEM) FEI Nova NanoSEM 650 with an integrated Energy-dispersive X-ray spectrometer (EDX). Electrochemical measurements were performed on potentiostat/galvanostat Autolab PGSTAT302N. Cyclic voltammetry (CV) was used to determine electrode oxidation and reduction states for half and full battery cells. Graphite electrode was used as a counter electrode, but Pt was utilized as a reference electrode. The sweep rate was 0.01 V s⁻¹. Chronopotentiometry measurements were utilized with 0.1; 1 or 10 mA s⁻¹ current during charge-discharge and cycling measurements. Battery charge-discharge performance was evaluated with the following chronopotentiometry sequence: OCP measurement -120 s, discharge/charge cycling with +/-1 mA s⁻¹ for 100 cycles (each charge/discharge cycle length limited to 120 s), OCP measurement for 120 s then discharge/charge sequence repeats as mentioned before, and last OCP measurement after 200 cycles for 120 s. OCP measurements were utilised with Autolab and Agilent (34970A) data logger switch unit. Mettler Toledo SevenGo SG3 conductivity metre was used to measure hydrogel conductivity. Galvanostatic charge-discharge curves for two-layered batteries were measured at 20, 25 and 35 mA g⁻¹ current densities. The potential window was limited to 2.0 V lower potential for discharge and 2.85 V upper potential for charging.

3. Results and discussion

Aqueous amphoteric Zn-MnO₂ battery cell (Fig. 1) was constructed of

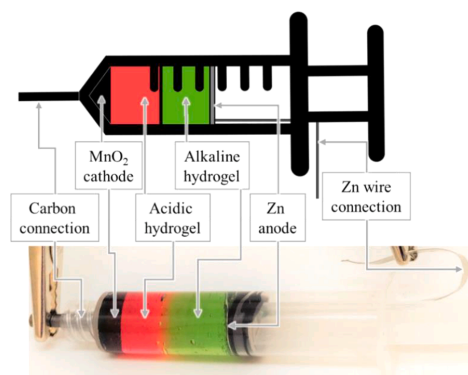
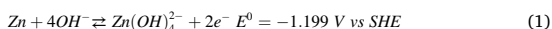


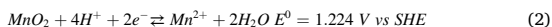
Fig. 1. Scheme and photo of the obtained battery cell with indicated components.

Zn metal anode, alkaline and acidic Pluronic F-127 hydrogel electrolyte, and β - MnO_2 /carbon cathode. The battery materials were analyzed with XRD, SEM, EDX and Raman spectroscopy before and after the battery discharge/recharge. Properties of the used materials are described in the supplementary information (Figs. S2–S11). In this battery design, no membranes were used. By operating the Zn metal anode in an alkaline hydrogel and MnO_2 cathode in an acidic hydrogel, this battery design yields an overall theoretical battery potential of 2.42 V. This is considerably higher than the primary alkaline Zn- MnO_2 battery (1.4 V – 1.7 V) [28]. The corresponding reactions and standard potentials versus standard hydrogen electrode (SHE) of amphoteric Zn- MnO_2 are as follows (Eqs. (1)–(3)):

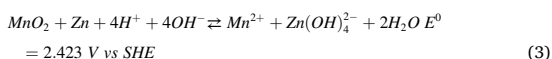
The anode in alkaline anolyte:



The cathode in acidic catholyte:



Overall reaction:



To determine theoretical cathode and anode behavior during battery operation cyclic voltammetry measurements were performed. MnO_2 and Zn electrode half-cells were measured against Pt reference electrode in acidic (0.5 M H_2SO_4) and alkaline (1 M KOH) hydrogels respectively. According to the presented combined data (Fig. 2(a)), amphoteric battery OCP is around 2.3 V. OCP measurements of the several prepared amphoteric batteries cells (inset of Fig. 2(a)) confirm that battery potential varies from 2.3 V to 2.4 V. The expected minimal battery discharge potential according to combined measurements should be

around 1.6 V.

The potential window of hydrogel electrolytes (Fig. S12) was also evaluated by cyclic voltammetry measurements. For the measurements, the hydrogel samples were placed between two graphite paper electrodes separated with a 2 mm Teflon spacer. Pluronic F-127 hydrogel electrolytes (1 M, 0.5 M KOH and 0.5 M, 0.25 M H_2SO_4 (equinormal to KOH)) were tested. Results show that electrolyte and graphite electrode cell configuration show capacitor behavior and no side reactions can be observed in a potential window of -2.2 V to $+2.2 \text{ V}$. However, Raman measurements of discharged battery anode reveal the formation of Pluronic F-127 hydrogel reduction products (Fig. S11). These reduction products observed in the measurement can be explained by ZnO photocatalytic activity [29], which could promote the degradation of the Pluronic F-127 hydrogel on the ZnO substrate in the presence of strong Raman laser radiation. Moreover, in the Raman spectrum of hydrogel from dismantled cycled batteries (Fig. S10), only Pluronic F-127 vibrational modes can be seen, indicating that no side reactions (hydrogel reduction or oxidation) take place during battery discharging and charging.

Cyclic voltammetry of the Zn- MnO_2 amphoteric battery cell (Fig. S13) in a potential window of 1.8 V – 2.8 V was carried out to evaluate battery capacity changes during the first 10 charge/discharge cycles. It revealed that the battery capacity increases due to MnO_2 recrystallization directly on the conductive carbon substrate during cycling. Also, Li with co-authors [30] and Gao with co-authors [31] have discussed this capacity modification and attributed it to activation of MnO_2 phase transition through recrystallization, powder morphology and grain size change [32–34].

To evaluate theoretical battery cut-off potential, full discharge of the Zn- MnO_2 amphoteric battery cell was carried out (Fig. 2(b)). The discharge plateau with a 10 mA s^{-1} current rate, confirms that the

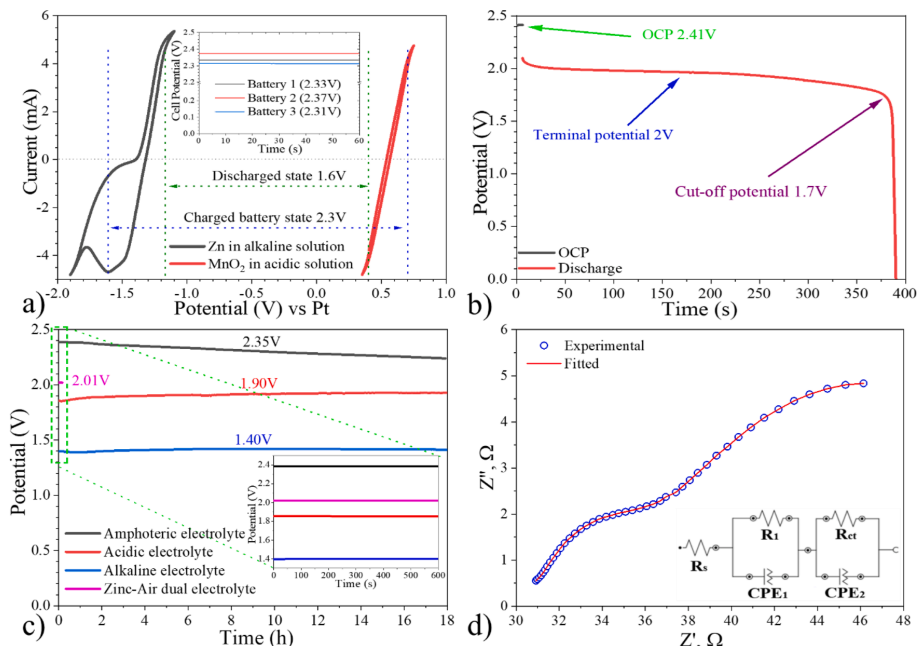


Fig. 2. Properties of an amphoteric battery: a) Cyclic voltammetry of battery half-cell electrodes in their corresponding electrolytes (scan rate 0.01 V s^{-1}) and comparison of battery cell performance after cell construction. b) Amphoteric Zn- MnO_2 battery OCP and discharge potential (discharge current 10 mA s^{-1}). c) OCP during 18 h of different pH electrolyte Zn- MnO_2 batteries compared to amphoteric Zn-air battery [27]. d) Impedance spectra for assembled amphoteric battery with OCP 2.319 V. The inset figure represents the equivalent circuit and the red line shows fitted results.

battery's lowest potential (cut-off potential) is around 1.7 V–1.6 V and corresponds with theoretical estimations from Fig. 2(a). The OCP at the start of the measurement was 2.4 V and the terminal potential around 2.0 V. Also, at a discharge current of $100 \mu\text{A s}^{-1}$ the terminal potential was 2.34 V (Fig. S14), however, during a 10 h discharge period the potential decreased to 2.2 V.

To evaluate the advantage of amphoteric Zn-MnO₂ battery, OCP measurements for acidic, alkaline, and stacked acidic/alkaline hydrogel electrolyte batteries are compared in Fig. 2(c). From these results, we can see that amphoteric hydrogel electrolyte Zn-MnO₂ battery OCP is higher (2.31 V) than acidic (1.91 V) and alkaline (1.41 V) hydrogel electrolyte batteries. The OCP of the amphoteric electrode battery corresponds with theoretical standard potential according to reaction (3). Also, acidic and alkaline OCP corresponds with their theoretical standard potential according to reactions (S1-S3) and (S4-S6). According to H. Yang and his co-author's work [35] ZnMn₂O₃ formation decreases battery performance, however, the cathode electrode can be reactivated with help of 0.1 M H₂SO₄ solution returning partial capacity of the MnO₂ electrode. Thus, in amphoteric and acidic Zn-MnO₂ batteries there is a low possibility of ZnMn₂O₃ formation on the electrode surface due to the acidic environment around the MnO₂ cathode electrode.

Moreover, we have compared our battery OCP results with Zn-air battery OCP (2.02 V) from Zhao and co-workers' work [27] (Fig. 2(c)) which also uses dual (acidic and alkaline) Pluronic F-127 hydrogel as electrolyte. Comparing the OCP of both batteries, our battery shows a higher OCP (2.31 V) due to the different standard potential reactions. In addition, the battery concept proposed here has advantages over the Zn-air battery such as better performance in a longer duration as the Zn-air battery is not sealed and the electrolyte hydrogel will evaporate water. Moreover, the battery concept proposed here is sealed and will contain its water content and electrolyte conductivity enabling the possibility of rechargeability, which is discussed below.

To evaluate and observe battery element behavior and resistance change during battery life electrochemical impedance spectroscopy was used for a fully assembled amphoteric battery. The Nyquist plot is demonstrated in Fig. 2(d). The imaginary part of the impedance is plotted versus its real component in the frequency range from 100 mHz to 10 kHz with a sinusoidal excitation signal of 10 mV. The 2 Constant Phase Element (CPE) model was used to fit the experimentally obtained Nyquist plot, and the fitting results (red line) are in good agreement with the experiment (blue dots). The series resistance obtained from the intercept with the Z' axis combines the resistance of the wire and the electrolyte. As shown in Table 1, its value is 30.5 ohms, which is large and characterizes the resistance of the gel electrolyte. As shown in Fig. 1, the thickness of the gel layer in the syringe is about 3 cm, which means a large distance between the electrodes and large series resistance. The first semicircle at high frequencies characterizes the interphase layer formed between the electrolyte and the electrode. In the equivalent circuit, this layer is characterized by the resistance R₁ and CPE₁ parallel connection. The R₁ value obtained in the model is 17 Ω and the CPE₁ equivalent capacity is 102 mF (see Table 1). Both are sensitive to the electrolyte composition [36] and the surface porosity at the electrode [37,38]. The second semicircle in the low-frequency range reflects a Faraday reaction. R_{ct} describes the charge transfer resistance and the value obtained in the model is 6.7 Ω. CPE₂ characterizes the double layer capacity and has a value of 39 mF. Equivalent circuit parameter values

Table 1
Fitted parameter values obtained from impedance data.

Parameter	Value	Error%
R _s	30,5 Ω	0,2
R ₁	17,2 Ω	6
C ₁	106 mF	3
R _{ct}	6,7 Ω	7
C _{dl}	39,1 mF	4

are summarised in Table 1.

Prolonged measurement of the OCP showed that after about 18 h, the OCP dropped from 2.25 to 1.9 V (Fig. S15). To better understand this drop, the impedance spectrum was measured every two hours and Nyquist plots of those measurements are shown in Supplementary Fig. S16. Nyquist plots show that during the time increases the value of the series resistance that characterizes the resistance of the electrolyte. In parallel with impedance measurements, a change in colour indication was also observed. Both the impedance spectra and the colour change indicate a mixing of alkaline and acidic media resulting in an increase in electrolyte resistance as the concentration of ions in the electrolyte decreases. Nyquist plot changes significantly at low frequencies after a potential drop. Such a change may characterize the presence of another electrochemical reaction, in which the resistance of the charge transfer is significantly different. As can be seen from the colour change (insets of Fig. S15), after 18 h the pH gradient has practically disappeared, and the cell is weakly acidic (the cell is orange). In the presence of an acid electrolyte, the reaction of Zn with an H⁺ in an acid medium is permissible according to the corrosion reaction (4) mentioned before. This may also explain the significant change in Nyquist plots at low frequencies after the disappearance of the pH gradient.

During all measurements, visible pH neutral layer formation in-between two hydrogels was observed. It can be assigned to the diffusion of H⁺ and OH⁻ ions from acidic and alkaline regions where they neutralize each other by forming water that further dilutes the acidic and alkaline hydrogels and creates extra resistance of the electrolyte. For this reason, the stability of amphoteric conditions was tested by constructing batteries with equinormal (1 M KOH/0.5 M H₂SO₄) or with alkaline/acidic hydrogel in supremacy (1 M KOH /0.25 M H₂SO₄ or 0.5 M KOH/0.5 M H₂SO₄). For these batteries, OCP was measured for 75 h (Fig. S17). Results show that in time batteries with equinormal acidic/alkaline hydrogels become neutral due to diffusion of acidic and alkaline hydrogels. As a result of the neutralization reaction, water content increases and H⁺ and OH⁻ ion content decreases. This leads to a rapid ion concentration and overall conductivity decrease. In the case of acidic hydrogel in supremacy, after diffusion mixing of hydrogels, the electrolyte becomes overall acidic and battery potential stays at around 1.9 V corresponding with our acidic battery OCP measurements (Fig. 2(c)) and other acidic Zn-MnO₂ batteries discussed in the literature [17,39,40]. It is important to note that as the acid diffused through hydrogel to the anode, a H₂ gas evolution (Eq. (4)) was observed due to corrosion reaction and is also discussed as a problem in literature [20,41,42].



However, the OCP of battery cell with alkaline hydrogel in supremacy (Fig. S17) gradually decreases reaching 1.5 V after 70 h. Observations and measurement results also match the OCP of our alkaline hydrogel battery cell (Fig. 2(c)) and the potential of the commercial alkaline Zn-MnO₂ primary cell [28]. The above-mentioned batteries, with different concentrations of acid/alkali, were discharged (Fig. S18) by connecting them to an external load (red light-emitting diodes with a forward potential of 1.7 V - 1.8 V). The aim was to discharge the batteries to the almost empty state and observe the potential and behavior of the discharged batteries in time. This measurement indicated that the energy stored in the battery can be discharged before the pH gradient in the electrolyte mixes and disappears. From the results, we observed that a battery with equinormal acidic/alkaline hydrogel electrolyte during and after discharge gradually loses its potential as electrolyte resistance slowly increases. The potential of a battery with an acidic hydrogel electrolyte in supremacy after discharge drops to 1.5 V. When the electrolyte turns acidic (after 7 h), the potential of the battery increases to 1.7 V–1.8 V. A battery with an alkaline electrolyte concentration in supremacy behaved similarly to a battery with acid hydrogel electrolyte concentration in supremacy, overtaking the acidic part of the electrolyte after 10 h and turning it into an alkaline battery cell. The potential of

this discharged battery was 0.6 V–0.7 V, and corresponds with an empty commercial primary alkaline battery (the state of an empty battery is defined as the potential below 0.9 V [14]).

Chronopotentiometry results for Zn-MnO₂ rechargeable battery with acidic and alkaline hydrogels (1 M KOH/0.5 M H₂SO₄) are shown in Fig. 3(a) and the OCP measurements before, after 100 cycles and after 200 cycles are shown in Fig. 3(b). Battery charge potential was around 2.7 V and discharge potential 2.2 V–2.3 V. OCP measurements (Fig. 3 (b)) indicate that the 2.34 V potential of amphoteric hydrogel battery remains stable throughout almost 14 h discharge-charge measurements. During measurement, the ion diffusion was observed with visible pH neutral layer formation in-between two hydrogels. This can be attributed to the diffusion of H⁺ and OH⁻ ions, where the acidic and alkaline regions meet and neutralize each other to form water. This further dilutes the acid and alkali and creates additional electrolyte resistance. Also, ion diffusion through hydrogel is inevitable as electrolyte does not have any Zn²⁺ or Mn²⁺. Furthermore, K⁺ and SO₄²⁻ ions (which are alkali and acid counter ions and provide the ion conductivity in the electrolyte) migrate to the middle of the battery too. Due to the limited potassium sulphate solubility in water (120 g L⁻¹ at 25 °C), it crystallizes in the middle of the battery and creates another extra resistance to the electrolyte. To overcome this salt formation, Na⁺ and Li⁺ or other inert cation hydroxides could be added to the electrolyte (hydrogel) to decrease K⁺ ion concentration and decrease insoluble salt formation since the solubility in water for sodium sulphate (281 g L⁻¹ at 25 °C) and lithium sulphate (349 g L⁻¹ at 25 °C) is better.

The previously discussed reactions Eqs. (5)–(7) are as follows:

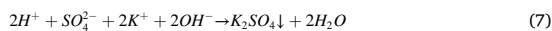
Neutralization reaction:



Excess salt formation reaction:



Overall reaction:



To confirm these claims, we have analyzed the solid precipitate from the middle of the battery with Raman spectroscopy. In the Raman spectra (Fig. S19) few intensive peaks can be seen. All the peaks correspond with vibrations of SO₄²⁻ but the peak precise position indicates that the material is K₂SO₄. For other cation-saturated sulphates, the peaks for the corresponding modes are shifted. The peak at 455 cm⁻¹ corresponds to ν₂(E) mode, 619 cm⁻¹ to ν₄(F₂) mode, 983 cm⁻¹ to ν₁(A₁) mode, however 1107 cm⁻¹ and 1145 cm⁻¹ to ν₃(F₂) mode [43].

Regarding the formation of water and salt crystals in the battery, the charge and discharge cycles were limited to 120 s. This was implemented because the battery could not be recharged efficiently enough after a longer discharge cycle due to the formation of water and salt causing a significant increase in internal resistance. Further research on electrolytes is needed to determine the need for salts and their specific concentrations for optimal battery performance. Both electrolytes should consist of Zn²⁺ and Mn²⁺ ions in some form, which would limit diffusion and increase the battery stability. Also, the performance of electrodes should be optimized. Since the MnO₂ active material is nonconductive it should be embedded in a conductive matrix. CB does not provide enough rigid and stable matrix, therefore other conductive matrices should be investigated like graphdiyne [44–48].

To evaluate the effects of the neutral layer in the battery design, we have tested battery configurations with a specific concentration of neutral hydrogel between acidic and alkaline hydrogels as well

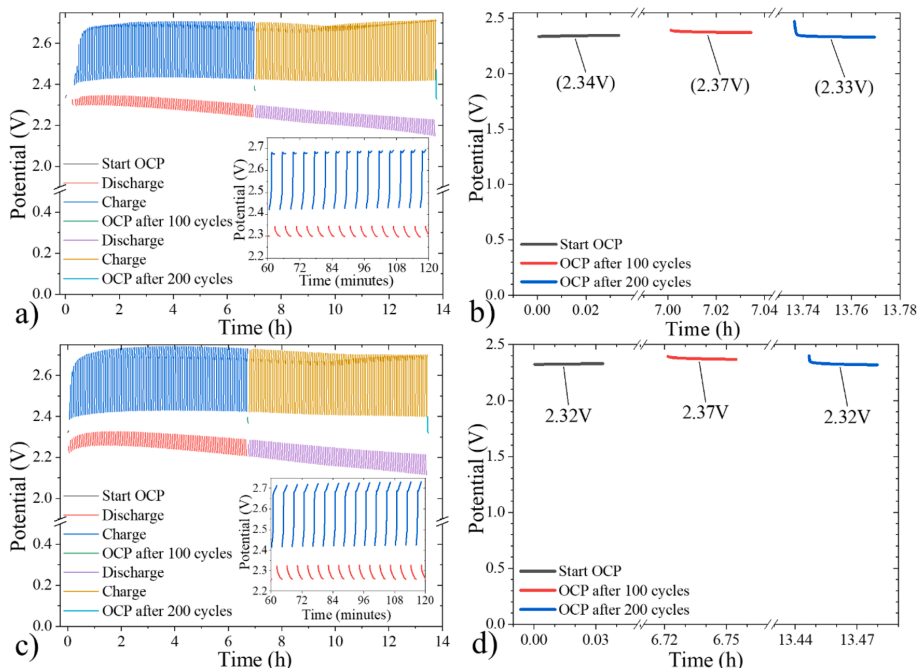


Fig. 3. Chronopotentiometry measurements of Zn-MnO₂ amphoteric battery with acidic and alkaline (1 M KOH / 0.5 M H₂SO₄) hydrogel electrolyte layers ((a)-(b)): (a) charge/discharge curves and (b) OCP before, after 100, and 200 charging/discharging cycles. Measurements of Zn-MnO₂ amphoteric battery with acidic, neutral, and alkaline (1 M KOH / 0.5 M K₂SO₄ / 0.5 M H₂SO₄) hydrogel electrolyte layers ((c)-(d)): (c) charge/discharge curves and (d) OCP before, after 100, and 200 charging/discharging cycles. Charge-discharge current ± 1 mA s⁻¹ and the time for each operation is limited to 120 s.

(Fig. S20). The neutral electrolyte concentration varied with respect to the alkali/acid concentration with lower, equal, or higher K_2SO_4 normality, respectively. K_2SO_4 concentrations in the neutral layer were 0.4 M, 0.5 M and 0.6 M. According to measurements, a three-layer (acidic/neutral/alkaline) electrolyte holds potential better than acidic/alkaline electrolyte battery. In three-layer electrolyte batteries, the pH gradient stability is more pronounced than in two-layer batteries. These batteries were also connected to the diode circuit to monitor their behavior while being discharged. Nonetheless, all batteries (both alkaline/acidic and alkaline/neutral/acidic with different concentrations of K_2SO_4 in the neutral layer) behave similarly within 40 h, and their potential decreases to 1.6 V - 1.7 V (Fig. S21).

Also, chronopotentiometry and OCP measurements (Fig. 3(c) and (d)) were performed with a three-layer electrolyte (alkaline/neutral/acidic - 1 M KOH/0.5 M K_2SO_4 /0.5 M H_2SO_4) battery. OCP for three-layer hydrogel battery (Fig. 3(d)) stayed stable (2.32 V) similarly as for two-layer battery shown in Fig. 3(b). Three-layer hydrogel battery charge potential was 0.5 V higher, and discharge potential was 0.5 V lower than two-layer hydrogel battery potential (Fig. 3(a)). The charge and discharge potential discrepancy is due to larger hydrogel electrolyte resistance in three-layer hydrogel electrolyte. For 0.5 M H_2SO_4 hydrogel, the conductivity is 83.6 mS cm^{-1} (23 °C, gelled). Meanwhile, for 1 M KOH hydrogel conductivity is 78.6 mS cm^{-1} (23 °C, gelled). However, the conductivity of the neutral 0.5 M K_2SO_4 hydrogel is 12.6 mS cm^{-1} (23 °C, gelled). Thus, the conductivity of the neutral gel is more than 6 times lower than that of the acidic and alkaline hydrogels. Meaning, that the overall resistance of a three-layer electrolyte is significantly larger than that of a two-layer electrolyte and creates the discharge and charge potential discrepancy.

Also, the galvanostatic charge-discharge curves with specific capacities of the amphoteric Zn-MnO₂ are shown in Fig. S22. When charging/discharging at a current density of 35 mA g⁻¹, the battery cannot be operated efficiently. However, by reducing the current density to 25 mA g⁻¹ and 20 mA g⁻¹, it is possible to reach a battery capacity of 12 mAh g⁻¹ and 25 mAh g⁻¹ at a limited battery discharge to 2.0 V. Below this threshold a deep discharge is reached, after which the battery capacity drops rapidly. This phenomenon has also been described elsewhere in the literature [49].

4. Conclusion

We have developed an aqueous Zn-MnO₂ amphoteric rechargeable battery with an OCP of 2.4 V. During the operation of the Zn-MnO₂ amphoteric battery, we managed to perform 200 charge-discharge cycles. Owing to an innovative approach, which combines acidic and alkaline electrolyte hydrogels, it is possible to create a pH gradient that provides the desired conditions at the MnO₂ cathode and Zn anode and increases both electrode half-reaction standard potentials and rechargability. By employing only acidic or alkaline hydrogels the obtained battery OCP is only 1.9 and 1.4 V, accordingly. It should be noted that ion-selective membranes separating acidic and alkaline electrolyte media have not been used to ensure battery performance. The resulting batteries can maintain the pH gradient for more than 25 h. Also, a neutral layer forms in the contact area between the acidic and alkaline hydrogels. However, after the battery employment for several hours, a K_2SO_4 precipitate is observed in the contact area due to ion mixing between both hydrogels and the limited solubility of K_2SO_4 . Thus, by optimizing hydrogels, electrodes, and electrolytes, battery life could be extended and the rechargability improved, allowing these batteries to be recharged and discharged thousands of times.

CRedit authorship contribution statement

Ramona Dürëna: Conceptualization, Validation, Formal analysis, Investigation, Writing – original draft, Visualization. **Anzelms Zukuls:** Conceptualization, Methodology, Validation, Formal analysis,

Investigation, Resources, Writing – original draft, Visualization, Supervision, Project administration, Funding acquisition. **Martiņš Vanags:** Validation, Formal analysis, Investigation, Writing – original draft. **Andris Šutka:** Resources, Writing – review & editing.

Declaration of Competing Interest

The authors declare that they have no known competing financial interests or personal relationships that could have appeared to influence the work reported in this paper.

The authors declare the following financial interests/personal relationships which may be considered as potential competing interests:

Data Availability

Data will be made available on request.

Acknowledgement

This work was supported by the Latvian Council of Science in the framework of FLPP (Investigation of electrodes and electrolytes for obtaining amphoteric decoupled rechargeable batteries, lzp-2021/1-0142).

Supplementary materials

Supplementary material associated with this article can be found, in the online version, at doi:10.1016/j.electacta.2022.141275.

References

- [1] International Energy Agency, World Energy Outlook 2021, October 20 (2021) 1–386. <https://www.iea.org/reports/world-energy-outlook-2021>.
- [2] Q. Jiang, S.I. Khattak, M. Ahmad, P. Lin, Mitigation pathways to sustainable production and consumption: examining the impact of commercial policy on carbon dioxide emissions in Australia, *Sustain. Prod. Consum.* 25 (2021) 390–403, <https://doi.org/10.1016/j.spc.2020.11.016>.
- [3] T.Y. Chen, C.J. Huang, A two-tier scenario planning model of environmental sustainability policy in Taiwan, *Sustainability* 11 (2019) 2336, <https://doi.org/10.3390/su11082336>.
- [4] I. Kougiyas, N. Taylor, G. Kakoulaki, A. Jäger-Waldau, The role of photovoltaics for the European green deal and the recovery plan, *Renew. Sustain. Energy Rev.* 144 (2021), 111017, <https://doi.org/10.1016/j.rser.2021.111017>.
- [5] S. García-Freites, C. Gough, M. Röder, The greenhouse gas removal potential of bioenergy with carbon capture and storage (BECCS) to support the UK's net-zero emission target, *Biomass Bioenergy* 151 (2021), 106164, <https://doi.org/10.1016/j.biombioe.2021.106164>.
- [6] A.K. Barik, S. Jaiswal, D.C. Das, Recent trends and development in hybrid microgrid: a review on energy resource planning and control, *Int. J. Sustain. Energy* 41 (2022) 308–322, <https://doi.org/10.1080/14786451.2021.1910698>.
- [7] G. Massabí, Renewable energy sources (Basics). Venezuela: A Petro-State Using Renewable Energies, VS Verlag für Sozialwissenschaften, Wiesbaden, 2008, pp. 84–109, https://doi.org/10.1007/978-3-531-91003-1_4.
- [8] T. Placke, R. Kloepsch, S. Dühnen, M. Winter, Lithium ion, lithium metal, and alternative rechargeable battery technologies: the odyssey for high energy density, *J. Solid State Electrochem.* 21 (2017) 1939–1964, <https://doi.org/10.1007/s10008-017-3610-7>.
- [9] Y. Sui, C. Liu, R.C. Masse, Z.G. Neale, M. Atif, M. AlSalhi, G. Cao, Dual-ion batteries: the emerging alternative rechargeable batteries, *Energy Storage Mater.* 25 (2020) 1–32, <https://doi.org/10.1016/j.ensm.2019.11.003>.
- [10] J. Song, K. Xu, N. Liu, D. Reed, X. Li, Crossroads in the renaissance of rechargeable aqueous zinc batteries, *Mater. Today* 45 (2021) 191–212, <https://doi.org/10.1016/j.mattod.2020.12.003>.
- [11] D. Akinyele, J. Belikov, Y. Levron, Battery storage technologies for electrical applications: impact in stand-alone photovoltaic systems, *Energies* 10 (2017) 1760, <https://doi.org/10.3390/en10111760> (Basil).
- [12] J. Shin, J.K. Seo, R. Yaylian, A. Huang, Y.S. Meng, A review on mechanistic understanding of MnO₂ in aqueous electrolyte for electrical energy storage systems, *Int. Mater. Rev.* 65 (2020) 356–387, <https://doi.org/10.1080/09506608.2019.1653520>.
- [13] Y.G. Lee, M.G. Choi, K.Y. Kang, K.M. Kim, Preparation and electrochemical performance of 1.5V and 3.0V-class primary film batteries for radio frequency identification (RFID), *J. Electrochem. Sci. Technol.* 1 (2010) 39–44, <https://doi.org/10.5229/JECST.2010.1.1.039>.

- [14] E. Faegh, T. Omasta, M. Hull, S. Ferrin, S. Shrestha, J. Lechman, D. Bolintineanu, M. Zuraw, W.E. Mustain, Understanding the dynamics of primary Zn-MnO₂ alkaline battery gassing with operando visualization and pressure cells, *J. Electrochem. Soc.* 165 (2018) A2528–A2535, <https://doi.org/10.1149/2.0321811jes>.
- [15] H. Pan, Y. Shao, P. Yan, Y. Cheng, K.S. Han, Z. Nie, C. Wang, J. Yang, X. Li, P. Bhattacharya, K.T. Mueller, J. Liu, Reversible aqueous zinc/manganese oxide energy storage from conversion reactions, *Nat. Energy* 1 (2016) 16039, <https://doi.org/10.1038/nenergy.2016.39>.
- [16] Q. Duan, Y. Wang, S. Dong, D.Y.W. Yu, Facile electrode additive stabilizes structure of electrolytic MnO₂ for mild aqueous rechargeable zinc-ion battery, *J. Power Sources* 528 (2022), 231194, <https://doi.org/10.1016/j.jpowsour.2022.231194>.
- [17] D. Chao, W. Zhou, C. Ye, Q. Zhang, Y. Chen, L. Gu, K. Davey, S. Qiao, An electrolytic Zn-MnO₂ battery for high-voltage and scalable energy storage, *Angew. Chem. Int. Ed.* 58 (2019) 7823–7828, <https://doi.org/10.1002/anie.201904174>.
- [18] B.J. Hertzberg, A. Huang, A. Hsieh, M. Chamoun, G. Davies, J.K. Seo, Z. Zhong, M. Croft, C. Erdonmez, Y.S. Meng, D. Steingart, Effect of multiple cation electrolyte mixtures on rechargeable Zn-MnO₂ alkaline battery, *Chem. Mater.* 28 (2016) 4536–4545, <https://doi.org/10.1021/acs.chemmater.6b00232>.
- [19] D. Perez-Antolin, I. Sáez-Bernal, A. Colina, E. Ventosa, Float-charging protocol in rechargeable Zn-MnO₂ batteries: unraveling the key role of Mn²⁺ additives in preventing spontaneous pH changes, *Electrochem. Commun.* 138 (2022), 107271, <https://doi.org/10.1016/j.elecom.2022.107271>.
- [20] A. Mitha, H. Mi, W. Dong, I.S. Cho, J. Ly, S. Yoo, S. Bang, T.K.A. Hoang, P. Chen, Thixotropic gel electrolyte containing poly(ethylene glycol) with high zinc ion concentration for the secondary aqueous Zn/LiMn₂O₄ battery, *J. Electroanal. Chem.* 836 (2019) 1–6, <https://doi.org/10.1016/j.jelechem.2019.01.014>.
- [21] C. Qiu, X. Zhu, L. Xue, M. Ni, Y. Zhao, B. Liu, H. Xia, The function of Mn²⁺ additive in aqueous electrolyte for Zn/8-MnO₂ battery, *Electrochim. Acta* 351 (2020), 136445, <https://doi.org/10.1016/j.jelelectacta.2020.136445>.
- [22] Y. Huang, Z. Li, Z. Pei, Z. Liu, H. Li, M. Zhu, J. Fan, Q. Dai, M. Zhang, L. Dai, C. Zhi, Solid-state rechargeable Zn/NiCo and Zn-Air batteries with ultralong lifetime and high capacity: the role of a sodium polyacrylate hydrogel electrolyte, *Adv. Energy Mater.* 8 (2018), 1802288, <https://doi.org/10.1002/aenm.201802288>.
- [23] K. Lu, T. Jiang, H. Hu, M. Wu, Hydrogel electrolytes for quasi-solid zinc-based batteries, *Front. Chem.* 8 (2020) 1–12, <https://doi.org/10.3389/fchem.2020.546728>.
- [24] G.G. Yadav, D. Turney, J. Huang, X. Wei, S. Banerjee, Breaking the 2V barrier in aqueous zinc chemistry: creating 2.45 and 2.8V MnO₂-Zn aqueous batteries, *ACS Energy Lett.* 4 (2019) 2144–2146, <https://doi.org/10.1021/acscenergylett.9b01643>.
- [25] C. Zhong, B. Liu, J. Ding, X. Liu, Y. Zhong, Y. Li, C. Sun, X. Han, Y. Deng, N. Zhao, W. Hu, Decoupling electrolytes towards stable and high-energy rechargeable aqueous zinc-manganese dioxide batteries, *Nat. Energy* 5 (2020) 440–449, <https://doi.org/10.1038/s41560-020-0584-y>.
- [26] S. Zhao, T. Liu, Y. Dai, Y. Wang, Z. Guo, S. Zhai, J. Yu, C. Zhi, M. Ni, All-in-one and bipolar-membrane-free acid-alkaline hydrogel electrolytes for flexible high-voltage Zn-air batteries, *Chem. Eng. J.* 430 (2022), 132718, <https://doi.org/10.1016/j.cej.2021.132718>.
- [27] M.B. Lim, T.N. Lambert, B.R. Chalmala, Rechargeable alkaline zinc-manganese oxide batteries for grid storage: mechanisms, challenges and developments, *Mater. Sci. Eng. R Rep.* 143 (2021), 100593, <https://doi.org/10.1016/j.mser.2020.100593>.
- [28] K. Qi, B. Cheng, J. Yu, W. Ho, Review on the improvement of the photocatalytic and antibacterial activities of ZnO, *J. Alloys Compd.* 727 (2017) 792–820, <https://doi.org/10.1016/j.jallcom.2017.08.142>.
- [29] Y. Li, S. Wang, J.R. Salvador, J. Wu, B. Liu, W. Yang, J. Yang, W. Zhang, J. Liu, J. Yang, Reaction Mechanisms for Long-Life Rechargeable Zn/MnO₂ Batteries, *Chem. Mater.* 31 (2019) 2036–2047, <https://doi.org/10.1021/acs.chemmater.8b05093>.
- [30] Y. Gao, J. Zhou, L. Qin, Z. Xu, Z. Liu, L. Wang, X. Cao, G. Fang, S. Liang, Crystal plane induced in-situ electrochemical activation of manganese-based cathode enable long-term aqueous zinc-ion battery, *Green Energy Environ.* (2022), <https://doi.org/10.1016/j.gee.2022.02.009>.
- [31] S.R. Srither, A. Karthik, M. Selvam, K. Saminathan, V. Rajendran, K.V.I.S. Kaler, Nano-sized MnO₂ particles produced by spray pyrolysis for a Zn/MnO₂ primary cell: comparative discharge performance studies with their bulk counterparts, *RSC Adv.* 4 (2014) 42129–42136, <https://doi.org/10.1039/C4RA05060F>.
- [32] D.S. Li, Q.L. Gao, H. Zhang, Y.F. Wang, W.L. Liu, M.M. Ren, F.G. Kong, S.J. Wang, J. Chang, MnO₂ particles grown on the surface of N-doped hollow porous carbon nanospheres for aqueous rechargeable zinc ion batteries, *Appl. Surf. Sci.* 510 (2020), 145458, <https://doi.org/10.1016/j.apsusc.2020.145458>.
- [33] Z. Tang, W. Chen, Z. Lyu, Q. Chen, Size-dependent reaction mechanism of λ-MnO₂ particles as cathodes in aqueous zinc-ion batteries, *Energy Mater. Adv.* 2022 (2022) 1–12, <https://doi.org/10.34133/2022/9765710>.
- [34] H. Yang, W. Zhou, D. Chen, J. Liu, Z. Yuan, M. Lu, L. Shen, V. Shulga, W. Han, D. Chao, The origin of capacity fluctuation and rescue of dead Mn-based Zn-ion batteries: a Mn-based competitive capacity evolution protocol, *Energy Environ. Sci.* 15 (2022) 1106–1118, <https://doi.org/10.1039/D1EE03547A>.
- [35] W. Choi, H.C. Shin, J.M. Kim, J.Y. Choi, W.S. Yoon, Modeling and applications of electrochemical impedance spectroscopy (EIS) for lithium-ion batteries, *J. Electrochem. Sci. Technol.* 11 (2020) 1–13, <https://doi.org/10.33961/jecst.2019.00528>.
- [36] C. Hitz, A. Lasia, Experimental study and modeling of impedance of the her on porous Ni electrodes, *J. Electroanal. Chem.* 500 (2001) 213–222, [https://doi.org/10.1016/S0022-0728\(00\)00317-X](https://doi.org/10.1016/S0022-0728(00)00317-X).
- [37] L. Birry, A. Lasia, Studies of the hydrogen evolution reaction on raneey nickel-molybdenum electrodes, *J. Appl. Electrochem.* 34 (2004) 735–749, <https://doi.org/10.1023/B:JACH.0000031161.26544.6a>.
- [38] C.F. Bischoff, O.S. Fitz, J. Burns, M. Bauer, H. Gentscher, K.P. Birke, H. M. Henning, D. Biro, Revealing the local pH value changes of acidic aqueous zinc ion batteries with a manganese dioxide electrode during cycling, *J. Electrochem. Soc.* 167 (2020), 020545, <https://doi.org/10.1149/1945-7111/ab6c57>.
- [39] A.S. Poyraz, J. Laughlin, Z. Zec, Improving the cycle life of cryptomelane type manganese dioxides in aqueous rechargeable zinc ion batteries: the effect of electrolyte concentration, *Electrochim. Acta* 305 (2019) 423–432, <https://doi.org/10.1016/j.electacta.2019.03.093>.
- [40] V.P. Hoang Huy, L.T. Hieu, J. Hur, Zn metal anodes for Zn-ion batteries in mild aqueous electrolytes: challenges and strategies, *Nanomaterials* 11 (2021) 2746, <https://doi.org/10.3390/nano11102746>.
- [41] A. Bayaguud, Y. Fu, C. Zhu, Interfacial parasitic reactions of zinc anodes in zinc ion batteries: underestimated corrosion and hydrogen evolution reactions and their suppression strategies, *J. Energy Chem.* 64 (2022) 246–262, <https://doi.org/10.1016/j.jechem.2021.04.016>.
- [42] J. Qiu, X. Li, X. Qi, Raman spectroscopic investigation of sulfates using mosaic grating spatial heterodyne raman spectrometer, *IEEE Photon. J.* 11 (2019) 1–12, <https://doi.org/10.1109/JPHOT.2019.2939222>.
- [43] Y. Fang, Y. Liu, L. Qi, Y. Xue, Y. Li, 2D graphdiyne: an emerging carbon material, *Chem. Soc. Rev.* 51 (2022) 2681–2709, <https://doi.org/10.1039/D1CS00592H>.
- [44] J. An, H. Zhang, L. Qi, G. Li, Y. Li, Self-expanding ion-transport channels on anodes for fast-charging lithium-ion batteries, *Angew. Chem. Int. Ed. Engl.* (2022) 61, <https://doi.org/10.1002/anie.202113313>.
- [45] F. Wang, Z. Zuo, L. Li, K. Li, F. He, Z. Jiang, Y. Li, Large-area aminated-graphdiyne thin films for direct methanol fuel cells, *Angew. Chem.* 131 (2019) 15152–15157, <https://doi.org/10.1002/ange.201910588>.
- [46] X. Luan, Z. Zheng, S. Zhao, Y. Xue, Y. Li, Controlled growth of the interface of CdWO₃/GDY for hydrogen energy conversion, *Adv. Funct. Mater.* (2022), <https://doi.org/10.1002/adfm.202202843>.
- [47] C. Huang, Y. Li, N. Wang, Y. Xue, Z. Zuo, H. Liu, Y. Li, Progress in research into 2D graphdiyne-based materials, *Chem. Rev.* 118 (2018) 7744–7803, <https://doi.org/10.1021/acs.chemrev.8b00288>.
- [48] N.D. Ingale, J.W. Gallaway, M. Nyce, A. Couzis, S. Banerjee, Rechargeability and economic aspects of alkaline zinc-manganese dioxide cells for electrical storage and load leveling, *J. Power Sources* 276 (2015) 7–18, <https://doi.org/10.1016/j.jpowsour.2014.11.010>.



Ramona Zukule (dzim. Dūrena) dzimusi 1996. gada 18. decembrī Limbažos. Rīgas Tehniskajā universitātē (RTU) ieguvusi inženierzinātņu bakalaura grādu ķīmijas tehnoloģijā (2019) un inženierzinātņu maģistra grādu nanomateriālu tehnoloģijās (2021).

Kopš 2021. gada studē RTU doktorantūrā, pētot ūdens bāzes cinka-mangāna dioksīda (Zn-MnO_2) baterijas, to elektrolītu modifikācijas un elektrodu stabilizācijas mehānismus. No 2022. līdz 2024. gadam bijusi RTU pētniece un strādājusi FLPP projektā "Elektrodu un elektrolītu izpēte amfotēras atsaistītas uzlādējamās baterijas iegūšanai". Iepriekš strādājusi arī Latvijas Universitātes Cietvielu fizikas institūtā, kopš 2025. gada februāra ir SIA "AAA Law Latvia" patentpilnvarnieka asistente. Zinātniskās intereses saistītas ar ūdens bāzes Zn-MnO_2 bateriju attīstību, elektrolītu un elektrodu mijiedarbības izpēti un nanomateriālu lietojumu elektroķīmiskajās sistēmās.

Ramona Zukule (née Dūrena) was born on 18 December 1996 in Limbaži. She obtained a Bachelor's degree in Chemical Technology (2019) and a Master's degree in Nanomaterials Technologies (2021) from Riga Technical University (RTU). Since 2021, she has been pursuing doctoral studies at RTU, focusing on water-based zinc-manganese dioxide (Zn-MnO_2) batteries, their electrolyte modifications, and electrode stabilization mechanisms. From 2022 to 2024, she was a researcher at RTU and participated in the FLPP project "Investigation of electrodes and electrolytes for obtaining amphoteric decoupled rechargeable batteries." She has also worked at the Institute of Solid State Physics, University of Latvia, and since February 2025, has been a patent attorney assistant at AAA Law Latvia Ltd. Her scientific interests are related to the development of water-based Zn-MnO_2 batteries, the study of electrode-electrolyte interactions, and the application of nanomaterials in electrochemical systems.